

NASA Contractor Report 185219

2348

The Effect of Hydrogen and Microstructure on the Deformation and Fracture Behavior of a Single Crystal Nickel-Base Superalloy

William S. Walston
Carnegie-Mellon University
Pittsburgh, Pennsylvania

April 1990

Prepared for
Lewis Research Center
Under Grant NAG3-463

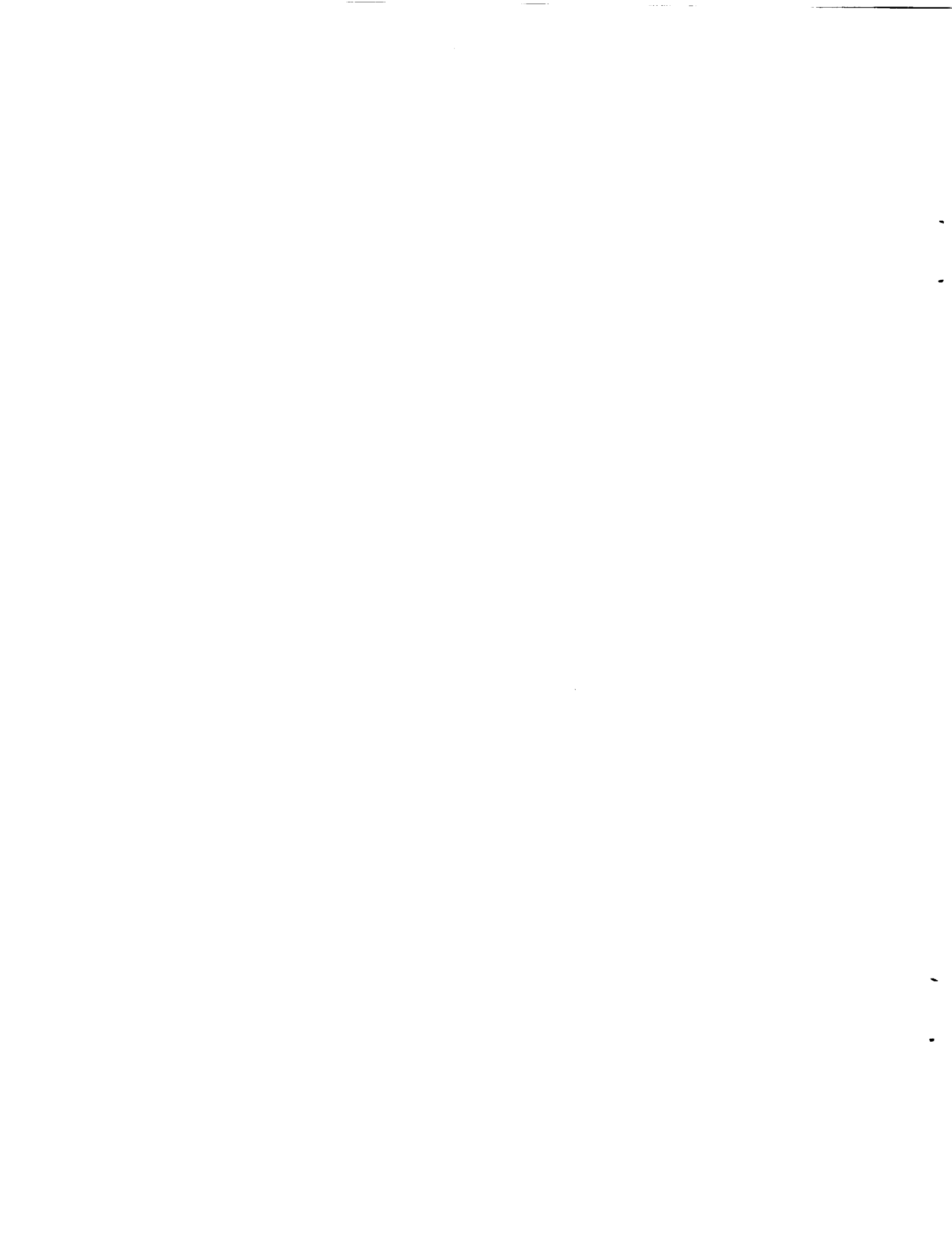


National Aeronautics and
Space Administration

(NASA-CR-185219) THE EFFECT OF HYDROGEN AND
MICROSTRUCTURE ON THE DEFORMATION AND
FRACTURE BEHAVIOR OF A SINGLE CRYSTAL
NICKEL-BASE SUPERALLOY Final Report Ph.D.
Thesis (Carnegie-Mellon Univ.) 254 p

N90-21849

63/26 0275663
Unclas



ABSTRACT

A study has been conducted on the effects of internal hydrogen and microstructure on the deformation and fracture of a single crystal nickel-base superalloy. In particular, room temperature plane strain fracture toughness and tensile tests were performed on hydrogen-free and hydrogen charged samples of PWA 1480. The role of microstructure was incorporated by varying the levels of porosity and eutectic γ/γ' through hot isostatic pressing and heat treatment.

The room temperature behavior of PWA 1480 was unusual because precipitate shearing was not the primary deformation mechanism at all strains. At strains over 1%, dislocations were trapped in the γ matrix, and an attempt was made to relate this behavior to compositional differences between PWA 1480 and other superalloys. Another unique feature of the tensile behavior was cleavage of the eutectic γ/γ' , which is believed to initiate the failure process. Fracture occurred on {111} planes and is likely a result of shear localization along these planes. Elimination of the eutectic γ/γ' greatly improved the tensile ductility, but porosity had no effect on tensile properties.

Large quantities of hydrogen (1.74 at.%) were gas-phase charged into the material, but surprisingly this was not a function of the amount of porosity or eutectic γ/γ' present. Desorption experiments suggest that the vast majority of hydrogen is at reversible lattice trapping sites. This large, uniform concentration of hydrogen dramatically reduced the tensile strain to failure, but only slightly affected the reduction in area. Further evidence of strain localization due to hydrogen was observed in the deformation structure. Available hydrogen embrittlement models were examined in light of these results and it was found that the hydrogen enhanced localized plasticity model can explain much of the tensile behavior.

K_{IC} fracture toughness tests were conducted, but it was necessary to also perform J_{IC} tests to provide valid data. Unexpectedly, the values from these tests did not agree; further, the crack growth behavior and fractography differed greatly. The eutectic γ/γ' behaved differently in these two types of tests, and the possible effect of the unloading present in J_{IC} tests on this constituent was examined.

ACKNOWLEDGEMENTS

The research described herein was made possible by the financial support of NASA Lewis Research Center. The support and assistance of project monitor Dr. R.L. Dreschfield is gratefully acknowledged. I would like to thank my advisors, Drs. I.M. Bernstein, A.W. Thompson and J.C. Williams. They made the changing of the guards as easy as possible, and I am indebted to each of them for the guidance and encouragement they have provided along the way.

Special thanks are due to Dr. N.R. Moody of Sandia National Laboratories, who graciously performed the hydrogen charging of all samples. His cooperation and assistance, as well as many helpful discussions on hydrogen effects are greatly appreciated. Thanks are also extended to Dr. J.P. Lucas of Sandia for performing the short rod fracture toughness tests. Through the course of this work, there were many who provided insight and assistance, including Dr. M. Dollar of Illinois Institute of Technology, Dr. J. Chené of Université Paris Sud, Dr. L.G. Fritzemeier of Rocketdyne and Dr. W.M. Garrison, Jr. of Carnegie Mellon University.

Finally, I would like to thank my family for their encouragement throughout this endeavor. My parents were wise enough to instill in me the desire to learn and the will to accomplish my goals. Above all, I owe my deepest appreciation to my wife, Courtney, who not only understood the rigors and crazy hours of graduate school, but also was willing to use her skills in proofreading this document.

TABLE OF CONTENTS

1 INTRODUCTION.....	1
2 BACKGROUND.....	5
2.1 Single Crystal Nickel-Base Superalloys.....	5
2.1.1 General Background.....	5
2.1.1.1 Solidification process	6
2.1.1.2 Heat treatment and hot isostatic pressing	10
2.1.1.3 Composition effects	14
2.1.1.4 Anisotropy.....	15
2.1.2 Deformation Behavior	17
2.1.2.1 General characteristics	18
2.1.2.2 Flow stress modeling	20
2.1.2.3 Tension/Compression asymmetry	27
2.1.3 Fracture Behavior	28
2.1.3.1 Crystallographic fracture.....	28
2.1.3.2 Relation to microstructure	31
2.1.4 Effect of Hydrogen on Superalloys.....	32
2.2 PWA 1480	36
2.2.1 Relevant Studies.....	37
2.2.2 Effect of Hydrogen	39
2.3 Hydrogen Embrittlement Processes.....	40
2.3.1 Trap Theory.....	41
2.3.1.1 Determination of the trap binding energy	43
2.3.2 Hydrogen Enhanced Localized Plasticity.....	47
2.4 Fracture Toughness of Polycrystal and Single Crystal Superalloys	49
2.4.1 Micromechanistic Fracture Initiation Models	51
2.5 Background Summary.....	53
3 EXPERIMENTAL PROCEDURES	55
3.1 Material Preparation.....	55
3.1.1 As-Received Material	55
3.1.2 Laue X-ray Analysis.....	55
3.1.3 Heat Treatment	56
3.1.4 Hot Isostatic Pressing	59
3.1.5 Hydrogen Charging, Analysis and Desorption.....	60

3.2	Microstructural Characterization.....	61
3.2.1	Metallography	61
3.2.2	Quantitative Metallography.....	62
3.3	Mechanical Testing.....	65
3.3.1	Tensile Testing	65
3.3.2	Compression Testing.....	66
3.3.3	K_{IC} Testing	67
3.3.4	J_{IC} Testing	68
3.4	Deformation and Fractography Characterization	70
3.4.1	TEM Foil Preparation and TEM Procedure	70
3.4.2	Slip Band Analysis.....	72
3.4.3	Sectioning Experiments	73
3.4.4	Pre-Strain and Pre-Charge Tensile Tests.....	74
3.4.5	Quantitative Fractography.....	74
3.4.6	Crystallographic Fracture Orientations	75
3.4.7	Fractographic Analysis Techniques.....	77
4	RESULTS.....	80
4.1	Microstructural Characterization.....	80
4.1.1	Alternate Heat Treatment	84
4.1.2	Hot Isostatic Pressing	85
4.2	Hydrogen Trapping Characteristics.....	89
4.3	Mechanical Properties	93
4.3.1	Tensile Properties	93
4.3.1.1	Effect of hydrogen.....	93
4.3.1.2	Effect of eutectic γ/γ'	99
4.3.1.3	Effect of porosity	101
4.3.2	Compression Properties.....	103
4.3.3	Fracture Toughness.....	103
4.3.3.1	K_{IC} results.....	103
4.3.3.2	J_{IC} results.....	104
4.4	Deformation Behavior in Tension and Compression	106
4.4.1	Development of Deformation Structure.....	106
4.4.1.1	Effect of hydrogen.....	113
4.4.1.2	Effect of eutectic γ/γ'	118
4.4.2	Slip Character.....	119
4.4.3	Double Notch Tensiles and Sectioned Tensiles.....	125

4.4.4	Pre-Strain and Pre-Charge Tensile Tests.....	127
4.5	Tensile Fracture Behavior.....	128
4.5.1	General Fracture Characteristics.....	128
4.5.2	Effect of Hydrogen	135
4.5.3	Effect of Alternate Heat Treatment and HIP'ing.....	137
4.6	Fracture Toughness.....	137
4.6.1	Fracture of K_{IC} Samples	137
4.6.2	Fracture of J_{IC} Samples	142
5	DISCUSSION.....	149
5.1	Hydrogen Solubility and Trapping.....	150
5.2	Tension and Compression Properties.....	155
5.3	Deformation and Fracture Behavior without Hydrogen	162
5.4	Deformation and Fracture Behavior with Hydrogen.....	170
5.5	Analysis of Strengthening.....	175
5.6	Fracture Toughness.....	177
6	CONCLUSIONS.....	184
7	SUGGESTIONS FOR FUTURE RESEARCH.....	189
8	REFERENCES	192

APPENDICES

APPENDIX A	Metallography Data and Tensile Properties.....	202
APPENDIX B	Deformation and Fracture Behavior of <130> Samples	207
APPENDIX C	Short Rod K_{IC} Testing	213
APPENDIX D	Hydrogen-induced Crack Growth.....	222
APPENDIX E	Tritium Autoradiography	234
APPENDIX F	Quantitative Results of Reppich CRSS Model.....	244

CHAPTER 1

INTRODUCTION

Nickel-base superalloys must possess a favorable balance of high temperature properties, such as creep strength, thermal fatigue resistance and oxidation resistance, for use in gas turbine and rocket engine applications.¹ It is possible to attain this wide array of mechanical properties by adjusting the complex compositions of these alloys, which in turn affect the characteristics of the microstructure produced. Nickel-base superalloys consist of a nickel-rich fcc γ phase and an ordered fcc (L_{12} -type) γ' phase based on Ni_3Al . The γ' phase precipitates from the γ phase by an aging reaction, with modern superalloys usually containing a high volume fraction (~60-70%) of cuboidal γ' precipitates. These γ' precipitates are typically coherent with the γ matrix having mismatches of less than 0.5%. The γ' precipitate strength can more than double with temperature up to 700°C,² which gives nickel-base superalloys their excellent high temperature strength.

The compositions of nickel-base superalloys generally are very complex, and many of the properties are controlled by the partitioning of these elements to the γ or γ' phase.³ Al, Ti, W, and Ta preferentially segregate to the γ' phase, and thus are added to increase the γ' volume fraction and provide solid solution strengthening.⁴ Solid solution strengthening of the γ phase is accomplished by additions of Cr and Mo, as well as W and Al.³ Cr and Al also are very important in providing oxidation and corrosion resistance.¹ In order to obtain a finite difference between the γ' solvus temperature and the incipient melting temperatures, elements such as Co are added.⁵ There are many other elements that are typically added to nickel-base superalloys, and the reader is referred to several reviews of compositional effects for further details.^{1,3,4}

It is important in achieving maximum engine performance to operate at the highest possible temperature. Thus, increasing the working temperature of superalloys has been a

major driving force behind superalloy design and development. Initially, compositional and microstructural variations provided higher temperature benefits, but increases during the last 20 years have primarily stemmed from processing advances. Directional solidification and single crystal casting techniques have pushed the operating temperature of superalloys past 1100°C (about 85-90% of the melting temperature).⁶ Pratt and Whitney pioneered the development of directional solidification, which culminated in 1980 with the production of single crystalline PWA 1480.⁷ PWA 1480 and other single crystal superalloys have demonstrated superior performance over conventionally cast superalloys primarily because of their higher melting temperatures and γ' solvus temperatures. These advantages stem from the elimination of grain boundary strengthening elements necessary in polycrystals.⁷

Based on the superior performance of single crystal superalloys under ambient conditions, their potential use in hydrogen-fueled engines is under consideration.⁸ Many potential single crystal alloys have been screened using notch tensile tests and other mechanical tests performed in hydrogen atmospheres designed to simulate service conditions.⁸ These tests provided valuable initial data, but did not completely evaluate the alloy's resistance to hydrogen embrittlement. To this end, NASA began a program at Carnegie Mellon to fundamentally characterize the effect of hydrogen on single crystal superalloys. PWA 1480 was one of the alloys chosen based on promising results of tests conducted in hydrogen atmospheres.

This study concentrated primarily on room temperature properties since hydrogen embrittlement is generally most severe near this temperature. As-received PWA 1480 contained substantial amounts of porosity and eutectic γ/γ' , and the effects of these were systematically studied because of their possible role as hydrogen trapping sites. Hydrogen was introduced into the material by gas-phase charging resulting in a uniform internal concentration, followed by testing in air. Gas-phase charging was used, as opposed to cathodic charging,^{9,10} because it is easier to assess hydrogen's effects when a uniform

concentration is present, in contrast to a thin surface layer. There have been only two other investigations of the effect of a uniform concentration of hydrogen on single crystal superalloys,⁹⁻¹¹ and both of these were performed on CMSX-2. Therefore, it was important to first determine the role of hydrogen trapping in this type of alloy by means of tritium autoradiography and hydrogen desorption experiments. To study the effect of internal hydrogen and microstructure on the deformation and fracture behavior, series of tensile tests were performed, followed by TEM studies and the use of a variety of fractographic examination techniques.

The fracture toughness of these types of alloys has never been studied before, although it could be an important design criterion should a crack develop in service. Thus, the crack growth behavior and fracture toughness were studied on compact tension specimens as a function of hydrogen and microstructure. In a parallel study covered in Appendix C, Dr. J.P. Lucas of Sandia National Labs performed short rod fracture toughness tests using fractured halves of full size toughness samples that had been previously tested at Carnegie Mellon. This study was done to expand the knowledge and characterization of this novel testing technique to a new class of alloys.

Another important situation that could be encountered in service is crack propagation at values below K_{IC} due to the presence of a hydrogen atmosphere. Again, this area has not been studied on single crystal superalloys, and hydrogen-induced crack growth experiments in a hydrogen gas atmosphere were performed at Sandia under the direction of Dr. N.R. Moody. The background, description and results of these tests are given in Appendix D.

In summary, the main goals of this work were:

- 1) To characterize the extent of hydrogen trapping and its effect on mechanical properties.

- 2) To characterize the effect of hydrogen and microstructure on the tensile deformation and fracture behavior. To relate the observed behavior to available hydrogen embrittlement models.
- 3) To evaluate the crack growth behavior and fracture toughness as a function of hydrogen and microstructure. To relate the fracture toughness to microstructural crack initiation sites through micromechanistic models.
- 4) To evaluate the resistance to hydrogen-induced crack growth and to compare the results to tests on internally charged specimens.
- 5) To compare all observations to similar work on polycrystal and single crystal superalloys in an attempt to make generalizations concerning the effect of hydrogen and microstructure on this class of alloys.

Chapter 2

BACKGROUND

2.1 Single Crystal Nickel-Base Superalloys

2.1.1 General Background

The technology that led to single crystal superalloys is primarily responsible for the increase in the use temperature of superalloys over the past twenty years.¹² Single crystal processing research was pioneered by Pratt and Whitney in the 1970s, culminating in the production of PWA 1480 in 1980.⁷ Major advantages of single crystals are the increases achieved in melting and solution heat treatment temperature, as well as in the γ' solvus temperature. These increases stem from the elimination of the grain boundary strengthening elements; boron, carbon, hafnium, and zirconium, which are necessary additions in polycrystals to eliminate grain boundary failure. Elimination of these elements also prevents borides and carbides from acting as fatigue initiation sites, which results in improved single crystal fatigue properties. Single crystals also possess superior high temperature creep strength and ductility compared to polycrystals and directionally solidified superalloys.¹³ However, single crystal superalloys are not perfect, and many of their problems are a direct result of the crystal growth process. Among these are localized recrystallization, segregation, incipient melting, anisotropy and porosity. Through extensive research, these problems are now becoming understood and can be controlled, as the next few sections discuss.

First, the single crystal solidification process will be covered, outlining the formation of all phases and constituents. Local elemental segregation occurs during solidification, and the discussed heat treatment attempts to reduce this segregation. The

heat treatment also maximizes the γ' precipitate size and volume fraction, which control the mechanical properties. Also as a result of the solidification process, porosity is formed, and its elimination by Hot Isostatic Pressing (HIP'ing) will be discussed. Finally, the effect of the complex composition and the inherent anisotropy on several physical and mechanical properties will be covered.

2.1.1.1 Solidification process

The single crystal solidification process plays a key role in affecting subsequent properties. Therefore, it is important to understand the origin of such deleterious phenomena as interdendritic porosity, eutectic γ/γ' and segregation, to better assess their roles in the performance of single crystal nickel-base superalloys.

A schematic of the generic single crystal solidification process is shown in Figure 2.1. The molten superalloy is poured into a ceramic mold, and dendritic solidification begins at the the water cooled chill plate in the form of several grains of various orientations. The mold temperature⁷ is usually around 1500-1600°C, and the thermal gradient is approximately 70°C/cm. The $\langle 001 \rangle$ orientation has been shown to have the highest growth rate, and after a certain distance, the $\langle 001 \rangle$ grains overtake all others and proceed into the helical grain selector. The most favorably oriented of these grains emerges and fills the mold. The resulting single crystal is usually within 10° of the $\langle 001 \rangle$ orientation with dendrites aligned along the three orthogonal $\langle 001 \rangle$ directions.

Within the microstructure, the γ phase has formed as well as any other constituents, such as eutectic γ/γ' , or mu and sigma phases. In PWA 1480, the only other constituent besides γ and γ' is the eutectic $\gamma-\gamma'$. Upon solidification, the γ phase forms first, but as the temperature drops, and there is still molten metal in the interdendritic region, the eutectic γ/γ' is nucleated. It has been noted that there are two types of eutectic γ/γ' present in superalloys:¹⁵ The eutectic γ/γ' formed at higher temperatures, which is finer and lacelike

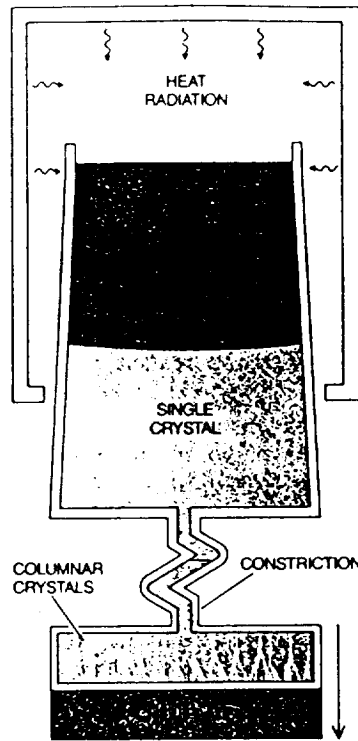


Figure 2.1 Schematic of the single crystal solidification process.¹⁴

in appearance, and that formed at lower temperatures, which appears more uniform and consists of mostly γ' . Yaoxiao, et al.,¹⁵ also divide the eutectic γ/γ' into three distinct regions: nucleation, core and cap. The appearance of each kind of eutectic γ/γ' in PWA 1480 will be discussed later, as will the significance of each regime.

There also is porosity present in the interdendritic region along with the eutectic γ/γ' . Porosity is found in cast superalloys due to the molar volume decrease that occurs upon solidification. Campbell¹⁶ was the first to treat this problem in depth and proposed an equation to describe pore nucleation:

$$P_g + P_s = P^* \quad (2-1)$$

where P_g is the gas pressure in the liquid, P_s is the shrinkage pressure and P^* is the pressure to nucleate a pore. P_g will be very small in superalloys due to the low solubility of gases in nickel.¹⁷ This analysis has been extended¹⁸ to include variables that may either

be controlled during the single crystal solidification process or changed through compositional variations. One variable that relates to this thesis is the thermal gradient, and it has been observed that the amount of porosity decreases as the gradient is increased.^{18,19} It also was found that increasing the amounts of Al, Ti and Co increase porosity, while higher amounts of Cr decrease porosity.¹⁶

Campbell¹⁶ stated that for Fe and Al alloys, P^* is very high and cannot be attained by homogeneous nucleation. Therefore, nuclei will most likely be needed to facilitate nucleation, and as an example, he suggested inclusions containing poorly-wetting solid and liquid phases. This suggestion of heterogeneous nucleation of pores is of particular interest for PWA 1480 due to the relationship found to exist between pores and eutectic γ/γ' , as discussed later.

Thermal stability of the pores was studied by Anton and Giamei¹⁷ in a single crystal nickel-base superalloy. They found that even a small amount of time at the solution temperature would dramatically increase the volume fraction and slightly increase the size of the as-cast porosity. They explained these increases by the Kirkendall mechanism of pore growth, which relies on compositional gradients and subsequent associated vacancy diffusion. The increase in growth rate and volume fraction would be expected to level off after a certain time because of the competition between Kirkendall-induced migration and loss of vacancies to the surface. In fact, it was found that the increase in size and volume fraction was only significant at times up to 1.2 hour, and at times longer than 4 hours the pores began to shrink and disappear.¹⁷ This is an important result for this study because time spent at the solution temperature was used as a variable.

Besides porosity, the solidification process also leads to macroscopic and microscopic segregation of elements. On a macroscopic scale, there are composition gradients associated with the dendritic macrostructure, which are determined by the partition coefficients of each alloy. In a study on CMSX-2,²⁰ a similar single crystal superalloy, it was found that Ta and W segregated heavily to the dendrite core and arms,

while Co and Cr showed a slight increase in this region over the average composition. There was very little change in the composition profiles of Al or Ti. Elements also will partition between the γ or γ' phase. Table 2.1 shows the results of an atom microprobe analysis on PWA 1480.²¹ Al, Ta, Ti and W primarily segregate to the γ' phase, while Cr and Co segregate to the γ phase.

Table 2.1 Microprobe analysis of the composition (at%) of the γ and γ' phases in PWA 1480.

	Al	Ti	Cr	Ni	Co	Ta	W
γ matrix	2.79	0.17	34.03	49.26	11.01	0.56	2.15
γ' precipitate	15.4	2.85	2.17	70.10	3.10	4.59	1.68

An unusual result was observed in the γ' phase of CMSX-2.²¹ A local concentration gradient was observed in the γ' near the γ/γ' interface. This most likely occurred due to the growth during the second aging heat treatment of the γ' particles that were nucleated in the first aging treatment. The two stage aging heat treatment will be explained in the next section. This local concentration gradient is quite narrow in comparison to the total γ' size, but it may prove important in terms of dislocation behavior in as much as a changing composition can affect the APB energy and therefore the stress to move dislocations in this region. These results for CMSX-2 should be quite similar to those that would be found in PWA 1480 due to the similar compositions, microstructures and two-stage aging heat treatment.

2.1.1.2 Heat treatment and hot isostatic pressing

The heat treatment of single crystal nickel-base superalloys involves a solution heat treatment stage followed by an aging treatment and is similar to other precipitation heat treatments in alloys such as Al-Cu. The solution heat treatment in PWA 1480 is designed to homogenize the segregation that occurred during solidification and to dissolve any unwanted constituents, such as primary γ' or eutectic γ/γ' .²² The solution heat treatment temperature is in the equilibrium γ phase field; above the γ solvus and below the incipient melting temperature (IMT). Incipient melting is the local melting of any low melting temperature alloy constituents. This is a serious problem in many single crystals because the heat treatment window (difference between the γ solvus and the IMT) is normally very small. Careful control and ramping of the temperature is thus essential to avoid incipient melting.

Figure 2.2 shows a normal solution heat treatment cycle with the resulting incipient melting temperature (IMT). The IMT increases in this figure due to the diffusion and homogenization of any low melting temperature alloy constituents such as the eutectic γ/γ' . This heat treatment cycle characterizes the type used in this work. It can be seen from this figure that any slight temperature fluctuations could lead to incipient melting. It is estimated that in the as-cast condition, PWA 1480 has an incipient melting point of 1290°C-1292°C when this type of heat treatment cycle is followed.²³ This is only slightly above the solution heat treatment temperature of 1288°C used in this study, so incipient melting was a real concern.

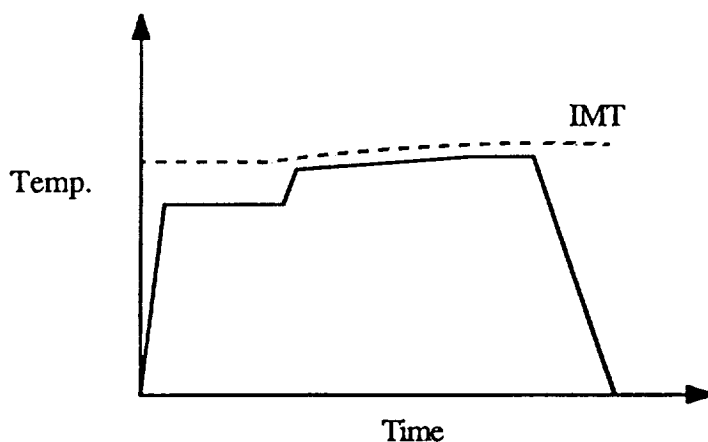


Figure 2.2 Typical solution heat treatment cycle for PWA 1480 and the corresponding incipient melting temperature (IMT).

The solution heat treatment stage is always followed by rapid cooling to avoid unwanted precipitation of the γ phase. A two-stage aging heat treatment follows with the nucleation of the γ phase controlled in the first aging heat treatment stage. There also is some growth of the γ precipitates during the first aging treatment, while in the second aging heat treatment the growth process continues until the desired volume fraction and size of γ has precipitated. The second aging treatment was originally designed for diffusion bonding of coatings to the alloy for service needs; however, this step is now commonly used on uncoated samples to obtain better control of the γ precipitation process.

Pratt and Whitney has received a recent U.S. patent on a modified solution heat treatment, which claims a more homogeneous material free of incipient melting.²⁴ In fact, it is further claimed that material which has undergone incipient melting can be healed by this treatment with no loss in mechanical properties.²⁴ The novel approach calls for the IMT to actually be exceeded. Figure 2.3 shows the proposed solution heat treatment cycle. The key is that sufficient time must be spent at the final temperature of 1302°C to allow the damage of incipient melting to heal by substantial diffusion. As it is held at this temperature, the IMT is continuously increasing so that the material is soon below the IMT. The purposeful exceeding of the IMT and the subsequent healing guarantee that the

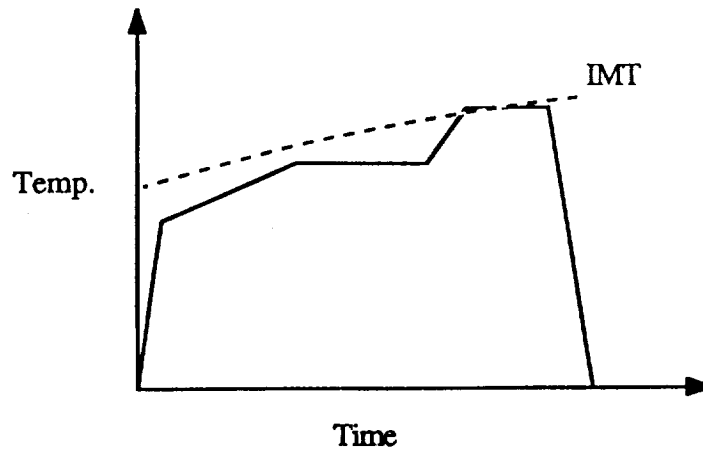


Figure 2.3 Modified heat treatment for PWA 1480 showing how IMT is exceeded.

resultant microstructure will be more compositionally homogeneous. This technique has recently been successfully demonstrated on PWA 1480 by Rocketdyne.²⁵ Unfortunately, this modified solution heat treatment could not be used in this work, because its existence was not known until the majority of samples had already been heat treated. It is reported here simply for completeness, as well as to contribute to the understanding of the phenomenon of incipient melting.

The removal of porosity through Hot Isostatic Pressing (HIP'ing) will now be discussed. It is well known that porosity resulting from solidification shrinkage in superalloy castings can serve as crack initiation sites, reducing the useful life of the alloy under conditions of fatigue or creep. HIP'ing has been used for many years on polycrystal superalloys to eliminate porosity and improve mechanical properties.²⁶⁻²⁸ Studies also have been carried out on single crystals that show improved properties after HIP'ing.^{19,28,29} While there are associated drawbacks to HIP'ing, including altered microstructures and unwanted carbides,^{28,30} modifications to the HIP'ing cycle and post-HIP heat treatments can usually overcome these. With single crystals, special care is needed to avoid recrystallization, particularly as the absence of grain boundary strengthening elements would result in severe degradation of mechanical performance.

It has been observed that when conventional HIP'ing cycles were employed with single crystals, local recrystallization usually occurred,^{31,32} believed due to the deformation associated with closing the pores. Conventional HIP'ing cycles have been modified to avoid such recrystallization.^{32,33} A conventional cycle would involve increasing the pressure and temperature up to desired levels and then holding for a period of time. A less severe pressure and temperature versus time schedule was needed for single crystals, and Eridon and Dalal³² have developed a cycle at Howmet Corp. that involves a two-step increase in pressure. During heating to a value near the normal solution temperature, pressure is first applied below the level needed to close the pores. The pressure is provided by a gaseous atmosphere, usually argon. Once the desired temperature is reached, it is held for a period to assure a uniform temperature throughout the sample. Finally, the pressure is increased at a moderate rate up to the pressure necessary to close the pores. The samples are left under these conditions for a period of time to allow diffusional processes to occur. The authors have outlined the specific conditions needed for PWA 1480 as follows:³²

- 1) Heat to 1288°C under pressure of 34.5 MPa.
- 2) Hold for 1-2 hours.
- 3) Increase pressure at a rate of 0.4-0.55 MPa/min. to 103.5 MPa.
- 4) Hold for 4 hours.

Rocketdyne³³ has developed a similar cycle, which has been used on the samples in this work. Unfortunately the details of that cycle currently are restricted by a U.S. Patent Secrecy Order, although it is likely similar to the one cited above. It is claimed for PWA 1480 that this HIP'ing cycle completely removes the casting porosity,³³ while avoiding recrystallization. Furthermore, the microstructure is said to be better homogenized due to the extended time at the solution temperature during HIP'ing. The same study showed no effect of HIP'ing on the tensile properties but an increased stress-rupture life and improved fatigue properties.³³ Crack initiation now occurred at surface defects, eutectic γ/γ or isolated small carbides instead of subsurface pores.

2.1.1.3 Composition effects

The occurrence of compositional segregation is important due to the effect that composition has on many physical and mechanical properties. In terms of this thesis, it is most relevant to know the effect of certain elements on the solid solution strengthening of γ and γ' , the stacking fault energy, and the antiphase boundary energy. These quantities are known for some alloys of simpler compositions, and as a rough estimate it may be inferred from the compositional differences of PWA 1480 what these values may be, or at least the trend that should be followed.

PWA 1480 is an advanced superalloy with some significant compositional differences from most other superalloys. Of course, grain boundary strengthening elements such as C, B, Zr and Hf are not present. A key characteristic is the large amount of Ta added to give high creep strength and oxidation resistance.⁷ Cr and Al levels also are relatively high to ensure oxidation and corrosion resistance. The W level is lower than in many alloys, as is the Co level. It also should be mentioned that Mo and V are not present, particularly as comparisons will be made in the thesis to CMSX-2, which contains a slight amount of Mo, a lower Ta level and a higher W level with all other elemental levels being similar.

In these single crystal high volume fraction γ' superalloys, strengthening below 60% of the melting temperature is due to overcoming the Anti-phase Boundary (APB) energy, the presence of a high volume fraction of particles and solid solution strengthening. The largest contribution is the APB energy,² and thus knowledge of compositional effects on this quantity is important. It also is important to determine the effect of composition on the Stacking Fault Energy (SFE), since dislocations splitting in the γ matrix would have a profound effect on the deformation behavior. A low SFE would make it harder to constrict the partials and shear the γ' precipitates. The information concerning compositional effects on stacking fault energy (SFE) and antiphase boundary energy (APBE) are not very

conclusive. It is believed that Ni has a high SFE,³⁴ but the resultant effect on this value of many elements acting in combination is not known. It has been reported that Ti strongly increases the SFE in Ni₃Al alloys, while Cr and Co slightly increase it.¹ There is no evidence on the effect of other alloy elements, and no available data on the SFE of PWA 1480 or similar alloys.

There has only been one detailed study of the effect of various elements on the APBE of Ni₃Al-based alloys.³⁵ Brown and Ham concluded that Cr increases and Ti decreases the APBE. This is not especially relevant for PWA 1480 considering Cr strongly segregates to the γ phase, and Ti is only present in the alloy in a small amount. Nguyen³⁶ reports, without reference, that Ta should increase the APBE, but Decker³ states that Ti and Ta should not significantly change the APB energy. Therefore, it is clear that the trend in the SFE or APBE cannot be estimated *a priori* for PWA 1480.

In examining the effect of composition on solid solution strengthening, it is clear that one of the main differences between PWA 1480 and other superalloys is the increased level of Ta. It is well known that Ta is a strong solid solution hardener, and it has been shown to strongly segregate to γ .²¹ Other compositional differences are not as great, and it is not thought they would play a significant role in altering solid solution strengthening in comparison to similar alloys. Many studies have shown that small amounts of Ta dramatically increase the yield stress of Ni₃Al-based alloys.^{4,37-39} Thus, it is probable that PWA 1480 has a higher γ yield stress than most other superalloys.

2.1.1.4 Anisotropy

Single crystal superalloys are very anisotropic, and therefore it is necessary to know the value of physical constants as a function of orientation. Elastic constant data will be important in subsequently analyzing the fracture toughness data and the dislocation behavior in the γ and γ' phases. To begin with, the Young's modulus, E, for cubic

materials can be calculated from:⁴⁰

$$1/E = S_{11} - 2(S_{11} - S_{12} - 1/2 S_{44})(l_1^2 l_2^2 + l_2^2 l_3^2 + l_3^2 l_1^2) \quad (2-2)$$

where S_{ij} are the elastic compliances and l_{ij} are the direction cosines. In many cases, the elastic data are reported in the form of the stiffness, C_{ij} , which can be converted into elastic compliance. The shear modulus can be calculated from:⁴¹

$$1/G = 4/3(S_{11} - S_{12}) + 1/3 S_{44} \quad \text{on } (111)[1\bar{1}0] \quad (2-3)$$

Thus, the necessary elastic constant data can be obtained from elastic compliance values. Many authors concerned with the elastic properties of superalloys have merely estimated the superalloy constants from the results of Ni and Ni₃Al.^{12,42} The purpose of this section is to take advantage of the measured data from superalloys and determine the best estimate for PWA 1480. While there have been relatively few actual measurements on γ/γ' alloys,⁴³⁻⁴⁵ considerable data exists for both Ni and Ni₃Al.^{40,46-48} Perhaps the best study on Ni₃Al was done by Kayser and Stassis,⁴⁸ and their data are shown in Table 2.2 along with data on Ni.⁴⁰ The data on Ni are much older and may be less reliable.

Wallow, et al.,⁴³ performed an excellent study on a few different γ/γ' alloys examining the effect of temperature, composition and volume fraction of γ' . They analyzed Nimonic 105 with γ' volume fractions of 10% and 50%. From this data they extracted the elastic constants of the γ' phase by assuming that C_{ij} was linear with the volume fraction of γ' . The γ' elastic constants were calculated from an alloy made of the γ' composition. These results are shown in Table 2.2 as 105 γ' and 105 γ' .

The data of Wallow, et al., compare favorably with other γ/γ' alloys of different compositions.^{44,45} From this information, it may be concluded that composition only affects the elastic constants slightly. The closeness of the γ and γ' values also suggests that modulus hardening is not important and any modulus effects on dislocation behavior should be negligible.

Table 2.2 Elastic Compliances of Various Alloys (10^{-6}MPa^{-1})

	S_{11}	S_{12}	S_{44}
Ni	7.99	-3.12	8.44
Ni_3Al	9.52	-3.79	7.99
105 γ	7.86	-3.02	7.28
105 γ'	8.03	-3.08	7.80
PWA 1480A	9.06	-3.59	8.13
PWA 1480B	7.98	-3.06	7.64

Nimonic 105: (at.%) Ni, 10Al, 18Co, 16Cr, 1.5Ti, 3Mo, plus minor elements

The elastic compliances for PWA 1480 have been calculated from a rule of mixtures method using 70% γ . The results also are shown in Table 2.2 as PWA 1480A and PWA 1480B, where A was calculated from Ni and Ni_3Al , and B was calculated from 105 γ and 105 γ' . The elastic compliances for A and B differ somewhat, but the difference in the Young's modulus turns out to be fairly small. The two extremes of the Young's modulus, $\langle 001 \rangle$ and $\langle 111 \rangle$ have been calculated:

$$\begin{aligned} E_{100}^A &= 110 \text{ GPa} & E_{111}^A &= 300 \text{ GPa} \\ E_{100}^B &= 125 \text{ GPa} & E_{111}^B &= 316 \text{ GPa} \end{aligned}$$

All further calculations in this study, will be made using an average value from method A and B above. Thus, in the [001] orientation, Young's modulus is 118 GPa and the shear modulus is 54.5 GPa.

2.1.2 Deformation Behavior

The deformation of single crystal nickel-base superalloys is mainly controlled by the nature of the γ/γ' microstructure. Most importantly, there is a coherent interface between the γ matrix and the γ' precipitate with a typical misfit of less than 0.5%. This allows for matrix dislocations to penetrate the interface and shear the ordered γ' precipitates

provided this is energetically favorable. Furthermore, since there is a large volume fraction (>60%) of γ precipitates, dislocation bypass is not possible, except at high temperatures.⁴⁹ Therefore, at the temperatures of interest in this work, shearing of the γ precipitates by dislocations should be the primary mode of deformation.

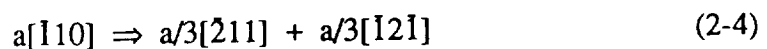
2.1.2.1 General characteristics

Since the γ precipitate is an $L1_2$ -type phase, it is necessary for pairs of dislocations to travel through the phase so that the second dislocation may restore the order that the first dislocation altered. Before the pair can enter the γ precipitate from the matrix, the antiphase boundary (APB) energy of the γ precipitate must be provided by the applied stress.⁵⁰ There also are other factors to consider that are examined in the next section. The normal shearing process that occurs in superalloys involves a pair of $a/2\langle 110 \rangle$ dislocations lying on a $\{111\}$ plane separated by a distance determined by the APB energy. This type of behavior has been observed in many single crystal superalloys at the low temperatures (<400°C) used in this work.^{11,51-53} The only difference between deformation in single crystals versus polycrystals would, of course, be due to grain boundaries. In a single slip orientation, there would be no obstacles to dislocation motion in a single crystal. However, in this study, [001] samples primarily were used, which undergo multiple slip in tension. From simple Schmid factor calculations, it is apparent that there are multiple systems that are equally stressed, which can quickly lead to dislocation-dislocation interactions and "polycrystal" type behavior.

Although shearing of the γ precipitate by pairs of $a/2\langle 110 \rangle$ dislocations occurs in most superalloys at low temperatures, it is not the only deformation mechanism operating. Single dislocations, as well as loosely associated pairs, are free to move through the narrow γ phase.⁴⁹ However, large amounts of deformation cannot be obtained in this manner, and shearing of the γ precipitate invariably occurs as the deformation proceeds.¹¹ There are exceptions to this, and it has been observed in some superalloys that dislocations

are not able to easily penetrate the γ' precipitate, if at all.^{11,54} Care must be exercised in accepting this conclusion, since Copley and Kear have shown that even when dislocations were primarily observed in the γ phase, massive shearing of the γ had still occurred.² This was rationalized by considering the rate of dislocation movement in each phase, and it was concluded that the dislocations spent the majority of time in the γ phase. Therefore, it could be expected to observe dislocations primarily in the γ phase even in alloys where precipitate shearing was the main deformation mechanism. In other high volume fraction γ' superalloys, shearing was evidenced by long, straight screw dislocations extending across the γ and γ' phases.¹¹ Thus, it cannot be assumed that shearing has not occurred simply because dislocations are not observed in the γ' phase.

It also is possible to find a variety of stacking faults in superalloys that may participate in the deformation process. Inside the γ' precipitate it is possible to have superlattice intrinsic stacking faults (SISF's), superlattice extrinsic stacking faults (SESF's) and other complex faults (CF's).⁵⁵ It has been shown that the energy of SISF's and SESF's should be lower than the APB energy in γ/γ' superalloys,⁵⁵ and the relative appearance of stacking faults and APB's depends upon their relative energies in the system of interest.^{49,56} The most common faults observed in $L1_2$ -type alloys and γ/γ' superalloys are the SISF and APB faults. APB faults have previously been mentioned, and SISF's briefly will be covered now. An SISF can form by dissociation of an $a\langle 101 \rangle$ type dislocation as follows:⁵⁷



This is only one of a number of possible reactions, and many others have been reported.⁵⁸⁻⁶⁰ In a γ/γ' alloy, SISF's can form by a reaction at the γ/γ' interface⁶¹ or by two intersecting APB-type pairs in the γ' precipitate.⁶² After formation, the SISF can play a role in the deformation process.^{57,63} It should be re-emphasized that while SISF's have been reported in superalloys, deformation under tensile-type strain rates is invariably

dominated by APB-type pairs.^{49,62} This is not to say that SISF's cannot play a role in and affect the overall deformation behavior. The micromechanisms of the formation of each type of fault will not be covered in further detail, and the reader is referred to reviews by Pope and Ezz,⁴⁹ and Kear, et al.⁵⁵

2.1.2.2 Flow stress modeling

Utilizing models developed to predict the critical resolved shear stress (CRSS) can assist in interpretation of observed deformation behavior. Models of the yielding process and (CRSS) in low volume fraction γ' alloys are well-developed^{35,64-69} and are based upon Fleischer-Friedel⁷⁰ statistics, which deal with dislocations interacting with a dilute array of point obstacles. Extended models to treat high volume fraction γ' must not only account for the higher concentration of particles, but also the fact that the dislocation pair can be in the same particle simultaneously. Figure 2.4 illustrates the difference in deformation behavior between low volume fraction and high volume fraction γ' alloys. It is not enough to simply alter the low fraction theories accounting for a higher volume fraction as Ardell, et al., did.⁷¹ Ardell, et al.,⁷¹ modified the equation by Brown and Ham³⁵ for a low volume fraction γ' alloys. The dislocation configurations are different for high volume fraction γ' alloys and this was not considered in this study. Ardell, et al., obtained good agreement between experimental results and their CRSS equation, but the highest volume fraction used was only 36%.⁷¹ This equation has not been applied to higher volume fractions,⁶⁹ and it is believed that different models should be used, which incorporate the differences in the dislocation configurations that are present in high volume fraction γ' alloys.

Different approaches must be considered and the two that are commonly used are that of Copley and Kear,² and Reppich.⁷³ Copley and Kear² were the first to develop a dynamic model for yielding in alloys containing coherent, stress-free, ordered particles.

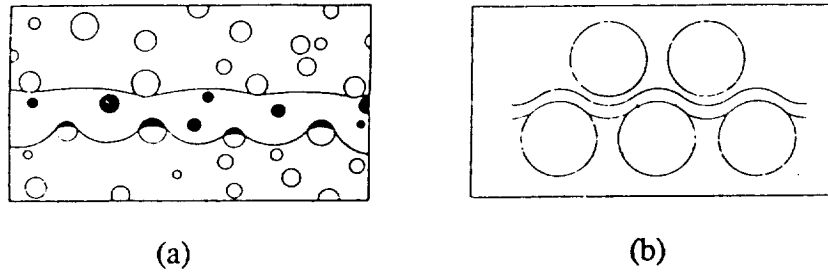


Figure 2.4 Dislocation structure in (a) low volume fraction and (b) high volume fraction γ alloys.⁷²

Their model is based upon a dislocation dynamics approach where dislocations were assumed to move according to an exponential velocity-stress function.⁷⁴ This velocity-stress function can be evaluated if the alloy structure, APB energy of the ordered phase, and the drag stresses of the matrix and precipitate phases are known. They tested this approach in the polycrystalline alloy MAR-M 200, which contains about 60 volume percent γ dispersed in a γ matrix with about 5 volume percent carbides present. The γ particles were spherical and had a diameter of approximately 0.25 μm , while the carbides were found to have no effect on the yielding behavior.

The model develops a force balance for a pair of dislocations attempting to enter a γ precipitate. The forces that are incorporated are:

- 1) force τb ; τ = resolved shear stress.
- 2) force $-\gamma$; γ = APB energy.
- 3) repulsive force, $c/\Delta x$, due to trailing dislocation; $c = \mu b^2/2\pi$.
- 4) force $T(x)$ due to line tension; x = displacement of dislocation segment.

In these expressions, μ is the shear modulus and b is the Burgers vector. From these forces, velocity components for the leading and trailing dislocations are calculated in the

matrix and precipitate. All of the above forces are incorporated in the velocity-stress function for the precipitate, while the APB energy term is omitted in the matrix equations. The average velocities of the dislocation pairs were calculated for various positions relative to the matrix-particle interface, and it was found that penetration of the first dislocation into the particle was the rate-limiting step during yielding. They obtained the following expression for the critical resolved shear stress (CRSS), τ_c , of the γ/γ' material:

$$\tau_c = \frac{\gamma}{2b} - \frac{T}{br} + \frac{K'(\tau_m + \tau_p)}{2} \quad (2-5)$$

$$K' = \frac{(\ln v^*/v)}{K} \quad K = \frac{D_m + D_p}{2(\tau b + T/r) - \gamma} \quad (2-6, 2-7)$$

where r is the radius of curvature of the particles, τ_m and τ_p are the CRSS of the matrix and precipitate, v^* is a velocity near the shear wave velocity, v is the average dislocation velocity, and D_m and D_p are the drag stresses of each phase. Copley and Kear also derived a yield stress equation based now on static arguments that is similar in form to equation 2-5 with K' equal to unity.

The application of equation 2-5 requires the calculation or estimation of a number of parameters. First, Copley and Kear measured the drag stresses and CRSS of each phase by testing alloys of similar composition to the γ and γ' phases, as shown in Figure 2.5. Then the CRSS of each phase, τ_m and τ_p , was calculated as a function of temperature. The drag stresses for each phase were calculated using the equation:

$$D = \ln(v^*/v)\tau_c \quad (2-8)$$

The APB energy calculation used by Copley and Kear yielded a value of 164 ergs/cm² on {111} planes. For the line tension, they assumed the approximation $T = \mu b^2/2$, however, this has been shown to be a poor approximation for these types of alloys.^{69,75} The rest of the parameters are experimentally obtainable.

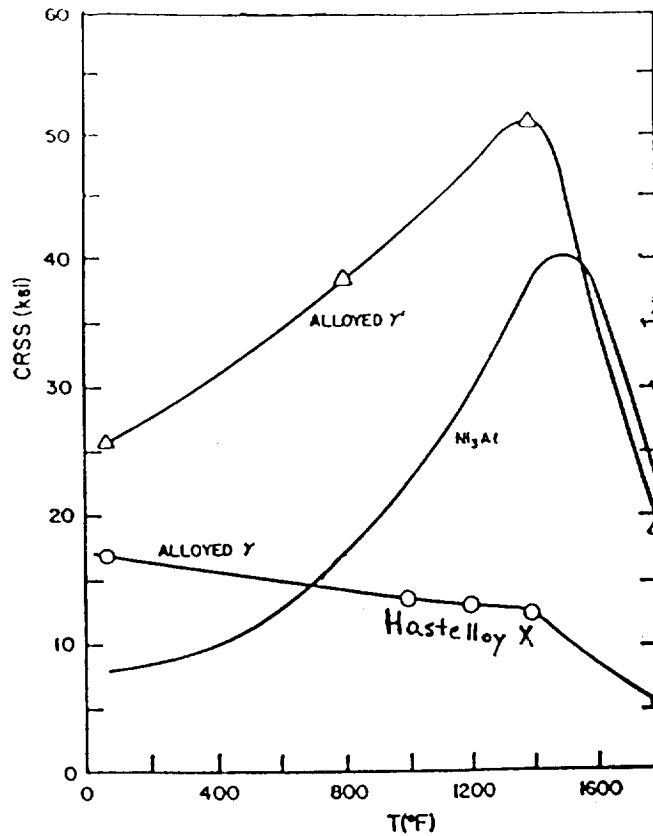


Figure 2.5 CRSS of γ and γ' phases as a function of temperature.²

Obtaining values for the dislocation dynamics is difficult, and most investigators use the version of the model based upon static arguments with $K' = 1$.^{76,77} This has been successfully done by Dollar and Bernstein⁷⁷ to predict the temperature dependence of the flow stress in CMSX-2 and PWA 1480. In PWA 1480, a small modification had to be made to account for the unusual behavior in which most of the dislocations were trapped in the γ matrix and did not shear the precipitates. This led to a work hardening term being added to the Copley and Kear equation for the temperatures where trapping occurred:⁷⁷

$$\tau_c = \frac{\gamma}{2b} - \frac{T}{br} + 0.41(\tau_m + \tau_p) + \alpha\mu b\rho^{1/2} \quad (2-9)$$

where α is a constant and ρ is the dislocation density in the γ matrix. The term 0.41 was added to account for Schmid's Law.⁷⁸

The other model generally applied to high volume fraction γ alloys is by Reppich. Reppich⁷³ used the Schwarz and Labusch⁷⁹ correction for high volume fraction γ alloys and applied it to the low volume fraction model by Huther and Reppich.^{80,81} The latter is designed to predict the increase in the CRSS due to a low volume fraction of coherent, stress-free, ordered particles.

Huther and Reppich^{80,81} begin with the premise that for low volume fractions of small particles, the models based upon the work of Fleischer and Friedel,⁷⁰ which propose that the CRSS will increase with particle size are valid. However, at some critical particle size the dislocations will change from being loosely coupled to being tightly coupled, resulting in a hyperbolic decrease in the cutting stress. An equation for this change in cutting stress, $\Delta\tau_o$, was derived:

$$\Delta\tau_o = 0.86 \frac{Twf^{1/2}}{bd} \left(1.28 \frac{d\gamma}{wT} - 1 \right)^{1/2} \quad (2-10)$$

where f is the volume fraction, d is the mean particle diameter and w is a term accounting for the elastic repulsion between paired dislocations outside the particles. By equating this equation with the one for small particles, the peak stress and a critical diameter for the peak stress, d_c , can be calculated:

$$d_c = 0.78w \left(\frac{2T}{\gamma} \right) \quad \Delta\tau_{\text{peak}} = 0.56 \left(\frac{\gamma}{b} \right) f^{1/2} \quad (2-11, 2-12)$$

Finally, depending upon the shape of the particle, Orowan looping may become favorable at larger particle sizes. Figure 2.6 sums up the Huther-Reppich model for spherical particles.

Schwarz and Labusch⁷⁹ looked at simulated motions of a dislocation through a random array of weak obstacles of finite size, and coined a parameter, η_o , which is proportional to the ratio of the average angle that the dislocation makes by zigzagging

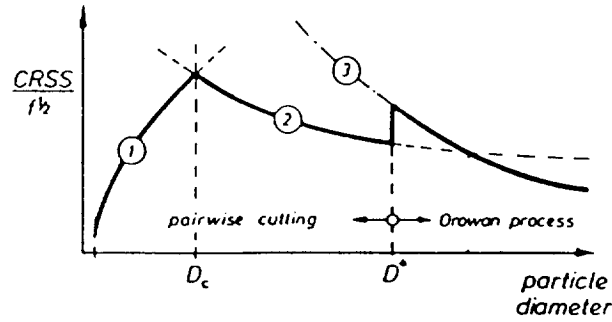


Figure 2.6 Huther-Reppich model for spherical particles.⁸⁰ Plot of CRSS vs. particle size. Curve 1 is equation 2-10 in text.

through the obstacles to the maximum angle that the dislocation can sustain without cutting. η_o is called the normalized obstacle depth and for spherical particles can be expressed as:

$$\eta_o = \left(\frac{2fT}{F\pi} \right)^{1/2} \quad (2-13)$$

where F is the dislocation obstacle interaction force. When $\eta_o \ll 1$, Fleischer-Friedel type models are valid. However, Reppich⁷³ substituted realistic values for nickel-base γ/γ' alloys and concluded that η_o is almost never $\ll 1$. Finally, Schwarz and Labusch derived an expression that relates the increase in CRSS due to a high volume fraction of γ' particles, $\Delta\tau_o$, to the increase found due to small volume fractions, $\Delta\tau_{FF}$:⁷⁹

$$\Delta\tau_o = 0.95(1 + C\eta_o)\Delta\tau_{FF} \quad (2-14)$$

where $\Delta\tau_{FF}$ is the CRSS calculated from the Fleischer-Friedel model and C is a calculable constant. For large particles and high volume fractions, $F = 2T$ and $\eta_o = (f/2\pi)$.

Now, we are in a position to apply the Huther-Reppich hardening model in combination with the Schwarz-Labusch correction for high volume fraction γ' alloys. The modified values of CRSS vs. particle size for spherical particles are shown in Figure 2.7.

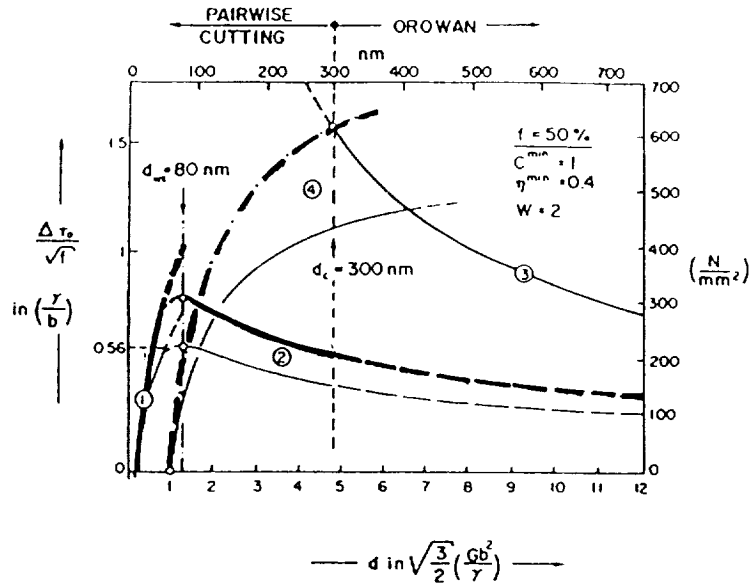


Figure 2.7 Reppich model accounting for large V_f of spherical particles. Curve 1: cutting stress for weakly-coupled dislocation pairs. Curve 2: cutting stress for strongly-coupled dislocation pairs. Curve 3: Orowan stress. Curve 4: penetration stress.⁷³ Thin lines are results of low volume fraction model and thick lines are correction.

The thin lines represent the conventional model, and the thicker lines employ the Schwarz-Labusch correction.

A minimum value of C was used in these calculations, and obtaining C seems to be a difficult task. Further, Huther and Reppich admit that their value of g and w could contain large errors.⁸¹ A serious concern is that in practice w becomes a term determined by fitting the experimental data. In other words, "it contains all the uncertainties of the theory."⁸⁰ Further, Ardell⁶⁹ points out that there is a large spread in the values obtained by different investigators for the constants C and w .^{75,82-85} Ardell⁶⁹ concludes that the use of the Labusch and Schwarz model may hold some promise, but currently there are too many unknown variables to reliably predict the CRSS.

2.1.2.3 Tension/Compression asymmetry

It has only recently been discovered that Ni₃Al-based alloys exhibit a tension/compression flow stress asymmetry.⁸⁶⁻⁹⁰ It was generally found that for the <001> orientation the flow stress in tension exceeds that in compression. For most other orientations, the compressive flow stress was greater than the tensile flow stress. D.P. Pope and co-workers⁸⁶⁻⁸⁹ have led research in this area studying Ni₃Al-based alloys, as well as PWA 1480. The most recent paper by Heredia and Pope⁸⁸ provides an overview of the previous models and experimental observations.

Paidar, et al.,⁸⁶ were the first to describe a model to explain this asymmetry. It actually is a generalized version of the Takeuchi and Kuramoto (TK) model,⁶⁰ which explained the anomalous increase in flow stress with temperature. The TK model worked well in explaining this effect, but incorrectly predicted the tension/compression asymmetry. Paidar et al., looked at the effect of the applied stress tensor on the dislocation core width and not just on cross slip, as was the case for the TK model. After deriving an activation energy for cross slip and relating this to the flow stress, they were able to show how the direction of applied stress could affect the flow stress. This supports the premise that dislocation core constriction or expansion plays a larger role than the stress driven cross slip in determining the tension/compression flow stress asymmetry in these alloys.

Shah and Duhl⁹⁰ observed the same flow stress asymmetry in PWA 1480 but considered the splitting of dislocation partials as the explanation. They find that in the <001> orientation an applied tensile stress causes the partials to constrict and a compressive stress expands them. Since it is necessary to bring the partials together before cross slip occurs, it is argued that the samples pulled in tension will be stronger than those under compression. This analysis also was successfully used to predict the orientation at which no asymmetry occurred in the yield strength.

The Paidar, et al.,⁸⁶ model has been experimentally proven not only in their own work using previous data on Ni₃(Al,Nb) single crystals,⁸⁹ but also in separate work on

$\text{Ni}_3(\text{Al,Ta})$ single crystals⁸⁷ and on PWA 1480.⁸⁸ Each of these studies report the same orientation dependence of the flow stress asymmetry, as well as similar temperature effects. Therefore, it can be concluded that this model utilizing the effect of the applied stress tensor on the dislocation core is widely applicable. However, the similar, yet simpler model of Shah and Duhl also predicts the correct trends, and a final decision on appropriateness of each is not yet possible.

2.1.3 Fracture Behavior

2.1.3.1 Crystallographic fracture

The fracture behavior of single crystal nickel-base superalloys is very different from their polycrystal counterparts. In single crystal superalloys, it is very common for the fracture to occur along specific crystallographic planes and to have a cleavage-like appearance. This type of fracture has been observed in other fcc single crystals⁹¹⁻⁹⁴ and is thought to be a general phenomenon of fcc single crystals. All of these studies report failure along $\{111\}$ planes, however $\{001\}$ failure has been reported in some instances.^{9,95,96} This behavior has been primarily studied under fatigue conditions,⁹⁴⁻⁹⁹ although it also is observed in monotonic loading.^{9,100,101}

In most cases the fracture surface has the appearance of cleavage at low magnifications, but with evidence of moderate amounts of fractographic plasticity at higher magnifications.^{9,95,100} Physical measurements such as reduction-in-area and crack-tip strain also indicate that this is a plastic process. For failure along $\{111\}$ planes, it is commonly observed that more than one $\{111\}$ variant is involved.^{95,96,97,100} Figure 2.8 illustrates this type of fracture in an $[001]$ compact tension specimen with a transverse orientation of $[010]$. The determination of which planes are active in the fracture is not a difficult process for single crystals and is treated elsewhere¹⁰², as well as in section 3.4.6.

Chan and co-workers^{97,101,103} have studied this phenomenon of crystallographic failure from a viewpoint of the stresses involved. This subject is now discussed, as well as in section 2.4 because of its importance in linear elastic fracture mechanics analysis.

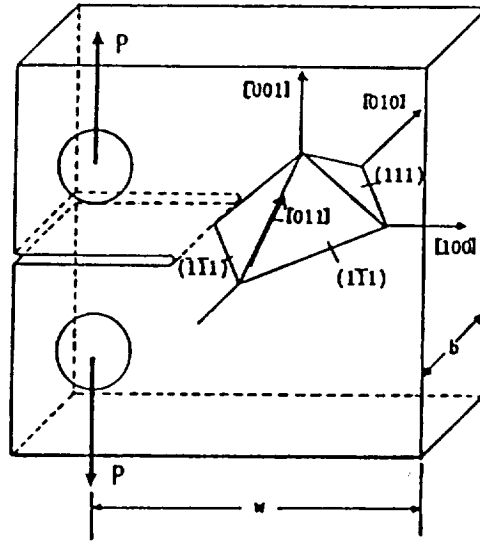


Figure 2.8 Schematic of $\{111\}$ crystallographic fracture in an $[001]$ CT specimen.⁹⁵

In the crystallographic failure of fcc single crystals, the crack path occurs along planes which can have large shear stresses; however the fracture surface has a cleavage-like appearance. Koss and Chan¹⁰¹ found that large normal stresses build up ahead of the crack tip when fracture is occurring along a coplanar slip band. These normal stresses are about three times what one would find ahead of a crack tip when uniform multiple slip is involved. It is believed that the large normal stresses do not allow the crack to deviate, and this results in the fracture path remaining exactly along the coplanar slip band.

This same analysis also shows that for fcc single crystals, fracture along a planar slip band is stable and secondary slip is very difficult.¹⁰¹ They obtained an expression for r_p^s/r_p , where r_p is the plastic zone size for a coplanar slip band and r_p^s is the plastic zone size in the plane of the crack due to secondary slip. This ratio is an indication of whether uniform multiple slip, or non-uniform coplanar slip should occur at the tip of a moving crack. When $r_p^s/r_p \ll 1$, then coplanar slip is expected and vice versa. Koss and Chan's

results showed that for fcc single crystals this ratio would be 0.07, so coplanar slip would be stable.

Koss and Chan¹⁰¹ also suggest that the fracture along coplanar slip bands is due solely to the "elastic-plastic" state of stress involved and that the dislocation configuration ahead of the crack tip is of secondary importance. Further, this type of fracture is expected to be associated with a low fracture toughness, but this degradation of toughness can be altered by means of tortuous crack paths, crack branching or renucleation of a shear band at a boundary.

The formation of ridges on the fracture surface also was examined by Chan,¹⁰³ who showed that they are the result of fracture along more than one {111} plane. In previous work,¹⁰¹ Chan showed that coplanar slip did not relax the normal stresses ahead of the crack tip, and thus concluded that cross slip alone cannot reduce the normal stresses ahead of the crack tip.¹⁰³ The result is that large normal stresses can occur on the coplanar slip plane, as well as the cross slip plane. The combination of large normal stresses and localized shear on both planes can thus explain the observation of simultaneous {111} cross-slip planes leading to ridges on the fracture surface. While Chan did not extend this to include two pairs of cross-slip systems, it would seem logical to do so. This could then explain the presence of all four {111} variants on a fracture surface.⁹⁵ An important consequence of this analysis is that the crack growth direction is predicted to be $\langle 110 \rangle$, which is common to both cross-slip planes. Support for this is provided in a fatigue study on MAR-M 200,¹⁰³ where fatigue striations were observed perpendicular to the $\langle 110 \rangle$ direction proving that $\langle 110 \rangle$ was the direction of crack growth.

The presence of facets also was analyzed by Telesman and Ghosn⁹⁵ from the point of view of the resolved shear stress on these planes. This approach also was used by Chan, Hack and Leverant⁹⁷ and was successful for predicting which planes would be present on the fracture surface, but only when a single plane traversed the entire fracture. When there were fracture ridges with two planes active, the model was not applicable.

The Telesman and Ghosn model⁹⁵ calculates the resolved shear stress on all the possible slip systems and then predicts which systems should operate and when. The limiting value of this resolved shear stress is defined as:¹⁰⁴

$$K_{\text{rSS}} = \lim_{r \rightarrow 0} \tau_{\text{rSS}} \sqrt{2\pi r} \quad (2-15)$$

where r is the distance to the crack tip and τ_{rSS} is defined as the projection of the stress tensor, σ , on a plane whose outward normal is \bar{n} in the direction of slip \bar{b} . Cracking is assumed to occur along the slip systems with the highest K_{rSS} value. While it is difficult to assess whether the authors are implying crack growth across the facets or parallel to them, it will be assumed that growth is perpendicular to the facets based on Chan's evidence¹⁰³, as well as evidence in this work. Telesman and Ghosn suggest that crack growth begins on one system, and after some unspecified distance, the crack then will turn and propagate on another system of high K_{rSS} .⁹⁵ The criteria for choosing which $\{111\}$ system, or exactly why and when the crack changes direction, is not given. They also consider that the same behavior occurs for the other pair of $\{111\}$ systems and, hence, development of the fracture ridges directly follows. Unfortunately, this model is not intuitively obvious, and there are other systems with similar K_{rSS} values that also appear to be valid possibilities for crack growth. Further, it also is difficult to imagine how the crack advances using this model. It seems better at this point to use Chan's simplified cross slip argument¹⁰³ and assume that the two pairs of slip systems merely intersect and that there is not a change in crack direction.

2.1.3.2 Relation to microstructure

The relationship between the γ/γ' microstructure and the fracture surface has been studied by several researchers.^{9,11,95,105} When fracture occurs on $\{001\}$ planes, it is quite easy to see the γ/γ' outline on the fracture surface.^{9,95} Further, it is clear that the matrix is the more ductile phase as evidenced by tear ridges through the γ phase, while the γ' has a

more brittle appearance. However it is not clear if the final fracture is occurring through the γ matrix or at the γ/γ' interface,⁹ although some evidence suggests fracture through the γ phase.¹¹ Telesman and Ghosn⁹⁵ believe that this type of fracture suggests that the only deformation occurring is in the γ phase since {001} cube slip is not observed at room temperature.⁵² This leads one to believe that the fracture across the γ' precipitate is a rapid, brittle fracture. Sherry supports this conclusion by stating that quasi-cleavage of the γ' is occurring with alternate shear of the γ by octahedral slip.¹⁰⁵

When fracture occurs on {111} planes, as is more typical, it is difficult to ascertain the role of the γ/γ' microstructure. However, the same mechanisms may apply, with the exception of failure of the γ' on {111} planes. The fracture of the γ' is still brittle-looking, but is now along the slip plane. This brittle-type fracture can be rationalized using the above argument of Koss and Chan,¹⁰¹ identifying the larger than usual normal stresses ahead of the crack tip in this type of fracture.

2.1.4 Effect of Hydrogen on Superalloys

The effect of hydrogen on superalloys has been studied for over twenty years, primarily driven by the environmental conditions present in the Space Shuttle Main Engine (SSME). A large amount of data currently exists on hydrogen embrittlement, mainly from screening tests on a wide variety of superalloys; much of this information has been compiled by Fritzemeier and Chandler.⁸ Tests on superalloys most often were performed under a 34.5 MPa hydrogen atmosphere to simulate the SSME conditions with comparative tests performed in a 34.5 MPa helium atmosphere. But there were some tests done on internally charged specimens tested in air or a hydrogen atmosphere.⁸⁻¹⁰

No attempt will be made to analyze results outside the scope of this thesis, and the reader is referred to reference 8 and its references for further details. The review⁸ covered over 35 superalloys, and compiled much of the work done in the area of tensile properties,

creep rupture, fatigue and fracture mechanics. There was no obvious trend between wrought, conventionally cast and single crystalline material as far as hydrogen embrittlement was concerned. It was found, not unexpectedly, that the worst embrittlement occurred at room temperature as opposed to cryogenic or elevated temperatures. It also was concluded that trends seen in other alloys tested in hydrogen, such as strain rate, frequency and pressure, were equally observed in superalloys. In summary, there were no superalloys found to be totally resistant to hydrogen-induced degradation of properties when subjected to severe enough conditions. Specific results in the literature that are applicable to this work will now be discussed.

The effect of single crystal orientation on hydrogen embrittlement has been studied, and in PWA 1480 it was noted that the $\langle 001 \rangle$ orientation appeared to be the most severely embrittled orientation in terms of notch tensile strength.¹⁰⁶ Despite this result, the advantages of the $\langle 001 \rangle$ orientation in other areas, particularly creep behavior, continue to make it the most attractive orientation for rocket engine applications. Generally the notch tensile strength of [001] single crystals tested in a hydrogen atmosphere at room temperature was reduced by at least 40%, and the reduction of area (R.A.) in smooth specimens was reduced by more than 20% in all specimens.⁸ But the R.A. may not be a valid indicator of hydrogen embrittlement based on results in this thesis and those of Fritzemeier.²⁵ Fritzemeier found that most single crystal superalloys tested in hydrogen showed a much larger corresponding loss of strain to failure compared to the decrease in R.A. It was generally found that the more severe the embrittlement for a given alloy, the larger this discrepancy became. It is believed that these differences reflect strain localization, a manifestation of hydrogen-enhanced localized plasticity, as will be discussed later in the work.

Various observations will now be mentioned including an effect of microstructure was observed in the CMSX series of alloys, where larger, more uniform cuboidal precipitates improved the alloys' resistance to hydrogen embrittlement.⁸ It is possible that

the homogeneous deformation associated with this microstructure, compared to the localized slip observed in the CMSX alloys with smaller, non-uniform precipitates, led to the improved properties. Cracks were observed on the tensile gage surface in MAR-M 246 tested in hydrogen, which initially started on {001} planes and then propagated on to {111} planes.²⁵ Surface cracking also has been seen on internally charged CMSX-2 tested in air, however, no analysis of the crack orientation was performed.⁹ In separate experiments, the effect of testing pre-charged samples in air and hydrogen was studied on MAR-M 246, and it was observed that the combination of internal and external hydrogen produced slightly worse properties than for either case tested separately.⁸

Only a few studies have carefully analyzed the structure/property relations in the hydrogen embrittlement of superalloys,^{9,10,25,77} and these will be discussed now. In CMSX-2, the role of microstructure in the hydrogen embrittlement of cathodically charged and gas-phase charged tensile specimens has been carefully studied.^{9,10,107} It was concluded that gas-phase charging produced more severe embrittlement, with the difference directly related to the concentration profiles resulting from the different charging conditions. Under both charging conditions, the role of hydrogen trapping at heterogeneities on properties was studied using desorption experiments and tritium autoradiography.^{9,10,107} It was found that the pores accumulate hydrogen in cathodic charging, but probably not in the gas-phase charged specimens, where the charging temperature of 350°C, is thought to be too high for effective trapping.¹⁰ Hydrogen also was observed to accumulate in the eutectic γ/γ' , either due to direct trapping or because of a higher solubility in the eutectic γ/γ' compared to the rest of the γ/γ' microstructure.¹⁰ A microprobe analysis using a deuterium probe, attempted to determine the trapping and solubility characteristics of the γ and γ' phases,¹⁰⁸ and while no consistent conclusions could be drawn from this work, evidence suggests there is a higher concentration of hydrogen at the γ/γ' interface. This work on CMSX-2¹⁰ also revealed that there was no effect of tensile strain rate on embrittlement over a range of 5×10^{-4} to $5 \times 10^{-2} \text{ sec}^{-1}$. This

is contrary to results in many other alloys¹⁰⁹ where the effect of hydrogen was found to be less severe at high strain rates because of a reduced interaction between dislocations and hydrogen. In CMSX-2, it was suggested that this argument does not apply because of the high, uniform concentration of hydrogen in the sample, thus minimizing dynamic effects.

Further studies on CMSX-2¹¹ performed at Carnegie Mellon showed similar results to the above studies. The work to be discussed now focused on the dislocation structure as a function of hydrogen and strain in an attempt to correlate these observations with companion tensile properties and fracture behavior. The presence of hydrogen led to dislocations being trapped in the γ phase at all strains instead of the extensive shearing of precipitates observed in uncharged specimens. This dislocation trapping led to strain localization and failure in the γ matrix, as revealed directly by fractographic evidence.¹¹ Strain exhaustion is the most likely explanation as the work hardening also increased in hydrogen charged samples, prompted by the high concentration of dislocations in the narrow γ phase. Hydrogen also led to a change from fracture along $\{111\}$ planes to an $\{001\}$ fracture where the γ and γ' phases could easily be seen on the fracture surface. Apparently, hydrogen is causing the majority of deformation to occur by $\{111\}$ slip in the γ matrix leading to failure in this phase.¹¹ For those dislocations present in the γ' phase at room temperature, hydrogen-induced cross slip onto the $\{001\}$ planes was observed.¹¹ This was rationalized using the Takeuchi and Kuramoto model⁶⁰ in terms of hydrogen retarding the "dynamical break away" process described in this model. All of the above observations are important to this work because they involve the effects of internal hydrogen on single crystal superalloys. Thus, the results of this work will be heavily compared to the above studies in hopes of further defining the effect of hydrogen on this type of alloy.

2.2 PWA 1480

Except for the CMSX-2 work, most studies have concentrated on screening alloys for hydrogen application. A notable exception has been PWA 1480 and since its introduction in 1980, it has been one of the most studied single crystal superalloys. In an effort to evaluate its potential for use in jet and rocket engines, there have been many tests performed both in air and hydrogen environments. However even here many of these studies have concentrated on data accumulation and have ignored structure/property relations, and deformation and fracture behavior.

The major testing efforts have been in the areas of low and high cycle fatigue,^{19,76,110-115} fatigue crack growth,^{95,113-115} creep and stress rupture^{7,113,114,116,117} and elevated temperature tension testing.^{23,76,77,90,113,116,118,119} There have been many tests performed in hydrogen gas at 34.5 MPa to simulate the space shuttle main engine operating conditions,^{106,113,115,118,120} but there have only been two studies concerned with the effect of internal hydrogen on mechanical properties.^{25,112} Porosity was found to play a large role in many of these tests, but there have been few published results on hot isostatically pressed material.^{19,23,112} Thus, it appears that the areas of hydrogen and microstructural effects are in need of further research.

Some of the points to come out of these studies that are useful to this work are discussed below and include the highly anisotropic nature of the mechanical properties due to the anisotropy of the elastic modulus.^{90,114,118} It also was observed that fractures were very crystallographic at low temperatures and non-crystallographic at higher temperatures¹¹⁴ probably due to the decrease in predominance of octahedral slip. In the low cycle fatigue studies, it was found that fatigue crack initiation sites were invariably the casting porosity.^{23,114,115} Like other nickel-base alloys,^{8,121} hydrogen similarly degraded the low cycle fatigue, notch tensile strength and tensile ductility of PWA 1480.^{25,106,113,118,120} However, the adverse effects of hydrogen were often less severe

in comparison to other single crystal and directionally solidified superalloys. The following sections will focus on properties and observations of direct relevance to the research reported in this work.

2.2.1 Relevant Studies

The first study to carefully characterize the microstructure and deformation behavior of PWA 1480 was by Shah and Duhl,⁹⁰ who examined the effects of orientation, temperature and γ' size on yield strength. They tested three major orientations, [001], [011] and [111], in tension and compression and noted a tension/compression asymmetry. They attributed this to the role of thermally activated cube cross-slip, as discussed in section 2.1.2.3. The [001] orientation was found to be the strongest in tension and weakest in compression at all temperatures, with a slight drop in the yield strength at 400°C. Schmid's law was not obeyed,⁷⁸ which was explained by differences in the propensity for cross slip in each orientation. At low temperatures, the smallest γ' size microstructure was the strongest, but at intermediate temperatures the differences became small. In the discussion of these results, Shah and Duhl assumed that dislocations sheared the γ' precipitates at all temperatures, however there was no TEM evidence provided to support this contention.

In a later study, Milligan and Antolovich⁷⁶ also looked at the effect of temperature on yield strength of PWA 1480 containing ~60% volume fraction of γ' precipitates with an average size of 0.5 μm . The alloy also had a volume fraction of porosity of 0.15-0.20%, and 4.5-5.0% of eutectic γ/γ' . The γ/γ' mismatch had been measured from extracted γ' precipitates in a related study and was reported to be 0.28%.¹²² Milligan and Antolovich performed interrupted tensile tests to fixed plastic strains and analyzed the deformation substructure of [001] oriented samples. They observed that at low temperatures, (<760°C), shearing of the γ' was the dominant deformation mechanism. At higher temperatures, γ'

bypass occurred and eventually became dominant. It should be mentioned that temperatures between 20°C and 705°C were not tested, so the previously observed drop in strength around 400°C⁹⁰ was not observed.

Milligan and Antolovich⁷⁶ attempted to model the measured critical resolved shear stress (CRSS), but with limited success. They found that although the Copley and Kear model² apparently described PWA 1480 at low temperatures, one of the assumptions in the theory was violated, namely that penetration of the leading dislocation into the γ precipitate was the rate-controlling step. In contrast to this assumption, it was observed that 8-10 dislocations could reside in the γ before the first dislocation completely traversed it. Therefore, for PWA 1480, they concluded that the rate controlling step is instead the drag stress of the precipitate, and further that there is not a currently available CRSS model to predict the deformation behavior.

In a later paper,¹²³ Milligan and Antolovich studied the yield drop between room temperature and 400°C and linked this behavior with their observation of a large density of Superlattice Intrinsic Stacking Faults (SISF's) in the γ precipitates at room temperature. They proposed that these faults act as barriers to glide and raise the CRSS at room temperature. The density of SISF's is reduced at higher temperatures, and thus the drop in CRSS up to 400°C. Above 400°C, no SISF's were observed and the rise in CRSS is credited to the thermally activated cube cross-slip mechanism.¹²⁴

In another study of PWA 1480, Dollar and Bernstein⁷⁷ attempted to describe in more detail the effect of temperature on the development of the deformation structure. They examined tensile properties and deformation structures at temperatures of 20°C, 400°C, and 730°C, and at various plastic strain levels. At room temperature, superdislocations were observed trapped in the γ matrix in the early stages of plastic deformation. With increasing plastic strain, the dislocation density increased in both the precipitate and matrix but still was substantially higher in the matrix. They argued that since the yield stress of the γ phase is considerably less than the yield stress of the superalloy,² superdislocations can

move into the γ' below the overall yield stress. However, when they enter the γ phase they cannot move back into the γ' because of the additional APB energy required. It should be mentioned that there was not a large density of SISF's reported in the γ' precipitates at room temperature, in contrast to the study of Milligan and Antolovich.¹²³

At 400°C and 730°C, the dislocations were no longer trapped in the matrix at low strains. The superdislocations observed at 400°C were now long, straight $a/2\langle 110 \rangle$ screw dislocations, but at 730°C the screw dislocations were no longer straight. These dislocation configurations were attributed to the cross slip of superdislocations, as originally proposed by Kear and Wilsdorf.¹²⁵ Dollar and Bernstein also noted a decrease in strength up to 400°C. In order to explain the yield drop at 400°C and to model the CRSS in this temperature regime, they used the deformation structure observations to modify Copley and Kear's model. This analysis is detailed in section 2.1.2.2.

In yet another study on PWA 1480, Fritzsche determined the effects of high thermal gradient casting, hot isostatic pressing (HIP'ing) and heat treatment on the mechanical properties.^{19,23} It was found that using a higher thermal gradient during the solidification process yielded a material that was easier to HIP with fewer and smaller pores, as well as a more compositionally homogeneous casting. While it was possible to eliminate all pores by HIP'ing, this had no effect on subsequent tensile properties. The primary aim was to improve the fatigue properties, which was accomplished by HIP'ing. The tensile ductilities are higher than many other reported values, and this could be due to microstructural variations or more likely, orientation effects.

2.2.2. Effect of Hydrogen

The majority of tests designed to evaluate the susceptibility of PWA 1480 to hydrogen embrittlement have been performed in a hydrogen atmosphere of 34.5 MPa. Often a comparison of the notch tensile strength in high pressure helium versus hydrogen

was done, and PWA 1480 generally performed better than other alloys in its class.^{25,106,118,120} Fritzemeier has made some observations on tensile samples tested in hydrogen gas,²⁵ which are of particular interest to this work. In general, the slip lines on the tensile gage surface of the samples tested in helium were more homogeneous than on those samples tested in hydrogen. Furthermore, the reduction in area was not affected as drastically by testing in hydrogen as was the strain to failure. Both of these observations lead to the conclusion that hydrogen-induced localized plasticity^{126,127} is occurring in PWA 1480. Similar observations were made on other single crystal nickel-base superalloys,²⁵ as reported in section 2.1.4.

2.3 Hydrogen Embrittlement Processes

There have been many proposed processes or mechanisms for hydrogen embrittlement of metals, but none can yet satisfactorily explain all of the experimental results reported in the literature. While a given process may explain the mechanical behavior in the same system, the same process may not operate in the same or another system under different conditions of hydrogen fugacity, temperature, stress state, etc. The most widely accepted hydrogen embrittlement processes will be discussed, along with the concept of hydrogen trapping. These can be broken down into four categories:

1. Hydride precipitation
2. Decohesion
3. Trap theory
4. Hydrogen enhanced local plasticity

The first of these relates to systems that form hydrides or martensitic phases.¹²⁸ This phase is normally brittle, and failure occurs along or through this phase. While pure nickel has been reported to form hydrides, it is not possible at the hydrogen concentrations

or fugacities used in this work.¹²⁹ Further, there is no evidence of hydride formation in nickel-based alloys under any conditions. Therefore, this mechanism is of little interest in relation to this thesis.

The decohesion mechanism proposes that the presence of hydrogen solutes decreases the atomic bond strength of the metal causing a brittle fracture when the local stress exceeds the atomic bond strength.^{130,131} This brittle failure process can occur in conjunction with general plasticity in the sample, and therefore is in competition with other failure mechanisms. This theory has come under recent criticism because of the lack of consistent experimental evidence and a sound theoretical basis.¹²⁷ However, it remains a popular mechanism and may be the only explanation for hydrogen embrittlement in some systems. We believe the two most relevant mechanistic possibilities in single crystal superalloys are the last two, and these will be considered in more detail.

2.3.1 Trap Theory

The trap theory states that a crack will initiate at a hydrogen trapping site when the quantity of trapped hydrogen at the site exceeds a "critical concentration."^{132,133} Trapping of hydrogen at microstructural sites has been observed in superalloys,^{9,10} so this hydrogen embrittlement process will be covered in detail. The theory does not usually directly consider any particular transport mode for the hydrogen to reach the trap, but recognizes that diffusion along short circuit paths or by dislocation transport would shorten the time to reach the critical concentration. There is no evidence of "critical concentrations" nucleating cracks, and this theory will be approached from the viewpoint that it can explain hydrogen trapping. Thus, it is not a bonafide hydrogen embrittlement mechanism but rather a process by which embrittlement may occur.

The number and strength of traps, and whether the traps are reversible or not, play a key role in the effect of hydrogen on the material. For this reason, it is important to

identify those internal defects that could act as hydrogen trapping sites, as well as to analyze their relative trapping strengths. There is experimental evidence that supports the idea that cracks nucleate at trapping sites,^{107,132,134} however it is not known if this is due to a "critical concentration" being reached. Direct experimental observation of trapping sites can be obtained by the use of tritium autoradiography. Further details of tritium autoradiography and its application to a number of other systems are given in Appendix E. A thorough review of observed trapping sites in many different alloys and their relation to hydrogen embrittlement has been given by Lacombe, Aucoeur and Chene.¹⁰⁷

Trapping sites can include grain boundaries, inclusions, dislocations, voids and interstitial sites in the lattice. A classification approach has been used,¹³² where all trapping sites can be broken down into physical traps, attractive traps or a combination of both. Physical traps such as voids or inclusions are modifications to the crystal lattice and generally are considered moderate to strong trapping sites; attractive traps are regions where hydrogen atoms are acted upon by an attractive force, such as the stress field of a dislocation. These traps are invariably more reversible than physical traps, because the probability of the hydrogen atom diffusing from this region or being left behind by a moving dislocation is greater. The trap strength and reversibility of most traps often can be determined by desorption experiments.^{9,135,136}

Trapping can also be evaluated in terms of internal versus external hydrogen embrittlement and reversible versus irreversible traps.¹³² Pressouyre states that some of the differences found in hydrogen embrittlement under different testing conditions can be explained by the types of traps involved.¹³² Irreversible traps always will act as sinks, and reversible traps can be a source or sink depending upon the testing conditions and their interaction with other traps. It has been shown that in samples with both types of traps, it is easier to reach a critical concentration of hydrogen at a potential crack nuclei when the specimen is internally charged rather than if the same specimen is tested in hydrogen gas. This is believed to occur because all traps act as sinks in the external case, while reversible

traps may actually contribute hydrogen to the potential crack nuclei by dislocation transport in internally charged specimens. Pressouyre points out many cases where the above argument is borne out in experiments.¹³²

While the trap theory of hydrogen embrittlement explains hydrogen trapping in the microstructure, it is rather unsatisfactory in explaining how crack propagation and failure occurs. Therefore, the trap theory is not complete in itself, and one of the other mechanisms, such as decohesion, must be invoked to explain how the crack is nucleated.

2.3.1.1 Determination of the trap binding energy

As mentioned, the trap strength and reversibility of the traps are important in characterizing the effect of hydrogen on material behavior. There are several methods to determine the binding energy of hydrogen to microstructural features, and the desorption method will be covered here. This technique involves heating a pre-charged sample and measuring the rate or amount of hydrogen diffusing out of the free surface. The most accurate desorption profiles are obtained by using deuterium- or tritium-charged samples and continuously monitoring the release rate. In all cases, it is important to have reliable diffusion data. Table 2.3 gives an overview of available hydrogen diffusion data in nickel-base alloys.¹³⁷⁻¹⁴⁰ It can be seen that the data scatter is extremely large, especially in the γ/γ' alloys. Estimates for CMSX-2^{9,10} suggest that the data of Robertson¹³⁷ for pure Ni may best fit this type of alloy. Robertson's data is a compilation of literature values, and the resulting diffusivity value is smaller than almost all of the others in Table 2.3. It is apparent that quality diffusion studies of hydrogen in high volume fraction γ' alloys are needed.

Table 2.3 Diffusion data of hydrogen in nickel-base alloys.

Alloy	D_0 (cm ² /s)	Q (cal/mole)	Reference
IN 718	1.07×10^{-2}	-11,900	140
IN 903	2.46×10^{-2}	-12,590	140
IN 903	4.00×10^{-2}	-7,715	138
Waspalloy	15.5×10^{-2}	-8,278	138
René 41	3.90×10^{-1}	-8,668	138
MAR-M 246	2.0×10^{-2}	-6,954	138
Ni	4.76×10^{-3}	-11,411	139
Ni	6.44×10^{-3}	-9,610	137

Hirth¹⁴¹ has compiled the large body of existing data of trap energies in iron, but there has been substantially less work published on fcc alloys.^{107,136} Hirth reports a binding energy of 0.61 eV for hydrogen trapping on internal free surfaces, which is slightly less than the estimated value of hydrogen trapped at pores in CMSX-2.⁹ In nickel, the trap binding energy of thoria particles has been estimated to be 0.30 eV,¹³⁵ and the binding energy to dislocations in nickel is around 0.10-0.15 eV.¹³⁶ It is clear from these few examples that there is a wide range of binding energies to crystal defects and microstructural features.

A general drawback in using desorption data to calculate binding energies is that it is very difficult to determine the exact relationship between a given binding energy and the specific microstructural features. All microstructural components, as well as dislocations in the material, can contribute to the observed binding energy, and it requires many tests to separate out the effects of each microstructural site. However, desorption tests are

relatively simple to perform, and the trapping data obtained are useful in understanding the effect of hydrogen on the material's behavior.

To be most useful, the presence and strength of trapping sites should be determined by desorption experiments, but as yet there is no standard method of converting such data into trap binding energies. The number of methods currently used^{9,135,136} should be applicable to the data obtained in this work, namely, the amount of hydrogen desorbed as a function of time and temperature.

Lee and Lee¹³⁵ have proposed an expression for obtaining the trap binding energy by performing desorption experiments as a function of temperature:

$$\ln \left(\frac{N_T}{C_T} - 1 \right) = \ln \frac{N_L}{C_o} + \frac{E_o - E_b}{RT_H} \quad (2-16)$$

where N_T and N_L are the concentration of trap sites and normal lattice interstitial sites, C_T and C_o are the trapped and equilibrium concentration of hydrogen, E_B is the trap binding energy, E_o is the heat of solution, R is the gas constant, and T_H is the desorption temperature. Estimates are made for values such as N_T , N_L and E_o , and the desorption curves yield C_T and C_o . Finally, by plotting Equation 2-16 the binding energy is obtained. This method requires very accurate desorption curves over a wide range of temperatures. Further, estimating N_T is a difficult task and can severely influence the binding energy. Thus, although this approach has some success in predicting the binding energy of hydrogen to thoria particles in nickel,¹³⁵ it is not known if it can easily be applied to other desorption data, such as in this work.

Thomas¹³⁶ has used measurements of the desorption of deuterium in nickel to obtain values of the binding energies of hydrogen to dislocations and to Fe or Ti impurities. The desorption was performed as a function of time and temperature resulting in detailed

plots that, as above, were then used to fit the following expression for a one-dimensional case:

$$\frac{dc(x,t)}{dt} = \frac{d}{dx} \left[D \frac{dc(x,t)}{dx} \right] - \frac{dc_T}{dt} \quad (2-17)$$

where $c(x,t)$ is the lattice concentration of hydrogen and dc_T/dt is the trap rate minus the detrapp rate.

$$\frac{dc_T}{dt} = \frac{Dc(x,t)}{\lambda^2} [N_T - fc_T] - (c_T \nu) \exp \left[\frac{-(E_D + E_T)}{kT} \right] \quad (2-18)$$

In this expression, c_T is the trapped concentration of hydrogen, D is the diffusivity, λ is the jump distance, N_T is the density of traps, ν is the attempt frequency (10^{13} sec^{-1}), E_T is the trap binding energy, E_D is the lattice activation energy, k is a constant and T is the temperature. Again, estimates had to be made for some parameters, while others were calculated by data fitting. Instead of using the entire equation, as proposed by Thomas, it appears possible that the detrapp rate portion could simply be used to analyze the desorption data:

$$\frac{dc_T}{dt} = -(c_T \nu) \exp \left[\frac{-(E_D + E_T)}{kT} \right] \quad (2-19)$$

A problem in this approach is that the attempt frequency, ν , is so large it dominates the equation, and unrealistically small binding energies are calculated. However, the more general method used by Thomas is physically appealing, and application of this method to the desorption data in this work was attempted.

A much simpler method to determine binding energies from desorption data was used by Baker, et al.,⁹ to obtain the binding energy of hydrogen to pores in CMSX-2 by

using an equation proposed by Hirth¹⁴¹ and solving for the binding enthalpy, H_b :

$$\frac{c}{1-c} = (kp^{1/2})\exp\left[\frac{H_b - H_s}{RT}\right] \quad (2-20)$$

where c is the atomic fraction of trapped hydrogen, k is a solubility constant, p is pressure, H_s is the heat of solution, R is the gas constant and T is temperature. The solubility data was taken from a similar alloy,^{9,140} and the pressure was the equilibrium partial pressure of hydrogen in air at 1 atm. The amount of trapped hydrogen can be estimated from the desorption data and a binding energy found. This method is perhaps the least accurate, but its ease of application make it the most promising for use in this study.

2.3.2 Hydrogen Enhanced Localized Plasticity

The final explanation for hydrogen embrittlement to be covered is based on the premise that hydrogen embrittlement is a macroscopically brittle fracture process, which results from a hydrogen-enhanced localized plasticity (H.E.L.P) at the crack tip.¹²⁶ Again, this is a process by which hydrogen embrittlement can occur and not a complete mechanism. Birnbaum and co-workers have studied the H.E.L.P. mechanism using an environmental cell TEM with *in situ* deformation of thin foils.^{127,142-147} Bulk specimens also have been used to substantiate the occurrence and importance of H.E.L.P.¹⁴⁸⁻¹⁵⁰ Fritzemeier²⁵ has preliminary results that suggest H.E.L.P. is occurring in single crystal superalloys, and thus this hydrogen embrittlement process will be covered in detail.

Macroscopic embrittlement as measured by decrease in strain to failure or reduction in area can be caused by localization of high plastic strains to the region of the crack tip. It is believed that the strains are localized because hydrogen reduces the stress to generate and move dislocations, and thus the dislocation activity remains in a local area, leading to high

local strains. Hydrogen can interact with the dislocations by either entering through the crack tip, diffusing to it or being present from charging. This effect also can be manifested in a decrease in the flow stress since dislocation motion and generation is easier. The effect of hydrogen pressure on dislocation velocity is schematically shown in Figure 2.9,¹²⁷ an analysis apparently valid for both screw or edge dislocations, as well as for loops and Frank-Read sources. It was developed by using the concepts of dislocation shielding where hydrogen atoms shield the elastic interaction of one dislocation with another.¹²⁷ This means that two-edge dislocations that normally repel, could instead attract and small, atomic-scale slits open up along the slip plane.¹²⁷

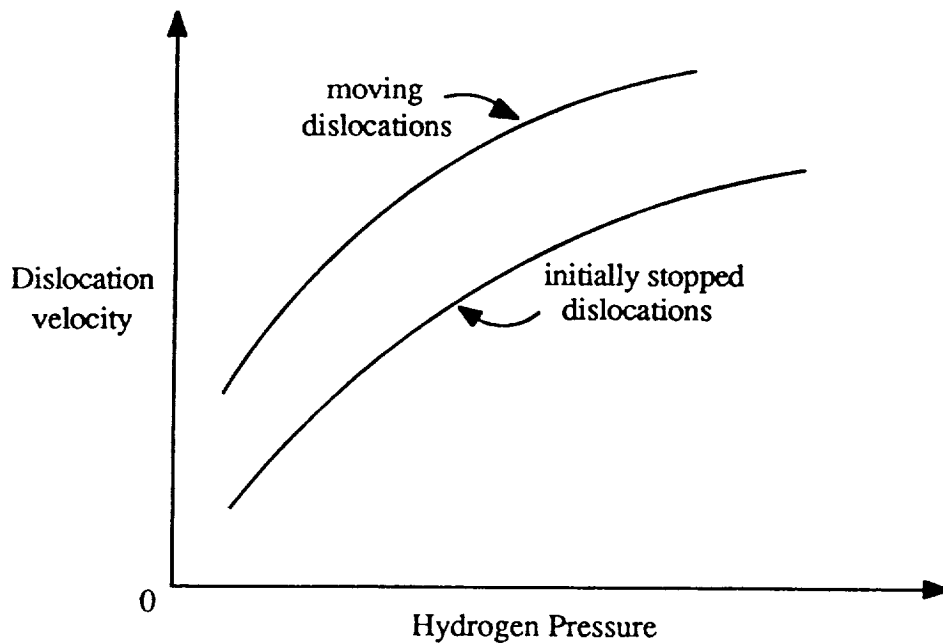


Figure 2.9. Schematic of the effect of hydrogen pressure on dislocation velocity.

The experimental confirmation of H.E.L.P. in a number of alloy systems has mainly come from observations of *in situ* deformation of thin foils. Evidence was obtained that suggests hydrogen aids in the generation and mobility of dislocations in Fe,¹⁴² Ni,¹⁴³ IN 903,¹⁴⁴ SS 310,¹²⁷ α Ti,¹⁴⁵ high purity Al,¹⁴⁶ 7050 Al and 7075 Al¹⁴⁷, and

microscopic fracture along slip planes also has been observed.¹²⁷ There also has been supportive evidence based on flow stress and fractographic observations made in bulk samples of various alloys.¹⁴⁸⁻¹⁵⁰ The macroscopic fracture generally reflects the external stress systems and other variables, and the correlation with the observed microscopic slits on the slip plane remains to be done. From results on single crystal superalloys,^{9,10,25} it appears that the trap theory and H.E.L.P. may be useful in explaining some of the results of this work.

2.4 Fracture Toughness of Polycrystal and Single Crystal Superalloys

While the fracture toughness of superalloys is generally considered to be of less importance than fatigue behavior in their design and application, an existing crack in service can amplify the importance of crack initiation toughness under initial static loading conditions. Fracture toughness also can be an important quantity used to determine the initial stress levels in hydrogen-induced crack growth tests, as was done in this work. Fatigue crack growth of superalloys is currently a well-developed field, but there has been little work in the area of fracture toughness,¹⁵¹⁻¹⁵⁶ particularly the effect of hydrogen.^{152,153,155} Table 2.4 gives the available fracture toughness values for some nickel-base alloys and iron-based superalloys. To the best of the author's knowledge, there are no published data on high volume fraction γ' superalloys, let alone single crystal superalloys, and for that reason alone obtaining the fracture toughness of PWA 1480 as a function of microstructure and hydrogen was a primary goal of this work. Determining the fracture toughness of a single crystal presented certain problems that are addressed below. In as much as earlier fatigue studies showed that porosity can be a favored crack initiation site,^{19,114,157} it was believed that some micromechanistic fracture models could be used to describe the fracture process in PWA 1480. Therefore, these also are reviewed.

Table 2.4. Fracture Toughness Values of Nickel-Base Alloys and Iron-Base Superalloys.

	K_{IC} (MPa \sqrt{m})	J_C (kPa-m)	K_{IH} (MPa \sqrt{m})	Reference
IN 600		382		151
IN 800		854		151
IN 903	90		50 [†]	152
JBK 75	139		77 [†]	153
A 286	140-165			154
A 286	98		94 ^{††}	155
IN 718	78-122			156
IN 718	92-122		84-111 ^{††}	155
IN 625	57		63 ^{††}	155

† internally charged to 5000 appm for IN 903 and 8000 appm for JBK 75.

†† tested in hydrogen gas at 34.5 MPa pressure.

The crystallographic failure mode of single crystals was described in section 2.1.3, and perhaps the most pertinent question in this work is whether the Mode I Linear Elastic Fracture Mechanics (LEFM) approach is valid. The observed cracks in single crystals are always inclined to the stress axis and thus can involve all three modes of crack opening (I, II, III). Chan and Cruse⁴² used a two dimensional boundary integral equation (BIE) method and analyzed the multi-mode problem using a compact tension specimen design. To apply this method, it is necessary to measure the angles that the macroscopic crack makes with the width and thickness of the specimen, as shown in Figure 2.10. It was found that as long as the angle between the crack and the perpendicular of the stress axis, β , was less than 30°, then using a Mode I solution introduced negligible errors. This also assumed that a projected crack length, a' , is used where $a' = a \cos\beta + l$.

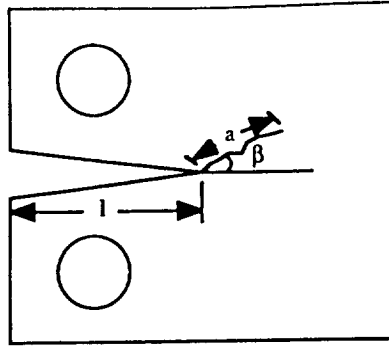


Figure 2.10. Schematic showing dimensions needed for measurement of a' .

This is a very important and simplifying finding for this work particularly because the use of Mode I solutions for this type of single crystal previously had been questioned in the literature.¹⁰⁰ Mode I solutions are commonly used in the analysis of single crystal superalloy crack growth data,^{95,114,115} and will be used in this study as well.

Another important point to examine when dealing with nickel-base single crystals is the effect of anisotropy. Chan and Cruse⁴² examined this effect and concluded that the anisotropy typical in nickel-base single crystals was not sufficient to significantly alter the expressions for K_I . Therefore, it appears that the effect of anisotropy can be conveniently ignored in using conventional K_I expressions designed for isotropic specimens. Thus, in subsequent calculations of stress intensities, the value of Young's modulus in the loading direction is simply used.

2.4.1 Micromechanistic Fracture Initiation Models

Micromechanistic fracture initiation models will be used to correlate the fracture toughness with the microstructure, in hopes of determining a microstructural crack initiation site. In particular, models¹⁵⁸⁻¹⁶⁴ that relate the crack tip opening displacement (CTOD) to microstructural parameters will be discussed. The following expressions were mainly developed for specimens that failed by microvoid coalescence, however, their

adaptation to other ductile fracture processes is possible. In order to calculate δ_{IC} , the expression relating the various fracture toughness parameters is used:¹⁵⁸

$$J_{IC} = \frac{K_{IC}^2}{E} = \frac{\delta_{IC} \sigma_c}{d_n} \quad (2-21)$$

where E is Young's modulus in plane strain, σ_o is the flow stress, and d_n is a term related to σ_o/E and the work hardening exponent n .

Rice and Johnson¹⁵⁹ used continuum equations for void growth¹⁶⁵ to obtain a relation between δ_{IC} and microstructural parameters. They considered the growth of a pre-existing void of radius R_o , which is at a distance X_o from the crack tip and obtained an expression for δ_{IC} :

$$\delta_{IC} = X_o F(X_o/R_o) \quad (2-22)$$

where F is a weakly varying function of X_o/R_o . X_o and R_o can be related by the expression for the average three dimensional nearest neighbor spacing between initiation sites:¹⁶⁶

$$X_o = 0.89R_o(f)^{-1/3} \quad (2-23)$$

where f is the volume fraction. Using this equation and the work of Rice and Johnson; Hahn, et al.,¹⁶⁰ showed that:

$$K_{IC} = (f)^{-1/6} (E\sigma_y R_o)^{-1/2} \quad (2-24)$$

It has been found that this equation does not work well for a wide variety of materials¹⁶⁷ most likely because failure is assumed to occur by impingement of voids, which is not the case in most materials. However, this model was a significant step towards modeling fracture initiation toughness by incorporating the microstructure.

More recent efforts have focused on the so-called characteristic distance model.¹⁶¹⁻
¹⁶⁴ The reasoning behind this model is that the equivalent plastic strain, ϵ_p , must exceed the critical fracture strain, ϵ_f^* , over some characteristic distance, l_o^* ; expressed as:

$$\delta_{IC} = \epsilon_f^* l_o^* \quad (2-25)$$

However, physically interpreting ϵ_f^* and l_o^* can be difficult. Values of ϵ_f^* have been obtained in a variety of ways, but there is no conclusive evidence that any one method is correct.¹⁶⁷ It also is unclear from existing experimental results exactly what the relationship of l_o^* is with regards to the microstructure.

Regardless of these shortcomings, this concept has been extended to include the growth of the initiation sites during deformation. A few models have employed this concept^{158,164,168} and seek to substitute the fracture strain with a measurable quantity obtained from the fracture surface. Garrison¹⁶⁴ has proposed an expression that relates δ_{IC} to the radius of the initiation site before fracture, R_i , and after fracture, R_v :

$$\delta_{IC} \sim X_o(R_v/R_i) \quad (2-26)$$

This expression has been shown to hold for some materials, but not others.¹⁶⁹ Application of this model was attempted here for PWA 1480, assuming that the pores are the fracture initiation sites. Their growth, if any, during the fracture process was assessed and used in the above expression.

2.5 Background Summary

It has been seen that while superalloy single crystals are microstructurally simple, they present many complexities when studying their behavior. The individual single crystal superalloy composition plays a large role in controlling the properties, and therefore much more research is needed in understanding this area. Some of these compositional effects are known, but much of the knowledge is only empirical. Based upon the literature in this

area, it appears that PWA 1480 should have comparable properties to similar alloys, with the possible exception of having a higher γ yield strength due to the presence of increased amounts of Ta. There also appeared to be a possible relation between the pores and the eutectic γ/γ' based upon the solidification literature, and this was explored. Incipient melting is a very real problem, as is the success of HIP'ing such materials, and these concerns were explicitly monitored.

It was found that it is possible the deformation of PWA 1480 differs from other superalloys in that dislocation shearing is not the primary deformation mechanism at room temperature; this was studied with the aid of flow stress models to assist in the interpretation of the tensile properties and deformation. Also, the manner in which hydrogen affects the deformation behavior is not known, and thus was a major goal of this work. Some studies have suggested that hydrogen can induce localized plasticity in these alloys, and this was examined in depth. The role of hydrogen trapping or of H.E.L.P on subsequent flow and fracture was also studied. The desorption method was used to obtain binding energies for hydrogen traps in an attempt to understand better the effect of hydrogen trapping sites on subsequent mechanical properties.

Superalloy single crystals tend to fracture along $\{111\}$ planes, and this has been explained in terms of the stress state present ahead of the crack tip. It is possible that the presence of internal hydrogen could alter this fracture mode in some way. Finally, it was discussed that the fracture toughness of single crystal superalloys has not been studied, and this appears to be a very fruitful area of research. Even polycrystal alloys, which are reported to have a relatively high fracture toughness, have had very little reported on fracture mechanisms. It was found that Mode I solutions can be used on these single crystals, as has been successfully done in fatigue crack growth studies of these type of alloys. Finally, it is hoped that the use of micromechanistic fracture initiation models will aid in interpretation of the data and possibly help identify any microstructural crack initiation sites.

Chapter 3

EXPERIMENTAL PROCEDURES

3.1 Material Preparation

3.1.1 As-Received Material

Twenty single crystal slabs of PWA 1480 produced by TRW Metals Division in December 1983 were obtained from NASA Lewis Research Center in December 1986. They were approximately 6.4 cm wide, 15.2 cm long, and 1.6 cm thick with the long direction being the growth axis. The samples were received in the solution heat-treated condition described below with orientation data provided for a few bars. It is believed that the ends of the bars had probably been sandblasted at TRW both to check the orientation and look for any small angle grain boundaries. The bulk composition was provided by TRW and in weight percent is as follows:

Major Elements

Al	Co	Cr	Ta	Ti	W	Ni
4.83	5.35	10.43	11.86	1.29	4.07	Bal.

Trace Elements

Fe	S	Si	Mn	P	C	Zr	Hf	B
0.08	0.0015	<0.02	<0.02	<0.015	42 ppm	<75 ppm	<75 ppm	< 15 ppm

3.1.2 Laue X-ray Analysis

The growth axis orientation of most of the slabs was determined by the Laue back-reflection technique using a Siemens Kristalloflex 2 x-ray source. Best results were

obtained when the ends of the slabs were electropolished or mechanically polished down to 0.05 μm Al_2O_3 slurry. A two-axis goniometer capable of being mounted to a wire saw was used when certain non-conventional orientations were desired. All Laue pictures were taken with a 3 cm distance between the sample and the Polaroid Type 57 film. Typically, 35 kV and 20 mA for 5 minutes gave a good pattern. Table 3.1 shows the growth axis orientation of all slabs and the transverse orientation of most slabs.

3.1.3 Heat Treatment

The normal heat treatment for PWA 1480, used by the majority of researchers,^{23,76,90,114,116} was followed. This consists of a solution heat treatment followed by a two-stage aging heat treatment. The first aging stage allows γ' precipitate nucleation, and the second stage allows some growth and maximizes the γ' volume fraction. All of the material was given the full heat treatment, even though TRW had previously given the material a partial heat treatment. This was done to achieve a uniform, desired γ' size and volume fraction. The heat treatment used was:

4 hours at 1288°C, air cool to room temperature

4 hours at 1080°C, air cool to room temperature

32 hours at 875°C, air cool to room temperature

At the beginning of the study, the samples were heat treated after machining and were encapsulated in quartz tubes back filled with 1/3 atm. argon. It was decided to discontinue this practice, however, due to dimensional changes, varying cooling rates and problems with the quartz tubing. The vast majority of all subsequent samples were heat treated as as-received slabs prior to machining. Some minimal oxidation occurred that was machined

Table 3.1 Solidification axis and transverse axis orientation of all PWA 1480 single crystals.

<u>single crystal slab #</u>	<u>growth axis</u>	<u>transverse axis</u>
16	2° off [001]	5° off <130> towards <110>
28	1° off [001]	2° off <120> towards <110>
32	1° off [001]	<230>
41	0° off [001]	<230>
60	1° off [001]	5° off <010>
78	4° off [001]	
80	3° off [001]	
107	4° off [001]	
114	5° off [001]	4° off <230> towards <110>
119	3° off [001]	2° off <230> towards <110>
131	4° off [001]	4° off <010>
134	7° off [001]	4° off <010>
166	4° off [001]	
167	4° off [001]	
169	2° off [001]	<110>
177	4° off [001]	
179	2.5° off [001]	
180	4° off [001]	<140>
183	2° off [001]	
192	3° off [001]	<130>

off. Further, the cooling rate at the center of the samples was monitored and found to be faster than the 115°/min suggested by Pratt and Whitney²⁴ to guarantee minimal precipitation of the γ' phase during cooling.

An isolated problem encountered during the solution heat treatment was incipient melting. The temperature difference between the γ' solvus and the incipient melting temperature (IMT) is only a few degrees when this heat treatment procedure is used.²⁴ To avoid overshooting above 1288°C, a ramp of 10°C/min to 1150°C followed by a 3°C/min ramp to 1288°C was used; however isolated instances of incipient melting of the eutectic γ/γ' still occurred. Figure 3.1 shows an example of such incipient melting.



Figure 3.1 Incipient melting that infrequently occurred during heat treatment.

In PWA 1480, the eutectic γ/γ' will melt if the IMT is exceeded, but it can also dissolve below the IMT if sufficient time is allowed for diffusion to occur. An alternate heat treatment was developed in order to minimize or eliminate the eutectic γ/γ' phase because of its undesirable properties described in a later section. The only difference between this alternate heat treatment and the normal heat treatment is that more time is spent

at the solution temperature to encourage the eutectic γ/γ' to completely dissolve. While the time needed varied with the material's prior history, it was found that 20 hours was needed for the as-received material. A normal two-stage aging heat treatment was then followed.

3.1.4 Hot Isostatic Pressing

Selected samples were Hot Isostatically Pressed (HIP'ed) to study the effect of grown-in porosity on mechanical properties. During heating to a level near the normal solution temperature, pressure is applied to a level that is below that needed to close the pores. The pressure is provided by a gaseous atmosphere, usually argon. Once the desired temperature is reached, it is held for awhile to assure a uniform temperature throughout the sample. Finally, the pressure is increased at a moderate rate up to the pressure necessary to close the pores. The key is to slowly ramp the temperature and pressure to avoid any recrystallization. The samples are left under these conditions for a period of time to allow diffusional processes to occur. The first attempt at HIP'ing was performed at Sandia National Laboratories in Livermore, Calif. The HIP'ing cycle was a single ramp to 1285°C and 103 MPa pressure. This level was held for one hour, followed by a quick helium cool. This produced a very slight reduction in porosity but no effect on mechanical properties. It was subsequently learned that Rocketdyne had developed a HIP'ing cycle specifically for PWA 1480, and this was attempted³³ at the Howmet facility in Whitehall, Mich. While the Rocketdyne cycle is under a U.S. patent secrecy order, it is known to be very close to a patented cycle developed at Howmet.³² For the latter case, the specific conditions for PWA 1480 are as follows:

- 1) Heat to 1288°C under a pressure of 34.5 MPa.
- 2) Hold for 1-2 hours.
- 3) Increase pressure at a rate of 0.42 to 0.55 MPa/min. to 103 MPa.
- 4) Hold for 4 hours.

It was found that this cycle only removed about half of the porosity, and it was believed that a longer time at the HIP temperature and pressure would completely remove the porosity. A second attempt was made at Howmet now holding the samples for 8 hours rather than 4 hours at 1288°C and 103 MPa. This increase was successful in virtually eliminating all porosity. Since the cooling rate in the HIP autoclave is insufficient to avoid γ precipitation, the samples must be re-solutionized and heat treated after HIP'ing.

3.1.5 Hydrogen Charging, Analysis and Desorption

All hydrogen-containing samples used in this study were gas-phase charged at Sandia National Laboratories in Livermore, Calif., under the direction of Dr. Neville Moody. The samples were charged for 15 days at 350°C and at a pressure of 103.4 MPa followed by a rapid cool while still under pressure. These severe conditions were necessary due to the low diffusivity of hydrogen in PWA 1480. Gas-phase charging was preferable to cathodic charging that has been used on similar alloys^{9,10} because of the uniform concentration of hydrogen obtained by gas-phase charging. After charging, the samples were packed in dry ice and shipped by overnight express to Carnegie Mellon where all samples were stored at 0°C until tested.

Hydrogen contents were analyzed by Luvak Inc. using vacuum hot extraction at 900°C. Samples were shipped to Luvak overnight in dry ice and stored at 0°C until analyzed. At least two samples in the same condition were analyzed, and the results for the two samples were always within 5%.

Hydrogen desorption experiments were performed by outgassing small cubes with an edge length of 3.8 mm in air at various temperatures and times. These were gas-charged along with the mechanical testing samples in the Sandia charging vessel. The cube size is believed sufficiently large to account for any variability in hydrogen trapping site density. Further, the use of two to three cubes for each analysis also provided more reliable

concentration data. A baseline was first established after each charging run by immediately analyzing the hydrogen content of a few samples after receipt. The loss of hydrogen at 0°C and room temperature also was measured as a function of time to account for extended periods at these temperatures.

3.2 Microstructural Characterization

3.2.1 Metallography

Most metallographic specimens were cold mounted using Quickmount self-setting resin. When edge retention was important, specimens were mounted in blue diallyl phthalate, which was hot-compacted in a Buehler Powermet Press. Mounting was followed by sequential hand grinding through 240, 320, 400 and 600 grit silicon carbide papers. The samples were then polished using 1 μm , 0.3 μm and 0.05 μm Al_2O_3 slurry. To avoid streaking and dimensional distortion of the pores, it was necessary to rotate the specimen opposite the wheel rotation while polishing. Further, to check any effect of the Al_2O_3 slurry on pore dimensions, polishing also was done with a diamond polishing compound. No quantitative differences resulted, so the easier method with the Al_2O_3 slurry was exclusively used.

Different etches were used depending upon which microstructural feature was to be viewed. The best etch to use when viewing the dendritic macrostructure or eutectic γ/γ was found to be 33% acetic acid, 33% nitric acid, 33% distilled water and a few drops of hydrofluoric acid applied for 10 seconds. Glyceregia (45% hydrochloric acid, 40% glycerol and 15% nitric acid) applied for 60 seconds was the best overall general etch and worked especially well for the γ/γ microstructure.

Samples were viewed optically on a Reichert Ultrastar metallograph using normal bright-field illumination. Occasionally, polarized light using Nomarski interference was

used to better view the dendritic macrostructure or eutectic γ/γ' , and all optical photographs were taken using Polaroid type 52 film.

3.2.2 Quantitative Metallography

Quantitative metallography was performed following the methods reviewed by Underwood.¹⁶⁶ Direct measurements of between 50 and 100 features were taken for each sample to determine the dimensions of the pores, eutectic γ/γ' and γ' precipitates. The pores were determined to be fairly spherical, with an aspect ratio of 1.10. Generally, the eutectic γ/γ' were oblong, so the longest and shortest dimension were measured. The average aspect ratio was 2.18, so the eutectic γ/γ' were classified as oblate spheroids following Underwood's nomenclature. To calculate the average size of the eutectic γ/γ' , all measurements were averaged. The edge length of the γ' precipitates were measured, and pictures were also taken to determine any γ' size differences between interdendritic and dendrite core areas, as well as regions bordering the eutectic γ/γ' .

A grid with spacings of 1 cm was used to measure the volume fraction and nearest neighbor spacings of the pores and eutectic γ/γ' . A 200x magnification was used for all pictures so that the grid size corresponded to the size of the object being measured, as suggested by Underwood. A minimum of 50 measurable objects were used for calculations, generally requiring between 10-12 photos for each sample. A point count approach was used to calculate the volume fraction.

Due to the high volume fraction of γ' precipitates, many standard quantitative metallography methods were difficult to implement.¹⁶⁶ Therefore, a method was devised that involved first counting all the γ' precipitates in an SEM micrograph. Next, the total number of possible γ' precipitates in a micrograph was calculated by using the average size and assuming a square array of impinging γ' precipitates. The actual number of γ' precipitates in the micrograph was divided by the calculated value yielding a volume

fraction. This method was fairly accurate, and the standard deviation between micrographs of the same sample was very low.

The importance of the spacing of the pores and eutectic γ/γ' in relation to the deformation and fracture behavior will be discussed in later sections. The general equation for the three dimensional (3-D) nearest neighbor distance, Δ_3 , is:

$$\Delta_3 = 0.554(N_V)^{-1/3} \quad (3-1)$$

where N_V is the number of particles per unit volume. For spheres (pores), this equation can be written in terms of more useful quantities:

$$\Delta_3 = 0.89R_o(f)^{-1/3} \quad (3-2)$$

where f is the volume fraction and R_o is the diameter of the object. A similar equation can be written for oblate spheroids (eutectic γ/γ') with an aspect ratio of two:

$$\Delta_3 = 0.71R_o(f)^{-1/3} \quad (3-3)$$

Equations 3-2 and 3-3 are based upon a narrow distribution of feature sizes and small volume fractions. The size distributions of the pores and eutectic γ/γ' are shown in Figures 3.2 and 3.3. Apparently, these distributions are not narrow enough because Δ_3 changes little after HIP'ing or the alternate heat treatment.

Therefore equation 3-1 must be used in its basic form. N_V can be related to the number of particles per unit area, N_A , and the number of particles per unit length, N_L , for the pores and eutectic γ/γ' . Both of these quantities are easily measured on micrographs.

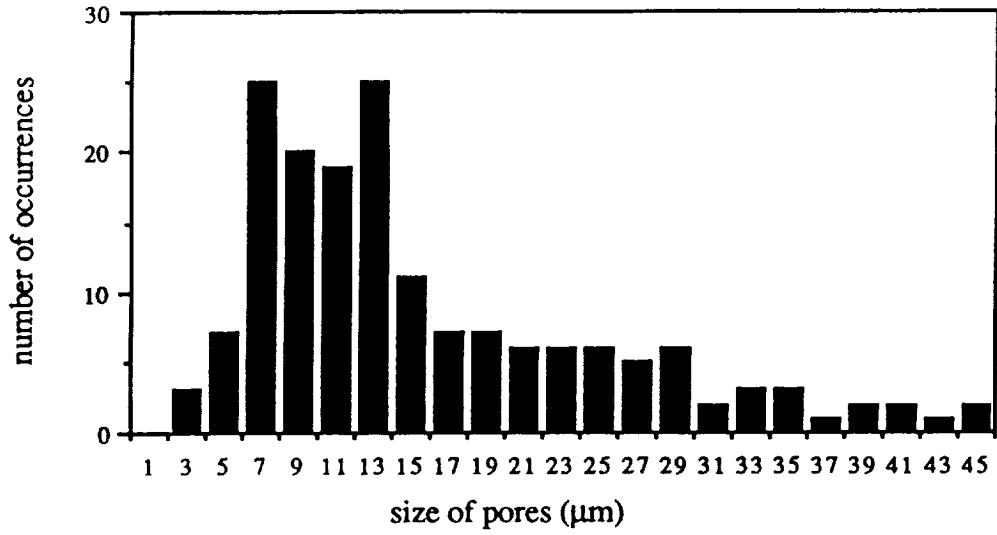


Figure 3.2 Size distribution of pores.

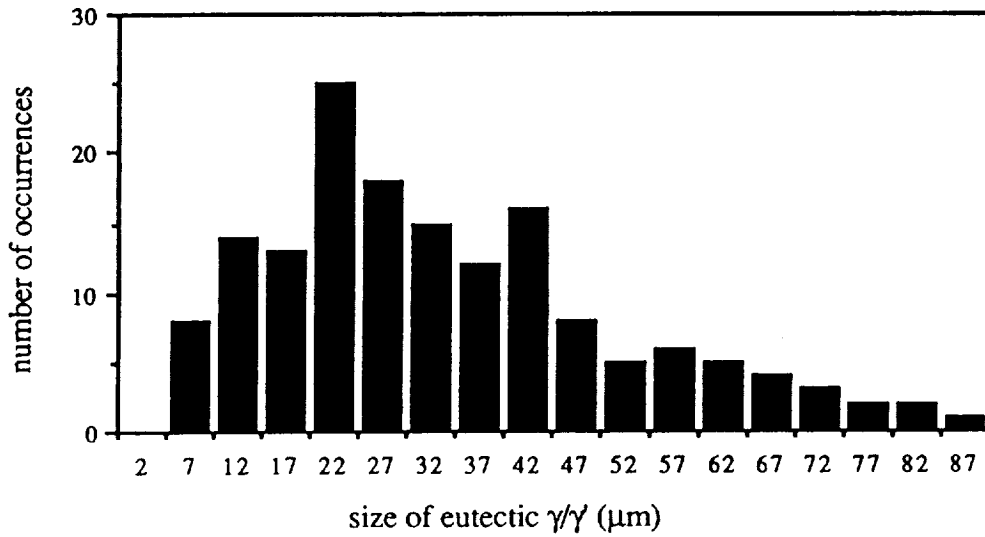


Figure 3.3 Size distribution of eutectic γ/γ .

The resulting equation used for pores is:

$$\Delta_3 = 0.600 \left(\frac{N_A^2}{N_L} \right)^{-1/3} \quad (3-4)$$

Likewise for the eutectic γ/γ' (oblate spheroids):

$$\Delta_3 = 0.668 \left(\frac{N_A^2}{N_L} \right)^{-1/3} \quad (3-5)$$

The values obtained from equations 3-4 and 3-5 were very consistent for each sample and varied as expected for HIP'ed or alternate heat treated samples.

3.3 Mechanical Testing

3.3.1 Tensile Testing

It was particularly important in the tensile samples, more so than in the fracture toughness samples, that the loading axis orientation be as close to [001] as possible to avoid any variations in the slip behavior. Therefore only single crystal slabs that were determined to be within 5° of [001] were used in tensile testing. These tensile specimens had a gage section of nominal length of 12.7 mm and diameter of 2.85 mm. The threads were 1/4-20UNC, and the gage had a machined finish of 16 millionths of an inch, which provided highly reproducible specimen-to-specimen results. Individual sample dimensions varied slightly, so each was measured on a travelling microscope. There was little difference found in the measured total strain whether an extensometer, usually with an 0.5 inch initial span, or the crosshead speed along with the chart speed was used to calculate

strain. Testing was done on an Instron model 1125 screw driven machine at a crosshead speed of 0.2 mm/min, corresponding to a strain rate of $2.6 \times 10^{-4} \text{ sec}^{-1}$.

Samples were pulled either to failure or to small plastic strains, the latter to monitor the development of the deformation process. Uncharged samples were strained to plastic strains of approximately either 0.0024 and 0.012. Charged samples could only be strained to a plastic strain of approximately 0.0015 due to the low strain to failure.

Elevated temperature tensile tests were done using the same Instron machine and a 3-stage Lindberg tube furnace mounted vertically on a portable stand. The temperature was allowed to equilibrate at least 20 minutes for each test as measured by a thermocouple placed directly beside the center of the specimen. Inconel pull rods were used, and it was possible to test up to 800°C.

3.3.2 Compression Testing

Compression tests were conducted on rectangular specimens measuring 5 mm on each side and 15 mm in length. All sides were flat and parallel to within 0.013 mm over the specimen length. Both the loading orientation and transverse orientations of the single crystals tested were determined by Laue back-reflection to assist in determination of subsequent slip traces. As with the tensile samples, the samples used all had a loading axis orientation within 5° of [001]. Prior to testing, the specimens were electropolished using a solution of 30% nitric acid in methanol at -25°C and 15 V for 60-90 seconds, sufficient to remove the machined finish layer. Final dimensions were then measured using a travelling microscope. Compression tests were performed on an Instron model 1125 screw driven machine using a crosshead speed of 0.2 mm/min, resulting in an initial strain rate of $2.2 \times 10^{-4} \text{ sec}^{-1}$. Strains were measured from the chart and crosshead speed, and were within 1% of dimensional changes.

Specimens were strained to varying levels of plastic strain to monitor the development of the deformation process. Both uncharged and charged samples were strained to plastic strain levels of 0.005, 0.012 and 0.030.

3.3.3 K_{IC} Testing

Plane-strain fracture toughness values were determined as a function of orientation and hydrogen according to ASTM E399-83.¹⁷⁰ Compact tension specimens without side grooves were used as shown in Figure 3.4. Specimens with the load axis near [001] were tested at CMU, while transverse orientation specimens were tested at Sandia. Prior to testing, samples were pre-cracked in accordance with ASTM E399-83 at alternating loads of 1400 lbs and 50 lbs at 3 Hz. This usually required 10,000-30,000 cycles to reach the desired crack length. After pre-cracking, specimens were hydrogen charged at Sandia in the manner previously described. Tests on both charged and uncharged samples were performed on a 20 kip MTS servohydraulic closed loop testing system, and were loaded under stroke control at a displacement rate of 1.0 mm/min, corresponding to a loading rate of approximately 100 lbs/sec. Loads and displacements were continuously recorded on an X-Y recorder and specimen displacement was measured by a clip gage (MTS model 632.03B-20) placed in the integral notch at the specimen mouth. After testing, the fatigue pre-crack was measured on a travelling microscope, and the load displacement results were analyzed in accordance with ASTM E399-83. From this data, a K_Q value was calculated. No K_{IC} samples met the thickness criteria of ASTM E399-83, and therefore it was necessary to perform J integral tests to obtain valid fracture toughness data.

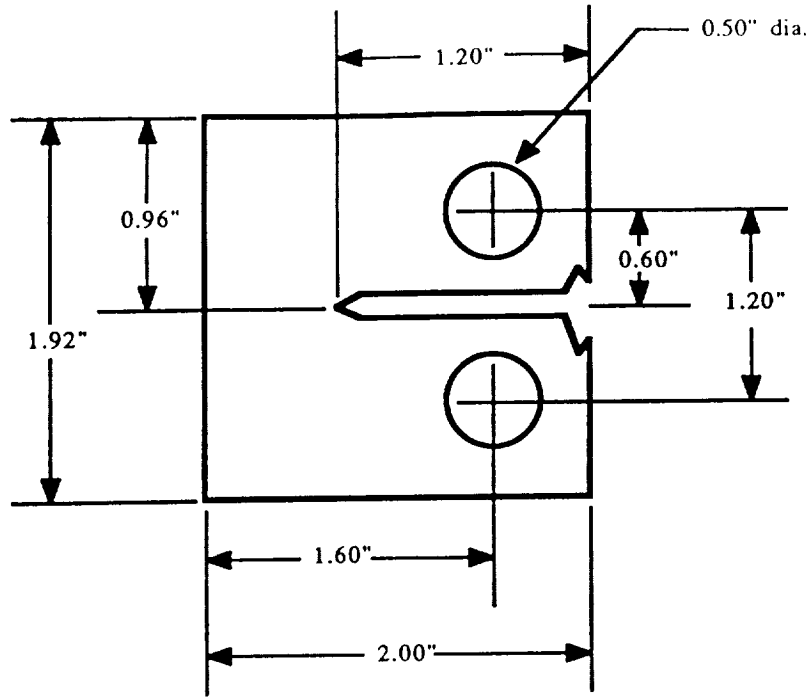


Figure 3.4 One-half inch thick compact tension specimen for K_{IC} testing.

3.3.4 J_{IC} Testing

Fracture initiation toughness values were determined by the J-integral fracture toughness test according to ASTM E813-87.¹⁷¹ Because of material limitations, the single specimen technique was used with compact tension specimens shown in Figure 3.5. Side grooves 1.25 mm deep were machined in after pre-cracking. All tests were performed on a 20 kip MTS servohydraulic closed loop testing system. Samples were pre-cracked in accordance with ASTM E813-87 at alternating loads of 2200 lbs and 50 lbs at 3 Hz, which usually required 10,000-30,000 cycles to reach the desired pre-crack length.

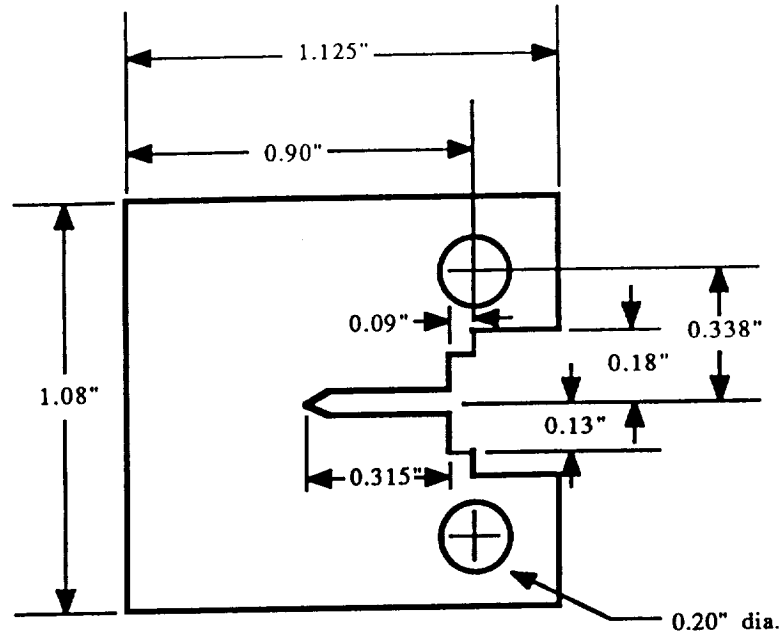


Figure 3.5 One-half inch thick compact tension specimen for J_{IC} testing.

After pre-cracking, some specimens were hydrogen charged at Sandia in the manner previously described. Load-point displacement was measured during the test using an extended arm clip gage (MTS model 632.03B-30). The clip gage was attached to razor blades along the load line, held in place by Permabond™ glue. Specimens were loaded in stroke control at a displacement rate of 2 mm/min, corresponding to a loading rate of 33 lb/sec. During testing, the specimens were repeatedly unloaded to an amount less than 20% of the current load at intervals of approximately 0.04 - 0.09 mm crack mouth opening displacement. Load and displacement were continuously monitored on an X-Y recorder, with portions of the unloading and reloading curve magnified ~20x using a zero-suppression circuit and recorded on a separate X-Y recorder. The compliance, C , was obtained from these unloading slopes and the crack length, a_i , was calculated using:¹⁷¹

$$\frac{a_i}{W} = 1.00196 - 4.06319\mu_{LL} + 11.242\mu_{LL}^2 - 106.043\mu_{LL}^3 + 464.335\mu_{LL}^4 - 650.677\mu_{LL}^5 \quad (3-6)$$

where:

$$\mu_{LL} = \frac{1}{(BEC)^{1/2} + 1} \quad (3-7)$$

and W is the length from load line to the specimen back face, B is the thickness and E is Young's modulus. The [001] value of Young's modulus of 118 GPa was used, which was calculated from the best literature values available as explained in section 2.1.1.3. This value compared favorably with the effective modulus calculated from ASTM E813-87. Hysteresis during unloading and reloading was kept to a minimum by using flat-bottomed clevis grips as suggested in ASTM E813-87. Tests were stopped after approximately 1.52 mm of stable crack growth, during which 12-16 unloading-reloading cycles were accomplished. Specimens were subsequently fatigued for a period of time to allow further crack growth and to determine the amount of crack growth that occurred during J-integral testing. The area under the load-deflection curves was measured on a Jandel Scientific digitizer using a program called Sigma-Scan. J-integral values were calculated from the equations given in ASTM E813-87. J_{IC} values were finally calculated from a J- Δa plot based on linear regression analysis of J- Δa points within the exclusion lines defined in ASTM E813-87.

3.4 Deformation and Fractography Characterization

3.4.1 TEM Foil Preparation and TEM Procedure

Transmission electron microscopy (TEM) specimens were cut from tensile and compression samples normally in the [001] orientation using a slow speed diamond cut-off wheel. Typically, an 0.4 mm slice was cut, and then thinned to 0.12-0.15 mm by hand grinding on 600 grit SiC paper. The introduction of dislocations was kept to a minimum by applying only a small amount of weight on the cut-off wheel and then applying as little pressure as possible when grinding. The punching of 3 mm discs from the thinned slices was able to be avoided in the tensile samples as the tensile gage diameter was approximately 3 mm.

These ground discs were then electropolished in a Fischione dual-jet polisher with a solution of 55% methanol, 35% butyl cellosolve and 10% perchloric acid at a temperature of - 20°C and voltage of 13.0 V. The latter corresponded to an amperage of between 8 and 11 mA. After polishing, the foils were rinsed in two separate methanol baths to minimize contamination. It was found that if the γ was preferentially polished, then the voltage was too low and vice versa for the γ phase. Generally, the success rate for quality foils was only about 30-40%.

[111] TEM foils were prepared from [001] oriented tensile and compression specimens as follows: The samples were oriented by the Laue back reflection technique using a two-tilt axis goniometer. The sample remained attached to the goniometer, while being cut on a South Bay Technology wire saw using 0.010 inch diameter diamond impregnated wire blades. The slices were then thinned and polished as described above.

TEM observations were made on a JEOL 120CX electron microscope operating at 120 kV using a two-axis tilt specimen holder. Dislocation types were identified by standard two-beam dynamical imaging. Most of the pictures were taken with the deviation vector, s_g , slightly greater than zero. Weak-beam dark field images were made using g - $3g$ diffraction conditions, primarily with $g = \langle 200 \rangle$.

Dislocation densities were measured using the method of Bailey and Hirsch,¹⁷² where the total dislocation line length in a given volume is measured. Due to the inhomogeneous distribution of dislocations between the phases, this method was preferred over one using a random line intersection technique.¹⁷³ The method used requires the thickness of the thin foil to be measured, and a simple geometric relation was employed utilizing the projected width of features such as dislocations or stacking faults.¹⁷³ Measuring dislocation densities is a detailed process and care must be taken not to introduce large errors. An attempt to reduce such errors was made in this study by using an enlarger to produce images six times larger than the negative. This facilitated measurements by allowing individual dislocations to be distinguished easier. The total dislocation line length

was measured on a digitizer using a program called Sigma Scan. No estimate of the total error can be made, but the standard deviation was always within 20% of the average value, which is not bad for these types of measurements.

3.4.2 Slip Band Analysis

Slip band behavior as a function of strain and hydrogen was quantitatively analyzed using the measurement techniques developed by McInteer, Thompson and Bernstein.¹⁷⁴ The average slip band spacing and the degree of waviness were measured, as illustrated in Figure 3.6. Measurements of these parameters were taken from optical micrographs, and TEM replicas of the specimen surface were not made. This fact will likely increase the error associated with the measurements made in this study. It was not the intent to measure individual slip lines, but rather the collection of slip lines referred to as slip bands. For each condition of strain and hydrogen, 5-7 photos were used resulting in measurements of over 100 slip lines.

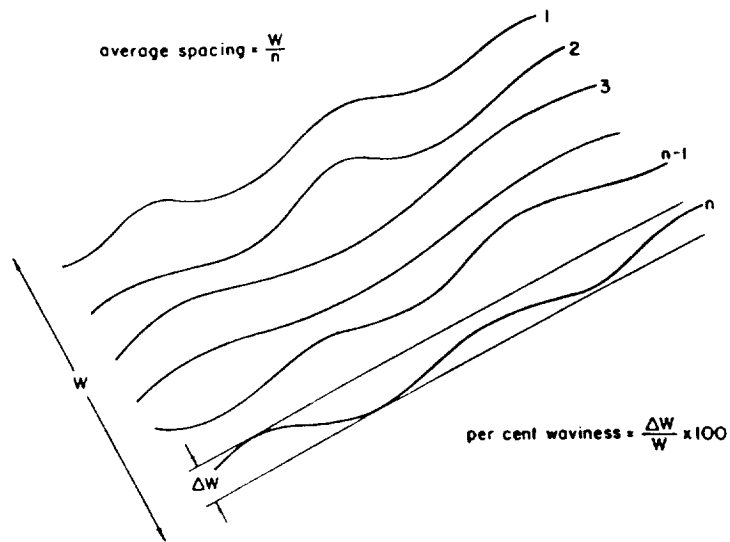


Figure 3.6 Schematic showing average slip band spacing and the degree of waviness.¹⁷⁴

3.4.3 Sectioning Experiments

Sections were made of failed tensile samples and double notch tensile samples in an attempt to better understand the failure process and mechanisms involved. Longitudinal sections were prepared from fractured tensile specimens, and K_{IC} and J_{IC} samples. Prior to sectioning, the fracture surface was nickel-plated to avoid damage to the surface or rounding during polishing. Electroless nickel plating was used with a solution of: 1 liter distilled water; 37.7 g. $NiSO_4 \cdot H_2O$ (nickel sulfate); 26.4 g. $NaH_2PO_2 \cdot H_2O$ (sodium hypophosphite); 15.9 g. $CH_3CO_2Na \cdot 3H_2O$ (sodium acetate), and 5-6 drops of sulfuric acid. The fracture surface and sample were first cleaned in acetone using an ultrasonic bath, followed by immersion for 1-3 hours in the above solution heated to 82°C. This yielded a deposit of a few micrometers over the entire sample. The samples were then sectioned on a slow speed diamond cut-off wheel and mounted using the blue diallyl phthalate, as previously described. Samples were observed on the optical microscope specifically for the presence of sub-surface cracks.

Double-notch tensile specimens were employed to look for cracks in the material that may have occurred during deformation and to attempt to observe events just prior to fracture. Samples were prepared and tested in the same manner as smooth cylindrical tensiles, except that two 60° notches were machined in the tensile gage with a root radius of 0.025 mm. The notches were each 0.25 mm from the specimen center and were 0.70 mm deep. After fracture, the piece containing the unfractured notch was sectioned perpendicular to the loading axis using a slow speed diamond cut-off wheel. After sectioning, the sample was mounted as previously described and examined optically and on the scanning electron microscope.

3.4.4 Pre-Strain and Pre-Charge Tensile Tests

A series of special tensile tests was performed to investigate whether hydrogen was affecting the deformation process, the fracture process, or both. Two groups of samples were prepared from the same single crystal and tested as follows:

<u>Group A</u>	<u>Group B</u>
Strain to ~50% of ϵ_f	Charge with Hydrogen
Charge with Hydrogen	Strain to ~50% of ϵ_f
Pull to Failure	Remove all Hydrogen by Outgassing
	Pull to Failure

Group A tests were designed to determine if hydrogen affected the fracture process, and Group B to determine if hydrogen affects the deformation process. Tensile tests were performed in the same manner as described in section 3.3.1. Hydrogen charging was performed using the same conditions as in section 3.1.5, and subsequent outgassing was done at 300°C for 75 hours, a temperature and time determined to result in less than 5 ppm hydrogen remaining in the sample.

3.4.5 Quantitative Fractography

Quantitative fractography was performed on tensile samples, as well as on K_{IC} and J_{IC} samples. Primarily, the area fraction of the eutectic γ/γ' and porosity was measured. Typically, 15 micrographs from each sample were randomly taken on the SEM at a 400x magnification. This was higher than the 200x magnification used in quantitative metallography, because the features were harder to identify on the fracture surface. Because of the higher magnification used, a grid spacing of 2 cm was employed for the point counting method of determining area fractions. To check the repeatability of this method, matching fracture surfaces were analyzed, and the quantitative fractography results

for both surfaces was within 5%. Changes in the pore size also were recorded by direct measurement.

3.4.6 Crystallographic Fracture Orientations

The crystallographic orientation of facets on the fracture surface was determined for cleavage facets and fracture ridges, as described below. Since all samples were single crystals loaded in the [001] orientation, analysis of facet orientation was greatly simplified. Due to the small scale involved, x-ray analysis of the fracture planes could not be used. While it was not necessary to use the detailed two-trace analysis,¹⁷⁵ as for samples of unknown orientation, the orientation of some cleavage facets and fracture ridges using two-trace analysis was done as a double-check of the techniques primarily used. As a prelude to all techniques, the loading axis orientation and, in some cases, the transverse orientation was determined by Laue back-reflection.

From prior observation, it was known that the cleavage facets were approximately perpendicular to the [001] loading axis. Therefore, it was assumed that the cleavage facets were on the {001} planes, and the goal was to prove this. First, a series of micrographs were taken of several cleavage facets at different sample angles. The sample was tilted until the beam direction was parallel to the sample sides to give a starting reference point. From this point, micrographs were taken at various known angles to the reference point. The first technique used micrographs of facets at the reference angle and tilt angles of 45-60°, and Figure 3.7 shows a schematic of this technique. For demonstration purposes, the [001] facet in the schematic is shown at a much larger scale than is realistic. Measurements are made on the cleavage facets at 0° tilt and at 60° tilt, for instance. If $x \cos 60^\circ = x'$, then it is concluded that cleavage facet x was perpendicular to the reference point. If this equality doesn't hold, then the angle of cleavage facet x from the reference point can be calculated

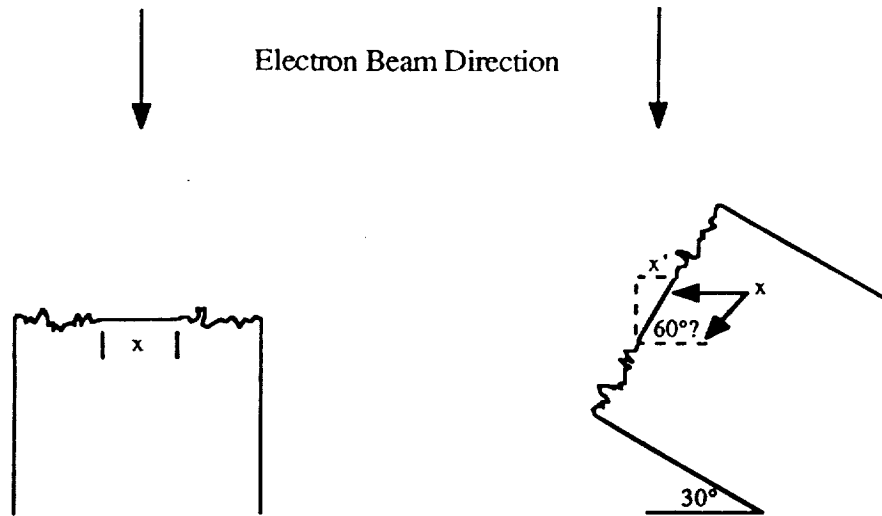


Figure 3.7 Schematic showing method to determine cleavage facet orientation. x is the cleavage facet width and x' is the projected width of the cleavage facet (not to scale). If $x \cos 60^\circ = x'$, then x was perpendicular to the beam initially.

using the Laue analysis of the sample's orientation. If the angle from the reference point is equal to the angle that the sample varies from [001], then the cleavage facet is exactly [001]. Otherwise, it is inclined to [001] by the difference between the two.

Another simple method can be applied to the cleavage facets, due to their apparent orientation relation with the loading axis. Once again, the beam is aligned perpendicular to the samples sides, and a series of micrographs taken at various angles. In this case, however, the angles are in increments of 2.5° up to a total angle of 15° , and the sample is rotated 90° after each series of micrographs. The projected width of the cleavage facet is measured, and in this way it can be determined exactly when the facet is perpendicular to the beam. Once again, this is compared to the Laue data to give the exact orientation of the cleavage facet.

Lynch reports that crack growth in fcc cleavage sometimes has a preferred orientation,^{176,177} so this possibility was explored. This was done on K_{IC} specimens where the transverse orientation of the sample was known. By simply turning the

specimen and recording the angle to the specimen side, it was possible to determine the line direction of the river markings and therefore the crack growth direction of the cleavage.

The orientation of the periodic ridges that appear on the fracture surface were analyzed in a similar simple manner as described above and also by a stereophotogrammetric analysis given by Wert and Robertson.¹⁷⁸ From the literature, it was suspected that these fracture ridges would be {111} facets.^{97,99,100}

As described above, the beam was aligned parallel to the sample sides. If the facets were of type {111}, then there would be a 45° angle to the [001] loading axis. Therefore, the sample was tilted 45° to the beam direction to determine if the facet was indeed now perpendicular to the beam. This was done in the same manner as described above, by tilting in small increments and measuring the projected width of the facet.

The second technique used was a stereophotogrammetric analysis method developed by Wert and Robertson, which requires that three variants of the crystallographic fracture plane exist on the fracture surface. This condition is satisfied with the fracture ridges. The technique is similar to the one described above, except it is more general because the specimen loading axis orientation need not be known. First, a suitable area of the fracture surface must be chosen so that three variants of the ridges are present and can be tilted through large angles. One of the variants is aligned parallel to the beam, and then the sample is tilted in increments of 10° up to a total tilt of 60°. From the given geometry and known orientation relations between {111} planes, it can be determined if the fracture ridges are indeed of the {111} type.

3.4.7 Fractographic Analysis Techniques

Various methods were used in an attempt to better understand the relationship between the fracture and the microstructure. The technique of plateau etching¹⁷⁹ was employed to directly observe any such relationship in tensile samples, as shown

schematically in Figure 3.8. First, the fracture surface was cleaned in acetone using an ultrasonic bath. This was an important step in order to assure better adhesion of the stop-off lacquer that was applied to part of the fracture surface. The rest of the sample was electropolished at -25°C using a solution of 30% nitric acid in methanol and applying a voltage of 15V for 1 minute. This was followed by application of a chemical etch to bring out the microstructure. Usually this etchant was 33% Nitric acid, 33% acetic acid, 33% distilled water and a few drops of hydrofluoric acid.

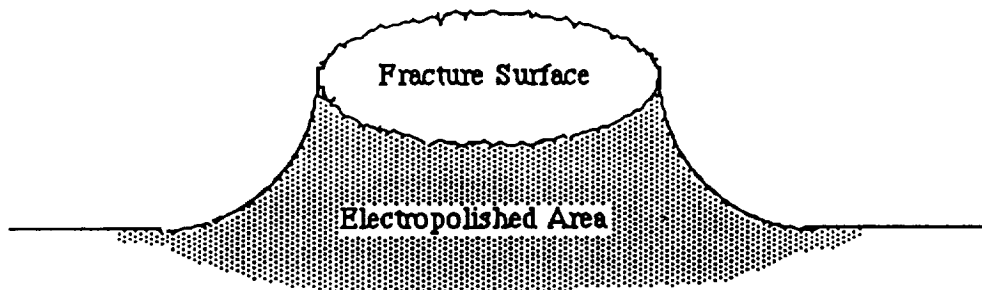


Figure 3.8 Schematic showing geometry of fracture surface-microstructure interface in plateau etching.

After etching, the stop-off lacquer was removed by immersion in an ultrasonic bath of acetone. Observation of the fracture surface-microstructure interface was done on the SEM. Typically, the fracture surface was tilted $20-40^{\circ}$ to the electron beam to yield the best view of the interface.

Another method used was to etch tensile fracture surfaces in an attempt to better determine the relationship between the γ/γ' microstructure and the fracture process. Areas were chosen and photographed on the SEM before etching to produce a reference micrograph. Glyceregia applied for 50-60 sec. was generally needed to observe any differences on the fracture surface. SEM micrographs were taken, and the fracture surface features were examined for relationships between the ductile voids and the γ/γ' , as well as for crystallographic information.

In order to view the fracture surface at higher magnifications, replicas were made for examination on the TEM. It was determined that two-stage replicas gave the best results. Cellulose acetate tape was placed on a clean tensile fracture surface after first softening the contact side with acetone. After the tape hardened, it was carefully stripped and shadowed at a 30° angle with Pt-C on a Veeco evaporator. This was followed by vertical deposition of carbon onto the tape. The tape was dissolved in successive baths of acetone, leaving the floating carbon replica. It was important to remove all traces of the cellulose acetate because of its detrimental effect on the cleanliness of the TEM. The remaining carbon replica was placed on a copper grid and examined in the JEOL 120CX TEM.

CHAPTER 4

RESULTS

4.1 Microstructural Characterization

PWA 1480 has a dendritic macrostructure with porosity and eutectic γ/γ' present in the interdendritic region. The macrostructure of samples given the normal heat treatment (sec. 3.1.3) was examined in the [001] and transverse orientations to determine any effect of growth direction on the size or shape of the porosity or of the eutectic γ/γ' . As the transverse orientation was not controlled during growth of these bars, it can vary randomly along the $\langle 010 \rangle$ - $\langle 110 \rangle$ line. The orientation of all bars was given in Table 3.1. All material was from the same batch provided by NASA, except a small amount received from Rocketdyne at a later date. Table 4.1 gives the average values for the pertinent macrostructural features of all of the NASA bars examined; the full table of values can be found in Appendix A along with the standard deviation of all measurements. Δ_3 is the three-dimensional nearest neighbor distance as explained in section 3.3.2, and is a useful quantity in interpreting the effect of microstructure on the deformation and fracture behavior. The aspect ratio is the largest diameter divided by the smallest and was measured to assist in subsequent quantitative calculations. There was no effect of orientation on the macrostructure, except for a slight effect on the average size of the eutectic γ/γ' . This difference is probably related to the solidification characteristics of the eutectic γ/γ' . The data for the bars from Rocketdyne are given in Table 4.2, and it can be seen that this material contained less initial porosity and eutectic γ/γ' . All future references will be made to the NASA material unless specifically noted otherwise.

The dendritic macrostructure also was quantitatively analyzed, and the following average dimensions were found: core diameter $\sim 150 \mu\text{m}$; arm diameter $\sim 400\text{-}500 \mu\text{m}$, and spacing $\sim 200 \mu\text{m}$. Figure 4.1 shows the dendritic structure along with the interdendritic

Table 4.1 Quantitative metallography results of unHIP'ed samples given the normal heat treatment. [001] orientation and transverse orientation averages shown.

	Pores				Eutectic γ/γ'			
	Average Size (μm)	Volume Fraction (%)	Δ_3 (μm)	Aspect Ratio	Average Size (μm)	Volume Fraction (%)	Δ_3 (μm)	Aspect Ratio
[001]	14.6	1.02	165.0	1.13	32.7	5.60	71.9	2.19
Trans.	14.9	1.04	152.5	1.12	27.4	5.90	67.3	2.09

Table 4.2 Quantitative metallography results of material received from Rocketdyne.

	Pores			Eutectic γ/γ'		
	Average Size (μm)	Volume Fraction (%)	Δ_3 (μm)	Average Size (μm)	Volume Fraction (%)	Δ_3 (μm)
Average	9.1	0.23	250.0	25.9	2.09	150.9

ORIGINAL PAGE
BLACK AND WHITE PHOTOGRAPH

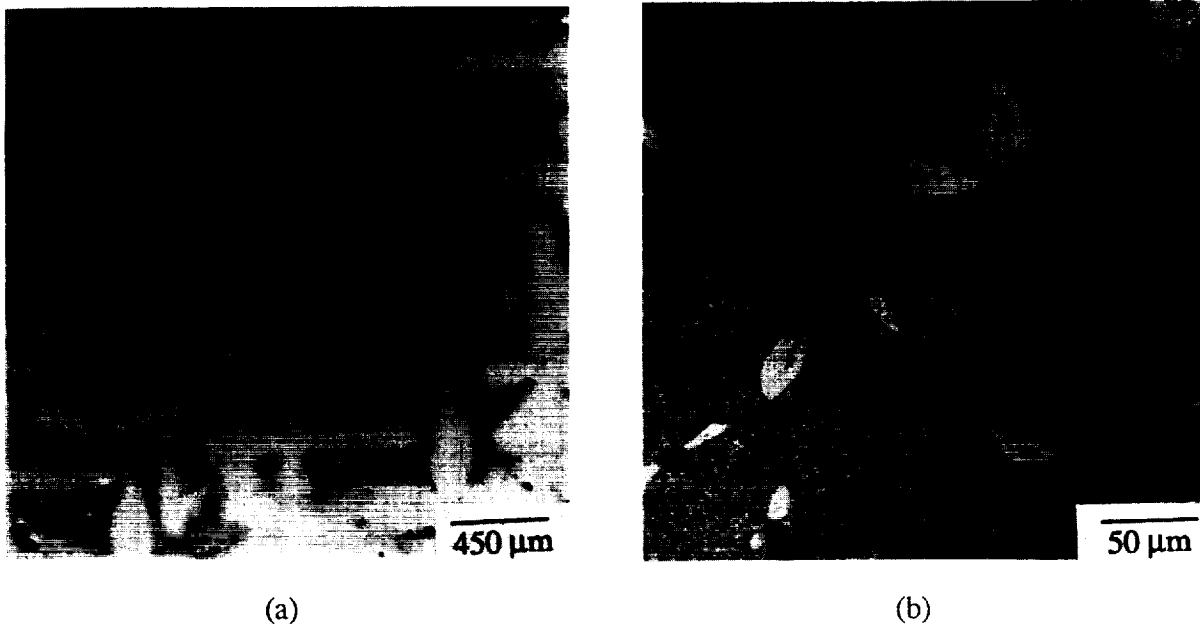


Figure 4.1 (a) Dendritic macrostructure of PWA 1480 and (b) interdendritic porosity and eutectic γ/γ' .

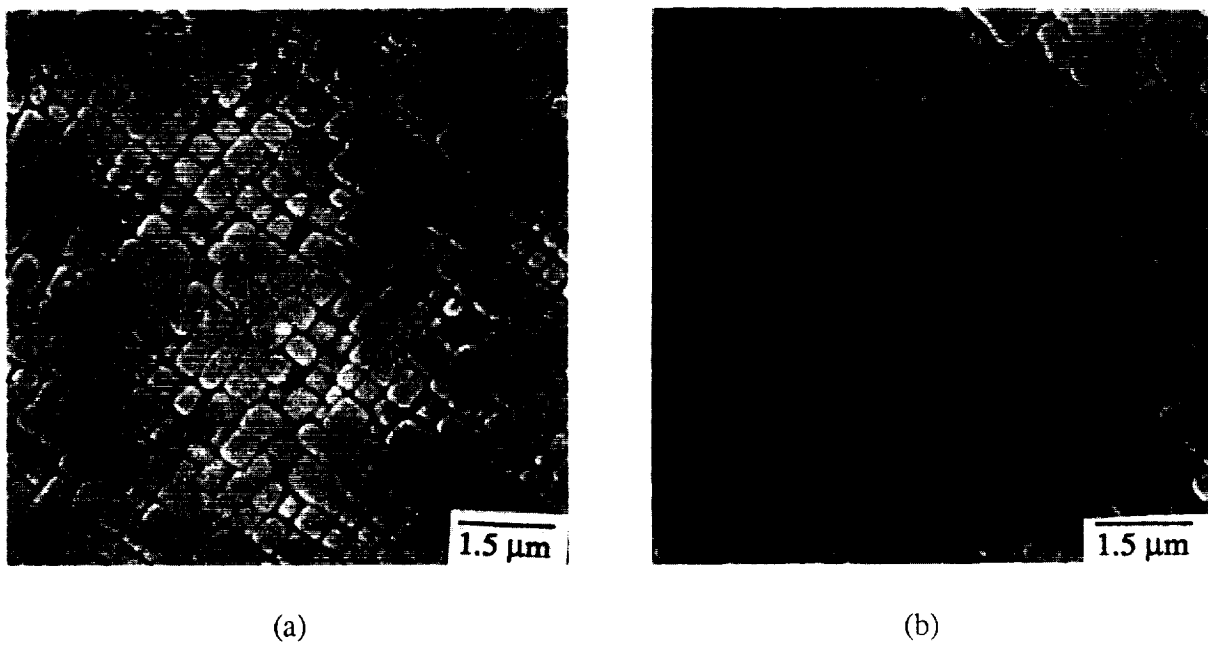


Figure 4.2 γ/γ' microstructure of PWA 1480; (a) inside dendrites and (b) in the interdendritic region.

porosity and eutectic γ/γ' . It was difficult to positively ascertain whether there was any relation between the positions of the eutectic γ/γ' and the porosity. It was discussed that the eutectic γ/γ' may act as nucleation sites for the pores,¹⁶ and thus each pore would be next to an eutectic γ/γ' . This may have been the case, but it was not possible to determine this from a series of 2-D micrographs. It was determined that because of the much larger volume fraction of eutectic γ/γ' , each eutectic γ/γ' was not necessarily associated with a pore. It also was mentioned in section 2.1.1.1. that it was possible for the eutectic γ/γ' to have a lacelike-appearance or a more featureless one. The vast majority of eutectic γ/γ' observed were essentially featureless, and based on other studies¹⁵ this suggests that the eutectic γ/γ' consists mostly of the γ' phase.

The effect of the dendritic structure on the resulting γ/γ' microstructure was studied. Figure 4.2a shows a representative γ/γ' microstructure in the dendrites and Figure 4.2b shows the microstructure in the interdendritic region. Table 4.3 gives the results for the average γ' precipitate size and volume fraction at various positions relative to the dendrites. While there was no effect of the dendritic structure on γ' volume fraction, the γ' size was clearly larger in the interdendritic region. Also, inside the dendrite core and arms, the γ' precipitates were of uniform size, but a bi-modal distribution of γ' was found in the interdendritic region with about 3% of the γ' precipitates having an edge length of

Table 4.3 Quantitative metallography results of γ/γ' microstructure.

Sample	Location of measurement	Average size (μm)	Volume fraction
4 hr #1	interdendritic area	0.485	74%
4 hr #2	interdendritic area	0.478	71%
4 hr #3	dendrite core	0.416	70%
4 hr #4	dendrite arm	0.402	72%

approximately 1 μm , and the remaining γ being less than 0.5 μm . However, even taking this bi-modal distribution into account it cannot explain the size difference, so it is apparent that the typical γ in the interdendritic region is indeed slightly larger than those found in the dendrites. No quantitative metallography was performed on the γ near the eutectic γ/γ' , but often there were 1 μm γ within a few μm of the eutectic γ/γ' . The volume fraction of γ' precipitates in Table 4.3 is slightly larger than other published values for PWA 1480,^{7,76,111} and the average size is slightly less. These variations could be due to differences in compositions, heat treating practice or measurement techniques. For completeness, it should also be mentioned that the γ/γ' misfit has been reported to be 0.28%.¹²²

4.1.1 Alternate Heat Treatment

It was established that additional time at the solution heat treatment temperature not only reduced compositional segregation but also dissolved most, if not all of the eutectic γ/γ' phase. For the as-received material, it was found that 20 hours at 1288°C was sufficient to eliminate almost all of the eutectic γ/γ' . This step was followed by the normal two-stage aging heat treatment, and this entire heat treatment will be subsequently referred to as the alternate heat treatment. In fact, this term has been generalized to refer to any heat treatment that removes the eutectic γ/γ' and is not limited to solutionizing times of 20 hours. Table 4.4 shows the quantitative metallographic results of samples solutionized for the normal time of 4 hours and for those solutionized for 20 hours. While no quantitative data were taken at points between these two times, it was observed that the eutectic γ/γ' began to break up after about 8-10 hours. There was no effect of solutionizing time on the γ/γ' microstructure of the samples studied.

A potential drawback to solutionizing for extended periods of time is incipient melting, which can occur with quite small fluctuations in temperature. In the set of samples

studied in Table 4.4, incipient melting occurred in all samples held longer than 20 hours, probably due to a temperature surge that can occur when the furnace door is closed after removing some of the samples. Other possible explanations which we believe less likely involve local concentration changes that could induce incipient melting. The former rationale could explain why incipient melting is more prevalent in samples that have repeatedly been exposed to this temperature surge. In support of this, separate samples were held at the solution temperature for over 50 hours successfully with no incipient melting, so long as the heat treatment was not interrupted by opening the furnace door. In future applications of the alternate heat treatment, careful experimental control was followed and unless otherwise stated, samples were held for 20 hours at 1288°C.

Table 4.4 Quantitative metallography showing results of alternate heat treatment.

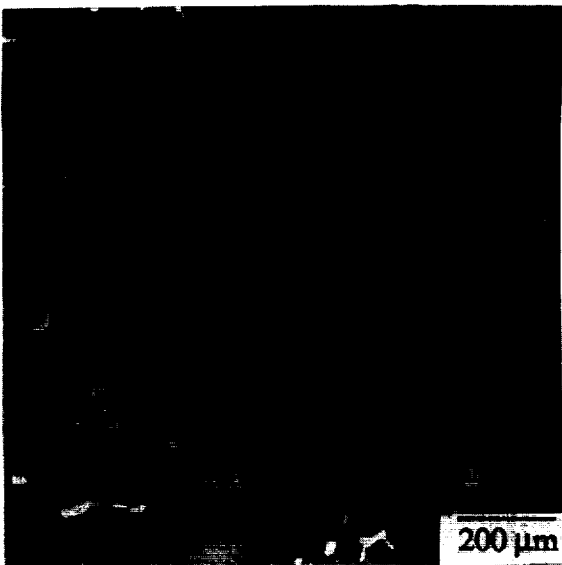
Material Condition	Pores		Eutectic γ/γ'	
	Average Size (μm)	Volume Fraction (%)	Average Size (μm)	Volume Fraction (%)
Normal Heat Treatment	14.6	1.0	31.9	5.3
Alternate Heat Treatment	15.5	1.0	10.0	0.48

4.1.2 Hot Isostatic Pressing

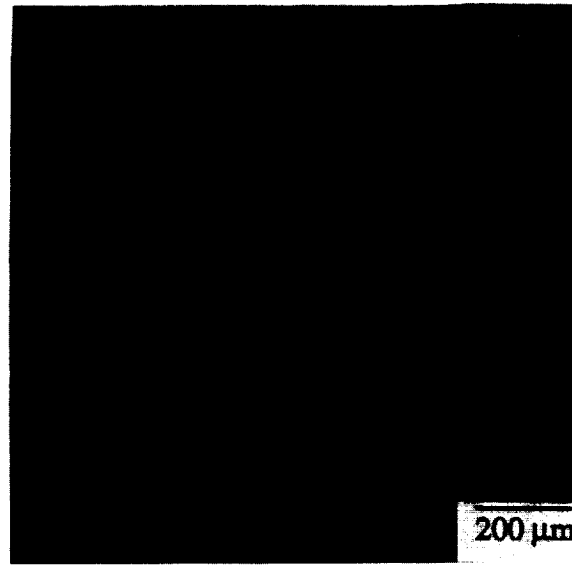
The removal of porosity by Hot Isostatic Pressing (HIP'ing) has been used by us and others^{23,28} to test the effect of porosity on tensile properties. The difficulties associated with HIP'ing these alloys is detailed in section 2.1.1.4, however, the cycle used in this thesis is believed to have overcome these problems. Table 4.5 shows the average quantitative metallographic results of the first HIP'ing cycle attempted and a second more successful attempt, with a hold time of 8 hours at the final temperature and pressure rather

Table 4.5 Quantitative metallography for HIP'ed samples.

	Pores			Eutectic γ/γ'		
	Average Size (μm)	Volume Fraction (%)	Δ_3 (μm)	Average Size (μm)	Volume Fraction (%)	Δ_3 (μm)
no HIP	14.4	0.99	174.2	33.4	5.25	78.0
HIP 1	8.3	0.57	206.5	19.9	3.04	101.8
HIP 2	4.3	0.035	398.4	15.8	1.43	147.4



(a)



(b)

Figure 4.3 Comparison between the macrostructure of (a) the as-received material and (b) the HIP'ed material given the alternate heat treatment.

ORIGINAL PAGE IS
OF POOR QUALITY

ORIGINAL PAGE
BLACK AND WHITE PHOTOGRAPH

than 4 hours. In the table, HIP 1 signifies the first HIP cycle used and HIP 2 the second. The average of the unHIP'ed values is reported in Table 4.5 as no HIP. Figure 4.3 illustrates the differences in porosity content between the as-received material and the HIP'ed material that was held for 8 hours and subsequently given the alternate heat treatment. There were no quantitative differences in the γ/γ' microstructure after either HIP cycle.

Recrystallization did occur in some of the samples that had been HIP'ed, as shown in Figure 4.4. This problem was associated with surface damage usually on the ends of the single crystal slabs, which may have been caused by a sandblasting procedure at TRW. Fortunately, sections for metallographic specimens had been removed from the ends of the slabs prior to HIP'ing, and although these sections were sometimes partially recrystallized, it is not believed that recrystallization affected any test samples taken from the slab interior.

Because HIP'ing is performed at a solution temperature of 1288°C, a decrease in eutectic γ/γ' size and volume fraction relative to unHIP'ed material is seen in Table 4.5. Furthermore, a separate solution heat treatment had to be performed after HIP'ing due to the slow cooling in the autoclave, thereby further reducing the eutectic γ/γ' size and volume fraction. The measurements in Table 4.5 were taken following the full heat treatment after HIP'ing. Since the amount of eutectic γ/γ' is reduced during HIP'ing, it was difficult to independently assess the role of pores and eutectic γ/γ' . However, Table 4.5 shows there still was some eutectic γ/γ' left after HIP'ing, so it was possible to apply the alternate heat treatment to these samples, and comparisons could be made between HIP'ed material with and without eutectic γ/γ' . Table 4.6 gives an overview of the effect of heat treatment and HIP'ing on the macrostructure.

ORIGINAL PAGE
BLACK AND WHITE PHOTOGRAPH

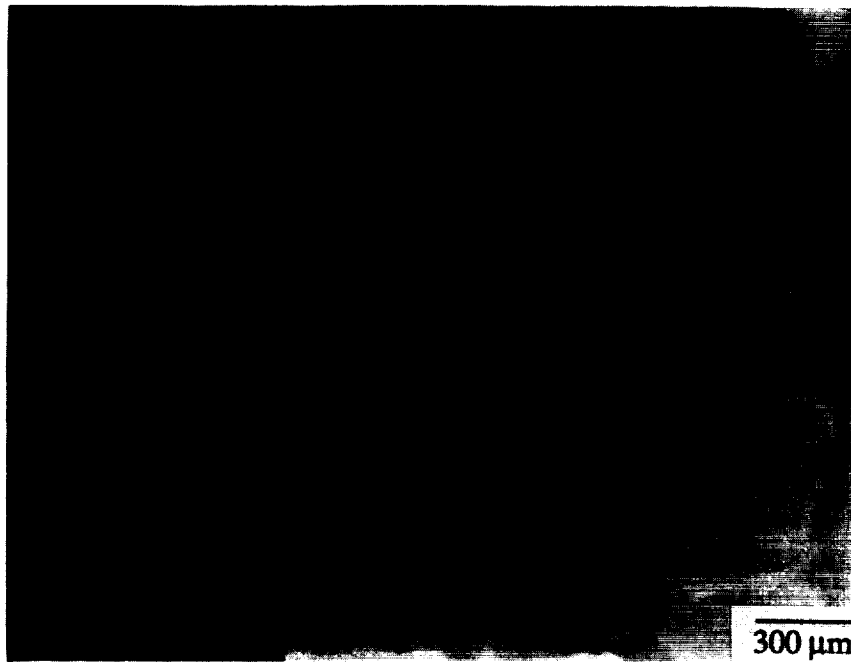


Figure 4.4 Recrystallization that occurred in some of the HIP'ed samples.

Table 4.6 Synopsis of the effect of HIP'ing and heat treatment on the macrostructure.

Sample condition	Pores		Eutectic γ/γ'	
	Average size (μm)	Volume fraction (%)	Average size (μm)	Volume fraction (%)
unHIP'ed normal HT	14.6	1.02	33.7	5.6
unHIP'ed alternate HT	15.5	1.00	10.0	0.48
HIP'ed normal HT	4.3	0.035	15.8	1.43
HIP'ed alternate HT	3.1	0.020	6.1	0.30

4.2 Hydrogen Trapping Characteristics

Hydrogen trapping was analyzed by performing desorption tests at various temperatures. To calculate the amount of hydrogen that would be left in a cube after outgassing and assuming no traps, the following equation was used:¹⁸⁰

$$C = C_o \left(\operatorname{erf} \frac{x}{4\sqrt{Dt}} \right) \quad (4-1)$$

where C_o is the initial hydrogen concentration, x is the edge length of the cube, D is the diffusion constant and t is time. At 0°C there was no measurable loss of hydrogen after 3 months, and at room temperature there was no measurable loss of hydrogen after 14 days. Figure 4.6 shows the measured results at 150°C for PWA 1480 along with calculated desorption profiles for similar alloys using the diffusion data described in section 2.3.1.1. At least two samples were used for each measured point for PWA 1480, and the hydrogen concentration differences were invariably well within 5%. To assist in interpretation, the multiplying factor to convert from ppm to appm is 58.6 for PWA 1480. It can be seen that the MAR-M 246 diffusion data is obviously too high, but the other diffusion data can be used. This conclusion is supported by recent work that suggested the diffusion constant of hydrogen in a similar single crystal, CMSX-2,¹⁰ was very close to that of hydrogen in IN 903. The desorption profile at 300°C is shown in Figure 4.6 and at 400°C in Figure 4.7. The measured data of PWA 1480 closely followed the calculated profile obtained using the diffusion data of IN 903 and assuming no traps.

In order to independently assess the trapping characteristics of the porosity and the eutectic γ/γ' , HIP'ed material was charged and outgassed. This HIP'ed material contained very close to zero percent porosity, and the results for desorption at 150°C are shown in Figure 4.8 and at 300°C in Figure 4.9. These figures are almost identical to Figures 4.5 and 4.6 showing that porosity has no effect on the amount of hydrogen that can be charged into the material or the rate of outgassing. It is important to point out that in samples without eutectic γ/γ' , it also was possible to obtain about 300 ppm hydrogen in the

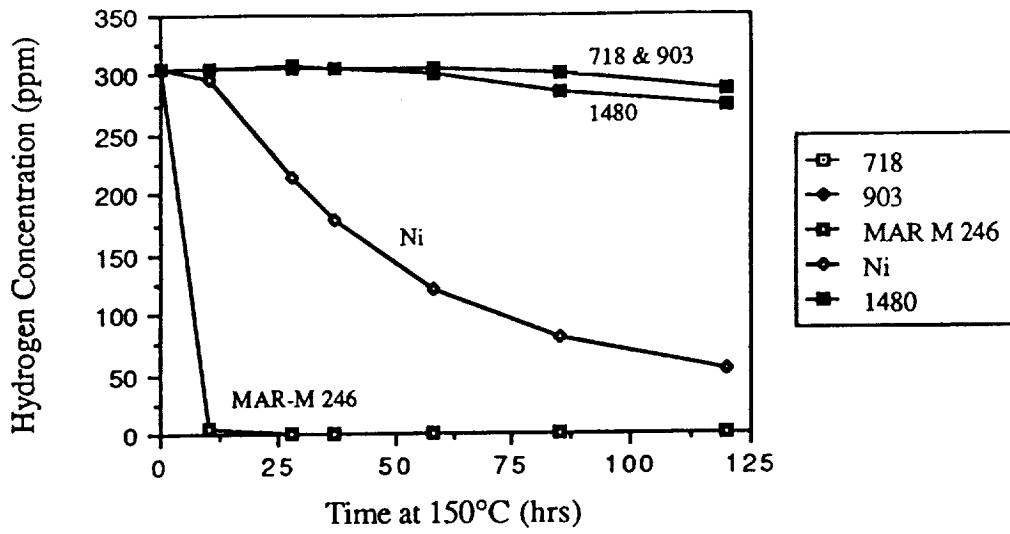


Figure 4.5 Desorption profile at 150°C showing the amount of hydrogen outgassed as a function of time.

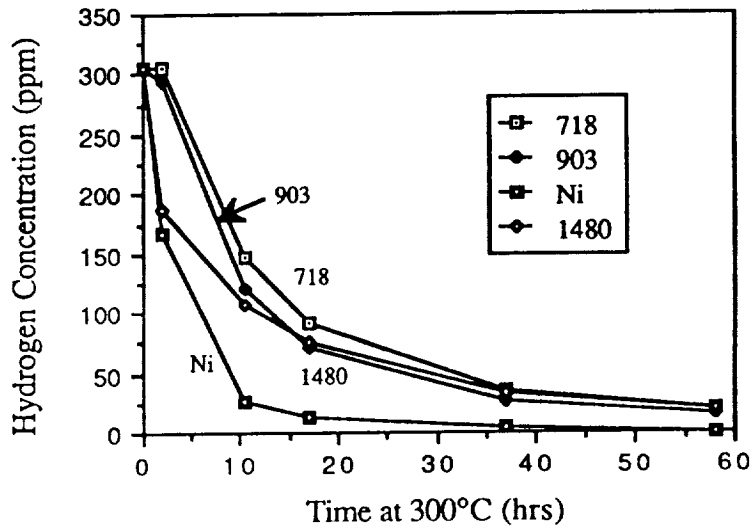


Figure 4.6 Desorption profile at 300°C showing the amount of hydrogen outgassed as a function of time.

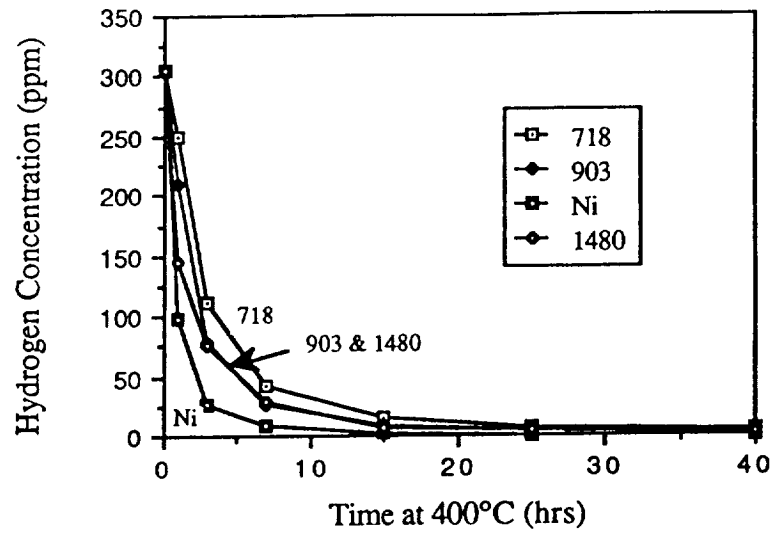


Figure 4.7 Desorption profile at 400°C showing the amount of hydrogen outgassed as a function of time.

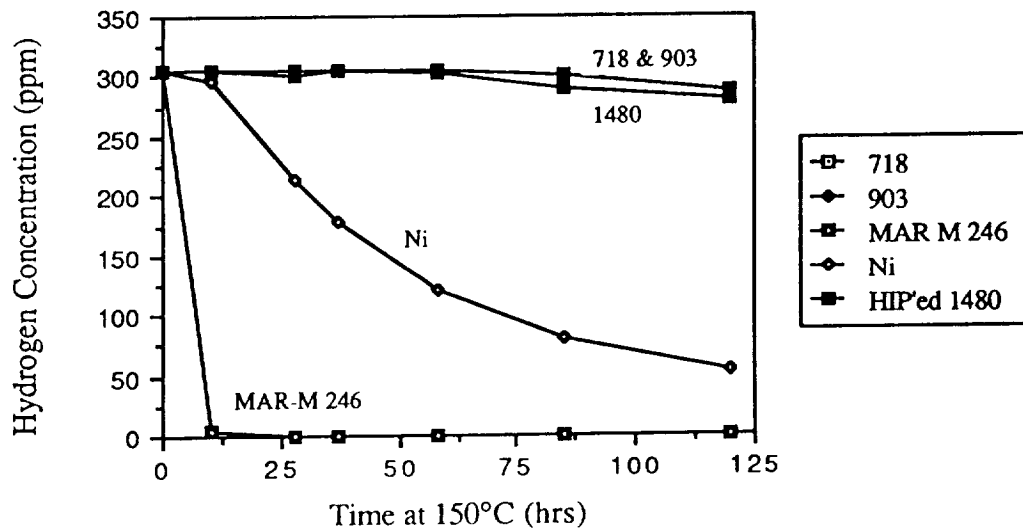


Figure 4.8 Desorption profile at 150°C for HIP'ed samples.

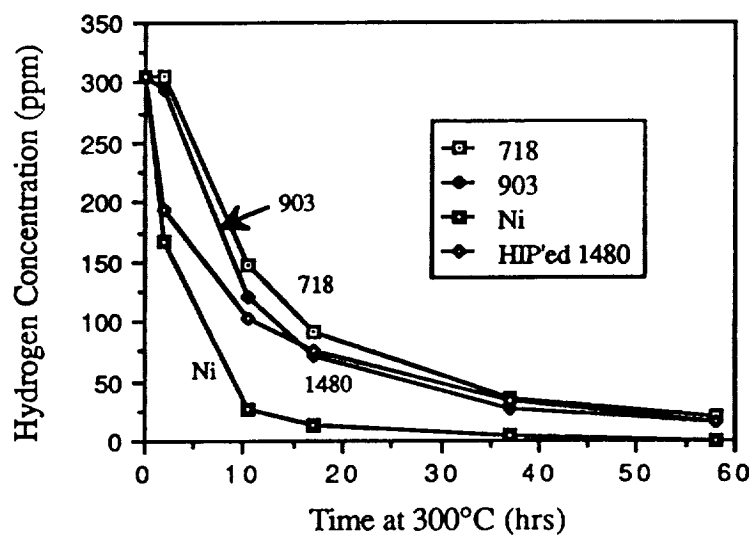


Figure 4.9 Desorption profile at 300°C for HIP'ed samples.

microstructure under the same charging conditions. This implies that neither the porosity nor the eutectic γ/γ' are important sinks for hydrogen during charging.

4.3 Mechanical Properties

4.3.1 Tensile Properties

The tensile properties of PWA 1480 were tested as a function of hydrogen content, eutectic γ/γ' and porosity. The average results of a dozen tests of uncharged tensile specimens given the normal heat treatment are shown in Table 4.7. The strength values are fairly constant from slab to slab, but the strain-to-failure values can vary quite a bit as documented in the complete results presented in Appendix A. The reduction-in-area (R.A.) values are reported for some specimens in this Appendix, but accurately measuring this value was difficult due to the specimen geometry and small changes involved. Appendix A also gives the standard deviation for all tensile properties. A schematic of a typical stress-strain curve is drawn in Figure 4.10. Generally, after two percent strain the curve began to rise again reflecting work hardening, which accounts for the slightly higher ultimate tensile strength than yield strength in most samples. In a few tests, the curve never rose above the yield strength again, and when this occurred, the reported ultimate tensile strength value is the yield strength.

4.3.1.1 Effect of hydrogen

Normal charging used a hydrogen pressure of 103.4 MPa at 350°C, which resulted in uniform total hydrogen contents of around 300 ppm (1.74 at. %). The average results of room temperature tensile tests on such samples, containing approximately 300 ppm hydrogen, are given in Table 4.8; the complete results for all samples tested are in Appendix A. The most striking result compared to uncharged samples was the order of magnitude decrease in strain to failure for the charged specimens, as shown in Figure 4.11.

Table 4.7 Room temperature tensile test results for samples that were unHIP'ed, uncharged and given the normal heat treatment.

	0.2% Y.S. (MPa)	U.T.S. (MPa)	ϵ_f (%)	R.A. (%)
Average	1112	1153	3.36	3.07

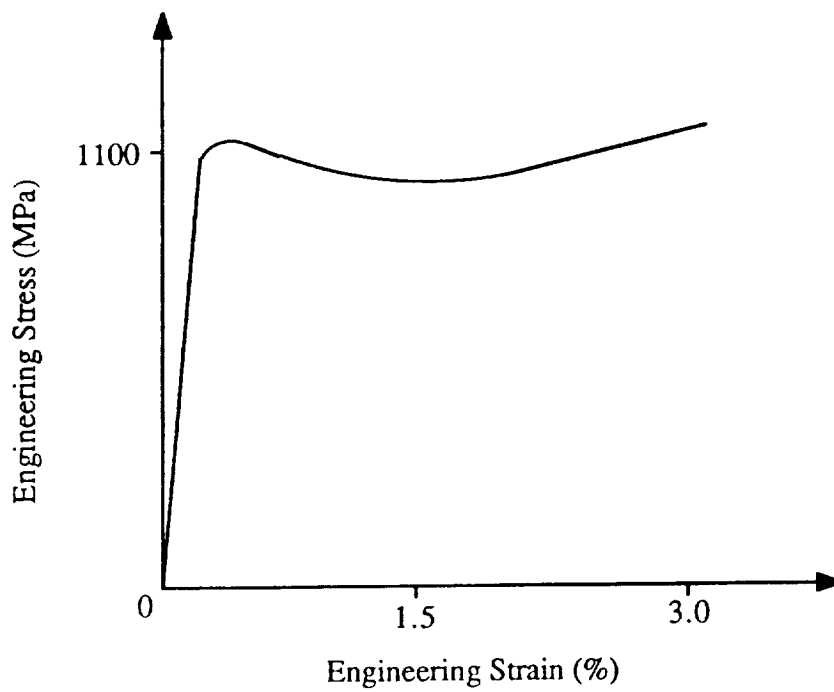


Figure 4.10 Typical stress-strain curve for uncharged samples.

Table 4.8 Room temperature tensile test results for samples that were unHIP'ed, charged and given the normal heat treatment.

	0.2 % Y.S. (MPa)	U.T.S. (MPa)	ϵ_f (%)	R.A. (%)
Average	1001	1011	0.26	2.40

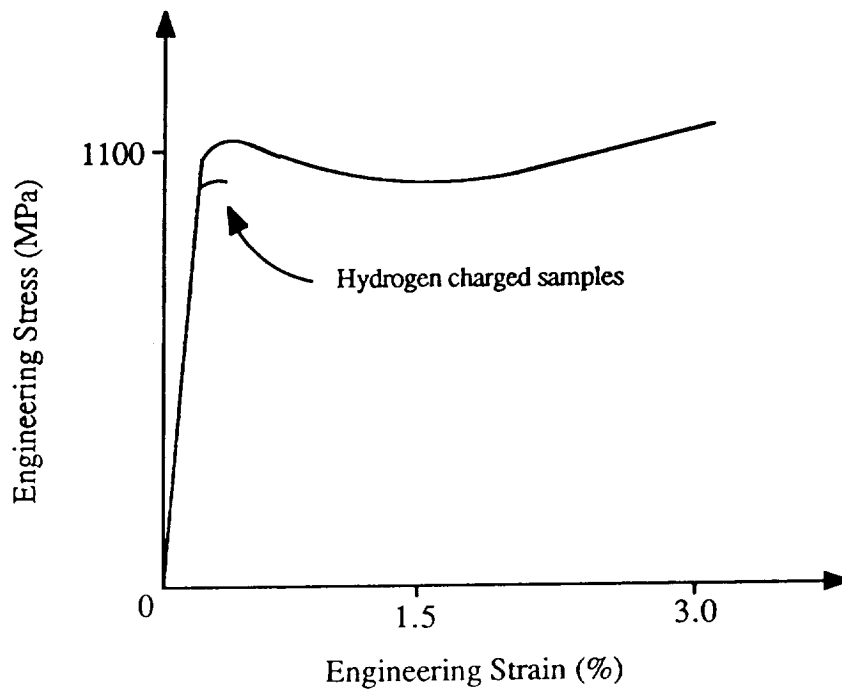


Figure 4.11 Typical comparative stress-strain curves for uncharged and charged specimens.

The R.A., however, was only slightly affected by hydrogen, but the yield stress was reduced by almost 10%.

The hydrogen content of tensile specimens was varied by changing the hydrogen gas pressure during charging or by desorption of the samples after normal charging. Different charging pressures of 13.8 MPa, 69.0 MPa and 138 MPa were used to now examine the effects of different hydrogen concentrations on the tensile properties. Table 4.9 shows there is little effect on the strength, and Figure 4.12 illustrates the effect of hydrogen concentration on the strain to failure. The average values for samples containing no hydrogen and 300 ppm hydrogen are included in Figure 4.12.

The hydrogen content of tensile samples also was varied by degassing samples that initially contained about 300 ppm hydrogen. Table 4.10 shows the tensile properties for samples that were degassed and then tested at 300°C. Once again there is little effect of hydrogen concentration on the strength or R.A. Table 4.10 and Figure 4.13 show the decreasing strain to failure with increasing hydrogen content. The end points of 0 ppm hydrogen and 300 ppm hydrogen in the figure are the average values of room temperature tests. Since it has been shown that the ductility of uncharged samples only changes slightly from 0°C to 300°C,⁷⁷ the introduction of these points should not introduce large uncertainties. Comparison of the curves in Figures 4.12 and 4.13 show them to be similar in shape, except that the minimum ductility occurs around 300 ppm in Figure 4.12 and 200 ppm in Figure 4.13.

Table 4.9 Room temperature tensile test results for samples charged under different hydrogen pressures and tested in air.

Charging Pressure	H Conc.	0.2% Y.S. (MPa)	U.T.S. (MPa)	ϵ_f (%)	R.A. (%)
uncharged	0	1112	1153	3.4	3.1
13.8 MPa	149	1032	1069	2.5	2.4
69.0 MPa	202	1035	1068	2.0	2.1
138 MPa	507	1022	1027	0.26	1.9

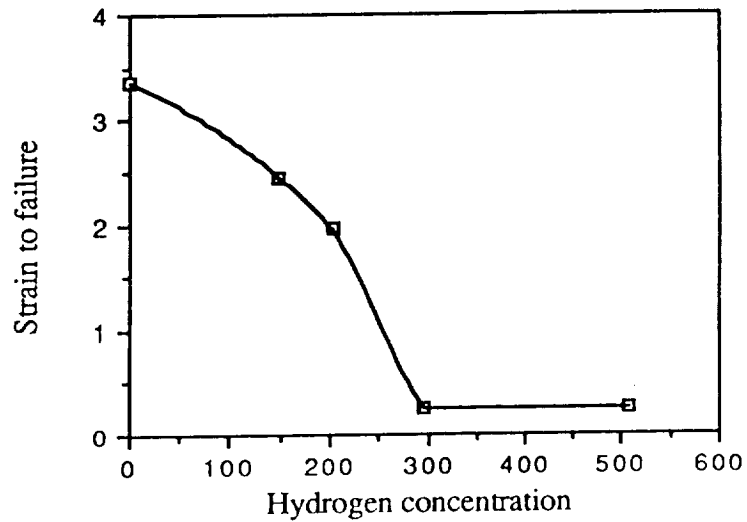


Figure 4.12 Strain to failure as a function of hydrogen concentration for samples charged under different hydrogen pressures.

Table 4.10 300°C tensile test results for samples desorbed to different hydrogen concentrations.

Hydrogen Conc. (ppm)	0.2% Y.S. (MPa)	U.T.S. (MPa)	ϵ_f (%)	R.A. (%)
55	1048	1100	2.2	2.5
135	1030	1060	1.2	2.3
159	1070	1118	0.9	2.6
195	1066	1114	0.4	2.1

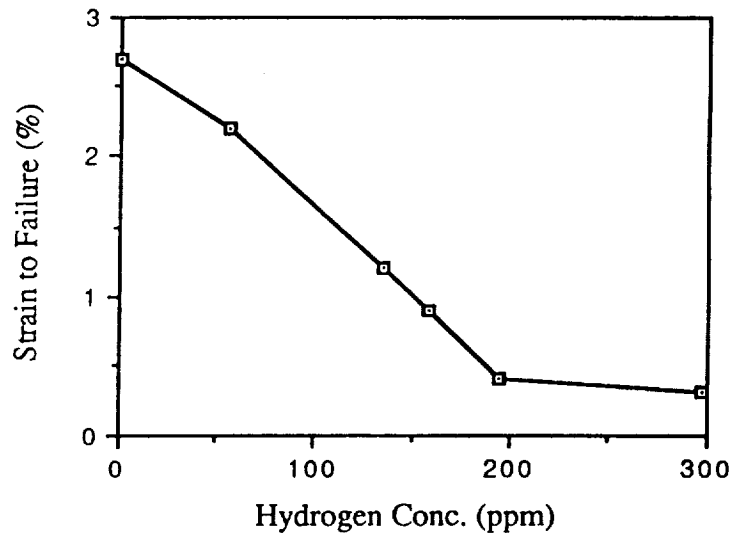


Figure 4.13 Strain to failure as a function of hydrogen concentration for samples that were outgassed for various times.

4.3.1.2 Effect of eutectic γ/γ'

After it was established that the eutectic γ/γ' could be eliminated by an extended solution heat treatment, a systematic study was undertaken to determine its effect on tensile properties. Tensile samples were held for solution times ranging from 4 to 29 hours, followed by the normal two-stage aging treatment. The results are graphically shown in Figure 4.14, which shows that while removal of the eutectic γ/γ' did not change the yielding behavior, there was a peak in both the U.T.S. and strain to failure at 20 hours solution time. The work hardening parameter, n , inexplicably increased from 0.04 at 4 hours to 0.08 at 20 hours.

Metallography was performed subsequently on the tensile thread section of the specimens, and it revealed that the eutectic γ/γ' was broken up at 15 hours and virtually eliminated at 20 hours. It also was found that incipient melting occurred in the samples held for 24 and 29 hours but not for shorter times. Therefore, it appears that the increased ductility and work hardening benefits derived from the removal of the eutectic γ/γ' are offset by the onset of incipient melting above 20 hours. This time is optimum under these conditions to remove the eutectic γ/γ' and improve tensile properties, and while longer times probably would not be detrimental, proper care must be taken during heat treatment.

Tensile tests also were performed on round bars received from Rocketdyne that were processed so that they contained less initial porosity and eutectic γ/γ' , as reported in Table 4.2. The average values of tensile tests are shown in Table 4.11 for samples given both the normal heat treatment and those given the alternate heat treatment to remove the eutectic γ/γ' .

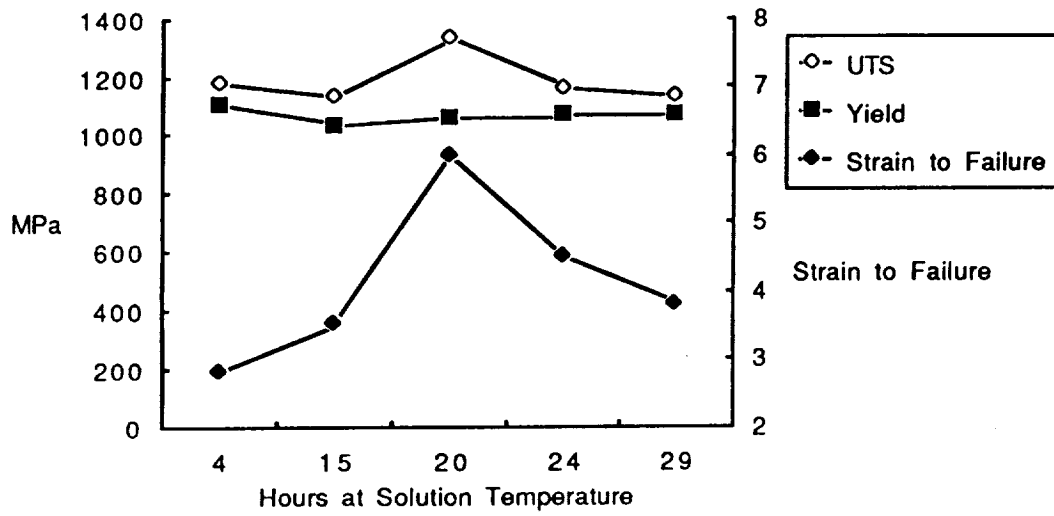


Figure 4.14 Effect of time spent at solution temperature on tensile properties.

Table 4.11 Effect of eutectic γ/γ' on tensile properties for Rocketdyne material.

Sample	0.2% Y.S. (MPa)	U.T.S. (MPa)	ϵ_f (%)	R.A. (%)
normal heat treatment	1138	1151	3.6	3.7
alternate heat treatment	1146	1191	5.4	6.5

The tensile curves in this batch were similar to those in Figure 4.11, except that those samples without eutectic γ/γ' exhibited higher uniform strains, which produced a higher UTS. The work hardening parameter, n , was not significantly different. The strain-to-failure differences due to heat treatment were not as dramatic in Table 4.11, as they were in Figure 4.14, probably because of the lower amount of initial eutectic γ/γ' in the Rocketdyne samples of Table 4.11.

4.3.1.3 Effect of porosity

The effect of porosity on tensile properties was studied at three different porosity levels: an initial level of about 1.0%; the level after the first HIP of 0.57%; and the level after the second HIP of 0.035%. Table 4.12 shows the tensile properties for these porosity levels; the no HIP results are different because the samples came from different single crystal slabs, and are shown so as to remove any effect of orientation on the tensile properties. It was found that there was no effect of porosity on any of the tensile properties, except for an increase in work hardening parameter from 0.04 to 0.07 after the first HIP attempt, absent in the second HIP attempt.

Table 4.13 gives the results of a series of tensile tests designed to independently determine the effects of hydrogen, porosity and eutectic γ/γ' using samples from the same single crystal bar. The results support all of the observations in this section, namely the lower yield stress in charged samples and an improved ductility in uncharged and charged samples without eutectic γ/γ' . Further, hydrogen had less of an effect on the R.A. than on the strain to failure, and there was no effect of porosity on the tensile properties.

Table 4.12 Effect of porosity on tensile properties.

	0.2 % Y.S. (MPa)	U.T.S. (MPa)	ϵ_f (%)	R.A. (%)
no HIP	1072	1100	6.8	6.4
HIP 1	1100	1233	7.4	8.7
no HIP	1138	1151	3.6	3.7
HIP 2	1118	1161	3.9	4.2

Table 4.13 Effect of hydrogen, porosity and eutectic γ/γ' on tensile properties of one bar.

	0.2 % Y.S. (MPa)	U.T.S. (MPa)	ϵ_f (%)	R.A. (%)
unHIP'ed, norm HT	1138	1151	3.6	3.7
unHIP'ed, alt HT	1146	1191	5.4	6.5
HIP'ed, norm HT	1118	1161	3.9	4.2
HIP'ed, alt HT	1140	1201	6.0	6.5
unHIP'ed, norm HT, w/H	985	985	0.20	2.5
unHIP'ed, alt HT, w/H	1008	1008	1.3	3.2
HIP'ed, norm HT, w/H	1013	1046	0.7	3.0
HIP'ed, alt HT, w/H	1020	1051	1.1	3.6

4.3.2 Compression Properties

Compression samples were used to obtain higher amounts of strain in charged samples, so that the deformation behavior could be studied at comparable strain levels with and without hydrogen. Comparative behavior of these samples is covered in section 4.4. The opportunity was taken to also investigate the reported tension/compression flow stress asymmetry^{88,90,116} and to extend this as a function of hydrogen. Table 4.14 lists the average yield strength of compression samples with and without hydrogen, along with the corresponding tensile yield strengths from the same slab, #16. The observed asymmetry supports previous claims^{88,90,116} that the tensile yield stress is slightly higher than compression in the [001] orientation. Further, it is now established that the presence of internal hydrogen does not affect the magnitude of the asymmetry.

Table 4.14 Effect of hydrogen on the tension/compression asymmetry.

	no hydrogen	with hydrogen
σ_{ys} (tension)	1135	1100
σ_{ys} (comp.)	1076	1060
$\sigma_{ys}^T/\sigma_{ys}^C$	1.05	1.04

4.3.3 Fracture Toughness

4.3.3.1 K_{IC} results

The effect of hydrogen on fracture toughness was studied using K_{IC} tests on compact tension specimens. [001] uncharged samples were found to have a fracture toughness value of 122 MPa \sqrt{m} , while samples with about 300 ppm hydrogen had a toughness of 103 MPa \sqrt{m} , a decrease of 16%. Each of these values is the average of two tests, and the fracture toughness values are similar to those reported in other nickel-base

alloys and iron-base superalloys (sec. 2.4). The fracture toughness tests passed all validity criteria in ASTM E-399, except for the thickness criterion. In order to be considered valid, the 1.27 cm-thick specimens would had to have been just over 2 cm thick. However, based upon valid short rod fracture toughness tests reported in Appendix C, it was believed that the obtained K_Q values were close to the true fracture toughness.

4.4.3.2 J_{IC} results

J_{IC} tests were subsequently conducted to obtain valid fracture toughness data as a function of hydrogen, porosity and eutectic γ/γ' , as shown in Table 4.15. All of the values in Table 4.15 are the average of two tests, and all samples were taken from the same slab. The hydrogen content of charged samples was approximately 300 ppm, and the initial porosity and eutectic γ/γ' volume fractions were 1.07% and 5.24%, respectively. As a result of HIP'ing and the alternate heat treatment, these values were then reduced to essentially zero and these changes were assessed. Table 4.15 shows that introduction of hydrogen had a minimal effect on J_{IC} , in contrast to the definite decrease observed in toughness in charged K_Q samples. This point will be discussed later in terms of the differences in testing techniques. There does not appear to be any effect of eutectic γ/γ' on the toughness, but eliminating the porosity did appear to slightly increase the toughness.

Due to the presence of stable crack growth in this material, the tearing modulus was calculated using:¹⁸¹

$$T = \frac{dJ}{da} \left(\frac{E}{\sigma_{ys}^2} \right) \quad (4-2)$$

where dJ/da is the slope of the J - Δa curve using points within $\Delta a \leq 0.06b_o$, and b_o is the initial remaining ligament length. Calculation of the tearing modulus was restricted to this region of Δa , since it has been reported that J -controlled crack growth does not extend

Table 4.15 J-integral fracture toughness values (kPa·m) as a function of hydrogen, porosity and eutectic γ/γ' .

	with pores		no pores	
	w/ hydrogen	w/o hydrogen	w/ hydrogen	w/o hydrogen
normal heat treatment (with eutectic γ/γ')	129	128	--	--
alternate heat treatment (without eutectic γ/γ')	130	134	140	148

Table 4.16 Tearing modulus values as a function of hydrogen, porosity and eutectic γ/γ' .

	with pores		no pores	
	w/ hydrogen	w/o hydrogen	w/ hydrogen	w/o hydrogen
normal heat treatment (with eutectic γ/γ')	9.6	7.2	--	--
alternate heat treatment (without eutectic γ/γ')	12.4	8.9	13.0	17.8

beyond this region.¹⁸¹ Table 4.16 shows the results of the tearing modulus calculations in dimensionless units. Once again the effect of hydrogen is inconclusive, there was no effect of eutectic γ/γ , and the elimination of porosity improves this measure of toughness.

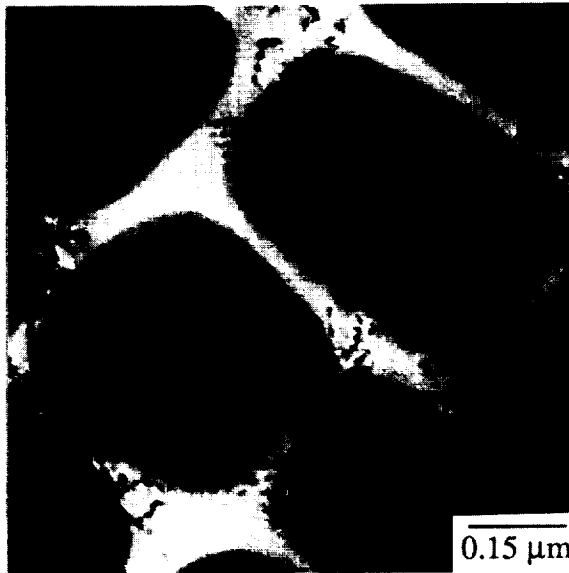
4.4 Deformation Behavior in Tension and Compression

4.4.1 Development of Deformation Structure

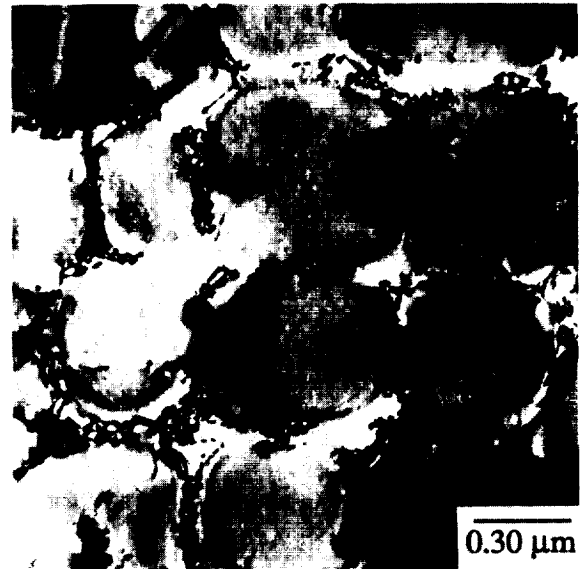
Room temperature tensile tests were interrupted at various plastic strain levels to monitor the development of the deformation structure. The as-received microstructure contained very few dislocations, as expected, likely because of the low reported γ/γ misfit.¹²² Micrographs of [001] foils in Figure 4.15 illustrate the development of deformation behavior in uncharged samples. At the smallest plastic strain level examined, $\epsilon_p = 0.24\%$, loosely associated $a/2\langle 110 \rangle$ dislocation pairs and single dislocations are seen in the γ matrix, as determined by conventional g·b analysis.¹⁸² At this strain, the deformation was inhomogeneous across the foil, and isolated deformation bands appeared to be the primary deformation mechanism. In these narrow bands, there was shearing of the γ precipitates by $a/2\langle 110 \rangle$ dislocation pairs. Densities were not measured in these bands because it was difficult to obtain accurate results due to the heavy activity in this region. However, the activity outside of these bands and in other regions consisted primarily of dislocations in the γ matrix with little activity in the γ precipitates.

The eutectic γ/γ was rarely observed in the thin foils, but when it was present, little dislocation activity inside the constituent was observed. The eutectic γ/γ phase appeared featureless, without even the expected lamellae-type structure. Figure 4.16 shows the interface between the γ/γ microstructure and the eutectic γ/γ in an uncharged tensile sample with 0.24% strain. There is a layer of γ matrix surrounding the eutectic γ/γ that contains a measured dislocation density of $5.2 \times 10^{10} \text{ cm}^{-2}$. This high density of dislocations at the

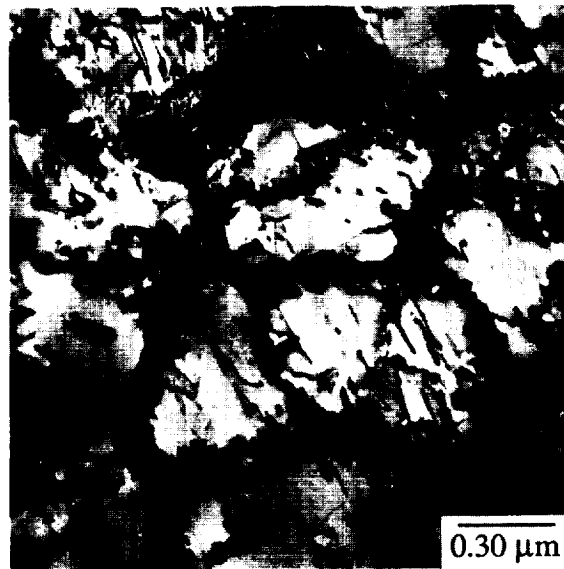
ORIGINAL PAGE
BLACK AND WHITE PHOTOGRAPH



(a)



(b)



(c)

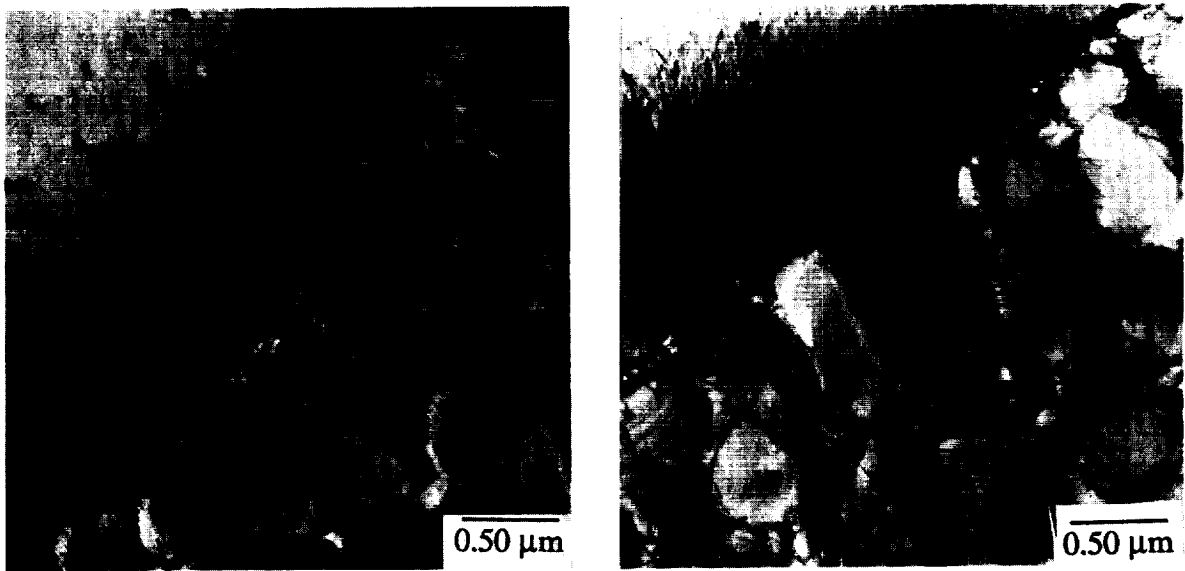
Figure 4.15 [001] foils showing deformation structure as a function of plastic strain in uncharged tensile samples. (a) $\epsilon_p = 0.24\%$. (b) $\epsilon_p = 1.2\%$. (c) $\epsilon_f = 3.0\%$.

eutectic γ/γ' interface was commonly observed in all samples.

At a higher plastic strain of 1.2%, as in Figure 4.15b, the deformation became much more uniform across the entire foil, although concentrated to the γ matrix, with very few dislocations in the γ' precipitates. At this strain, there is no longer any evidence of the local deformation bands seen at the smaller strain. Dislocation densities were measured in each phase, and it was found that the γ matrix contained 4.5×10^{10} dislocations/cm² and the γ' precipitates had 4.0×10^9 dislocations/cm². Figure 4.17 is a $\langle 111 \rangle$ foil at $\epsilon_p = 1.2\%$, suitably oriented to show dislocations on the slip plane, and it can be seen that the dislocations are bowing around and between the γ' precipitates, while attempting to maintain a screw orientation. There was no evidence for shearing found in these $\langle 111 \rangle$ foils implying that the deformation mechanisms in PWA 1480 are different than in most superalloys. It was previously mentioned that the γ' precipitates were slightly larger in the interdendritic areas with some precipitates as large as 1 μm ; however, there did not appear to be any effect of the γ' size on the deformation behavior at any strain level.

At the failure strain of 3.0%, Figure 4.15c, the dislocation density in the γ matrix was 1.0×10^{11} , with a slight amount of γ' shearing observed. The density in the precipitates at this strain was 4.9×10^9 . The trapping of dislocations in the γ matrix was still uniform across all of the foils. The dislocation density measurements show that the number of dislocations continue to increase steadily in the matrix with strain, but the dislocation activity in the precipitates does not increase as much with strain.

ORIGINAL PAGE
BLACK AND WHITE PHOTOGRAPH



(a)

(b)

Figure 4.16 Interface between eutectic γ/γ' and γ/γ' microstructure showing dislocation tangles at interface. $\epsilon_p = 0.24\%$.

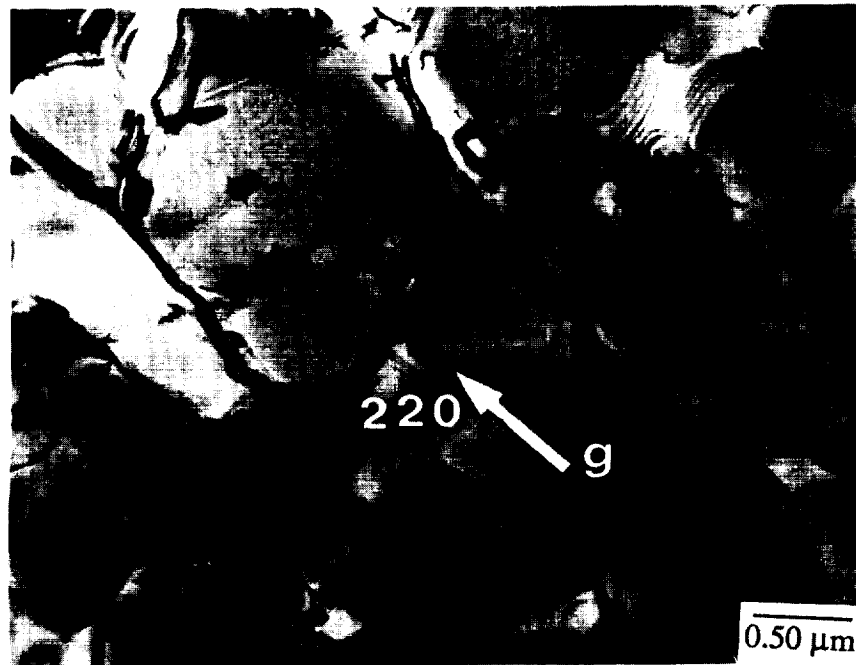


Figure 4.17 $\langle 111 \rangle$ foil in uncharged tensile sample showing dislocations bending around γ' precipitates, $\epsilon_p = 1.2\%$.

Several different $a/2\langle 110 \rangle$ Burgers vectors were found indicating that multiple slip was occurring, as expected. Occasionally, superlattice intrinsic stacking faults (SISF) were observed in the γ precipitate, as seen in Figure 4.18 and determined by comparisons of bright field and dark field TEM micrographs.¹⁸² These were not observed to the same extent in each foil, and they never appeared to play a major role in the overall deformation process.

The deformation behavior of compression samples also was examined at various plastic strains, and Figure 4.19 shows the progression of deformation in these samples. There was no significant differences observed in the deformation behavior between tension and compression samples. In both at low strains, Figure 4.19a, inhomogeneous deformation occurred in narrow bands, while at higher strains the deformation was uniform across the foil. As in tension, dislocation motion was primarily restricted to the γ matrix at higher strains, and this appeared to be the main deformation mechanism.

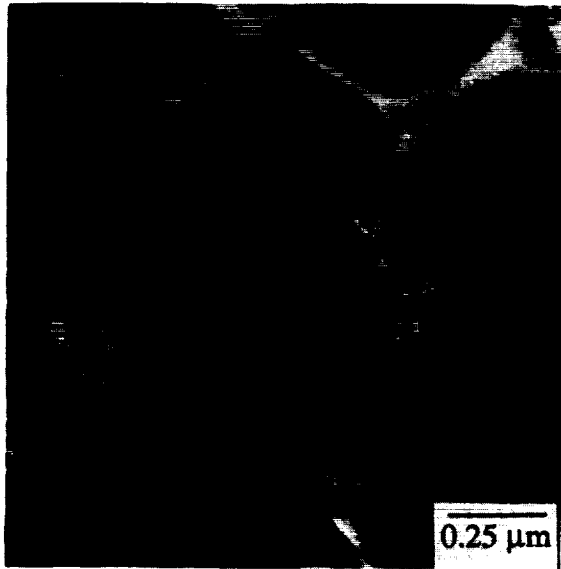
At a plastic strain of 3.0%, Figure 4.19c and 4.19d, a slight amount of activity was observed in the γ precipitate with a very high dislocation density in γ matrix. It was also observed, Figure 4.19c, that some γ' precipitates contained a moderate density of dislocations, while others contained very few, if any, dislocations. This observation also was made in tensile samples at $\epsilon_f = 3.0\%$. Various $a/2\langle 110 \rangle$ single dislocations and paired dislocations were analyzed, again indicating multiple slip, and it appeared that SISF's in the γ precipitate occurred to even a lesser extent than in tensile samples.

ORIGINAL PAGE
BLACK AND WHITE PHOTOGRAPH

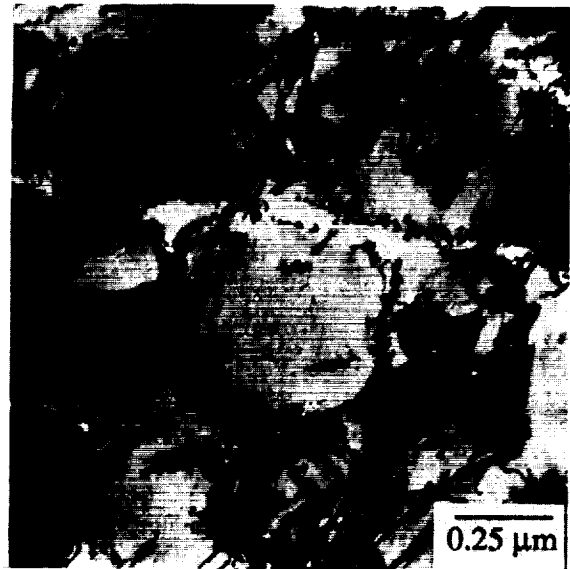


Figure 4.18 Superlattice intrinsic stacking faults occasionally observed in γ precipitate.

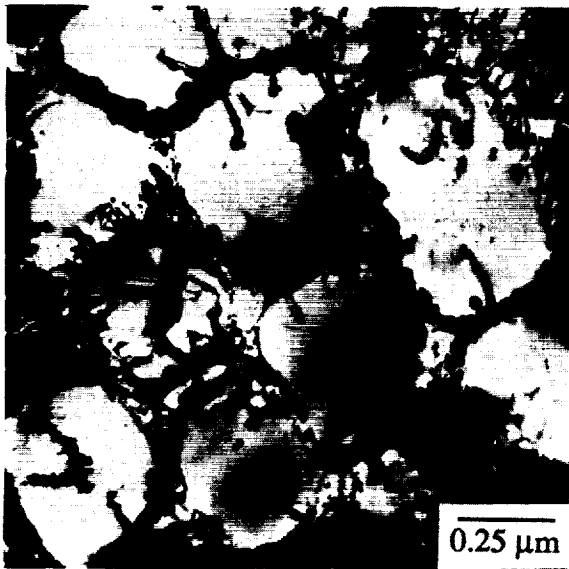
ORIGINAL PAGE
BLACK AND WHITE PHOTOGRAPH



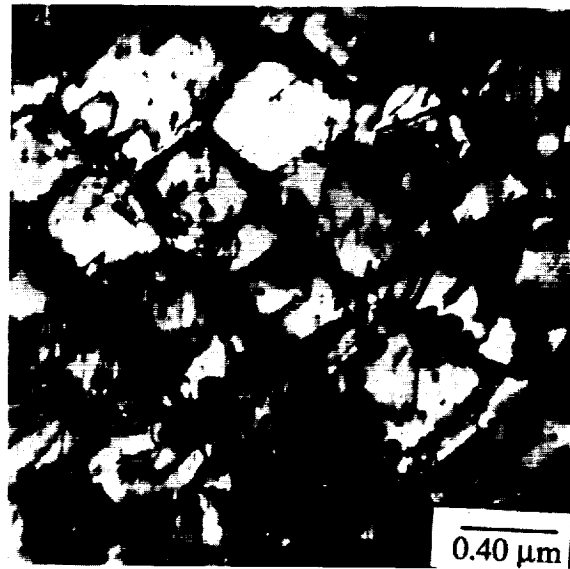
(a)



(b)



(c)



(d)

Figure 4.19 Deformation structure of uncharged compression samples at various strains. (a) $\epsilon_p = 0.5\%$. (b) $\epsilon_p = 1.3\%$. (c & d) $\epsilon_p = 3.0\%$.

4.4.1.1 Effect of hydrogen

The introduction of internal hydrogen per se did not visibly affect the microstructure or introduce any dislocations. Tensile samples containing approximately 300 ppm hydrogen were pulled to plastic strain levels of 0.15% and to the failure strain of 0.30%. Figure 4.20 shows the deformation behavior for both strains in [001] oriented foils. At $\epsilon_p = 0.15\%$, there was inhomogeneous deformation, as shown in Figure 4.20a and 4.20b, similar in appearance to the uncharged samples at $\epsilon_p = 0.24\%$. In regions outside these narrow bands of deformation, single dislocations and paired dislocations were observed exclusively in the γ matrix. At the failure strain of 0.30%, there was slightly more uniform dislocation activity, Figure 4.20c, but it appeared that the majority of deformation still was occurring in these thin bands, as shown in Figure 4.20d. These bands still were the only area in which shearing of the γ precipitates occurred. Dislocation densities were measured at this strain, but the average values are misleading because of the inhomogeneous deformation. The density in the matrix was $8.9 \times 10^9 \text{ cm}^{-2}$ and in the precipitate it was $4.1 \times 10^9 \text{ cm}^{-2}$. These measurements do show that the average dislocation density in the γ matrix of the failed, charged tensile samples was very much lower than was observed in failed, uncharged tensile samples pulled to higher strains, and this can be seen by comparing Figures 4.15c and 4.20b.

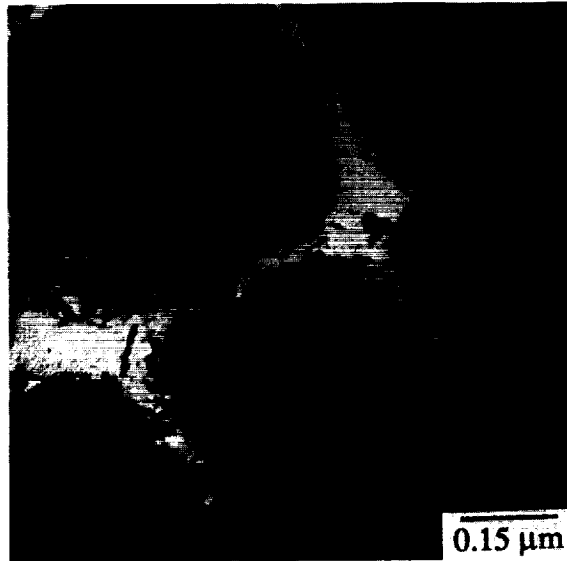
Burgers vectors of various slip systems were analyzed showing that multiple slip also occurred in charged samples. SISF's were seen on occasion, and it did not appear that the presence of hydrogen had any effect on their appearance or number.

The primary purpose of the compression samples was to permit equivalent plastic strain levels in samples with and without hydrogen to be reached. Figure 4.21 shows the compression deformation behavior of charged samples at strains up to the uncharged tensile failure strain, which can be compared directly to Figure 4.19.

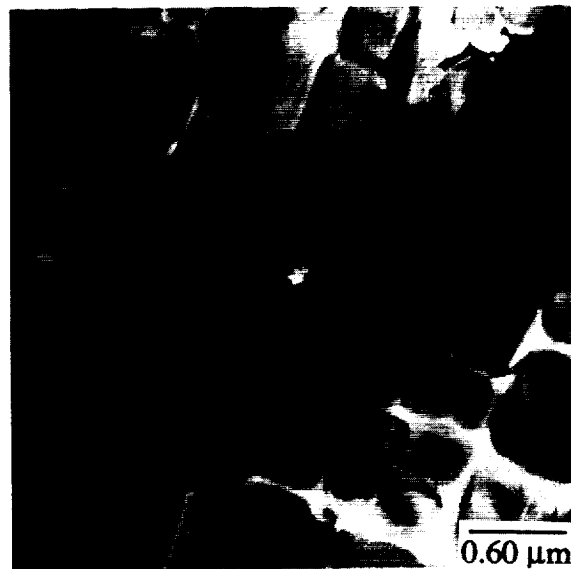
ORIGINAL PAGE
BLACK AND WHITE PHOTOGRAPH



(a)



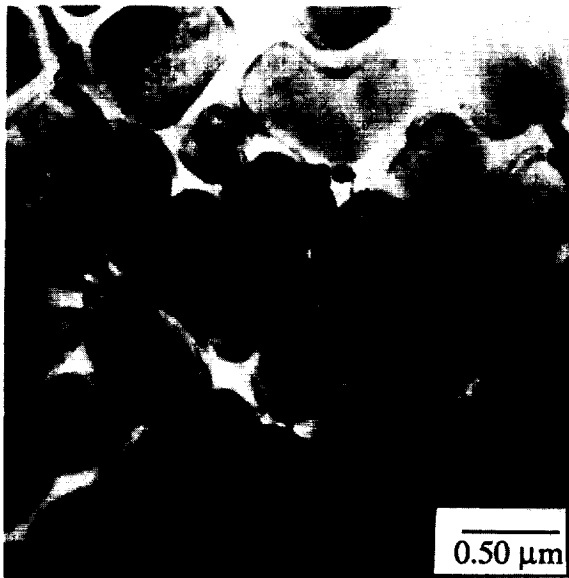
(b)



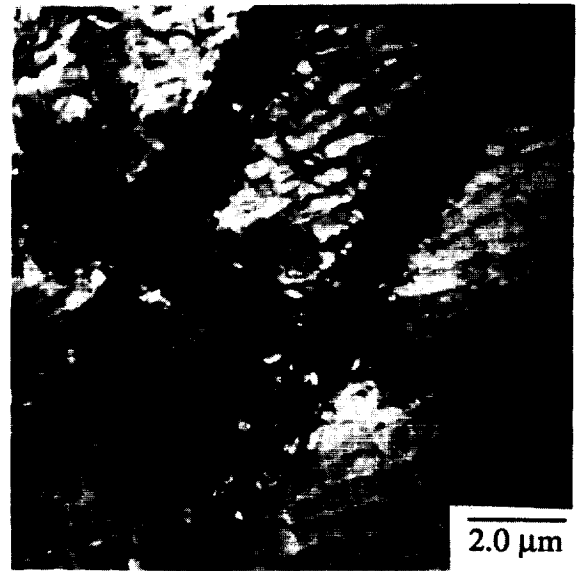
(c)

Figure 4.20 Deformation structure of tensile samples with hydrogen at various strains.
(a) $\epsilon_p = 0.15\%$. (b &c) $\epsilon_f = 0.3\%$.

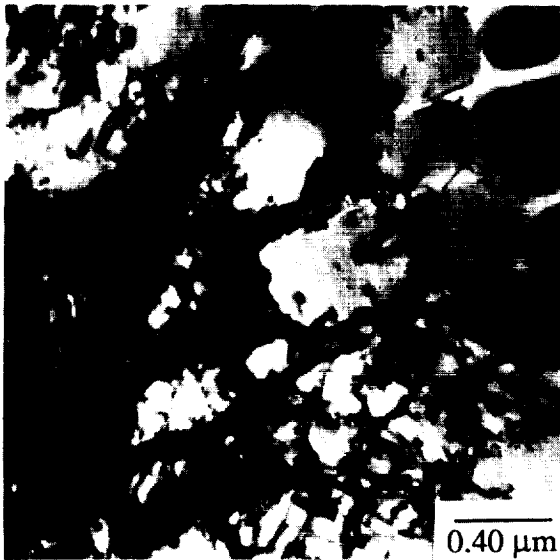
ORIGINAL PAGE
BLACK AND WHITE PHOTOGRAPH



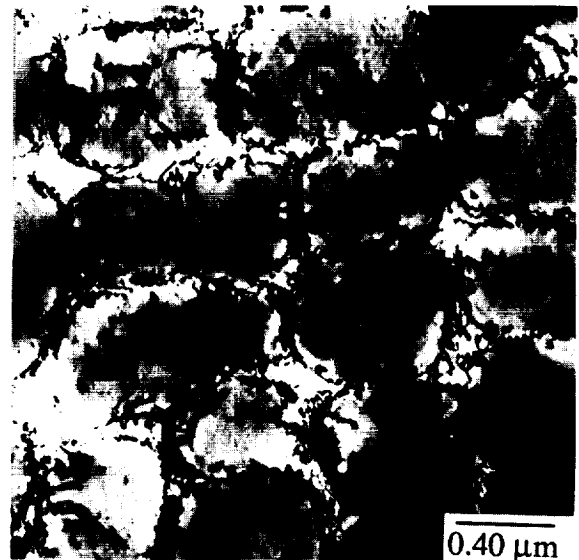
(a)



(b)



(c)



(d)

Figure 4.21 Deformation structure of compression samples with hydrogen at various strains. (a) $\epsilon_p = 0.5\%$. (b & c) $\epsilon_p = 1.3\%$. (d) $\epsilon_p = 3.0\%$.

At the smallest strain, $\epsilon_p = 0.5\%$, again there is evidence of local deformation bands, with little dislocation activity elsewhere. At 1.3%, there now is a definite pattern of localized bands of deformation, in marked contrast to the uniform deformation in uncharged samples at this strain. Figure 4.21b shows examples of several of these bands, and Figure 4.21c provides a close-up view of the edge of one of these bands showing the severe shearing of the γ precipitates inside the bands and dislocations trapped in the γ matrix just outside the bands. At $\epsilon_p = 3.0\%$ in charged compression samples, Figure 4.21d reveals that the deformation is now uniform across the foils, and the presence of dislocations in the γ matrix is the predominant observation. There still was some evidence of the intense band activity, but the deformation had now spread out more uniformly. Dislocation densities were measured at this strain, and it was found that there were 1.7×10^{11} dislocations/cm² in the matrix and 3.9×10^9 dislocations/cm² in the precipitates.

Figure 4.22 is a $\langle 111 \rangle$ foil of a charged sample at $\epsilon_p = 1.2\%$ showing an area where the dislocations are bowing around and between the γ precipitates. This can be compared to the uncharged sample at $\epsilon_p = 1.2\%$ in Figure 4.16, and it can be seen that they both display a similar deformation appearance. It is not inconsistent that the observations in the charged $\langle 111 \rangle$ foil show dislocations primarily in the γ matrix, while the [001] foils show bands of intense γ shearing. The areas outside these bands do contain dislocations that are trapped in the γ matrix, and since the bands can be widely spaced, it is believed they just were not observed in the limited viewing area afforded in the $\langle 111 \rangle$ foils. Since many more [001] foils were observed, it is felt that these bands of intense activity are representative of deformation behavior of charged samples at strains up to at least 1.2%.

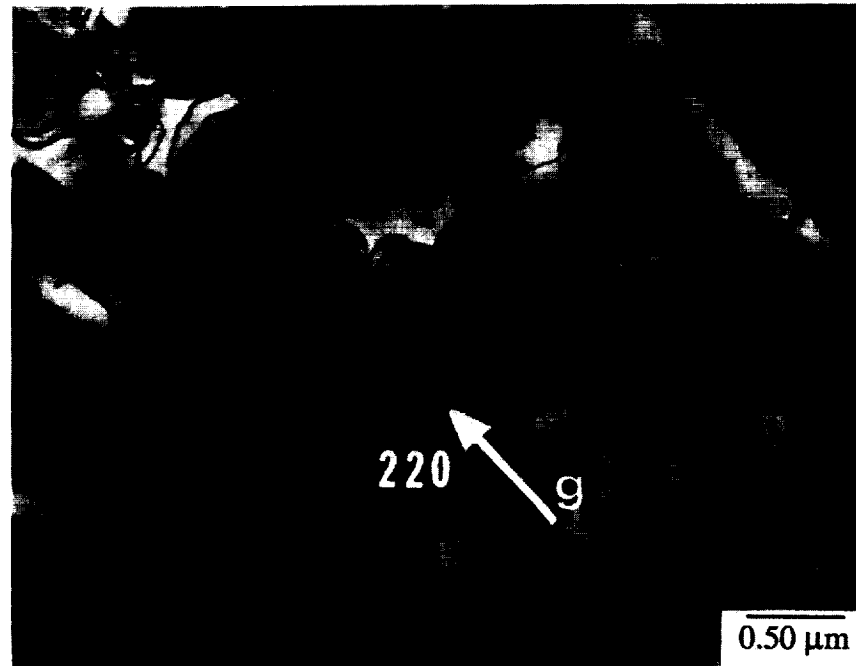
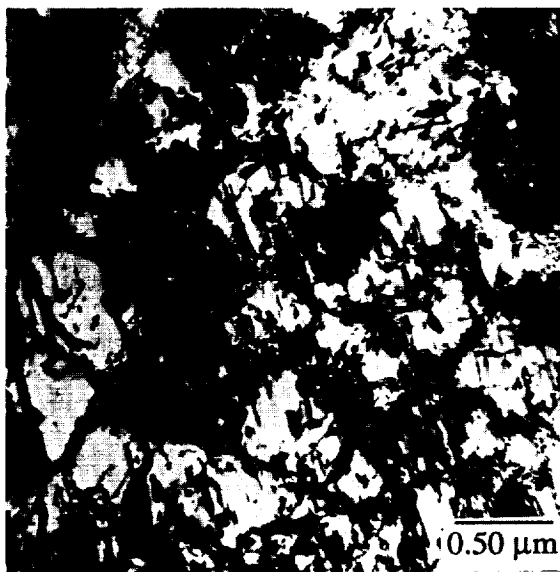
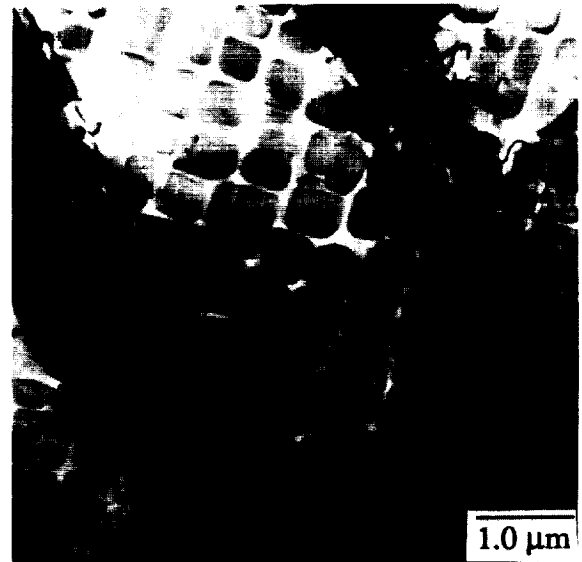


Figure 4.22 $\langle 111 \rangle$ foil showing deformation structure with hydrogen. $\epsilon_p = 1.2\%$.



(a)



(b)

Figure 4.23 Deformation structure of tensile samples without eutectic γ/γ' . (a) without hydrogen, $\epsilon_f = 5.3\%$. (b) with hydrogen, $\epsilon_f = 1.2\%$.

4.4.1.2 Effect of eutectic γ/γ'

Eliminating the eutectic γ/γ' resulted in higher strains to failure both in uncharged and charged tensile samples (Table 4.13). [001] thin foils were examined from such samples, and the observations are shown in Figures 4.23a and 4.23b. The uncharged samples in Figure 4.23a showed a much higher degree of γ' shearing than previously had been observed in any samples. There was now a high dislocation density in the γ matrix, but with much more activity in the γ' precipitate.

In the charged samples without eutectic γ/γ' shown in Figure 4.23b, the failure strain was about 1.2%, which was comparable to the strain level in the charged compression foils examined in Figure 4.21b. The deformation behavior of these two samples was similar, and the primary mode of deformation in both cases occurred by local intense bands of γ' shearing, with some activity in the rest of the foil in the form of dislocations trapped in the γ matrix.

In summary of the overall deformation behavior, there was no qualitative differences observed in the deformation behavior of samples tested in tension or compression. In uncharged samples deformation began in isolated bands consisting of intense shearing of the γ' precipitates along a single slip system. These bands eventually hardened and the deformation structure became uniform across the sample consisting primarily of dislocations trapped in the γ matrix. This activity persisted up to failure in tensile samples in contrast to the primary deformation mechanism of shearing in most superalloys.^{51,52,53,77} The disproportionate trapping of dislocations in the matrix is supported by the dislocation density measurements summarized in Table 4.17. The standard deviation on all measurements was within 20% of the reported average value. Hydrogen-charged tensile and compression samples initiated deformation in the same manner as uncharged samples with the isolated deformation bands. This activity continued up to failure in charged tensile samples and to 1.2% in compression samples. Densities were not measured in samples where deformation was accomplished primarily by the

narrow bands previously described, with the exception of the failed charged tensiles at $\epsilon_p = 0.3\%$. This continuation of localized deformation to higher strains than in uncharged samples represents the major effect of hydrogen on the deformation behavior and is consistent with hydrogen causing localized plasticity in other alloys.^{126,127,148,149,150} At 3.0% strain in charged compression samples, the bands had hardened, and the deformation structure resembled uncharged samples with dislocations primarily trapped in the γ matrix. Eliminating the eutectic γ/γ' allowed higher strains to be achieved, and while dislocations were still trapped in the γ matrix, shearing of the γ' precipitates also was observed in uncharged samples.

Table 4.17 Summary of all measured dislocation densities in cm^{-2} .

Sample Condition	Location of Measurement		
	γ	γ'	Eutectic γ/γ' interface
$\epsilon_p = 1.2\%$, no H	4.5×10^{10}	4.0×10^9	—
$\epsilon_p = 3.0\%$, no H	1.0×10^{11}	4.9×10^9	—
$\epsilon_p = 0.3\%$, w/H	8.9×10^9	4.1×10^9	—
$\epsilon_p = 0.24\%$, w/H	1.7×10^{11}	3.9×10^9	—
$\epsilon_p = 0.24\%$, no H	—	—	5.2×10^{10}
$\epsilon_p = 0.15\%$, w/H	—	—	3.9×10^{11}

4.4.2 Slip Character

The slip character was characterized on compression samples at plastic strains of 0.5%, 1.3% and 3.0%, following the guidelines proposed by Williams, Thompson and Baggerly.¹⁸³ The spacing of the slip bands and their degree of waviness was quantitatively measured following the methods used by McInteer, Thompson and Bernstein¹⁷⁴ and described in section 3.3.2. Measurements were made directly from optical micrographs of

the sample and may not be as accurate as if replicas of the slip bands were measured. At 0.5% strain, there was coarse planar slip with large areas that did not contain any slip traces. Figure 4.24 shows the slip bands present at $\epsilon_p = 1.3\%$, and it can be seen that there is evidence for considerable cross-slip. The dark bands associated with the slip lines have been analyzed by stereo microscopy and found to simply be inclinations on the surface.

At $\epsilon_p = 3.0\%$, the slip activity was more homogeneously spread across the samples, but the slip character could still be classified as coarse planar slip as illustrated in Figure 4.25. At this strain, cracks that opened up along slip bands were occasionally observed, in agreement with observations of slip band fracture discussed later. Nomarski contrast was used in Figure 4.26, and in this figure the cracks appear as black lines and the slip bands as white lines. This figure also shows the presence of some coarse wavy slip that was only infrequently observed at $\epsilon_p = 3.0\%$. Figure 4.27 graphically illustrates the results of the quantitative measurements for samples with and without hydrogen. It was found that the slip band spacing decreased continually with strain implying that new slip sources were continually operating. The degree of waviness also increased steadily with strain in uncharged samples suggesting that cross-slip was occurring to a larger extent.

Laue analysis of the specimen orientation in conjunction with slip trace analysis revealed that all of the planar slip bands were of $\langle 111 \rangle$ -type, as expected, and all four $\langle 111 \rangle$ planes were active. There did not seem to be any predominant slip system, and all $\{111\}$ planes were observed to occur approximately to the same extent. It also was consistently seen that the slip bands did not cut across the eutectic γ/γ' as seen in Figures 4.24, 4.25 and 4.28. This is consistent with the TEM observations in Figure 4.18 that show high densities of dislocations at the interface but little activity inside the eutectic γ/γ' .

ORIGINAL PAGE
BLACK AND WHITE PHOTOGRAPH



Figure 4.24 Compression slip bands at $\epsilon_p = 1.3\%$.



Figure 4.25 Compression slip bands at $\epsilon_p = 3.0\%$.

ORIGINAL PAGE
BLACK AND WHITE PHOTOGRAPH

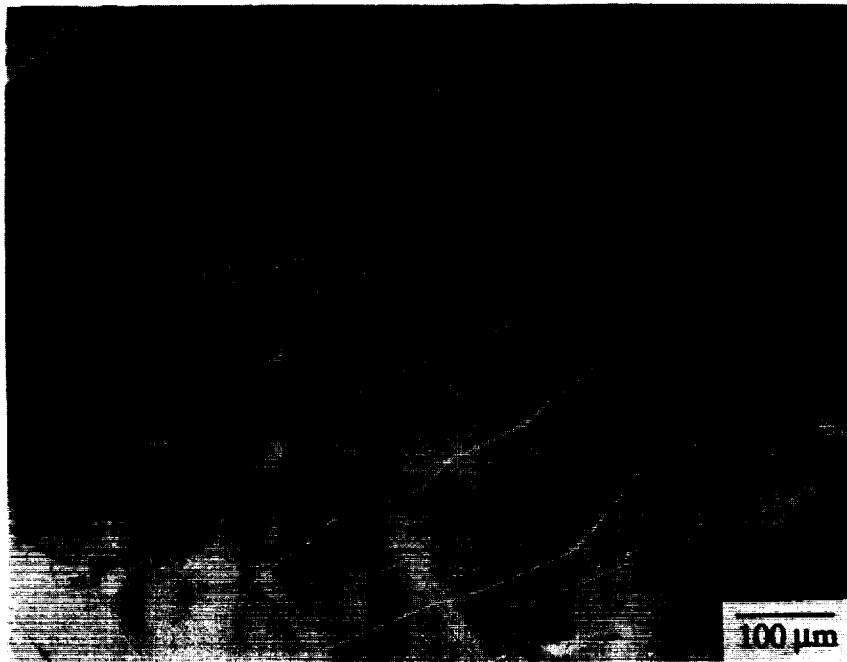
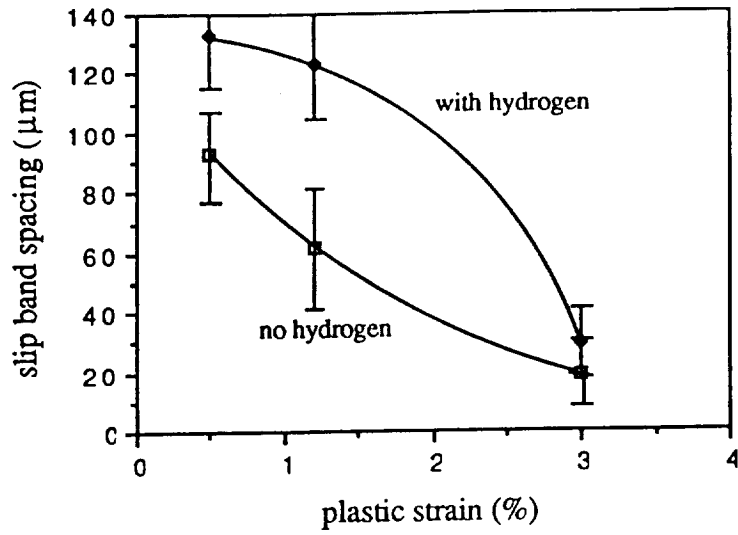
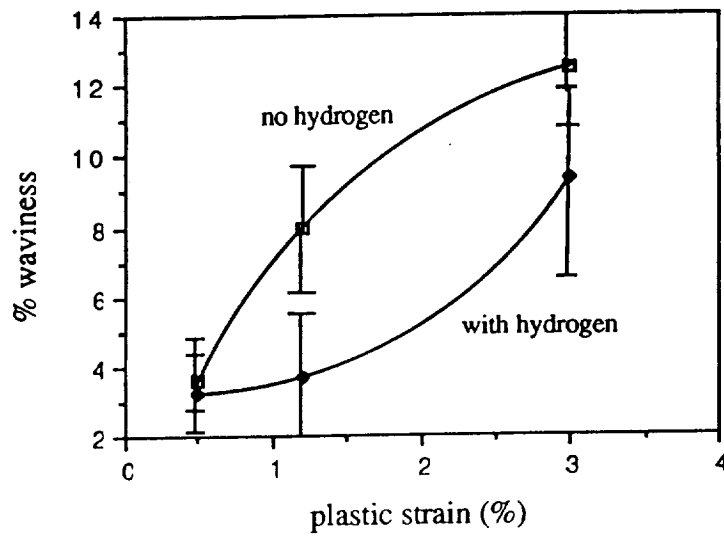


Figure 4.26 Compression slip bands at $\epsilon_p = 3.0\%$ showing cracks along slip bands and some wavy slip.



(a)



(b)

Figure 4.27 Quantitative results of slip band measurements as a function of strain and hydrogen showing (a) slip band spacing and (b) degree of waviness.

ORIGINAL PAGE
BLACK AND WHITE PHOTOGRAPH



Figure 4.28 Note that slip bands do not cut through the eutectic γ/γ .

The presence of 300 ppm internal hydrogen caused the slip to be confined to slightly fewer, but coarser slip bands, as shown by the larger average spacing for charged samples in Figure 4.27. The slip character was very similar to the uncharged samples at $\epsilon_p = 0.5\%$, but at $\epsilon_p = 1.3\%$ the slip bands in the charged samples remained more planar than in uncharged samples. This is in agreement with the TEM results showing that hydrogen causes localized planar slip up to higher strains than in uncharged samples. The same comparative trends continued to 3.0%, but the differences with uncharged samples became less obvious. Cracks were observed along some slip bands at $\epsilon_p = 3.0\%$, and coarse wavy slip was seen on a couple of occasions.

4.4.3 Double Notch Tensiles and Sectioned Tensiles

In order to determine the fracture initiation site, double notch tensile samples were tested. Due to material constraints, it was only possible to test samples without hydrogen. Sections were taken on the unfractured notch, parallel to and perpendicular to the stress axis, but cracks were never observed in any of the sections.

Next, previously tested and fractured tensiles were nickel-plated, and longitudinal sections were prepared. In all cases, there were some cracked eutectic γ/γ' within a few micrometers of the fracture surface. There was a slight tendency for there to be more cracked eutectic γ/γ' in charged samples. Failed tensile samples also were mounted, and the fracture surface was prepared by grinding so sections perpendicular to the stress axis could be observed. In these tensiles, some cracked eutectic γ/γ' were seen as in Figure 4.29. All of the observations support the idea that crack initiation began in the eutectic γ/γ' or at the eutectic γ/γ' interface.

ORIGINAL PAGE
BLACK AND WHITE PHOTOGRAPH



Figure 4.29 Failed tensile sample sectioned perpendicular to the tensile axis showing cracks running the eutectic γ/γ' .

4.4.4 Pre-Strain and Pre-Charge Tensile Tests

A study was initiated to determine if hydrogen affected either or both the deformation or fracture behavior. The details and rationale of the testing procedure are given in section 3.4.4, and Table 4.18 gives the conditions of each specimen along with the associated tensile properties. The pre-strained samples were intended to help determine whether hydrogen primarily affected the fracture behavior, while the pre-charged samples were designed to determine hydrogen's effect on the deformation behavior. The yield strength of all samples during the "straining only" portion of the test was within 3% of the yield strength obtained when the same samples were pulled again to failure.

The first two samples in Table 4.18 were used as reference points. The next two samples in Table 4.18 showed that hydrogen, as expected, had a dramatic effect on the fracture behavior. This can be argued since without the subsequent charging, the pre-strained samples would have attained a failure strain on the order of 3%. However, the hydrogen somehow initiated the fracture process at a much earlier strain and additional strains of around 0.2% were only possible. The last set of samples that were pre-charged suggested that hydrogen also affected the deformation behavior. Similar to the argument above, if hydrogen did not affect the deformation structure, then upon outgassing the sample would have attained a failure strain of around 3% in later testing.

This large effect of hydrogen on the deformation behavior and subsequent failure strain was not expected based on TEM studies, so the effect of hydrogen on these was analyzed using longitudinal sections of samples that had only been strained and not broken. It was found that in the sample that was pre-strained 2% without hydrogen, there were no cracks to be found in the gage section. However, in samples that contained hydrogen and had been strained to 0.2%, there were several cracked eutectic γ/γ' already present. This shows that hydrogen causes the eutectic γ/γ' to crack at a much earlier strain.

Table 4.18 Pre-strain, pre-charge tensile results.

Sample Condition	0.2% Y.S. (MPa)	U.T.S. (MPa)	ϵ_f (%)	R.A. (%)
pre-charge no hydrogen	1100	1108	0.33	2.9
	1145	1189	3.9	4.3
pre-strain 1%, charge pre-strain 2%, charge	1107	1107	0.16	2.0
	1093	1093	0.26	2.3
pre-charge, strain 0.1%, outgas pre-charge, strain 0.2%, outgas	1122	1136	0.57	2.2
	1129	1143	0.46	2.1

4.5 Tensile Fracture Behavior

4.5.1 General Fracture Characteristics

The majority of the tensile fracture surface appeared ductile, as shown in Figure 4.30a. At higher magnification, Figure 4.30b, the ductile "voids" are seen to consist of a flat region surrounded by a thin rim of ductile tearing. These "voids" are about 0.75 μm across and are essentially the same size throughout the fracture. There also were areas that have a similar appearance at high magnification, but were much more brittle-appearing at lower magnification. This type of fracture is illustrated in Figure 4.31; the facets have been identified as $\{111\}$ planes using techniques described in section 3.4.6. The more ductile-appearing fracture of Figure 4.30 also has been identified as occurring macroscopically on $\{111\}$ planes. Therefore there appear to be two types of fracture surfaces when viewed macroscopically, designated as Type A (rough) and Type B (smooth), for convenience. Type A fracture was more commonly observed in all tensile samples studied.

Crystallographic cleavage facets were also found on the fracture surface that varied in size from 20 μm to 50 μm . Figure 4.32a shows their relation to the general fracture, and Figure 4.32b is a higher magnification view of one of the cleavage facets. Typical river lines indicative of cleavage were seen on all facets, and the initiation site was always at the surface of the facet, which will be important in later discussions. Sometimes there is a pore at the initiation site, but the majority of cleavage facets had no identifiable microstructural feature at the initiation site. The orientation of the river lines was checked in view of Lynch's observations of fcc cleavage,^{176,177} but no consistent orientation of these features was found. Laue analysis of the specimen orientation and two-trace analysis have verified that these cleavage facets occurred on macroscopic {001} planes. Figure 4.33 shows a cleavage facet on an {001} plane with several {111} fracture planes surrounding it.

ORIGINAL PAGE
BLACK AND WHITE PHOTOGRAPH

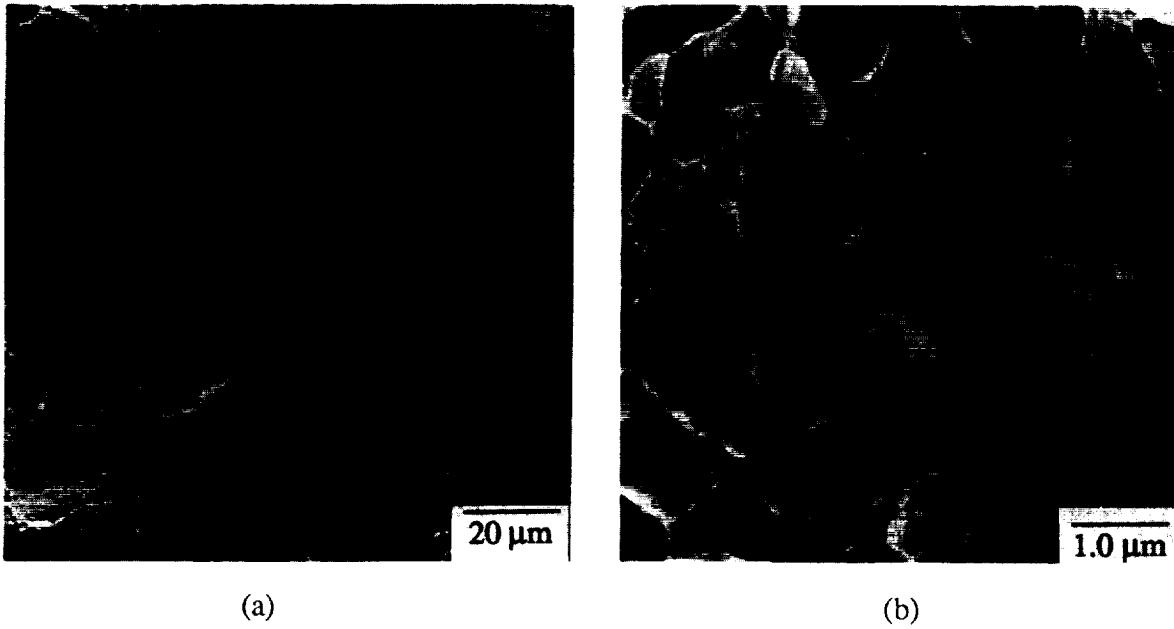


Figure 4.30 (a) Ductile fracture appearing over most of the tensile fracture surface.
(b) High magnification view of {111} facet.

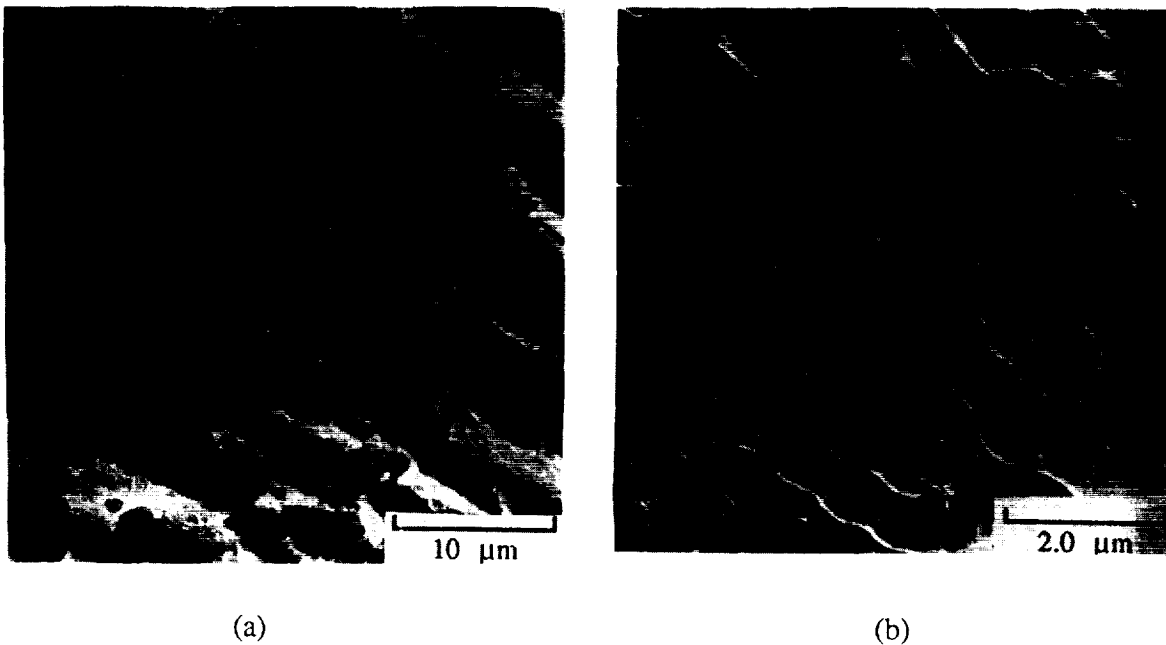
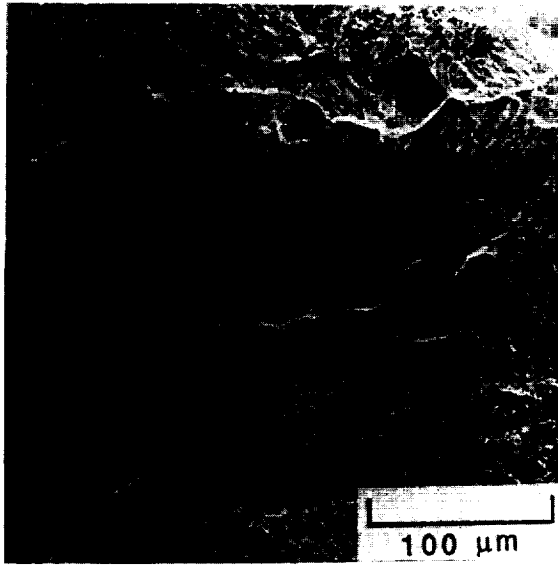
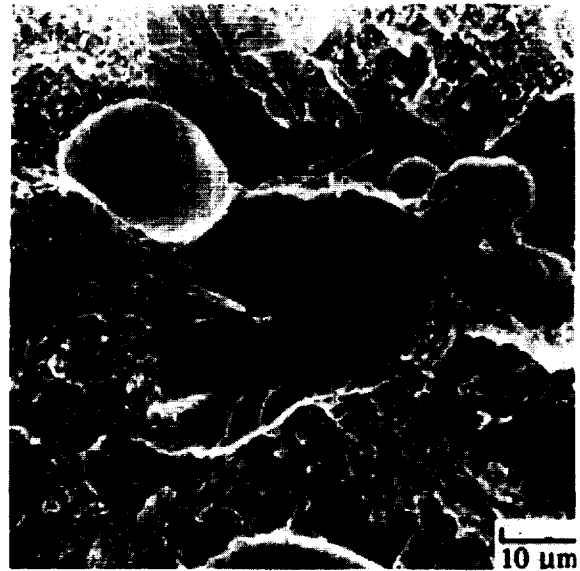


Figure 4.31 (a) Smooth {111} ductile fracture seen on parts of the tensile fracture surface. (b) High magnification view of {111} facet showing similar appearance to the fracture in Figure 4.30b.

ORIGINAL PAGE
BLACK AND WHITE PHOTOGRAPH



(a)



(b)

Figure 4.32 (a) Cleavage facets seen on the tensile fracture surface. (b) Single cleavage facet showing initiation site at the edge opposite of the pore.

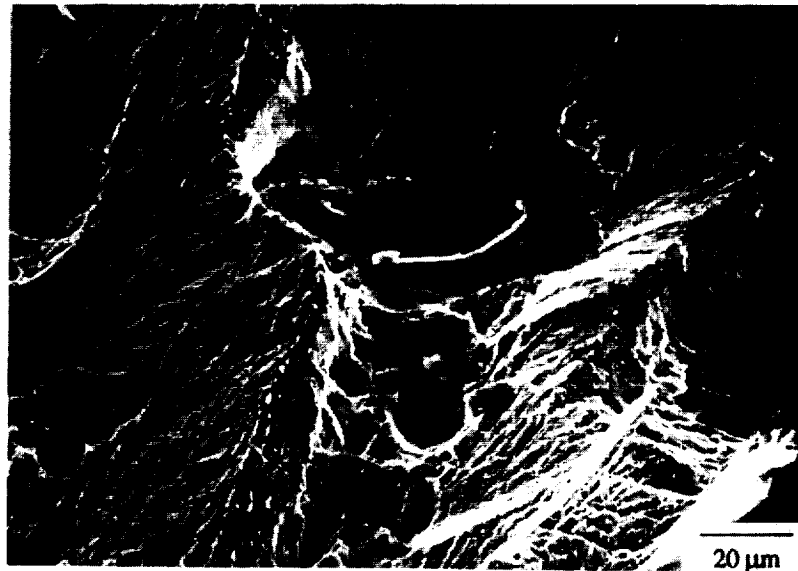


Figure 4.33 {001} cleavage facet surrounded by {111} ductile fracture planes.

Plateau etching was used to determine the relation of the microstructure to the ductile fracture of Figures 4.30 and 4.31 and to the cleavage facets. Figure 4.34 convincingly shows that the cleavage facets are the eutectic γ/γ' in the microstructure.

It was more difficult to make observations utilizing the plateau etching technique at higher magnifications, because the interface between the microstructure and fracture surface was not very clear. The etchant used to polish the sample was able to slightly penetrate under the stop-off lacquer, resulting in a narrow region of the fracture surface being slightly etched. But this turned out to also be beneficial, as Figure 4.35 shows a partially etched fracture surface illustrating the relation between the γ/γ' microstructure and the small ductile fracture areas. It appears that the flat fracture feature is the γ precipitate and that the ductile tearing is occurring through the γ matrix. TEM replicas were made to try to determine if any river lines or other evidence of cleavage existed in the flat region identified as the γ precipitate. The results of this attempt were not convincing one way or the other; this fracture will simply be referred to as "brittle".

Fracture surfaces were also heavily etched to bring out the γ/γ' microstructure, and Figure 4.36 shows the white tear ridges occurring along the γ phase as indicated by the arrows. Further evidence is shown in Figure 4.37 where microcracks were seen on a few occasions running along what appeared to be the γ matrix phase.

ORIGINAL PAGE
BLACK AND WHITE PHOTOGRAPH

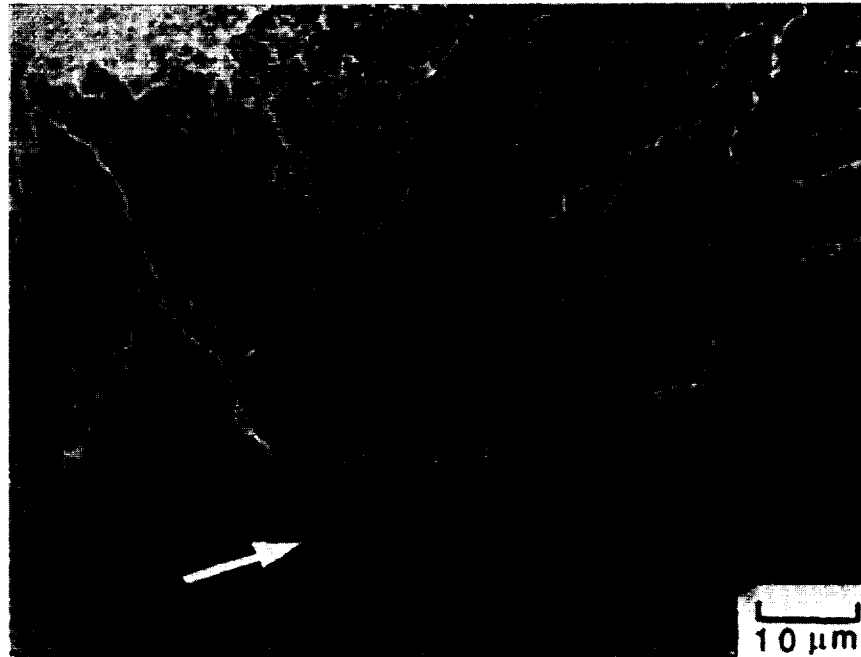


Figure 4.34 Plateau etch showing that the cleavage facet in the top half of the micrograph corresponds to the eutectic γ/γ' indicated by the arrow in the bottom half of the micrograph.

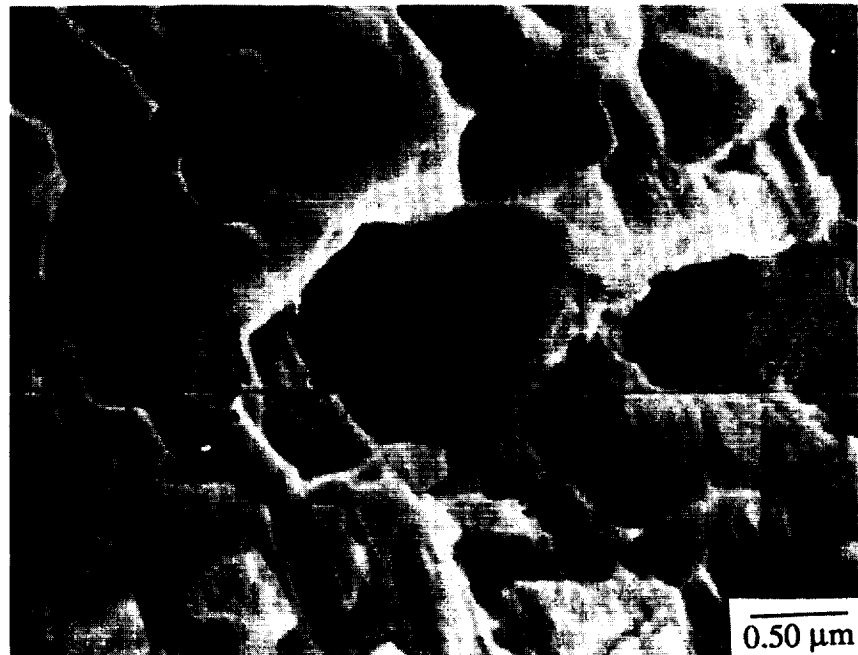


Figure 4.35 Plateau etch showing relationship between ductile fracture and γ/γ' microstructure.

ORIGINAL PAGE
BLACK AND WHITE PHOTOGRAPH



Figure 4.36 Type A {111} fracture showing triangular regions corresponding to γ' precipitates. The white tear ridges are occurring along the γ phase.

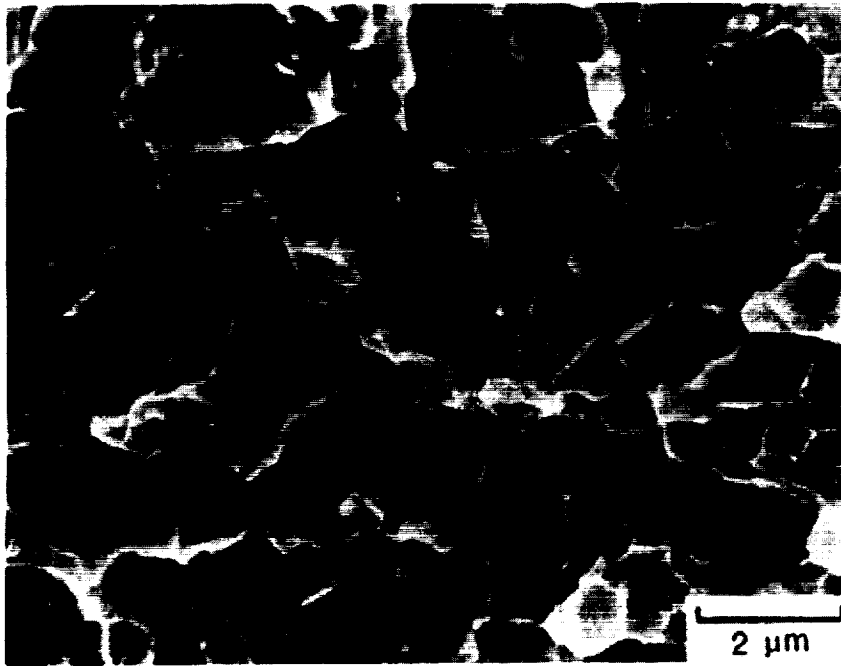


Figure 4.37 Microcracks on tensile fracture surface showing outline of γ/γ' microstructure.

When there is less ductile tearing as previously shown in Figure 4.31 (Type B), an outline of the γ/γ' microstructure can actually be seen on the fracture surface. Figure 4.38 shows a $\{111\}$ fracture facet with the outline of many triangular γ' precipitates evident. The cuboidal γ' faces are aligned along $\{001\}$ planes, and thus a $\{111\}$ section through the precipitate would appear triangular.

4.5.2 Effect of Hydrogen

The presence of internal hydrogen did not have any apparent effect the type of fracture features seen. The area surrounding the pores appeared the same with and without hydrogen, as did the ductile areas and cleavage facets. Type A $\{111\}$ fracture remained the predominant type of slip band fracture in tensile samples. The major effect of hydrogen on the fracture behavior was the large increase in the number of cleavage facets now observed on the fracture surface. Without hydrogen, the area fraction of cleavage on the fracture surface was consistently 5% to 6%, while the charged samples showed a larger and wider range of between 11% and 15%. No significant effect of hydrogen on the number of pores on the fracture surface was observed, suggesting that large pressures do not build up in the pores after charging that could lead to crack initiation, as suggested by others.⁹

Surface cracking was seen along the gage length only in tensile samples containing hydrogen. The cracks were comprised of segments along the $\{001\}$ plane and $\{111\}$ planes. Samples were subsequently heavily etched, and Figure 4.39 shows that the $\{001\}$ segment was always through a eutectic γ/γ' , while the $\{111\}$ segment was through the γ/γ' microstructure. There were numerous cases of isolated cracked eutectic γ/γ' on the surface, but only a few cracks were seen on $\{111\}$ planes that were not linked at some point to a eutectic γ/γ' .

ORIGINAL PAGE
BLACK AND WHITE PHOTOGRAPH

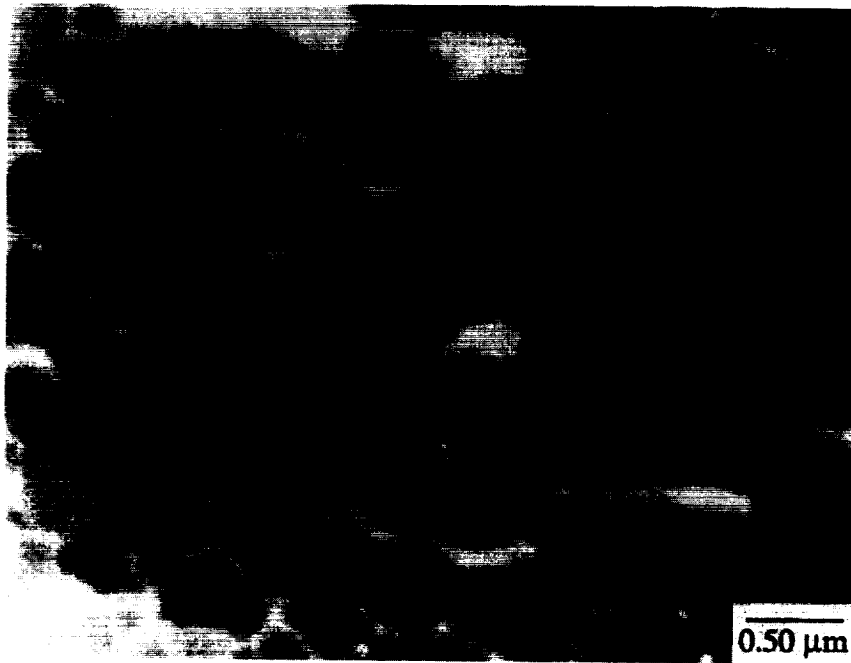


Figure 4.38 Relatively smooth {111} fracture facet showing the triangular outline of many γ' precipitates.

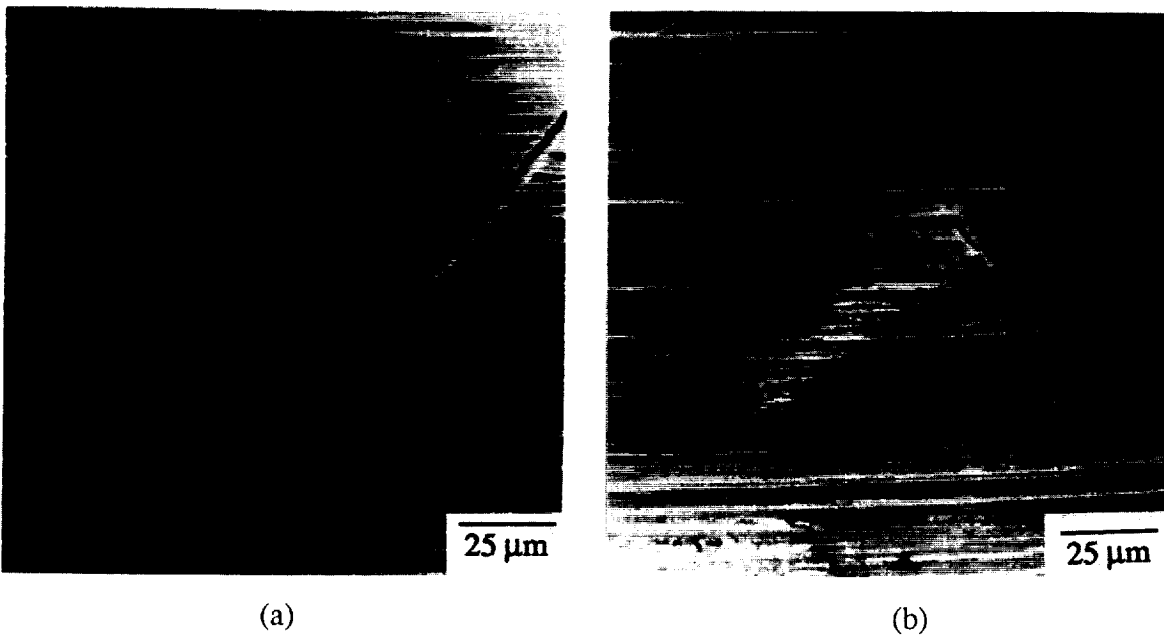


Figure 4.39 Surface cracking on charged tensile samples showing the eutectic γ/γ' cracked on the (001) plane and the crack propagating on a {111} plane.

4.5.3 Effect of Alternate Heat Treatment and HIP'ing

The effect of removing the eutectic γ/γ' and/or porosity did little to change the fracture surface other than eliminating these features. There was, however, some tendency to observe more of the smooth, type B {111} fracture in samples with less eutectic γ/γ' . The amount of cleavage seen on the fracture surface was very close to zero in the alternate heat treatment samples and also was reduced in the HIP'ed samples. The area fraction of cleavage approximately doubled in the charged HIP'ed samples compared to the uncharged HIP'ed samples, as it did in the unHIP'ed samples. These observations are all consistent with the metallographic observations and previous tendencies noted in uncharged samples.

4.6 Fracture Toughness

4.6.1 Fracture of K_{IC} Samples

The fracture appearance of K_{IC} fracture toughness samples was very similar to tensile samples in the type of features seen, but there were major differences found between the fractography of the K_{IC} samples and the J_{IC} samples. All four {111} planes were active in the fracture of both types of fracture toughness samples. The K_Q samples had a macroscopically rough fracture surface, and slightly more of the smooth, type B {111} fracture was seen than type A, as in Figure 4.40. Secondary cracks were seen emanating from many pores, and Figure 4.41 shows one such case.

Quantitative fractography of the observed cleavage facets revealed that the area fraction of cleavage facets on the fracture surface was about equal to the volume fraction of eutectic γ/γ' in the microstructure. This means that without hydrogen the crack path is moving randomly with respect to the eutectic γ/γ' . This is consistent with the observations in uncharged tensile samples. Longitudinal sections of the K_{IC} fracture surface revealed many cracked eutectic γ/γ' , as seen in Figure 4.42. There were even some cases where a few cracked eutectic γ/γ' linked up through the γ/γ' microstructure, as shown in Figure 4.43.

The presence of 300 ppm hydrogen caused the fracture to be much more tortuous, Figure 4.44, and type A {111} fracture predominated. Once again, there were many secondary cracks emanating from pores and a large number of cleavage facets. It was determined that on the fracture surface of charged K_{IC} samples there was an average area fraction of cleavage facets of 21.5%. This represents a four-fold increase over the amount of eutectic γ/γ' in the microstructure, and it can be concluded that the crack path is seeking out the eutectic γ/γ' in charged samples. This is analogous to the increased cleavage observed in charged tensile samples.

Longitudinal sections of the charged K_{IC} fracture surface showed a large number of cracked eutectic γ/γ' . The plastic zone size, r_y , was estimated using:¹⁸⁴

$$r_y = \frac{1}{6\pi} \left(\frac{K_I}{\sigma_{ys}} \right)^2 \quad (4-3)$$

where K_I is the stress intensity and σ_{ys} is the yield strength. It was found that all of the cracked eutectic γ/γ' were within the plastic zone, and it was calculated that approximately 12% of the eutectic γ/γ' in the plastic zone were cracked. There did not appear to be any relation between the eutectic γ/γ' size and whether or not the eutectic γ/γ' was cracked.

ORIGINAL PAGE
BLACK AND WHITE PHOTOGRAPH

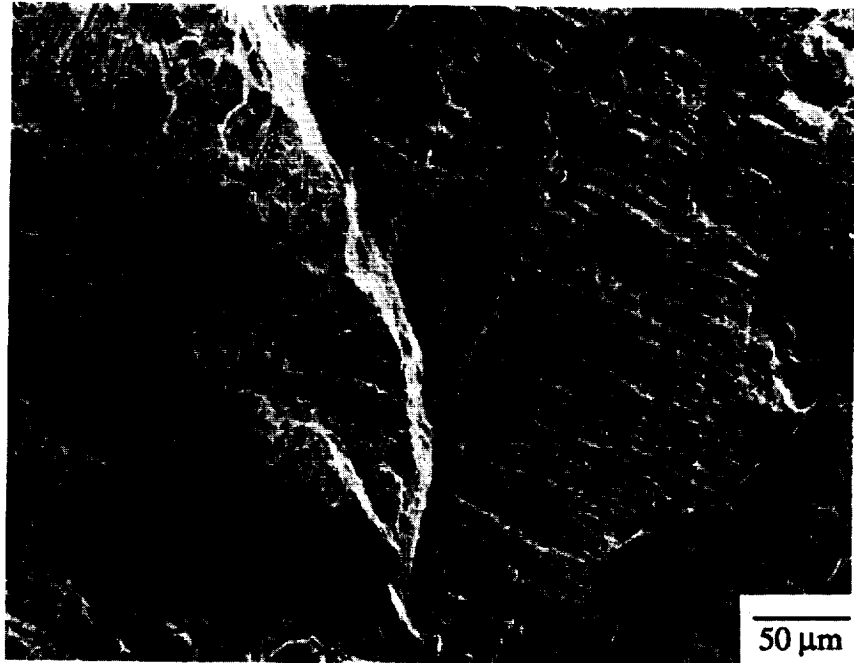


Figure 4.40 Fracture surface of uncharged K_{IC} samples.

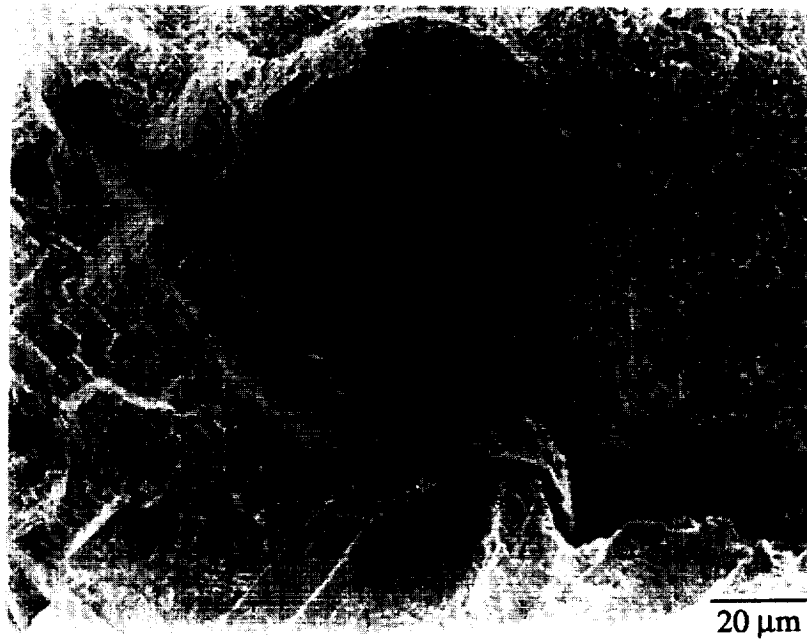


Figure 4.41 Secondary crack emanating from a pore on K_{IC} fracture surface.

ORIGINAL PAGE
BLACK AND WHITE PHOTOGRAPH



Figure 4.42 Longitudinal section of uncharged, failed K_{IC} sample showing several cracked eutectic γ/γ beneath the fracture surface.



Figure 4.43 Longitudinal section of fractured K_{IC} sample showing linked cracked eutectic γ/γ

ORIGINAL PAGE
BLACK AND WHITE PHOTOGRAPH

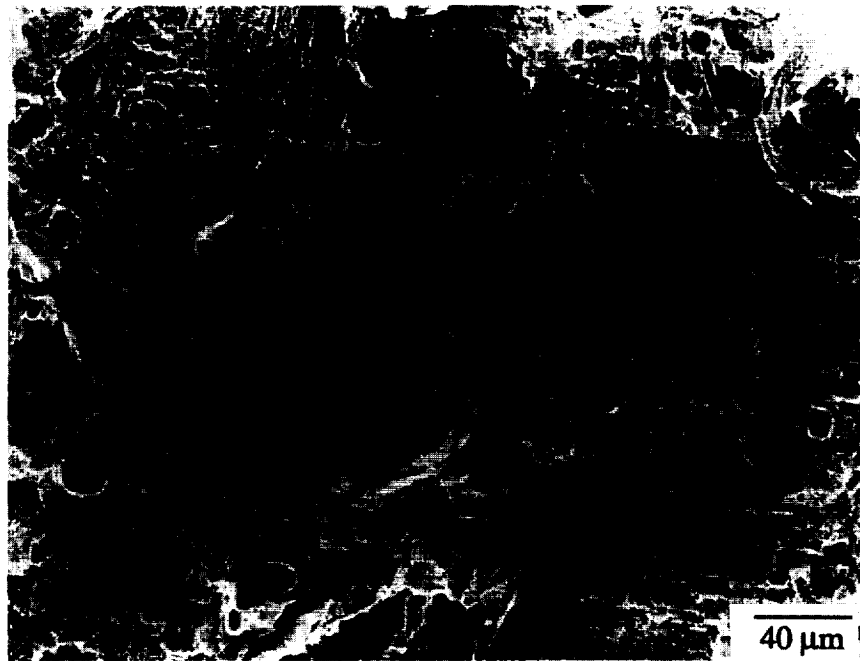


Figure 4.44 Fracture surface of charged K_{1C} sample.

4.6.2 Fracture of J_{IC} Samples

The fracture surface of the J_{IC} samples was macroscopically much flatter than the K_{IC} samples and consisted almost exclusively of smooth, type B {111} fracture, as seen in Figure 4.45. Once again the distance traversed on one {111} plane before switching to another {111} plane was around 5 μm , as found in the tensile samples and K_{IC} samples. There were some secondary cracks observed, Figure 4.46, and it is possible that these cracks occurred during the unloading-loading cycle in the J integral test. The spacing between cracks of 100-150 μm corresponds to approximately the length of crack growth that occurred in each loading cycle.

A crack also was consistently observed running between the end of the fatigue pre-crack and the beginning of the J integral test region, as shown in Figure 4.47. It was noted that the fracture in the fatigue pre-crack region was slightly different, having a smaller {111} facet size. It is important to note that in the final overload region after the second fatigue cycling, the fracture was much more macroscopically rough and resembled the K_{IC} fractography, as seen in Figure 4.48. The bottom of Figure 4.48a is the fatigue area used to identify the end of the J integral test region, and the upper portion of the photo is the overload region that occurred as a result of failure due to the fatigue conditions employed. The rate of loading was much faster in this overload region than in the J integral region.

ORIGINAL PAGE
BLACK AND WHITE PHOTOGRAPH

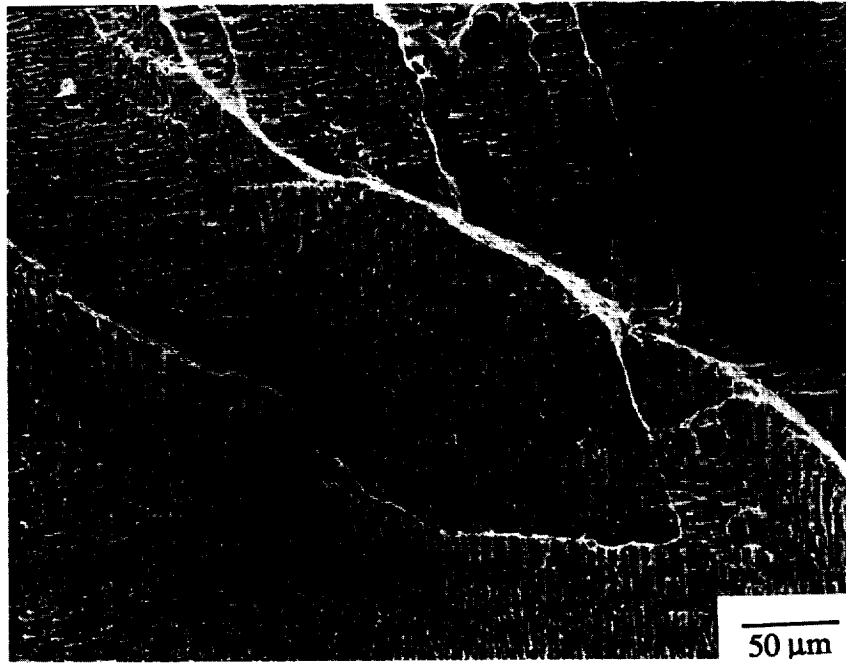


Figure 4.45 Fracture surface of uncharged J_{1C} sample.

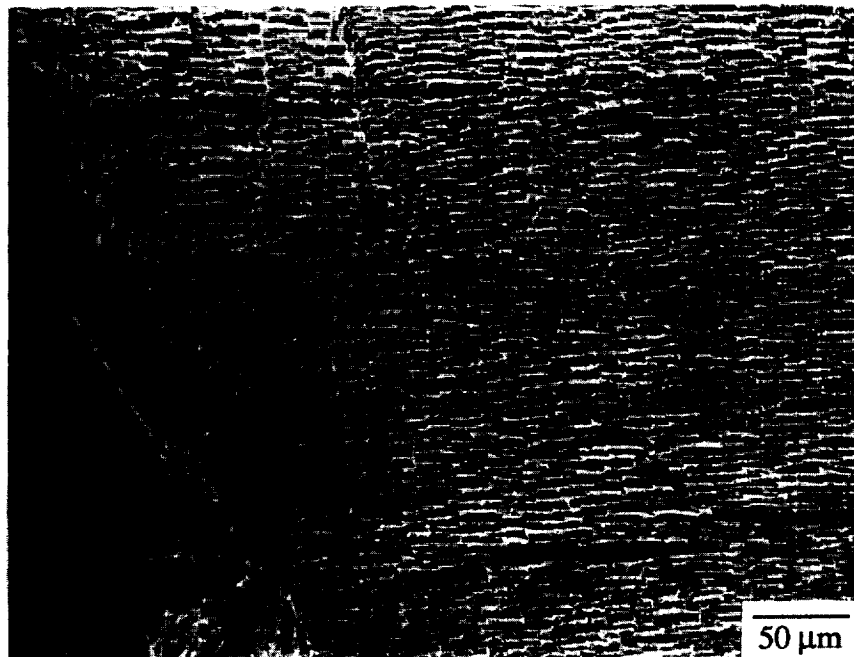


Figure 4.46 Secondary cracks on J_{1C} fracture surface.

ORIGINAL PAGE
BLACK AND WHITE PHOTOGRAPH

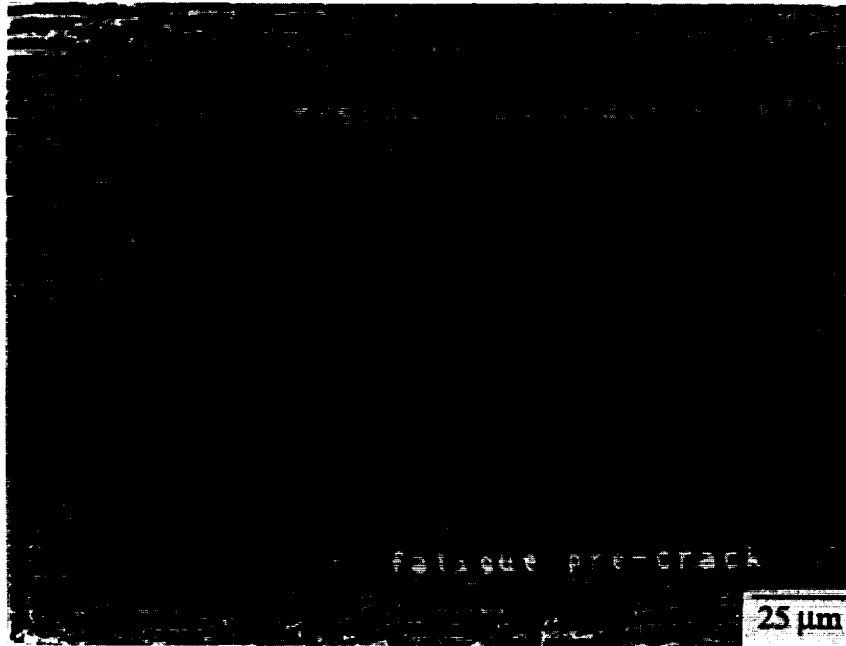


Figure 4.47 Crack running between fatigue pre-crack and beginning of J integral test.

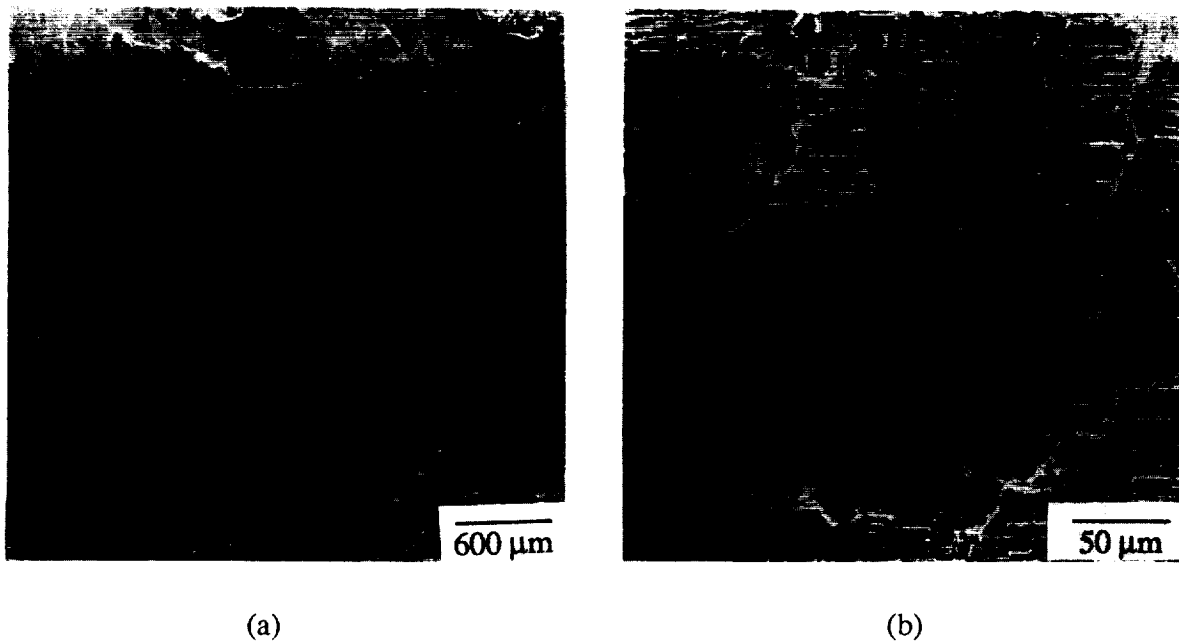


Figure 4.48 (a) Bottom half of the photo shows the J-controlled crack growth region, and the top half and (b) show the fracture behavior in overload region after completion of J integral test.

The pores on the J_{IC} fracture surface rarely had any secondary cracks around them, and their main effect was to slightly alter the crack path, as shown in Figure 4.49. The crack growth in this figure is occurring from the bottom of the photo to the top. The area fraction of porosity and eutectic γ/γ' on the fracture surface was approximately equal to the same quantities found in the microstructure, in agreement with uncharged tensile and K_{IC} samples. Longitudinal sections of interrupted J_{IC} tests supported the idea that the crack path was not affected by the presence of eutectic γ/γ' . In contrast to similar sections of K_{IC} samples, there were rarely any cracked eutectic γ/γ' in the plastic zone of J_{IC} samples, as shown in Figure 4.50.

Fortunately, the transverse orientation of the J_{IC} samples tested was close to $\langle 110 \rangle$ so that the crack growth could be easily observed, as in Figure 4.51. These sections also showed that crack growth occurred across a single $\{111\}$ facet and not along the sides of two $\{111\}$ planes. It appeared that in many cases cracks were opening up along $\{111\}$ planes slightly ahead of the main crack.

The presence of 300 ppm internal hydrogen did not alter the fracture surface appearance or the crack growth mechanisms, in contrast to K_{IC} samples. In J_{IC} samples, there were very few eutectic γ/γ' cracked in the plastic zone, and there was no quantitative increase of cleavage on the fracture surface. These fractographic differences between K_{IC} and J_{IC} samples were surprising and will be discussed further in the next chapter.

ORIGINAL PAGE
BLACK AND WHITE PHOTOGRAPH

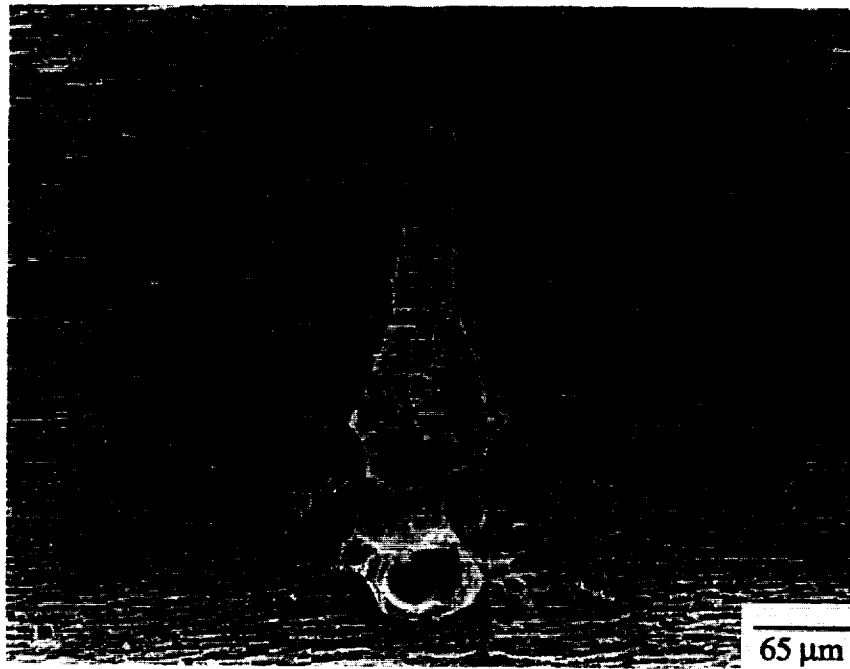


Figure 4.49 Effect of pores on the J_{IC} fracture behavior. Direction of crack growth is towards the top of the photo.

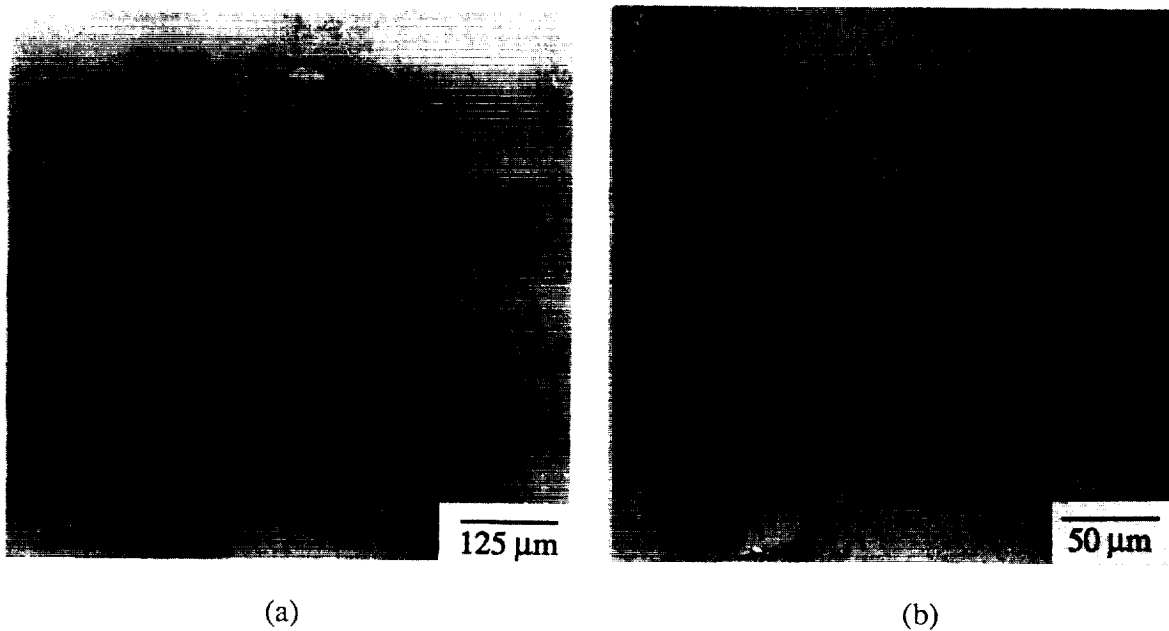
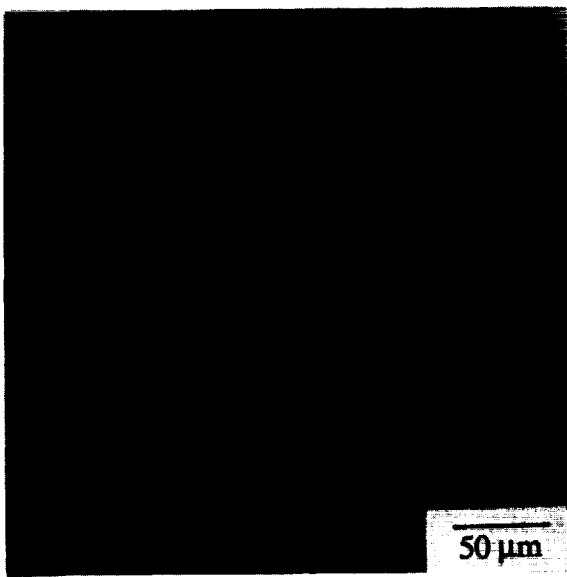


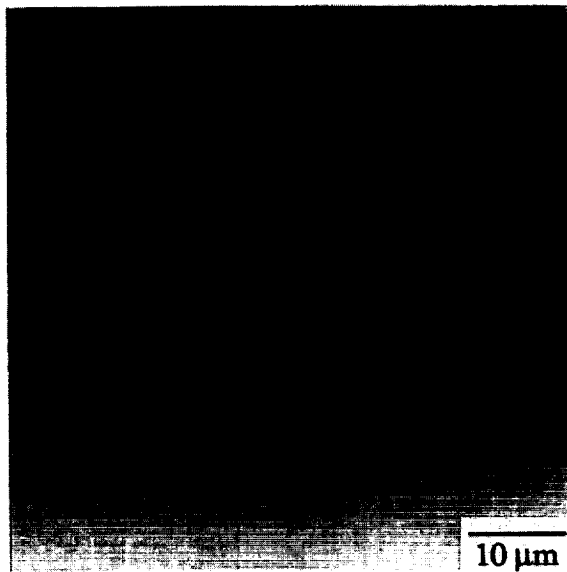
Figure 4.50 Sectioned J_{IC} sample showing little effect of porosity or eutectic γ/γ on crack growth.

There was no apparent effect of the alternate heat treatment on the J_{IC} fractography, except for eliminating the presence of cleavage, of course. HIP'ing the material eliminated the alteration of the crack path by the porosity, but there were no other effects on the fractography. Figure 4.52 is a longitudinal section of a HIP'ed J_{IC} sample given the alternate heat treatment, showing the crack growth mechanism to be identical to the sample in Figure 4.51, which contained porosity and eutectic γ/γ' .

ORIGINAL PAGE
BLACK AND WHITE PHOTOGRAPH

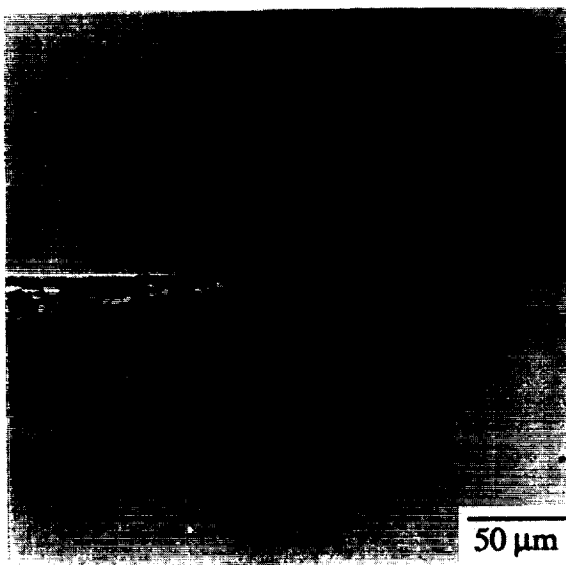


(a)

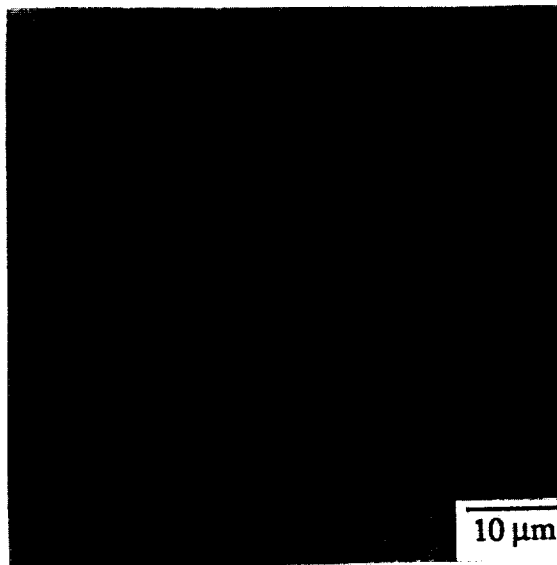


(b)

Figure 4.51 Crack growth along {111} planes shown in sectioned J_{IC} samples.



(a)



(b)

Figure 4.52 Crack growth behavior in a HIP'ed J_{IC} sectioned sample.

CHAPTER 5

DISCUSSION

The previous chapter showed there are many similarities and differences between PWA 1480 and other superalloys, and this chapter will attempt to explain many of these observations. One of the more surprising results was that the porosity and eutectic γ/γ' did not affect the amount of hydrogen that could be charged into the material, nor did they appear to act as irreversible trapping sites. Considering these observations, an alternative explanation is needed for the high hydrogen content found after charging, and possibilities will be offered.

The deformation behavior of uncharged samples differed from that of most superalloys^{11,51-53} because precipitate shearing was not observed at all strains. The factors that affect shearing will be covered in terms of how PWA 1480 may differ from similar alloys. The relationship between the deformation behavior and possible failure mechanisms also will be covered, as well as the role of the eutectic γ/γ' on both of these processes. Cleavage of the eutectic γ/γ' is one of the unique attributes of PWA 1480, and its origins and effects will be examined in detail. Finally, it was found that fracture occurs on {111} slip planes, in agreement with fracture of many other single crystal superalloys^{42,95,96,100} and fcc single crystals.^{91,92,94}

The effect of hydrogen on the tensile properties was similar to other single crystal superalloys,²⁵ in that the failure strain was reduced to a greater extent than the R.A. This suggests that hydrogen is localizing the plasticity, and this will be discussed in view of available models of hydrogen embrittlement processes.^{126,127,131,132,185} This observation is supported by analysis of the slip line characteristics, and agrees with observations in other alloys of increased slip planarity due to hydrogen.^{25,174,186,187} Again, the

relationship between the deformation structure and possible failure mechanisms will be explored.

The fracture toughness results were unusual because the K_{IC} and J_{IC} values did not agree as expected. Further, the fractography and crack growth behavior of these two types of samples was quite different, and this must be carefully examined. It appears that the role of the eutectic γ/γ' was not the same in each test, and this will be discussed in terms of possible differences in the testing techniques, such as the unloading involved in the J_{IC} test.

5.1 Hydrogen Solubility and Trapping

The desorption results suggested that no hydrogen was trapped at irreversible traps after gas-phase charging at 1020 atmospheres and 350°C. The measured rate of hydrogen outgassing for PWA 1480 closely followed the calculated profiles for IN 718 and IN 903 at all temperatures. This suggests that hydrogen is freely diffusing out of the material, and there is no hydrogen remaining behind at irreversible trap sites. Recent results for a similar alloy, CMSX-2,¹⁰ showed the estimated diffusion constant of hydrogen in this alloy to be very close to that of hydrogen in IN 718 and IN 903.¹⁴⁰ These results were obtained through a combination of outgassing experiments and permeation tests. Therefore, the use of diffusion data from IN 718 and IN 903 appears appropriate for single crystal nickel-base superalloys.

Because the absence of irreversible traps is somewhat surprising, the results warrant critical examination. It is possible that the hydrogen analysis technique of vacuum hot extraction performed at 900°C did not detect hydrogen at strongly trapped sites. The resultant binding energy of the traps for such an occurrence can be calculated by employing equation 2-20 that relates outgassing data and binding enthalpy. The subsequent binding energy is almost 2 eV, which is more than twice any previously reported binding energies.^{9,135,136,141} It is unlikely that traps of this strength would exist in PWA 1480,

and thus it is probable that the vacuum hot extraction technique did detect all of the hydrogen.

One should also consider the possibility of hydrogen rearrangement during desorption, which may affect interpretation of the results. This would involve diffusion of hydrogen from either the lattice or reversible traps into irreversible traps during desorption at a given temperature. It is not believed that this occurred during desorption at 300°C or higher based on the work of Baker, et al.,⁹ and Roux, et al., on CMSX-2,¹⁰ which showed there were no irreversible traps operating at these temperatures. However, it is possible that during desorption at 150°C the hydrogen could diffuse into irreversible traps and not be able to overcome the binding energy of the trap to diffuse out. Subsequent desorption data would suggest apparent trapping, but this effect was not seen in this study for the desorption times used at 150°C. This type of secondary trapping would be an artifact of the desorption test method and would not represent any trapping that occurred during charging. All room temperature mechanical testing was completed in times that were far shorter than required for significant diffusion and subsequent possible secondary trapping to occur. Thus, it is believed that the distribution of hydrogen after charging did not change before or during testing.

In other studies concerned with hydrogen trapping in similar alloys, irreversible trapping was observed in CMSX-2,^{9,10} but this occurred after cathodic charging at 150°C. The binding energy calculated by Baker, et al.,⁹ for the pores was such that trapping could occur during charging at 150°C but not during charging at higher temperatures. Roux, et al., report similar results of irreversible trapping in CMSX-2 after cathodic charging at 150°C but did not observe irreversible trapping after gas-phase charging at 350°C.¹⁰ These observations are consistent with the absence of irreversible trapping observed in this study after gas-phase charging at 350°C. Roux, et al., also performed tritium autoradiography tests that suggested a higher concentration of hydrogen can exist in the eutectic γ/γ than in the surrounding microstructure.¹⁰ In these tests, tritium was charged into the material at

150°C; it is possible that the eutectic γ/γ' behaves as an irreversible trap at this temperature but not at higher temperatures, such as 350°C.

In order to better evaluate the distribution of hydrogen after charging, it is important to analyze the solubility of hydrogen in the microstructure. In this study, analysis of the hydrogen content after charging showed that the amount of hydrogen in the material was essentially independent of the amount of porosity or eutectic γ/γ' in the microstructure. This in itself suggests that these features were not acting as large sinks for hydrogen during charging. Thus, the relatively high concentration of 300 ppm hydrogen must be due to other factors, and calculating the equilibrium solubility for the charging conditions will assist in determining if hydrogen exists in an equilibrium state inside the material or if it is reversibly trapped in the microstructure. The following expression can be used to approximate the hydrogen solubility:¹⁴⁰

$$S = S_0 p^{1/2} \exp\left(\frac{-H_s}{RT}\right) \quad (5-1)$$

where S is the solubility in $\text{cm}^3 \text{H}/\text{cm}^3$, p is the pressure in atmospheres, S_0 is the solubility constant, H_s is the heat of solution, R is the gas constant and T is the temperature. Table 5.1 shows the available solubility data for similar alloys. The data for each of these alloys reveals that the equilibrium solubility at 1 atm. and 25°C is less than 1 ppm. The gas-phase charging conditions of 1020 atmospheres and 350°C yield hydrogen solubilities ranging from 25-62 ppm. This is well below the average value of 300 ppm found in PWA 1480 after charging.

Thus, it is apparent that since neither the eutectic γ/γ' nor the porosity act as sinks, the γ/γ' microstructure must either have a much larger solubility than the alloys in Table 5.1, or there exists a large amount of hydrogen reversibly trapped in the lattice. The issue of higher hydrogen solubilities in single crystal superalloys compared to alloys such as IN 903 has been raised by Roux, et al.,¹⁰ in their study of CMSX-2. It was suggested that the

Table 5.1 Solubility data for nickel-base superalloys.

Alloy	S_o ($\text{cm}^3/\text{cm}^3 \cdot \text{atm}^{1/2}$)	H_s (cal/mole)	Reference
IN 903	0.166	1120	140
IN 718	0.89	1930	140
Hastelloy	0.53	1240	188

compositional differences between IN 903 and CMSX-2 could possibly explain the apparent solubility differences; in particular, it was thought that Ta could strongly increase hydrogen solubility. In their study,¹⁰ CMSX-2 was charged in the exact manner as in this work, and a hydrogen concentration of approximately 350 ppm was reported – only slightly higher than the amount of hydrogen in PWA 1480 found in this study. Since these values are similar, and PWA 1480 contains about twice as much Ta as CMSX-2, the effectiveness of Ta in increasing hydrogen solubility appears to be minor.

Suffice it to say that the solubility question remains open, and further work is needed in this area on single crystal nickel-base superalloys. If solubility differences cannot satisfactorily explain the discrepancy between equilibrium solubility and hydrogen content, it is possible that reversible lattice trapping can. Reversible traps are defined as microstructural features that can contain hydrogen and, under given test conditions, act either as sources or sinks for hydrogen.¹³² This is in contrast to irreversible traps, which always act as sinks until they are saturated. It is believed that during gas-phase charging, hydrogen is forced into lattice sites by the hydrostatic pressure and remains in this supersaturated state after cooling from 350°C to room temperature under pressure. This argument is supported by charging experiments conducted at different pressures that showed the hydrogen content to be proportional to the charging pressure.

The argument that hydrogen is only at lattice trapping sites is supported by the fact that CMSX-2 contained about the same hydrogen concentration after equivalent charging conditions. CMSX-2 contains no eutectic γ/γ' and less initial porosity than PWA 1480, but otherwise the γ/γ' microstructure is very similar. Thus, it makes sense that this similar microstructure contains about the same amount of hydrogen as PWA 1480. This also implies that small compositional differences are not important in determining the amount of hydrogen that can be charged into these types of alloys. Based on the similarities found between CMSX-2 and PWA 1480, there is no reason to believe that PWA 1480 would not respond similarly to cathodic charging at 150°C. In particular, it is probable that the pores and eutectic γ/γ' would act as irreversible trap sites during such charging.

While it appears that hydrogen is primarily at lattice sites in the γ/γ' microstructure, it is possible that hydrogen is not distributed uniformly between the γ and γ' phases because of different interaction parameters. But this is unlikely based on preliminary results of Chéne and co-workers on CMSX-2.¹⁰⁸ In their study, an atom microprobe with a deuterium tracer was used, and little, if any, partitioning to either of the phases was observed. A slight tendency for hydrogen trapping at the interface may have been observed, but this is not believed to be a strong trap because the γ/γ' mismatch in these alloys is very small (0.1-0.5%).

Although hydrogen appears to be "trapped" at lattice sites in PWA 1480, it is free to diffuse through the lattice at room temperature and higher, based on desorption results. Thus, it is believed that hydrogen is distributed uniformly through the microstructure and is probably located at tetrahedral or octahedral sites of the fcc lattice in the γ phase and in the same sites in the ordered $L1_2$ lattice of the γ' phase. Therefore, the traps can be defined as reversible under the testing conditions of interest; however, in actuality the diffusion constant at room temperature is so low that substantial diffusion is not likely. Stress-assisted diffusion should also be considered during testing, but Baskes¹⁸⁹ has suggested that this does not significantly aid the hydrogen diffusion process in fcc metals. Thus,

although hydrogen is able to diffuse during testing, it is not likely due to the short times involved in the tests of this study.

In summary, it appears that the presence of porosity and eutectic γ/γ' do not affect either the amount of hydrogen that was charged into PWA 1480 or the trapping characteristics, and based on desorption results, all hydrogen in the material is reversibly trapped. Further, the atom microprobe results of Chéne and co-workers¹⁰⁸ suggest that the hydrogen is uniformly distributed with respect to the γ/γ' microstructure. These results have major implications on how hydrogen affects the subsequent tensile behavior. Since the hydrogen concentration apparently is evenly distributed, dislocations will generally encounter the same hydrogen atmosphere throughout the material. This implies that whether hydrogen assists or hinders the motion of dislocations, the effect will be uniform through the material. The role of strain rate in hydrogen embrittlement is also minimized, because it is not as important for the hydrogen atmosphere to move with the dislocations since there will be a high, uniform concentration of hydrogen wherever the dislocations travel. This analysis is consistent with the results of Roux, et al.,¹⁰ that showed no effect of tensile strain rate on the degree of hydrogen embrittlement in gas-phase charged CMSX-2. Finally, any role of irreversible trapping sites that could contain large amounts of hydrogen and possibly lead to cracking is eliminated.

5.2 Tension and Compression Properties

The tensile properties of PWA 1480 were consistent with those found by other investigators.^{90,111,116} The yield stress was slightly higher than in some studies,^{23,76,90,111,116} and this can be correlated with the smaller γ' size reported in this study, as well as the use of tensile samples within 5° of [001]. At constant volume fraction of γ' precipitates, it has been shown that strength increases with smaller precipitate size.⁹⁰

To better illustrate the effect of orientation, one of the slabs tested (#134) was a few more degrees off of [001] than the other slabs, and consequently the properties were between the average for the [001] orientation and the single slip $\langle 130 \rangle$ orientation discussed in Appendix A. This indicates that multiple slip is being delayed longer in slab #134 than in other samples; this has been observed by Shah and Duhal in a careful study of orientation effects.⁹⁰ In another study, Fritzscheier²³ reported some exceptionally high strain-to-failure values. It is believed that these orientation effects, along with differences in the eutectic γ/γ' volume fraction of their material and that of this study, can explain these results.

The presence or absence of work hardening in these types of alloys is not well understood. Most investigations only report the tensile properties, with no analysis of work hardening behavior. In studies that have reported the stress-strain behavior,^{10,11,52,190} two types of curves have been observed for the [001] orientation at room temperature, as illustrated in Figure 5.1. Type I, Figure 5.1a, is typical of many polycrystalline metals and also has been observed in hydrogen charged CMSX-2^{10,11} and single crystal MAR-M 200.¹⁹⁰ Type II stress-strain curves have been observed in uncharged CMSX-2,¹¹ René N4⁵² and the PWA 1480 of this study. Type I behavior is indicative of simultaneous multiple slip, while Type II behavior is observed in single slip orientations. Type I behavior would occur if multiple slip is initiated uniformly across the sample, and this is observed in the two single crystals cited above that exhibit this behavior. Multiple slip is favored in single crystals with the [001] orientation, but it is possible to have multiple slip occur in the crystal and still observe Type II behavior. This could occur if slip initiated on isolated slip systems and continued uninterrupted along these systems. Narrow bands of intense dislocation activity would form, which would eventually lead to a more uniform slip across the sample as dislocation interactions and tangles occurred in these bands. This in turn would lead to an increased work hardening rate, as observed in Figure 5.1b. This scenario is exactly what is observed in this study

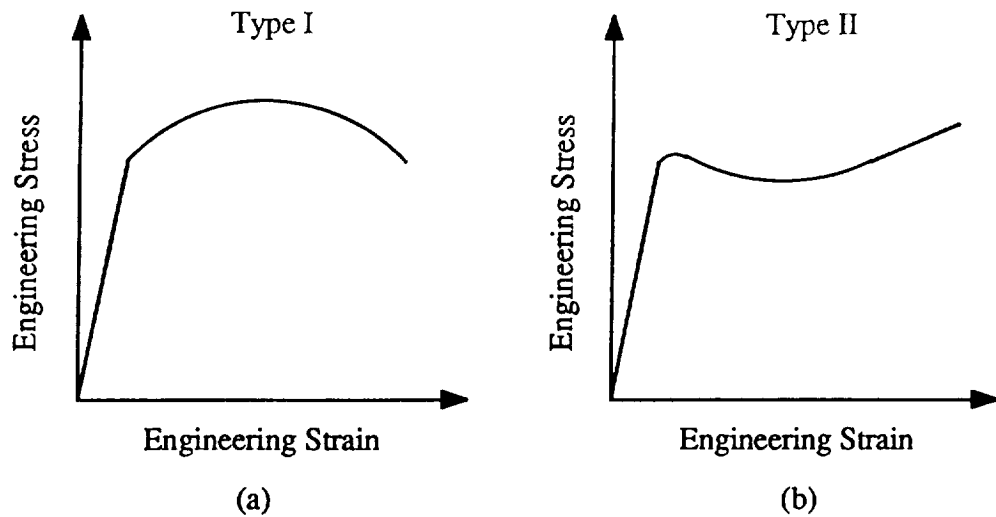


Figure 5.1 Two types of stress-strain curves observed in [001] single crystal nickel-base superalloys.

and will be discussed later. Tensile samples without eutectic γ/γ' showed the same stress-strain behavior as in Figure 5.1b, except that the curve was extended to higher stresses and strains. There was no effect of porosity on the tensile properties, which is consistent with other studies.^{23,28}

The tension/compression asymmetry found in the [001] orientation is similar to other investigations showing the critical resolved shear stress (CRSS) in tension to be about 5% greater than in compression.^{88,90,116} The models used to explain the tension/compression asymmetry are based on changes in the dislocation core⁸⁶ or the behavior of the partial dislocations with stress state.⁹⁰ In this study, hydrogen lowered both the tension and compression yield strength equally, and subsequently there was no effect of hydrogen on the tension/compression asymmetry. This may be used to argue that hydrogen does not substantially affect either of the above two factors. This is indirect evidence, and there have not been any studies done by others to substantiate this.

The effect of hydrogen on the tensile properties will now be discussed in terms of available models of hydrogen embrittlement processes. The presence of 300 ppm internal

hydrogen lowered the flow stress by about 10%, decreased the strain to failure by an order of magnitude and had little effect on the reduction-in-area (R.A.). All of these observations are consistent with the hydrogen-enhanced localized plasticity (H.E.L.P.) model,^{126,146} which argues that hydrogen enhances dislocation generation and motion. The large decrease in failure strain accompanied by little change in R.A. signifies that the majority of deformation is concentrated in a narrow region near the resultant fracture surface. This plastic strain localization has been observed in other single crystal superalloys tested in hydrogen.²⁵ Other experiments supporting the H.E.L.P. model have shown very localized deformation near crack tips in thin foils that are strained in a hydrogen atmosphere,^{142,143,145} which could be manifested in bulk samples by the strain localization described above. Another manifestation of H.E.L.P. observed in PWA 1480 is the lower flow stress observed in charged samples, which could be caused by enhanced dislocation generation.

There are alternative explanations for hydrogen embrittlement, but they do not satisfactorily explain the results of this study. The trap theory of hydrogen embrittlement argues that a critical concentration of hydrogen will reach a microstructural feature and possibly lead to cracking.^{132,133} This is unlikely to occur in PWA 1480 for a few reasons. First, the previous section demonstrated that there were no sites containing uniquely large concentrations of hydrogen, and hydrogen existed more or less uniformly across the microstructure. Therefore, hydrogen must diffuse to a site in order to attain the "critical concentration" required for hydrogen embrittlement. The issue of diffusion also was discussed previously, and it was believed that in room temperature testing, long-range diffusion would be insignificant. Further, the presence of stress fields would not likely aid diffusion very much.¹⁸⁹ Thus, the trap theory of hydrogen embrittlement is not applicable to this study, because there does not appear to be any trapping sites that contain significantly more hydrogen than the surrounding microstructure.

The decohesion model of hydrogen embrittlement could also be used to explain the degradation in tensile properties, but experimental proof for this model is difficult to obtain. The decohesion model argues that the presence of hydrogen solutes decreases the atomic bond strength of the metal causing a brittle fracture when the local stress exceeds the atomic bond strength.^{130,191} The fact that the tensile R.A. is largely unaffected by the presence of hydrogen suggests that this model is not applicable. Having similar R.A.'s for uncharged and charged samples implies that the fracture mechanism is not being greatly changed, which is not the effect that one would generally associate with a reduction in atomic bond strength. Further, there is quite a bit of fractographic plasticity on the fracture surface, especially in the matrix phase. Again, this does not correlate with a brittle fracture caused by weakened atomic bonds.

Thus, it appears that the concept of hydrogen-enhanced localized plasticity can be used to explain much of the observed tensile behavior of charged samples. The observation that hydrogen causes substantial embrittlement, as manifested by a four-fold decrease in failure strain in samples without eutectic γ/γ' , will now be examined. Previously, only embrittlement of samples with eutectic γ/γ' has been discussed, and in these samples a ten-fold decrease in failure strain was observed. Table 4.13 shows that in samples without eutectic γ/γ' , hydrogen still causes a decrease in the yield stress of about 10%. The failure strain is not decreased as much as in samples with eutectic γ/γ' and the R.A. is reduced about 50% instead of having little change. These are still manifestations of H.E.L.P., but the R.A. differences suggest that the plasticity is not as localized. For reasons discussed above, it is not felt that the trap theory or decohesion model are applicable. In charged samples containing eutectic γ/γ' , this constituent cracked at a very early stage of deformation, and it is possible that this crack could cause intense localized deformation, compounded by the effect of hydrogen on localizing the deformation. This scenario may explain why the deformation is more localized in charged samples that contain eutectic γ/γ' . In samples without eutectic γ/γ' , it is possible that only the effect of hydrogen

on localizing deformation is operating and not the effect of cracked eutectic γ/γ' . As a result, there is a decreased localization of plasticity and decreased embrittlement due to hydrogen, as measured by change in failure strain. All of the evidence used for hydrogen-enhanced localized plasticity in this study are bulk observations, and to definitively determine that hydrogen is enhancing dislocation motion and generation, *in situ* straining experiments on the TEM must be performed.^{142,143,145} This was not possible in this study, so the application of the H.E.L.P. embrittlement process remains based on bulk observations.

The effect of hydrogen concentration on tensile properties was studied in two sets of experiments. In both, a steady decrease in strain-to-failure was observed until a minimum value of about 0.3% was reached. The hydrogen concentration at which the minimum failure strain was achieved was different depending on the method used to vary the hydrogen concentration, and this discussion will be aimed at understanding this difference. One method used to vary the hydrogen content was gas-phase charging at different hydrogen pressures, which should result in a uniform concentration of hydrogen across the sample because of the long hold times during charging at 350°C. The second method used was to gas-phase charge the samples at a single hydrogen pressure and subsequently outgas them to different hydrogen concentrations. It is probable that this method would result in hydrogen concentration gradients. It only took 200 ppm total hydrogen content to fully embrittle these samples but 300 ppm to fully embrittle the samples charged at different pressures. It is possible that the lower total concentration of hydrogen required to obtain the minimum failure strain in outgassed samples is related to the presence of hydrogen concentration gradients. The outgassing was performed at 300°C, so long-range diffusion is possible, but any subsequent secondary trapping would not be expected because the binding energy of any irreversible traps is likely overcome at this temperature. To understand the differences in hydrogen distribution in the two sets of samples, consider samples that contain the same total amount of hydrogen. The one

charged at a lower pressure would have the hydrogen evenly distributed, whereas the outgassed sample would have the hydrogen concentrated more toward the center of the sample. Thus, the outgassed sample could have a much higher, local concentration at the center. This effect could lead to a degradation in properties at a lower total amount of hydrogen than in the ones charged at different pressures.

In analyzing these results, it should be noted that the outgassed samples were tested at 300°C, but the results for samples with close to 300 ppm hydrogen were very close to the results of tests conducted at room temperature. The fact that there was little difference in tensile properties of charged samples tested at room temperature and at 300°C brings up this question: At what temperature does hydrogen embrittlement cease? Higher temperatures were not tested due to material constraints, but the behavior at these temperatures can be surmised. Of course, this question cannot be answered without incorporating time, and thus 20 minutes will be used in this thought experiment, since this was the time allowed for the temperature to equilibrate before testing. Hydrogen will be able to diffuse out of the material, but based on the desorption results, this would only effect a narrow surface region of about 200 μm when held for 20 minutes at 300°C. The bulk of the sample should still contain a uniform, untrapped concentration of approximately 300 ppm. At higher testing temperatures, the depleted surface layer would become larger and more important, and eventually the properties would approach those of the uncharged material. Using diffusion data of IN 903,¹⁴⁰ it can be calculated that at 400°C after 20 minutes, there would still be over 290 ppm hydrogen in the sample, while at 500°C there would be 190 ppm, and at 600°C there would be 80 ppm left. Also at 600°C, about two-thirds of the specimen surface would be almost hydrogen-free after 20 minutes using the simple approximation of $x \approx \sqrt{Dt}$, where x is hydrogen-free surface layer.¹⁸⁰

Using these data and the results of tensile tests at 300°C, it appears that the uniformly charged samples would have to be tested at 600°C in order to obtain properties approaching those of uncharged samples. Further, the above discussion did not account

for the role of temperature on the deformation behavior. It has been shown by Dollar and Bernstein⁷⁷ that the deformation structure does not appreciably change from room temperature to 300°C. Above 300°C, there was more shearing of the γ' precipitates, however the ductility only increased slightly from room temperature to 600°C.¹⁹² Considering the slight increase in ductility with temperature, as well as the role of the hydrogen-free surface layer, it is possible that testing at 400°C-500°C could result in a large improvement in properties. This is important because hydrogen embrittlement is typically thought to be a low temperature phenomenon, and the possibility of hydrogen embrittlement at temperatures up to 500°C is a concern for service applications. Of course, this analysis applies to the specific case of an initially uniform hydrogen concentration, and any applications to situations involving surface gradients or different hold times may result in less severe conclusions.

5.3 Deformation and Fracture Behavior without Hydrogen

At the earliest strains studied in tension and compression samples, deformation was accomplished by narrow, widely-spaced, intense bands of dislocations shearing γ' precipitates. There was limited activity elsewhere in the form of single $a/2\langle 110 \rangle$ dislocations and $a/2\langle 110 \rangle$ pairs in the γ matrix. This type of dislocation procession has previously been observed in other Ni-base superalloys¹⁹³⁻¹⁹⁶ and aluminum alloys containing coherent, ordered particles.¹⁹⁷ It has been argued in these cases that a dislocation cutting an ordered particle will reduce its effective cross-sectional area, thereby weakening it by causing a region of decreased order.³⁵ Hornbogen¹⁹⁸ has quantified this process by modifying an existing low volume fraction γ' CRSS model,¹⁹⁹ now incorporating the decrease in CRSS due to the passage of dislocations along the same slip plane. The expression for the CRSS due to coherent, ordered, cuboidal particles, $\Delta\tau$,

accounting for the passage of n dislocations was written as:¹⁹⁸

$$\Delta\tau(n) = \frac{\sqrt{3}}{4} \frac{\gamma d}{bD} \left(1 - \frac{nb}{d} \right) \quad (5-2)$$

where γ is the APB energy, d is the effective particle diameter, b is the Burgers vector and D is the spacing between particles. This equation shows that the CRSS on a given slip plane is decreased for every dislocation that passes along the same slip plane. Therefore, at small strains it appears easier to move dislocations on isolated slip planes where shearing has already occurred, than it is to initiate slip uniformly across the sample.

At the next plastic strain level examined – 1.2% in tension and 1.3% in compression – narrow deformation bands were no longer observed, and more uniform deformation occurred across the samples. The vast majority of dislocations were in the γ matrix, and there was little evidence of precipitate shearing. The previous bands were not observed, probably because of their wide spacing and the fact that the heavy activity now occurring over the entire sample made their observation more difficult. This is not to say that they do not exist anymore, but that their relative importance in the deformation process has become minor. Thus, it appears that the isolated slip bands active at smaller strains have hardened, either by generation of multiple slip within the bands or by interaction with accumulated debris. The work hardening rate increases at this point because of more dislocation interactions and the trapping of dislocations in the γ matrix. This, along with the work softening described above, provide a possible explanation for the stress-strain behavior observed in Figure 5.1b.

At 3.0% strain, there was a very high dislocation density in the γ matrix and little activity in the γ' phase. Normally, in high volume fraction γ' superalloys, the deformation mechanism at these strains is thought to be continued shearing of the precipitates.^{11,51-53} To assist in interpreting the differences between PWA 1480 and other similar superalloys, the Copley and Kear approach to modeling the critical resolved shear stress (CRSS) can be

employed. The model is based on a force balance of a pair of dislocations trying to enter a γ precipitate. The CRSS can be expressed as:²

$$\tau_c = \frac{\gamma}{2b} - \frac{T}{br} + 0.5(\tau_m + \tau_p) \quad (5-3)$$

where T is the dislocation line tension, r is the particle radius on the slip plane, and τ_M and τ_p are the shear stresses of the matrix and precipitate, respectively. The APB energy of PWA 1480 is close to that of similar alloys,^{11,200,201} as is the precipitate size^{23,76,90} and shear modulus.⁴³⁻⁴⁵ Of the parameters in equation 5-3, only the matrix and precipitate flow stress of PWA 1480 may differ greatly from similar alloys. The matrix flow stress used was the one employed by Copley and Kear in their study of a similar alloy and should be fairly accurate, because the composition of the γ phase of PWA 1480 is not too different from their alloy.^{2,21} It was pointed out in section 2.1.1.2 that the γ flow stress in PWA 1480 may be higher than in most other superalloys because of the larger amount of Ta in PWA 1480. The cutting stress is proportional to the precipitate flow stress, so naturally a higher precipitate flow stress would make it more difficult for a pair of dislocations to enter the precipitate. Thus, it is possible that the γ flow stress could explain the differences in deformation structure between PWA 1480 and other superalloys.

As previously mentioned, there was little dislocation activity in the γ precipitates, but occasionally Superlattice Intrinsic Stacking Faults (SISF's) were observed in this phase. Their appearance was not consistent from foil to foil within the same sample, and the separation of the $a/3\langle 112 \rangle$ partials varied greatly with each SISF. These observations, along with the overall sparse occurrence of SISF's, lead to the conclusion that their role in the deformation process is minor. Further, Dimiduk suggested that the presence of SISF's in Ni_3Al was directly related to the thin foil preparation technique,²⁰² casting possible doubt on their reproducibility and meaningfulness. SISF's were seen to a lesser extent in compression samples in this study, but again this simply may be due to variations in

specimen preparation, since SISF's have previously been observed many times in compression.^{57,203}

These observations contradict those of Milligan and Antolovich,¹²³ who report a high density of SISF's within the γ precipitates after room temperature deformation. The density of SISF's shown in their micrographs is much higher than was ever observed in this study. Similar local areas may have been observed in this study, but the representative density of SISF's was much lower than that shown in their micrographs. These differences could be due to many factors, such as orientation, specimen preparation or testing conditions, but the most likely cause is slight compositional differences in the separate batches of material used. These compositional differences are only a possibility, and a definitive explanation for the differences observed in these two studies cannot be given.

The tensile fracture behavior of uncharged samples will now be discussed relating the deformation behavior and fractography to possible fracture mechanisms. The tensile fracture consisted of ductile separation on {111} planes combined with cleavage facets dispersed across the fracture surface. Sectioned hydrogen-free tensiles revealed that there were no cracked eutectic γ/γ' observed at 2.0% strain, which means that the eutectic γ/γ' cleaved very close to the fracture strain. Further, only a few cracked eutectic γ/γ' were observed on sectioned fractured tensiles, and these were very close to the fracture surface. Thus, it seems that cleavage of the eutectic γ/γ' was confined to the fracture zone and occurred very late in the deformation process. Although, this is not to say that the eutectic γ/γ' did not play a role in the fracture process. In fact, samples without eutectic γ/γ' achieved failure strains twice as high as in samples with eutectic γ/γ' . Further, there was no effect of eutectic γ/γ' on the deformation process per se, and these observations suggest that cleavage of the eutectic γ/γ' initiated the fracture process.

In analyzing the effect of cleavage on the fracture process, it must be recognized that the edge of the cracked eutectic γ/γ' can act as a local stress riser. This is analogous to

pre-cracked carbides in MAR-M 200,²⁰⁴ which also were cracked normal to the stress axis. Observations in that study showed localized slip along {111} planes emanating from the cracked carbides. A similar situation could occur for the eutectic γ/γ' in PWA 1480, thus creating shear localization in this manner. Continued shear localization across the samples could be aided by the stresses in the γ matrix created by the large density of dislocations there. It was found in another study that when only the matrix deforms, large stresses can build up within the precipitates.²⁰⁵ Shear localization caused by the cracked eutectic γ/γ' and exclusive deformation in the γ matrix could be manifested by rapid shearing across the γ' precipitates. If such shearing did occur, then it is possible that this could lead directly to failure. For instance, in another superalloy, Gell and Leverant²⁰⁴ argue that localized slip led to weakening of the atomic bonds across the slip plane. Then the normal stresses, which are not relaxed in these alloys,^{101,103} could separate the bonds and create a brittle-appearing fracture. This so-called "glide band decohesion" is believed to be a fairly common fracture mechanism in alloys that deform by shear of coherent particles.²⁰⁶ Completing the story, the ductile γ phase is the last to undergo final separation and thus necks down. This scenario is in agreement with the fractographic evidence showing that the eutectic γ/γ' cracked first, the γ' precipitates had a brittle appearance and the γ phase appeared ductile. It is also consistent with the TEM observations of high dislocation densities in the γ phase with little activity in the γ' precipitates. Intense shear on subsequent fracture planes would not be observed on TEM foils because the foils were taken from sections below the fracture surface.

In samples that do not contain eutectic γ/γ' , cleavage of this constituent cannot initiate fracture, but the fracture sequence could be much the same. In these samples, continued deformation leads to the initiation of significant precipitate shearing, while the γ phase continues to contain high dislocation densities. Previously, it was argued that precipitate shearing is difficult in PWA 1480, but it appears that the stresses created by the high dislocation density in the matrix may force initiation of shearing to partially relieve

these stresses. It is possible that this does not occur uniformly across the sample and in some areas large stresses continue to build up within the precipitates.²⁰⁵ This could, in turn, lead to a similar shear localization phenomenon as described above. This would explain the similar fracture surface appearance between samples with and without eutectic γ/γ' , even though the deformation behavior is slightly different. Thus, it appears that shear localization along slip planes offers a bridge between the observed deformation behavior and fractography.

In comparing the observed fractography to that of other alloys, it is found that this type of {111} crystallographic fracture with ductile tearing of the γ matrix has been observed in many other single crystal superalloys.^{95,96,97,100} So it appears that although the deformation behavior of PWA 1480 differs from most similar alloys, the fracture behavior does not. Further, shear localization leading to slip band fracture is apparently common in superalloys and other systems with coherent particles.^{204,206,207}

Another type of fracture has been observed in single crystal superalloys and will be discussed now. Crystallographic fracture along apparent {001} planes has been observed in another study of PWA 1480 under certain cyclic loading conditions.⁹⁵ This type of fracture was never observed in this study, but it is useful to examine its origin in the other study. A similar macroscopic type of fracture also has been observed in hydrogen-charged CMSX-2 tensile samples.⁹ Figure 5.2 is a schematic of a profile of this type of {001} fracture surface compared with the {111}-type fracture more commonly observed in these alloys. In both studies reporting the {001}-type fracture, it was suggested that the failure was confined to the matrix phase, and that the precipitates had not failed. Analysis of the deformation structure in CMSX-2 revealed cracking along {111} planes inside the γ matrix,¹¹ so it is believed that failure occurs inside this phase rather than at the γ/γ' interface. Cuboidal images of the precipitates were still observed on the fracture surface, because the matrix phase is so thin, causing the γ/γ' outline to be exposed. In the fatigue

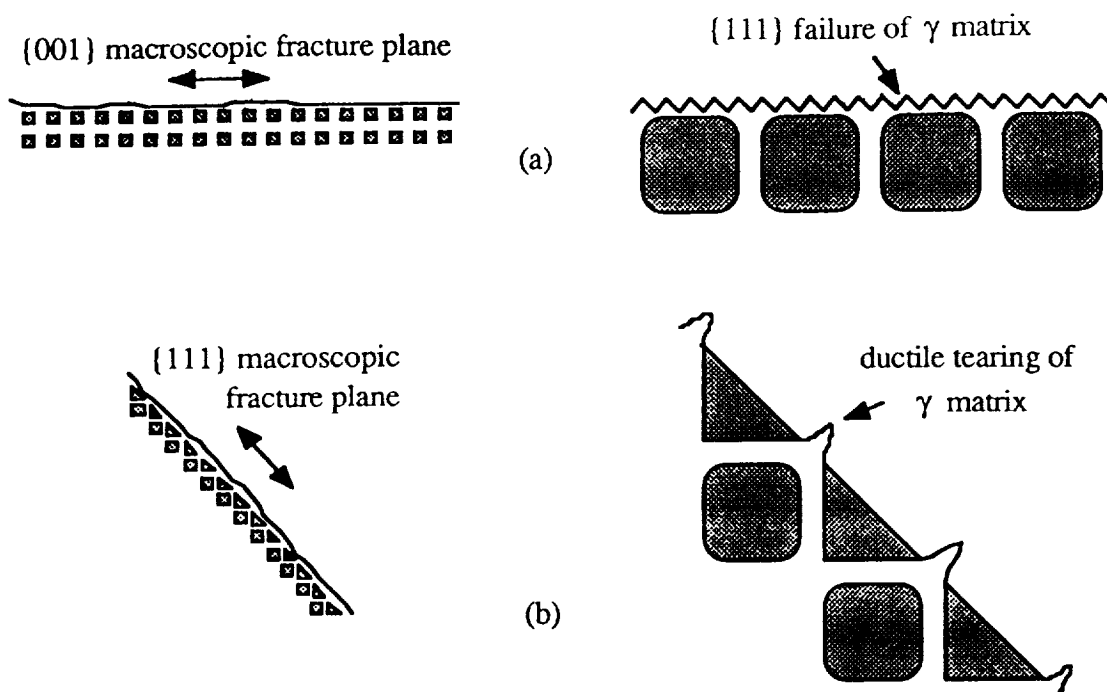


Figure 5.2 Profile of (a) the {001}-type fracture sometimes observed in single crystal superalloys at low and high magnifications and (b) {111}-type fracture observed in this study at low and high magnifications.

study of PWA 1480,⁹⁵ {001} fracture was confined to the lowest ΔK values tested, and {111} fracture was observed at all higher ΔK values. The {001} fracture appearance and limitation of fracture to the γ matrix can be explained by considering the dislocation structure. It was argued that at low ΔK values, the cutting stress for the precipitates had not been overcome, and thus deformation was limited to the matrix phase.⁹⁵ No relation between this behavior and the fracture was given, but in the hydrogen-charged CMSX-2 tensile samples, it was observed that the macroscopic {001} fracture appearance was caused by a high dislocation density in the γ matrix that led to strain exhaustion and failure through this phase along {111} planes.¹¹ This is illustrated in Figure 5.2a showing that macroscopically the fracture was {001}, but microscopically it was actually along {111} planes in the γ matrix. This is likely what happened in Telesman and Ghosn's fatigue samples at low ΔK . A {001}-type fracture was not seen in our study, because it is thought

that the high density of dislocations in the γ matrix caused shear localization across the γ precipitates. A {111}-type fracture was reported at higher ΔK values in the Telesman and Ghosn work, but there was no TEM evidence to determine if a similar scenario occurred as in the tensiles of this study.

Now that the ductile fracture observed in this and other studies has been discussed, the cleavage facets and their origin will be covered. Cleavage in an fcc material is unusual, and thus the observed cleavage of the eutectic γ/γ' warrants further examination. It is believed that this is crystallographic cleavage, which is supported by evidence that includes the flat fracture surface of the eutectic γ/γ' , the river markings present and the facets being parallel to a low index crystallographic plane. A theoretical analysis of fcc cleavage by Gilman²⁰⁸ suggests that the cleavage plane would be {001}, as found in this study. In practice, most fcc cleavage occurs in the presence of an aggressive environment,¹⁷⁶ so it is unusual that the eutectic γ/γ' cleaved in uncharged samples tested in air at room temperature. To understand the origins of this cleavage, the nature of the eutectic γ/γ' must be understood.

The modulus difference between the eutectic γ/γ' and the γ/γ' microstructure is not believed to be large, so this does not appear to offer an explanation for cleavage. The vast majority of eutectic γ/γ' showed little evidence of a lamellae structure and it is believed to consist mostly of the γ phase.¹⁵ Therefore, the behavior of the eutectic γ/γ' phase should be very similar to that of the γ precipitates. It has already been noted that dislocations did not easily penetrate the γ precipitates, and likewise, it was shown that surface slip lines did not cut through the eutectic γ/γ' phase. Further, the dislocation densities were higher in the immediate region of the eutectic γ/γ' and at the interface than in the surrounding γ/γ' microstructure. This leads to the likelihood of large stresses existing at the interface, which in turn could initiate cleavage.^{209,210} Also, it is probable that the eutectic γ/γ' is inherently more brittle than the γ precipitates, because the precipitates apparently underwent some shear before failure, but the eutectic γ/γ' seemingly did not. The impingement of slip bands

on the eutectic γ/γ' is only a possibility for why the eutectic γ/γ' appears to cleave and is not claimed to be definitive. However, it is consistent with the experimental evidence, including the observation that all cleavage initiation sites occurred at the edge of the cleavage facet. A similar finding was reported in MAR-M 200, where crack initiation of carbides was believed to be caused by impinging slip bands, but no experimental evidence was provided.²⁰⁴

It also has been observed that pores initiate cleavage in some cases, but there are two experimental observations that demonstrate that the pores cannot initiate the majority of cleavage facets. Perhaps the strongest evidence is that the vast majority of cleavage facets are not seen adjacent to pores. It is quite possible that a pore may abut the eutectic γ/γ' below the fracture surface, but this pore cannot initiate cleavage because cleavage is a normal stress-controlled process, so the initiation site must be on the fracture surface. Secondly, in HIP'ed samples containing essentially zero porosity, cleavage was observed to the same relative extent as in unHIP'ed samples.

5.4 Deformation and Fracture Behavior with Hydrogen

The deformation structure of hydrogen-charged samples was similar to uncharged samples at strains up to the failure strain of 0.3% in tension and 0.5% in compression. At these strains, narrow, widely-spaced bands of dislocations shearing the γ' precipitates dominated the deformation process. The deformation bands persisted in charged compression samples up to at least $\epsilon_p = 1.3\%$, whereas in uncharged samples uniform deformation was seen at $\epsilon_p = 1.3\%$. It has been observed in pure nickel and nickel-base superalloys that hydrogen promotes planar slip,^{25,174,187} causes localized deformation^{25,186,187} and possibly lowers the stacking fault energy.²¹¹ These observations are consistent with the persistence of the deformation bands to higher strains

in charged compression samples and the increased planarity of the slip lines shown in Figure 4.27. As in the uncharged samples, it is probable that the dislocation structure in these deformation bands eventually will become tangled because of initiation of multiple slip and debris accumulation. Thus, slip will initiate uniformly across the sample, as further slip in the local deformation bands becomes unfavorable. This was observed at a strain of 3.0%, resulting in little difference between the deformation structures of compression samples with and without hydrogen. Both consisted of uniform, multiple slip with the vast majority of activity in the γ matrix.

Dollar and Bernstein¹¹ have performed the only other study that has examined the effect of a uniform concentration of hydrogen on the deformation structure of a single crystal superalloy. Their study on CMSX-2 found that the presence of hydrogen caused the dislocations to be confined to the matrix phase instead of shearing the precipitates, as occurred in uncharged samples. This change in deformation behavior was believed to account for much of the decrease in ductility of charged samples. This type of matrix trapping behavior occurred in PWA 1480 without hydrogen, so such a dramatic change due to hydrogen was not possible, although the scale and extent of trapping could be affected by the presence of hydrogen. It was argued in CMSX-2 that the accumulation of dislocations in the γ matrix at small strains led to an increased local hydrogen concentration. This was followed by enhanced dislocation generation and a decreased mean free path in the γ matrix, which persisted up to failure. This scenario differs significantly from what is believed to occur in PWA 1480, where the trapping of dislocations in the matrix is thought to be due to the large γ flow stress, as previously explained. Dollar and Bernstein also observed room temperature hydrogen-induced cross slip of dislocations onto {001} cube planes.¹¹ No such observations were made in the PWA 1480 of this study, although the evidence may have been overlooked, because even in CMSX-2, cross-slip segments were not frequently observed.

The fracture behavior of charged tensile samples will now be examined in terms of the deformation structure, the role of the eutectic γ/γ' and the H.E.L.P. embrittlement process. The main difference between the uncharged and charged fracture surfaces is the drastic increase in the amount of cleavage on the fracture surface of charged samples. There was no qualitative difference observed in the ductile fracture along $\{111\}$ planes, and possible explanations of these two observations follows.

Sectioned tensiles revealed that the eutectic γ/γ' cracked at a much earlier strain in charged samples (0.2%) and to a greater extent than in uncharged samples. In some manner, the presence of hydrogen is initiating cleavage at an earlier strain. It was suggested in the previous section that cleavage may be initiated by the stress created from impinging of slip bands on the eutectic γ/γ' . If this does occur, then the H.E.L.P. model may offer an explanation for the increased cleavage in charged samples. At 0.2% strain, the deformation structure of uncharged and charged tensiles consisted of the narrow slip bands previously described. The H.E.L.P. model contends that hydrogen can enhance dislocation generation and motion, so one might expect higher densities of dislocations to be piled up at the eutectic γ/γ' interfaces in charged samples. In fact, the density in the γ matrix layer surrounding the eutectic γ/γ' was substantially higher in samples with hydrogen compared to uncharged samples at equivalent strains, as seen in Table 4.17. This supports the possibility that in charged samples higher stresses exist at the eutectic γ/γ' at a given strain. This could lead to cracking of the eutectic γ/γ' at earlier strains, as observed. Supposing hydrogen is enhancing the generation and motion of dislocations, it is likely that the critical stress for cracking would be reached at more eutectic γ/γ' before final fracture. This was observed, and thus it appears that the H.E.L.P. embrittlement process can be used to offer explanations for the increased cleavage in charged samples.

It should not be overlooked that the decohesion model of hydrogen embrittlement^{131,133} could also be used to explain the accelerated cleavage by arguing that the presence of hydrogen solutes decreases the atomic bond strength in the eutectic γ/γ' .

This model is usually applied to systems that change from a ductile to brittle fracture, but this is not necessary. It is not believed that the decohesion model can explain the increased propensity for cleavage in this study because the eutectic γ/γ' already cleaves in the absence of hydrogen. However, it cannot be proven that the decohesion model does not offer the means to enhance cleavage of the eutectic γ/γ' , and thus it must remain a viable alternative. It is not likely that the trap theory of embrittlement^{132,134} is applicable, since it was found that the eutectic γ/γ' was not a sink for hydrogen. Nor did it appear that substantial amounts of hydrogen would be able to diffuse to the eutectic γ/γ' during testing. Thus, it does not seem that a "critical concentration" of hydrogen necessary to cause embrittlement^{132,134} can be reached within the eutectic γ/γ' .

Turning now to the effect of hydrogen on ductile fracture, it is surprising that despite the increased propensity for cleavage and much smaller failure strains in charged samples, the ductile fracture regions are not affected. The fracture surface is generally rougher because the crack path is now seeking out pre-cracked eutectic γ/γ' , but the microscopic fracture still consists of the ductile "voids" on {111} planes. It was previously suggested that these ductile areas were a result of shear localization in the precipitates followed by a brittle-appearing fracture of the precipitates along {111} planes and ductile tearing of the matrix. This was supported by a large density of dislocations in the matrix that could create stresses sufficient to initiate shear localization. At first glance, this scenario does not appear possible in charged samples, because at the failure strain there was a relatively low density of dislocations in the matrix.

Therefore, it remains to explain why the ductile fracture behavior did not change with hydrogen, although the deformation behavior at fracture was apparently quite different than in uncharged samples. To approach this problem, the effect of the eutectic γ/γ' on the tensile behavior must be separated out. In charged samples with eutectic γ/γ' , the eutectic γ/γ' cracked at a small strain resulting in high subsequent stresses at the tip of the cracked eutectic γ/γ' . It was already suggested that this could lead to shear localization, but now

incorporating the ideas of H.E.L.P., it is possible that shear localization is directly enhanced by the presence of hydrogen. Independent experiments supporting this model show a large increase in the local dislocation activity surrounding a crack in charged samples compared to uncharged samples.¹⁴²⁻¹⁴⁷ This could lead to intense shear localization emanating from the cracked eutectic γ/γ' and eventually fracture along this slip band. This would likely occur in a narrow region encompassing the resultant fracture surface, and thus this activity would not be observed on the TEM thin foils. It was already suggested in uncharged samples that the final shear across the precipitates may not have been observed because it only occurred at the resultant fracture surface, and the same phenomenon may have occurred in charged samples.

In tensile samples without eutectic γ/γ' , there were no pre-existing cracks, so another mode of explanation must be used. In this case, the failure strain is increased to just over 1%, and the deformation structure still consists of the narrow slip bands. Due to this deformation structure, it cannot be argued, as in uncharged samples, that the stresses caused by the high dislocation density in the matrix promote strain localization and subsequent fracture in the precipitate along the slip band. Accounting for this difference and absence of pre-cracked eutectic γ/γ' , it appears that the most plausible explanation involves the observed narrow deformation bands. At 1.2% strain, these bands are much more developed than those observed at 0.2% strain, and the precipitates along this band have undergone massive shearing. Thus, it seems appropriate to cite the Gell and Leverant work²⁰⁴ that suggests the precipitates are greatly weakened after this massive shearing. Subsequently, the fracture occurs along these bands producing a similar fracture appearance to all other types of samples since ultimately the same shear localization mechanism was operative. So it appears possible that two different deformation processes occur in charged samples depending on the amount of eutectic γ/γ' present. When there is a large amount of this constituent, it cracks at an early stage of deformation, and this fact, along with the H.E.L.P. model, provide a means to shear localization and subsequent

fracture. In samples without any eutectic γ/γ' , the deformation structure consists of bands of intense shearing of the precipitates. This could directly lead to weakening along this slip plane and subsequent fracture there. Both of these possible scenarios would create similar appearing fracture surfaces. Further, the fracture is similar to uncharged samples because in the end, all processes culminate in slip band fracture of the precipitates and ductile separation of the matrix.

5.5 Analysis of Strengthening

In alloys containing a high volume fraction of coherent, ordered particles, the main strengthening contributions are from order strengthening and solid solution strengthening.³ There are two models that are commonly used in such alloys to predict the critical resolved shear stress (CRSS) and study the effect of various parameters on the CRSS. Reppich and co-workers^{73,80,81} have developed one of the models that analyzes the flow stress due to the presence of these particles as a function of their size and volume fraction. The quantitative application of this model to the PWA 1480 of this study is left to Appendix F because of its length and inconclusive results. In summary, the total CRSS predicted by this model is 1143 MPa, which is considerably higher than the 450 MPa obtained for PWA 1480 in this study. There are two reasons why the model did not predict the observed CRSS more closely. Perhaps the largest inaccuracy is that the Huther-Reppich model only considers the leading dislocation and does not account for the interaction term between the pair of dislocations. This would have reduced the CRSS by almost half, resulting in a reasonable value. Further, Ardell⁶⁹ points out that there is a large spread in the values of some of the constants obtained by different investigators,^{75,82-85} adding unreliability to the model.

The other model generally used was developed by Copley and Kear to predict the CRSS of alloys with a high volume fraction of coherent, ordered particles.² The model is

based on a force balance of a pair of dislocations trying to enter a γ' precipitate, and the CRSS can be expressed as:²

$$\tau_c = \frac{\gamma}{2b} - \frac{T}{br} + 0.5(\tau_m + \tau_p) \quad (5-4)$$

where r is the particle radius on the slip plane, and τ_M and τ_P are the shear stresses of the matrix and precipitate, respectively. Using $\tau_M = 115$ MPa and $\tau_P = 180$ MPa from Copley and Kear,² $G = 54.5$ GPa and $r = 0.32$ μm , a CRSS of 370 MPa was calculated. This is slightly lower than the CRSS of 450 MPa found in PWA 1480, but the agreement is not bad. Dollar and Bernstein used a similar approach and credited such a difference to work hardening that resulted from a high density of dislocations in the γ matrix.⁷⁷ However, Copley and Kear's model is based on events at yielding, and it is not believed that the contribution to strengthening due to work hardening would be very large at the microstrains involved.

Although the comparison between the predicted CRSS and the measured value for PWA 1480 in this study is relatively good, it is believed that better agreement is possible. It could be that the flow stresses used in equation 5-4 for the matrix and precipitates may be inaccurate. The APB energy of PWA 1480 is close to that of similar alloys,^{11,200,201} as is the precipitate size^{23,76,90} and shear modulus.⁴³⁻⁴⁵ The matrix flow stress used was the one employed by Copley and Kear in their study of a similar alloy and should be fairly accurate because the composition of the γ phase of PWA 1480 is not very different from their alloy.^{2,21} It was pointed out in section 2.1.1.2 that the γ' flow stress in PWA 1480 may be higher than in most other superalloys because of the larger amount of Ta in PWA 1480. Assuming that the flow stress of the γ' is totally responsible for the difference in CRSS values, then a value of $\tau_P = 340$ MPa would have to be used to eliminate the difference. This represents almost a 90% increase over the previous τ_P value, but this may not be unreasonable considering the large solid solution strengthening effect of Ta^{4,37-39}

and the fact that Copley and Kear's γ alloy did not contain any Ta.² This analysis is not meant to be exact, but it does point out that if more accurate values of the flow stresses of each phase are used, rather than simply using the values quoted by Copley and Kear,² better agreement can be obtained.

An alternate explanation for the effect of temperature on the CRSS of PWA 1480, independent of the Copley and Kear model, was provided by Milligan and Antolovich¹²³ incorporating the effect of Superlattice Intrinsic Stacking Faults (SISF's). They observed a high density of SISF's in the γ precipitates at room temperature, and proposed that the faults act as barriers to glide. They extend this idea to explain the effect of temperature on the CRSS and convincingly correlate their observations with the CRSS results. However, in this study there was not a consistent or large density of SISF's observed, so this possible strengthening effect cannot be assessed.

5.6 Fracture Toughness

The fracture toughness of PWA 1480 without hydrogen was similar to other nickel-based alloys shown in Table 2.4. Direct comparisons cannot be made though, because to the author's knowledge there have not been any other studies on high γ volume fraction superalloys, let alone single crystals. The fracture mechanisms also are quite different because of the generally crystallographic fracture of single crystals and the different microstructural features involved. Further, direct comparisons of charged samples cannot be made unless the same hydrogen-charging conditions are used.

There are several points to discuss concerning the differences observed in K_{IC} and J_{IC} samples of PWA 1480. To begin with, J_{IC} values can be converted to K_{IC} values using:¹⁵⁸

$$J_{IC} = \frac{K_{IC}^2}{E} \quad (5-5)$$

where E is Young's modulus in plane strain. It was found that the uncharged K_{IC} samples had a toughness value that was 10% less than in comparable J_{IC} samples, and the charged K_{IC} value was 20% lower. Normally, K_{IC} values would be higher than comparable J_{IC} values, as shown in Figure 5.3. This difference in values is believed to arise from the fact that J_{IC} measurements are taken at minimal (0.2 mm) crack extension, while K_{IC} is measured at 2% apparent crack growth.²¹² The agreement is a function of the slope of the R curve, with steeper R curves resulting in worse agreement. PWA 1480 has an intermediate R curve slope in comparison to those shown in Figure 5.3, and therefore K_{IC} should be slightly higher than J_{IC} . Further, the K_{IC} values used for comparison in this study were K_Q values and may have been slightly higher than true K_{IC} values because of thickness effects.¹⁸¹ The discrepancy in the J_{IC} and K_{IC} values can be better understood after examining the differences observed in the fracture surfaces.

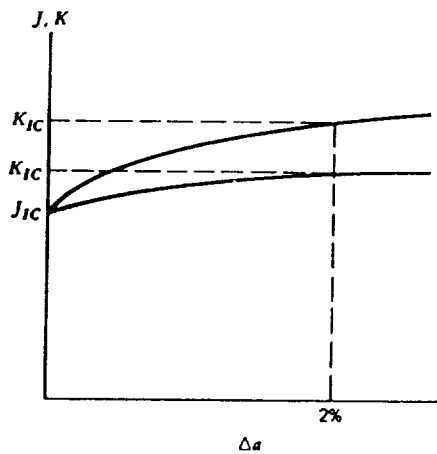


Figure 5.3 Comparison between J_{IC} and K_{IC} values based on the slope of the resistance curve.²¹²

Perhaps the most striking difference in the two tests is the role of the eutectic γ/γ . In K_{IC} samples, hydrogen caused the crack path to seek out this constituent in a similar manner to what occurred in tensile samples. But in J_{IC} samples, hydrogen does not

promote cleavage, nor does the eutectic γ/γ' appear to have an influence on crack growth in uncharged or charged samples. This, in itself, may offer an explanation for the differences in the toughness values of the two tests. Since many eutectic γ/γ' are cracked in the plastic zone of uncharged K_{IC} (~5% of all eutectic γ/γ') and charged K_{IC} (~12%) samples, this would probably lower the toughness of the material. However, in J_{IC} samples, there were virtually no eutectic γ/γ' cracked in the plastic zone, and intuitively this would lead to a higher J_{IC} toughness value than K_{IC} value.

There is apparently a difference in the two tests that is affecting cleavage of the eutectic γ/γ' . One would not expect to observe such marked differences in the fracture behavior and appearance of K_{IC} and J_{IC} samples when similar stress intensities are involved, as was the case. The stress intensity determines the plastic zone size, and therefore both types of samples should have comparable plastic zones. The loading rate of the K_{IC} samples was only slightly higher than in J_{IC} tests, but this difference is not believed to be a significant factor. Any orientation effects on the crack growth are not likely because the charged K_{IC} samples had a transverse orientation very close to the J_{IC} samples. The primary difference is the unloading-reloading cycles that occur in a J_{IC} test compared to the constant rising load in a K_{IC} test. This cycling can affect the strain energy stored in the plastic zone, as well as the deformation structure. It may be possible that the effects of unloading in the J_{IC} test could explain why crack growth is not affected by the presence of the eutectic γ/γ' .

In tensile samples, the possibility of cleavage being initiated by the stress created at impinging slip bands on the eutectic γ/γ' was raised. It seems likely that a similar process could operate in the plastic zone of the fracture toughness samples. This offers an explanation for the cracked eutectic γ/γ' in the K_{IC} samples, and it could be possible that the slip bands impinging on the eutectic γ/γ' in the J_{IC} samples did not provide a large enough stress to initiate cleavage. This may have occurred if the unloading cycle in the J_{IC} tests relaxed the deformation structure ahead of the crack tip in some manner. The observation

that the fractography in the final overload region of the J_{IC} samples resembled that of K_{IC} samples supports the idea of a load cycling effect because this fracture region was created by a more rapid rising load similar to the conditions of a K_{IC} test. Unfortunately, the loading rate or stress intensities involved in this final portion of the test were not monitored.

This above scenario incorporating the effect of unloading is only a possible explanation for the fractography differences, and it should be noted that generally the effect of small amounts of unloading on crack growth behavior is minimal.^{213,214} Thus, more work is needed in this area to either confirm the above scenario or to find a new explanation for the differences observed in K_{IC} and J_{IC} samples.

There were only minimal improvements in J_{IC} when the eutectic γ/γ was removed, and these differences are probably within experimental error. Based on the sectioned J_{IC} samples that showed no effect of the eutectic γ/γ on the crack path, it is not surprising that the eutectic γ/γ did not affect the J_{IC} values. There was an improvement in J_{IC} for HIP'ed samples, and this can be related to the fractography shown in Figure 4.48. The pores altered the crack path, and it is possible that the crack growth was locally accelerated. Elimination of the pores allows the regular, periodic crack growth along $\{111\}$ planes, which could be responsible for the higher toughness of the HIP'ed samples. The unloading-reloading cycles also may affect the behavior of the porosity, because in K_{IC} samples most of the pores were associated with secondary cracks, but few were in the J_{IC} samples.

The crystallographic fracture along $\{111\}$ planes has been explained by Chan and co-workers^{42,101,103} in terms of the stresses present at the crack tip. Fracture along coplanar slip bands is caused by the buildup of large normal stresses along these slip bands, which can explain why the crack does not deviate from the coplanar slip band. Simultaneous fracture along a pair of $\{111\}$ planes can occur because similar normal stresses build up on the cross-slip planes.¹⁰³ Fracture along these two planes give the

characteristic ridge pattern observed on fracture surfaces of PWA 1480 and other single crystal superalloys,^{42,95,96,100} as shown schematically in Figure 5.4. Fracture along pairs of cross slip systems implies that crack growth occurs along $\langle 110 \rangle$ directions. Sectioned J_{IC} samples clearly showed that the crack path was along a $\langle 110 \rangle$ direction, such that the crack travelled along a single $\{111\}$ plane and then changed angles to travel along another $\{111\}$ plane. Referring to Figure 5.4, this corresponds to growth in the $[101]$ direction along the $(\bar{1}\bar{1}1)$ and (111) planes. However, as seen in Figure 4.45, the fracture ridges also could be oriented parallel to the direction of crack growth, and in this case the crack path travels simultaneously along two $\{111\}$ planes. This would still correspond to crack growth in the $[101]$ direction in Figure 5.4, but now the crack grows simultaneously along the $(\bar{1}\bar{1}1)$ and (111) planes. This second type of crack path is the one used by Chan in explaining the presence of ridges on the fracture surface.¹⁰³ It is not known how the crack would grow when the $\langle 110 \rangle$ directions are at an angle other than 90° to the crack front, but it is possible that a combination of the above described paths could occur.

It would be useful to extend Chan's results to attempt to explain the repeatable, periodic nature of the fracture ridges in all samples. The distance that the crack traversed on one $\{111\}$ plane before switching to the corresponding cross-slip plane was typically around $5 \mu\text{m}$, as shown in Figure 5.4. Chan does not incorporate any such distance in his model,¹⁰³ and it does not appear possible to modify the model to derive this distance. It can only be assumed that when the crack is growing along a single $\{111\}$ plane, the normal and shear stresses on the associated cross slip plane are increasing until they reach a critical value. At this critical value, the crack turns and begins growth on the cross-slip system. The interesting point is that the ridge length was about $5 \mu\text{m}$ in both tensile samples and fracture toughness samples. The stress states in these two samples are different, but perhaps on a local scale the stresses on the $\{111\}$ cross-slip system are comparable.

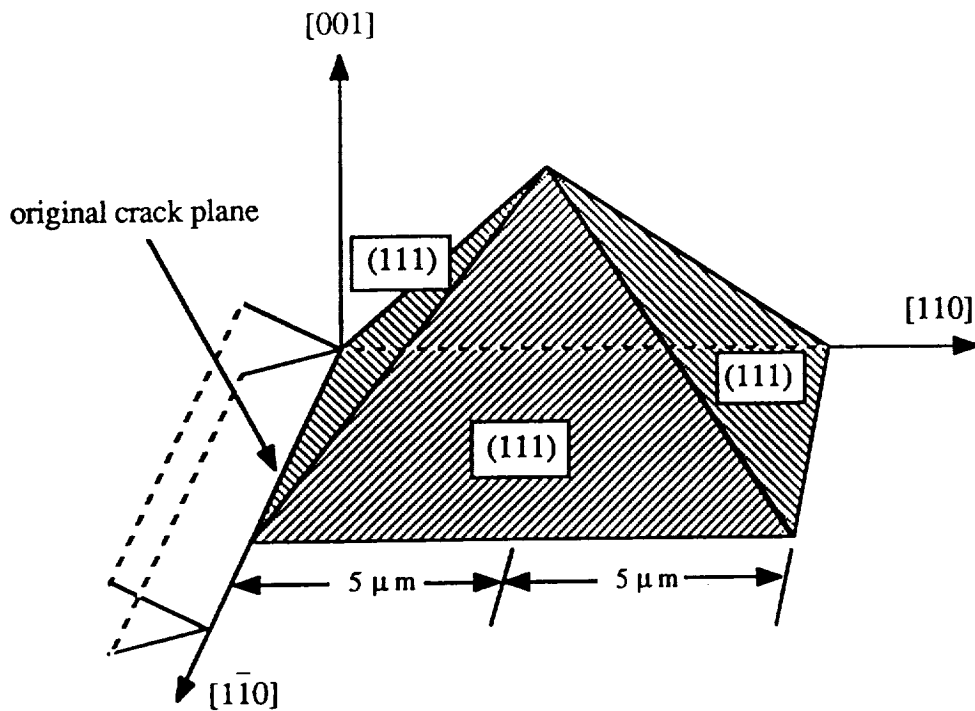


Figure 5.4 Schematic of the crystallographic fracture predominant in J_{IC} samples.

It was the original intent of this work to model the effects of microstructure on the fracture toughness using micromechanistic fracture initiation models.¹⁶¹⁻¹⁶⁴ In order to apply these models, there needs to be a clear understanding of the fracture initiation site, and the spacing of these sites must be small enough to affect the local fracture process. It is clear in K_{IC} samples that many eutectic γ/γ' are cracking in the plastic zone, and this constituent or the porosity may be a fracture initiation site. But in the J_{IC} samples, there is no indication of any fracture initiation sites ahead of the crack tip. Further, the three-dimensional nearest neighbor distances of the porosity and eutectic γ/γ' appear to be too large to affect the local fracture process based on other applications of these models.^{160,169,215-217} Another problem encountered is that the failure strain in many of these models^{158,164,168} is estimated by incorporating the growth of the initiation site during the deformation process. But the eutectic γ/γ' does not change size, and the increase in the pore size is minimal and not enough to give reasonable failure strain values using the

methods of these models.^{158,164,168} Therefore, using any of the available micromechanistic fracture initiation models to correlate fracture toughness and microstructure in PWA 1480 does not appear to be possible.

However, based on the apparent shear localization in tensile samples, it may be possible to model the fracture process in these terms. A problem arises in applying this to the J_{IC} samples, though. The eutectic γ/γ' does not appear to be a viable site for initiation of shear localization, as in the tensile samples, nor is the deformation structure known. Closer examination of these two factors in future work may allow modeling of the fracture process as a shear localization phenomenon. Using this approach, it may even be possible to model the apparently constant 5 μm distance over which crack growth occurs on a single $\{111\}$ plane before switching to another $\{111\}$ plane.

CHAPTER 6

CONCLUSIONS

1. Hydrogen desorption experiments revealed that hydrogen was not irreversibly trapped at microstructural heterogeneities after gas-phase charging at 350°C. Estimates of the hydrogen solubility showed that PWA 1480 contained much more hydrogen after charging than could be explained by available solubility data of similar alloys. It is possible that this data is not applicable to single crystal superalloys, but this was not proven and this area is in need of future research. It is more likely that reversible lattice trapping can explain the larger than expected hydrogen content after charging. Further, it is believed that the hydrogen exists uniformly throughout the microstructure with respect to the γ and γ' phases, as well as the eutectic γ/γ' , although the role of the γ/γ' interface is not presently well understood.
2. Uncharged samples initially deformed by slip on isolated single-slip bands resulting in work softening. This phenomenon was shown to be in common with other superalloys and precipitation hardened alloys. These bands eventually hardened and deformation became more uniform across the sample. Subsequent deformation was primarily confined to the γ matrix, which led to a higher work hardening rate. It is believed that large scale precipitate shearing did not occur, as with most other superalloys, because the γ' precipitates in the PWA 1480 of this study had a higher flow stress than precipitates of other superalloys.
3. Superlattice intrinsic stacking faults were seen only occasionally and never in large enough densities to play a role in the deformation process at room temperature, in contrast to observations by others in the same system.

4. The Copley and Kear flow stress model for high volume fractions of coherent, ordered particles was used to rationalize the CRSS of PWA 1480 at room temperature. Initial agreement was good, but it was shown that better results would be obtained if a more accurate value for the precipitate flow stress was available.
5. It was found that porosity had no effect on uncharged tensile properties and that eliminating the eutectic γ/γ' did not effect the strength, but did increase the ductility. The observed tension/compression flow stress asymmetry was in agreement with other studies, and it was found that hydrogen had no effect on this phenomenon.
6. In uncharged samples, it was shown that the the fracture process was initiated by cleavage of the eutectic γ/γ' along $\{001\}$ planes, which may have been caused by the stress created from impinging slip bands upon the eutectic γ/γ' . The cracked eutectic γ/γ' , in conjunction with the stresses caused by the high dislocation density in the matrix, likely causes shear localization in the precipitates. This localization of slip could then lead directly to fracture along this slip band, as suggested in other superalloys and precipitation-hardened alloys. In specially heat treated samples without eutectic γ/γ' , it was discussed how the same process can occur, but now without the assistance of the eutectic γ/γ' in initiating shear localization.
7. The tensile strength only changed slightly as a function of internal hydrogen content, but ductility continually decreased with larger concentrations until a threshold level of about 0.3% strain to failure was reached. It was shown that hydrogen may degrade properties up to testing temperatures of 500°C, when samples contain an initially high, uniform concentration of hydrogen. Many of the effects of hydrogen on the tensile properties and deformation behavior are explainable by the hydrogen-enhanced localized plasticity (H.E.L.P.) model. It was not believed that the decohesion model,

trap theory or any other embrittlement processes were especially applicable to this study.

8. It was found that porosity had no effect on charged tensile properties and that the material was more resistant to hydrogen embrittlement when the eutectic γ/γ' was eliminated. However, there was still a significant degradation in properties due to hydrogen in "clean" material without porosity or eutectic γ/γ' . It is possible that the ideas involved in the H.E.L.P. model can help to explain this, but a definitive explanation for this embrittlement remains elusive.
9. The presence of 300 ppm internal hydrogen caused the deformation on isolated single-slip bands to persist to much higher strains. This continuation of localized slip is consistent with the effect of hydrogen on many other alloys. This observation, along with a lower flow stress and localized plastic deformation in charged samples, can be satisfactorily explained by the H.E.L.P. model.
10. The primary difference in the fracture behavior of charged samples was that the eutectic γ/γ' cleaved at a much smaller tensile strain and to a greater extent. An explanation for these observations was offered, involving the impinging slip bands on the eutectic γ/γ' and the premises of the H.E.L.P. model. It was believed that the impinging slip bands would be more intense due to hydrogen's effect on the dislocation behavior, and thus create higher stresses at the eutectic γ/γ' at smaller strains than in uncharged samples. Experimental evidence for this suggestion was obtained in the form of higher densities at the eutectic γ/γ' interface in charged samples than uncharged samples at equivalent strains.
11. The failure process in charged samples was explained in a similar manner to uncharged samples using the concepts of shear localization and slip band fracture. It was suggested that samples containing eutectic γ/γ' initiated shear localization in the same

manner as uncharged samples, but now the shear localization was enhanced by the presence of hydrogen. Again, the shear localization is believed to lead directly to slip band fracture. More strain was obtained in tensile samples without eutectic γ/γ' , and thus it was thought that the observed deformation bands were sufficiently intense to weaken the slip plane and initiate fracture.

12. The fracture toughness of PWA 1480 was similar to other nickel-based alloys, although direct comparisons to similar alloys was not possible because no other work was found on high volume fraction γ' superalloys. In J_{IC} samples, the eutectic γ/γ' did not affect the fracture toughness, but eliminating the porosity slightly improved the toughness. Further, the presence of 300 ppm internal hydrogen did not influence the crack growth behavior or fracture toughness.
13. K_Q values were relatively lower than comparative J_{IC} values, and there was a large influence of porosity and eutectic γ/γ' on the K_Q fractography, as compared to the J_{IC} fractography. It appeared that differences in the amount of cleavage of the eutectic γ/γ' could be used to explain the differences in the toughness values, but the reasons for the different cleavage amounts was unknown. It is possible that the effect of unloading in the J_{IC} tests could explain these observations, but any definite conclusions were not reached.
14. Failure occurred in J_{IC} samples by fracture on pairs of $\{111\}$ planes resulting in periodic ridges on the fracture surface. Crack growth occurred in the $\langle 110 \rangle$ direction and could occur simultaneously along two $\{111\}$ planes or traverse a single $\{111\}$ plane at a time depending on the initial orientation of the sample. The eutectic γ/γ' did not influence the crack growth behavior or toughness value, but the pores apparently accelerated the crack growth and slightly reduced toughness.

15. In summary, it was shown that internal hydrogen severely degrades the properties of PWA 1480, not only at room temperature but likely at temperatures up to at least 500°C. Further, it was shown that the resistance to room temperature crack growth in a gaseous hydrogen atmosphere is very low. It was also found that the presence of a large amount of eutectic γ/γ' enhances the embrittling affect of hydrogen and should be eliminated whenever possible. Thus, it does not appear that PWA 1480 is an attractive candidate alloy for use in situations that may simulate the testing conditions examined in this work. More specifically, this would involve room temperature exposure of cracked parts to gaseous hydrogen or low temperature (<500°C) situations where there is a possibility of an uptake of large quantities of internal hydrogen followed by applications of stresses.

CHAPTER 7

SUGGESTIONS FOR FUTURE RESEARCH

The present study has pointed out several areas of study on hydrogen embrittlement of single crystal nickel-base superalloys that are in need of future research. Some of the areas listed below would best be served by further work on PWA 1480, but many are research topics applicable to any single crystal superalloy. Unless specifically necessary as an experimental variable, the presence of porosity and eutectic γ/γ' should be avoided, so results can be more easily compared to other alloys.

1. The results of this study suggested that the role of porosity, eutectic γ/γ' and composition are minor in determining the amount of hydrogen that can be gas-phase charged into these types of alloys. In order to learn what factors are important, there are two areas that should be examined. First, the role of the γ/γ' interface in hydrogen trapping must be better defined possibly through either atom microprobe studies or high resolution tritium autoradiography. Secondly, further research is needed on compositional effects on hydrogen solubility and distribution. Both of these areas are very important in terms of being able to fundamentally design a hydrogen-resistant single crystal superalloy. Also, to better determine the hydrogen trapping behavior of a given alloy, a wide range of charging methods should be used including gas-phase charging at different pressures and cathodic charging.
2. There were several indications in this study that hydrogen was enhancing the occurrence of localized plasticity. Similar observations have been made on other single crystal superalloys, providing an impetus for more work in this area. Definitive proof for hydrogen enhancement of dislocation generation and motion and localized deformation can best be obtained by performing *in situ* straining experiments on a

TEM hydrogen charging capabilities. In this way, bulk observations from this study can be linked to dislocation behavior and comparisons made on similar *in situ* tests that have already been performed on other alloys.

3. Countless studies have been performed on superalloys in an attempt to understand the effect of composition on tensile properties, but this area remains in need of more fundamental-type research. Comparisons of the PWA 1480 of this study with alloys of similar microstructures, such as CMSX-2 and MAR-M 200, have demonstrated that the tensile properties and deformation behavior can dramatically vary. It is likely that composition effects could explain some of these differences, and detailed studies are needed in areas such as the effect of composition on fault energy, γ/γ' misfit and the γ and γ' flow stresses.
4. It was found that strain localization played a major role in the tensile behavior of charged and uncharged samples. It is known that once shearing has begun, it is easier for dislocations to continue slip through ordered precipitates, but little is understood about the origins or results of this localization. This study has suggested links between the macroscopic stress state, stress risers and shear localization on slip planes, but more evidence for such links is necessary. Observation of slip traces emanating from eutectic γ/γ' and correlation with localized slip is needed, and may be accomplished by performing *in situ* SEM straining experiments in conjunction with TEM studies of the deformation structure. Finite element modeling of the γ/γ' microstructure could assist in interpretation of the development of the deformation structure and possibly suggest origins for the occurrence of localized slip. Finally, correlation of these microscopic events to the stress state could be aided by the use of plane strain tensile tests.

5. Differences in the fracture behavior of K_{IC} and J_{IC} samples remains an unresolved issue. It is possible that more sectioning experiments on both types of samples at different stages of testing could be useful. Thin foils taken from the plastic zone of each sample would also assist in determining any effect of unloading on the deformation structure.

CHAPTER 8

REFERENCES

1. R.F. Decker and C.T. Sims, *The Superalloys*, eds. C.T. Sims and W.C. Hagel, Wiley, New York, 1972, 33-77.
2. S.M. Copley and B.H. Kear, *Trans. TMS-AIME*, **239**, (1967), 984-992.
3. R.F. Decker, *Proc. Steel Strengthening Mechanisms Symposium*, 1969, 1-23.
4. M.V. Nathal and L.J. Ebert, *Superalloys 1984*, eds. M. Gell, et al., TMS-AIME, 1984, 125-133.
5. A.D. Cetel and D.N. Duhl, *Superalloys 1988*, eds. D.N. Duhl, et al., TMS-AIME, 1988, 235-244.
6. C.T. Sims, *Superalloys 1988*, eds. D.N. Duhl, et al., TMS-AIME, 1988, 173-182.
7. M. Gell, D.N. Duhl and A.F. Giamei, *Superalloys 1980*, eds. J.K. Tien, et al., ASM, 1980, pp. 205-214.
8. L.G. Fritzemeier and W.T. Chandler, *Superalloys, Supercomposites and Superceramics*, eds. J.K. Tien and T. Caulfield, Academic Press, Inc., San Diego, 1989, 491-524.
9. C.L. Baker, J. Chene, I.M. Bernstein and J.C. Williams, *Met. Trans.*, **19A**, (1988), 73-82.
10. R. Roux, A.M. Brass and J. Chene, *Hydrogen Effects on Material Behavior*, eds. N.R. Moody and A.W. Thompson, TMS-AIME, 1989, to be published.
11. M. Dollar and I.M. Bernstein, *Acta Met.*, **36**, (1988), 2369-2376.
12. M. Gell and D.N. Duhl, *Proc. of N.J. Grant Symposium; Advanced High Temperature Alloys: Processing and Properties*, eds. S.M. Allen, R.M. Pelloux and R. Widmer, ASM, 1985, 41-49.
13. M. Gell, D.N. Duhl, D.K. Gupta and K.D. Sheffler, *J. Metals*, **39**, (1987), 11-15.
14. B.H. Kear, *Scientific American*, Oct. **1986**, 159-167.
15. Yaoxiao, et al., *Superalloys 1988*, eds. D.N. Duhl, et al., TMS-AIME, 1988, 702-711.
16. J. Campbell, *The British Foundryman*, April **1969**, 147-158.
17. D.L. Anton and A.F. Giamei, *Mat. Sci. and Eng.*, **76**, (1985), 173-180.

18. J. Lecomte-Beckers, *Superalloys 1988*, eds. D.N. Duhl, et al., TMS-AIME, 1988, 712-721.
19. L.G. Fritzemeier, *Superalloys 1988*, eds. D.N. Duhl, et al., AIME, 1988, 265-274.
20. W.S. Walston, Carnegie Mellon University, unpublished research.
21. D. Blavette, et al., *Superalloys 1988*, eds. D.N. Duhl, et al., TMS-AIME, 1988, 305-314.
22. D.N. Duhl, *U.S. Patent 4,209,348*, June 24, 1980.
23. L.G. Fritzemeier, *NASA CR-182244*, "Advanced Single Crystals for SSME Turbopumps," 1989.
24. T.T. Field, et al., *U.S. Patent 4,583,608*, April 22, 1986.
25. L.G. Fritzemeier, Rocketdyne, unpublished research.
26. D.J. Kenton, *Diesel and Gas Turbine Prog.*, **March 1976**, 36-37.
27. H. Burt, et al., *Mat. Sci. and Eng.*, **53**, (1982), 245-250.
28. K.C. Antony and J.F. Radavich, *Superalloys 1980*, eds. J.K. Tien, ASM, 1980, 257-265.
29. D.A. Jablonski and S. Sargent, *Scripta Met.*, **15**, (1981), 1003-1006.
30. M.A. Burke, C.G. Beck and E.A. Crombie, *Superalloys 1984*, eds. M. Gell, et al., TMS-AIME, 1984, 63-71.
31. R.L. Dreschfield, *J. Metals*, **July 1987**, 16-21.
32. J.M. Eridon and R.P. Dalal, *U.S. Patent 4,743,312*, May 10, 1988.
33. L.G. Fritzemeier, *U.S. Patent Application # 07/033324*, 1989.
34. R.W. Hertzberg, "*Deformation and Fracture Mechanics of Engineering Materials*," Wiley and Sons, New York, 1989, p. 69.
35. L.M. Brown and R.K. Ham, *Strengthening Methods in Crystals*, eds. A. Kelly and R.B. Nicholson, Wiley, New York, 1971, 96-112.
36. H.C. Nguyen, *NASA CR 174779*, "The Effect of Ta and C on the Structure/Properties of a Single Crystal Nickel-Base Superalloy," 1984.
37. S. Chakravorty and D.R.F. West, *Metals Tech.*, **Oct. 1980**, 414-419.
38. F. Heredia and D.P. Pope, *MRS Symposia Proceedings, Vol 81*, eds. N.S. Stoloff, et al., 1980, 213-220.
39. Z. Meng, et al., *Superalloys 1984*, eds. M. Gell, et al., TMS-AIME, 1984, 563-572.

40. J.F. Nye, "*Physical Properties of Crystals*," Clarendon Press, Oxford, 1985, 131-149.
41. Y.I. Sirotnin and M.P. Shaskolskaya, "*Fundamentals of Crystal Physics*," Mir Publishers, Moscow, 1982, 336-337.
42. K.S. Chan and T.A. Cruse, *Eng. Frac. Mech.*, **23**, (1986), 863-874.
43. F. Wallow, et al., *Phys. Stat. Sol. (a)*, **99**, (1987), 483-490.
44. F.C. Douglas, *United Technologies Research Center Report R79-914549-1*, 1979.
45. H. Pottebohm, G. Neite and E. Nembach, *Mat. Sci. and Eng.*, **60**, (1983), 189-194.
46. R.W. Dickson, J.B. Wachtman, Jr. and S.M. Copley, *J. Appl. Phys.*, **40**, (1969), 2276-2279.
47. K. Ono and R. Stern, *Trans. TMS-AIME*, **245**, (1969), 171-172.
48. F.X. Kayser and C. Stassis, *Phys. Stat. Sol. (a)*, **64**, (1981), 335-342.
49. D.P. Pope and S.S. Ezz, *Int'l. Met. Rev.*, **29**, (1984), 136-167.
50. P.A. Flinn, *Trans. TMS-AIME*, **218**, (1960), 145-154.
51. A.A. Hopgood and J.W. Martin, *Mat. Sci. and Eng.*, **91**, (1987), 105-110.
52. R.V. Miner, R.C. Voigt, J. Gayda and T.P. Gabb, *Met. Trans.*, **17A**, (1986), 491-505.
53. M. Raguét, S.D. Antolovich and R.K. Payne, *Superalloys 1984*, eds. M. Gell, et al., TMS-AIME, 1984, 233-241.
54. P. Beardmore, R.G. Davies and T.L. Johnston, *Trans. TMS-AIME*, **245**, (1969), 1537-1545.
55. B.H. Kear, J.M. Oblak and A.F. Giamei, *Met. Trans.*, **1**, (1970), 2477-2486.
56. V. Paidar, M. Yamaguchi, D.P. Pope and V. Vitek, *Phil. Mag.*, **45**, (1982), 883-894.
57. L.R. Cornwell, G.R. Purdy and J.D. Embury, *Phys. Stat. Sol.*, **35**, (1969), K1-K3.
58. H.R. Pak, T. Saburi and S. Nenno, *Scripta Met.*, **10**, (1976), 1081-1085.
59. K. Suzuki, M. Ichihara and S. Takeuchi, *Acta Met.*, **27**, (1979), 193-200.
60. S. Takeuchi, E. Kuramoto, T. Yamamoto and T. Taoka, *Jap. J. Appl. Phys.*, **12**, (1973), 1486-1492.
61. B.H. Kear, A.F. Giamei, G.R. Leverant and J.M. Oblak, *Scripta Met.*, **3**, (1969), 123-129.

62. B.H. Kear, J.M. Oblak and A.F. Giamei, *2nd Int'l. Conf. on Strength of Metals and Alloys*, ASM, 1970, 1155-1159.
63. K. Enami and S. Nenno, *Jap. J. Phys. Soc.*, **25**, (1968), 1517.
64. V.A. Phillips, *Phil. Mag.*, **16**, (1967), 103-117.
65. H. Gleiter and E. Hornbogen, *Phys. Stat. Sol.*, **12**, (1965), 235-264.
66. D. Raynor and J.M. Silcock, *Metal Sci. J.*, **4**, (1970), 121-130.
67. V. Munjall and A.J. Ardell, *Acta Met.*, **23**, (1975), 513-520.
68. A. Melander and P.A. Pearson, *Metal Sci.*, **12**, (1978), 391-398.
69. A.J. Ardell, *Met. Trans.*, **16A**, (1985), 2131-2165.
70. R.L. Fleischer, *Acta Met.*, **11**, (1963), 203-209.
71. A.J. Ardell, V. Munjall and D.J. Chellman, *Met. Trans.*, **7A**, (1976), 1263-1268.
72. S.M. Copley and J.C. Williams, *Alloy and Microstructural Design*, eds. J.K. Tien and G.S. Ansell, Academic Press, New York, 1976, pp. 25-26.
73. B. Reppich, *Acta Met.*, **30**, (1982), 87-104.
74. J.J. Gilman, *J. Appl. Phys.*, **36**, (1965), 3195-3206.
75. B. Reppich, P. Schepp and G. Wehner, *Acta Met.*, **30**, (1982), 95-104.
76. W.W. Milligan and S.D. Antolovich, *Met. Trans.*, **18A**, (1987), 85-95.
77. M. Dollar and I.M. Bernstein, *Superalloys 1988*, eds. D.N. Duhl, et al., TMS-AIME, 1988, 275-284.
78. E. Schmid and W. Boas, "*Plasticity of Crystals*," F.A. Hughes and Co., 1950.
79. R.B. Schwarz and R. Labusch, *J. Appl. Phys.*, **49**, (1978), 5174-5187.
80. W. Huther and B. Reppich, *Z. Metallk.*, **69**, (1978), 628-634.
81. W. Huther and B. Reppich, *Mat. Sci. and Eng.*, **39**, (1979), 247-259.
82. M. Grohlich, P. Haasen and G. Frommeyer, *Scr. Met.*, **16**, (1982), 367-370.
83. P. Haasen and R. Labusch, *5th Int'l Conf. on Strength of Metals and Alloys*, eds. P. Haasen, V. Gerold and G. Kostorz, Pergamon Press, Oxford, 1979, 639-643.
84. E. Nembach, *Z. Metallkd.*, **72**, (1981), 401-405.
85. A.W. Thompson and J.A. Brooks, *Acta Met.*, **30**, (1982), 2197-2203.
86. V. Paidar, D.P. Pope and V. Vitek, *Acta Met.*, **32**, (1984), 435-448.

87. Y. Umakoshi, D.P. Pope and V. Vitek, *Acta Met.*, **32**, (1984), 449-456.
88. F.E. Heredia and D.P. Pope, *Acta Met.*, **34**, (1986), 279-285.
89. S.S. Ezz, D.P. Pope and V. Vitek, *Acta Met.*, **30**, (1982), 921-926.
90. D.M. Shah and D.N. Duhl, *Superalloys 1984*, eds. M. Gell, et al., TMS-AIME, 1984, 105-114.
91. A. Abel and R.K. Ham, *Acta Met.*, **14**, (1966), 1495-1503.
92. D.A. Ryder and R.E. Vian, *J. Inst. Metals*, **90**, (1961-62), 383-386.
93. B.H. Kear and B.J. Piarcey, *Trans. TMS-AIME*, **239**, (1967), 1209-1215.
94. M. Nageswararao and V. Gerold, *Met. Trans.*, **7A**, (1976), 1847-1855.
95. J. Telesman and L.J. Ghosn, *Superalloys 1988*, eds. D.N. Duhl, et al., AIME, 1988, 615-624.
96. J.S. Crompton and J.W. Martin, *Met. Trans.*, **15A**, (1984), 1711-1719.
97. K.S. Chan, J.E. Hack and G.R. Leverant, *Met. Trans.*, **17A**, (1986), 1739-1750.
98. D.J. Duquette, M. Gell and J.W. Piteo, *Met. Trans.*, **1**, (1970), 3107-3115.
99. G.R. Leverant and M. Gell, *Met. Trans.*, **6A**, (1975), 367-371.
100. D.L. Anton, *Mat. Sci. and Eng.*, **57**, (1983), 97-105.
101. D.A. Koss and K.S. Chan, *Acta Met.*, **28**, (1980), 1245-1252.
102. J.A. West and W.M. Robertson, *Metallography*, **15**, (1982), 367-381.
103. K.S. Chan, *Acta Met.*, **35**, (1987), 981-987.
104. Q. Chen and H.W. Liu, *NASA CR 182137*, "Resolved Shear Stress Intensity Coefficient and Fatigue Crack Growth in Large Crystals," 1988.
105. A.H. Sherry, Ph.D. Thesis, University of Manchester; England, 1987.
106. W.S. Alter, R.H. Parr, M.H. Johnston and J.P. Strizak, *NASA CP 2372*, "Advanced High Pressure O₂/H₂ Technology," 1984, pp. 150-163.
107. P. Lacombe, M. Aucouterier and J. Chéne, *Hydrogen Embrittlement and Stress Corrosion Cracking*, eds. R. Gibala and R.F. Hehemann, ASM, 1984, 79-102.
108. J. Chéne, Universite Paris Sud, unpublished research.
109. I.M. Robertson and H.K. Birnbaum, *Scripta Met.*, **18**, (1984), 269-274.
110. S. Majumdar and R. Kwasny, *NASA CR 175057*, "Effects of a High Mean Stress on the HCF Life of PWA 1480 and Correlation of Data by LEFM," 1985.

111. T.P. Gabb and G.E. Welsch, *Scripta Met.*, **20**, (1986), 1049-1054.
112. J. Gayda, T.P. Gabb and R.L. Dreschfield, *Hydrogen Effects on Material Behavior*, eds. N.R. Moody and A.W. Thompson, TMS-AIME, 1989, to be published.
113. D.P. Deluca, J.R. Warren, B.A. Cowles and M.C. VanWanderham, *NASA FR 14844*, "Mechanical Properties of Turbine Blade Alloys in Hydrogen at Elevated Temperatures," 1981.
114. D.P. Deluca and B.A. Cowles, *AFWAL-TR-84-4167*, "Fatigue and Fracture of Advanced Blade Materials," 1985.
115. B.A. Cowles, D.P. Deluca, J.R. Warren and F.K. Haake, *NASA CP 2437*, "Advanced Earth-to-Orbit Propulsion Technology Conference," 1986, 727-748.
116. M.G. Hebsur and R.V. Miner, *NASA TM 88950*, "Elevated Temperature Tension, Compression and Creep-Rupture Behavior of [001] Oriented Single Crystal Superalloy PWA 1480," 1987.
117. T. Khan, P. Caron and Y.G. Nakagawa, *J. Metals*, **July, 1986**, 16-19.
118. N.L. Weeks and J. Mucci, *NASA FR 19269*, "Mechanical Properties of Various Alloys in Hydrogen," 1986.
119. W.W. Milligan, *NASA CR 175100*, "Yielding and Deformation Behavior of the Single Crystal Nickel-Base Superalloy PWA 1480," 1986.
120. R.L. Dreschfield and R.A. Parr, *NASA TM 89877*, "Application of Single Crystal Superalloys for Earth-to-Orbit Propulsion Systems," 1987.
121. R.J. Walter, J.D. Frandsen and R.P. Jewett, *Hydrogen Effects in Metals*, eds. I.M. Bernstein and A.W. Thompson, AIME, 1980, 819-827.
122. R.R. Bowman, M.S. Thesis, Georgia Inst. of Tech., 1986.
123. W.W. Milligan and S.D. Antolovich, *Met. Trans.*, **20A**, (1989), 1888-1889.
124. C. Lall, S. Chin and D.P. Pope, *Met. Trans.*, (1979), 1323-1332.
125. B.H. Kear and H.G.F. Wilsdorf, *Trans. TMS-AIME*, **224**, (1962), 382-386.
126. C.D. Beachem, *Met. Trans.*, **3**, (1972), 437-451.
127. H.K. Birnbaum, *Int'l. Conf. on Environment-Induced Cracking of Metals*, ASM, 1988, to be published.
128. D.G. Westlake, *Trans. A.S.M.*, **62**, (1969), 1000.
129. B.A. Wilcox and G.C. Smith, *Acta Met.*, **12**, (1964), 371.
130. E.A. Steigerwald, F.W. Schaller and A.R. Troiano, *Trans. TMS-AIME*, **218**, (1960), 832.
131. R.A. Oriani and P.H. Josephic, *Acta Met.*, **22**, (1974), 1065-1074.

132. G.M. Pressouyre, *Acta Met.*, **28**, (1980), 895-911.
133. J.K. Tien, R.J. Richards, O. Buck and H.L. Marcus, *Scripta Met.*, **9**, (1975), 1097-1101.
134. G.M. Pressouyre, Ph.D. Thesis, Carnegie Mellon University, 1977.
135. J.Y. Lee and S.M. Lee, *Hydrogen Effects on Material Behavior*, eds. N.R. Moody and A.W. Thompson, TMS-AIME, 1989, to be published.
136. G.J. Thomas, *Hydrogen Effects in Metals*, eds. I.M. Bernstein and A.W. Thompson, TMS-AIME, 1980, 77-85.
137. W.M. Robertson, *Z. Metallkd.*, **64**, (1973), 436-443.
138. M.D. Danford, *NASA TP 2744*, "Hydrogen Trapping and the Interaction of Hydrogen with Metals," 1987.
139. J. Volkl and G. Alefeld, *Diffusion in Solids*, eds. A.A. Nowick and J.J. Burton, Academic Press, New York, NY, 1975, 232-295.
140. W.M. Robertson, *Met. Trans.*, **8A**, (1977), 1709-1712.
141. J.P. Hirth, *Met. Trans.*, **11A**, (1980), 861-890.
142. T. Tabata and H.K. Birnbaum, *Scripta Met.*, **18**, (1984), 231-236.
143. J. Eastman, et al., *Hydrogen Effects in Metals*, eds. I.M. Bernstein and A.W. Thompson, TMS-AIME, 1980, 397-409.
144. I.M. Robertson and H.K. Birnbaum, unpublished research.
145. D.S. Shih, I.M. Robertson and H.K. Birnbaum, *Acta Met.*, **36**, (1988), 111-124.
146. G.M. Bond, I.M. Robertson and H.K. Birnbaum, *Acta Met.*, **36**, (1988), 2193-2197.
147. G.M. Bond, I.M. Robertson and H.K. Birnbaum, *Acta Met.*, **35**, (1987), 2289-2296.
148. G. Hong and J. Lee, *Acta Met.*, **32**, (1984), 1581-1589.
149. J. Eastman, F. Heubaum, T. Matsumoto and H.K. Birnbaum, *Acta Met.*, **30**, (1982), 1579-1586.
150. J.E. Costa and A.W. Thompson, *Met. Trans.*, **13A**, (1982), 1315-1318.
151. W.J. Mills, *Eng. Frac. Mech.*, **26**, (1987), 223-238.
152. N.R. Moody, R.E. Stoltz and M.W. Perra, *Met. Trans.*, **18A**, (1987), 1469-1482.
153. S.L. Robinson and N.R. Moody, *J. Nucl. Mat.*, **140**, (1986), 245-251.

154. W.J. Mills, *J. Eng. Mat. Tech.*, **100**, (1978), 195-199.
155. J.A. Harris, Jr. and M.C. VanWanderham, *Pratt and Whitney FR 5768*, "Properties of Materials in High Pressure Hydrogen at Cryogenic, Room and Elevated Temperatures," 1983.
156. R.J. Walter and W.T. Chandler, *Env. Deg. of Eng. Mat.*, eds. M.R. Louthan, Jr. and R.P. McNitt, Virginia Polytechnic Inst., 1977, 513-522.
157. W.W. Milligan, E.S. Huron and S.D. Antolovich, *Fatigue 1987*, eds. E.A. Starke, Jr. and R.O. Ritchie, Eng. Mat. Advisory Board, 1987, 134-171.
158. R.C. Bates, *Metallurgical Treatises*, eds. J.K. Tien and J.F. Elliot, TMS-AIME, 1982, 551-570.
159. J.R. Rice and M.A. Johnson, *Inelastic Behavior of Solids*, eds. M.F. Kanninen, et al., McGraw Hill, New York, 1970, 641-672.
160. G.T. Hahn, M.F. Kanninen and A.R. Rosenfield, *Annual Rev. Mat. Sci.*, **2**, (1972), 372-404.
161. R.K. Pandey and S. Banerjee, *Eng. Fract. Mech.*, **10**, (1978), 817-829.
162. R.O. Ritchie, W.L. Server and R.A. Wullaert, *Met. Trans.*, **10A**, (1979), 1557-1570.
163. J.W. Hancock and D.K. Brown, *J. Mech. Phys. Solids*, **31**, (1983), 1-24.
164. W.M. Garrison, Jr., *Scripta Met.*, **18**, (1984), 583-586.
165. J.R. Rice and D.M. Tracey, *J. Mech. Phys. Solids*, **17**, (1969), 201-217.
166. E.E. Underwood, "*Quantitative Stereology*," Addison-Wesley Publishing Company, Reading, Mass., 1970, pp. 23-44, 80-108.
167. W.M. Garrison, Jr. and N.R. Moody, *J. Phys. Chem. Solids*, **48**, (1987), 1035-1074.
168. A.W. Thompson and M.F. Ashby, *Scripta Met.*, **18**, (1984), 127-130.
169. K.J. Handerhan, Ph.D. Thesis, Carnegie Mellon University, 1987.
170. *ASTM E399-83*, "1983 Annual Book of ASTM Standards", ASTM, Philadelphia, 1983, 518-553.
171. *ASTM E813-87*, "1987 Annual Book of ASTM Standards", ASTM, Philadelphia, 1987, 686-700.
172. J.A. Bailey and P.B. Hirsch, *Phil. Mag.*, **5**, (1960), 485-497.
173. P.B. Hirsch, et al., "*Electron Microscopy of Thin Crystals*," Krieger Publ. Co., Malabar, Florida, 1977, 418-424.

174. W.A. McInteer, A.W. Thompson and I.M. Bernstein, *Acta Met.*, **28**, (1980), 887-894.
175. C.S. Barrett and T.B. Massalski, "*Structure of Metals, 3rd ed.*," McGraw Hill, New York, NY, 1966, pp. 30-50.
176. S.P. Lynch, *Acta Met.*, **29**, (1981), 325-340.
177. S.P. Lynch, *Scripta Met.*, **20**, (1986), 1067-1072.
178. J.A. Wert and W.M. Robertson, *Metallography*, **15**, (1982), 367-381.
179. J.C. Chesnutt and R.A. Spurling, *Met. Trans.*, **8A**, (1977), 216-218.
180. P.G. Shewmon, "*Diffusion in Solids*," J. Williams Book Co., Jenks, Okla., 1983, pp. 6-19.
181. D. Broek, "*Elementary Engineering Fracture Mechanics, 3rd ed.*," Martinus Nijhoff Publishers, The Hague, 1984, p. 136.
182. J.W. Edington, "*Practical Electron Microscopy in Materials Science*," Van Nostrand Reinhold Co., New York, 1976, pp. 118-149.
183. J.C. Williams, A.W. Thompson and R.G. Baggerly, *Scripta Met.*, **8**, (1974), 625-630.
184. R.W. Hertzberg, "*Deformation and Fracture Mechanics of Engineering Materials*," Wiley and Sons, New York, 1989, pp. 291-296.
185. J.K. Tien, S.V. Nair and R.R. Jensen, *Hydrogen in Metals*, eds. I.M. Bernstein and A.W. Thompson, TMS-AIME, 1980, 37-56.
186. F. Heubaum and H.K. Birnbaum, *ONR Tech. Report USN 00014-75-C-1012*, "The Effect of Hydrogen on the Fracture and Slip Behavior of Nickel," 1981.
187. I.M. Bernstein, et al., *NASA CP 2437*, "Advanced Earth-to-Orbit Propulsion Technology," 1986, 698-714.
188. P. Tison, *C.E.A. Report r5240*, France, 1984.
189. M.I. Baskes and C.F. Melius, *Z. Phys. Chem. Neue Folge*, **116**, (1979), 289-299.
190. S.M. Copley, B.H. Kear and G.M. Rowe, *Mat. Sci. and Eng.*, **10**, (1972), 87-91.
191. R.A. Oriani and P.H. Josephic, *Acta Met.*, **25**, (1977), 979-988.
192. M. Dollar, Carnegie Mellon University, unpublished research.
193. G.R. Leverant and B.H. Kear, *Met. Trans.*, **1**, (1970), 491-498.
194. D.L. Anton and A.F. Giamei, *AFOSR-TR-86-0821*, "Plastic Strain Localization in Superalloy Single Crystals," 1986.
195. R.E. Stoltz and A.G. Pineau, *Mat. Sci. and Eng.*, **34**, (1978), 275-284.

196. H.F. Merrick, *Met. Trans.*, **5**, (1974), 891-897.
197. S.T. Bhat and C. Laird, *Acta Met.*, **27**, (1979), 1873-1883.
198. E. Hornbogen and K.Z. Gahr, *Metallography*, **8**, (1975), 181-202.
199. A. Kelly and R.B. Nicholson, *Prog. Mat. Sci.*, **10**, (1963), 149-391.
200. J.T.M. deHosson, *Mat. Sci. Eng.*, **81**, (1986), 515-523.
201. P.H. Thornton, R.G. Davies and T.L. Johnston, *Met. Trans.*, **1**, (1970), 207-218.
202. D.M. Dimiduk, Ph.D. Thesis, Carnegie Mellon University, 1989.
203. P. Veyssi re, J. Douin and P. Beauchamp, *Phil. Mag. A*, **51**, (1985), 469-483.
204. M. Gell and G.R. Leverant, *Trans. AIME*, **242**, (1968), 1869-1879.
205. T.M. Pollock and A.S. Argon, *Superalloys 1988*, eds. D.N. Duhl, et al., TMS-AIME, 1988, 285-294.
206. T.S. Cook, C.A. Rau and E. Smith, *Trans. ASME: J. of Eng. Materials and Tech.*, April 1976, 180-189.
207. J.P. Tanaka, C.A. Pampillo and J.R. Low, *ASTM STP 463*, 1970, 191-215.
208. J.J. Gilman, "*Fracture*," Wiley, New York, 1959, 193-222.
209. A.H. Cottrell, *Trans. TMS-AIME*, **211**, (1958), 192-203.
210. A.N. Stroh, *Adv. in Physics*, **6**, (1957), 418-465.
211. A.H. Windle and G.C. Smith, *J. Metals Sci.*, **2**, (1968), 187-191.
212. R.W. Hertzberg, "*Deformation and Fracture Mechanics of Engineering Materials*," Wiley and Sons, New York, 1989, p. 320.
213. N.E. Dowling and J.A. Begley, *ASTM STP 590*, "*Mechanics of Crack Growth*", 1976, 82-103.
214. J.W. Hutchinson and P.C. Paris, *ASTM STP 668*, 1979, 37-50.
215. W.M. Garrison, *Met. Trans.*, **17A**, (1986), 669-678.
216. S. Lee, L. Majno and R.J. Asaro, *Met. Trans.*, **16A**, (1985), 1633-1648.
217. R.E. Stoltz, N.R. Moody and M.W. Perra, *Met. Trans.*, **14A**, (1983), 1528-1531.

APPENDIX A

METALLOGRAPHY DATA AND TENSILE PROPERTIES

This appendix contains all of the metallography data and tensile property tables. The corresponding table of the average values in the main text will be given in italics. All samples are referred to by their slab number with T denoting transverse orientation. Standard deviations are given with the average values.

Table A.1 (4.1). Quantitative metallography results of unHIP'ed samples given the normal heat treatment. [001] and transverse orientation results shown.

Slab	Pores				Eutectic γ/γ			
	Average Size (μm)	Volume Fraction	Δ_3 (μm)	Aspect Ratio	Average Size (μm)	Volume Fraction	Δ_3 (μm)	Aspect Ratio
16	14.5	0.89	175.5	1.20	33.2	5.98	63.6	2.34
41	15.6	0.76	166.0	1.13	32.0	6.85	60.9	2.07
131	18.0	0.83	170.4	1.07	35.8	5.77	72.0	2.15
134	12.9	1.08	165.2	--	--	5.68	73.2	--
28	18.9	1.20	183.4	--	--	4.29	90.4	--
119	11.0	0.76	143.2	--	--	5.31	72.4	--
114	13.1	1.25	137.9	--	--	5.05	78.4	--
32	13.0	1.01	175.6	--	--	4.54	77.3	--
60	14.1	1.38	150.8	--	--	6.91	58.6	--
179	15.9	0.93	188.7	--	29.8	5.07	--	--
183	12.3	1.07	158.3	--	32.5	5.24	--	--

Table A.1 (4.1) Continued.

Slab	Pores				Eutectic γ/γ			
	Average Size (μm)	Volume Fraction	Δ_3 (μm)	Aspect Ratio	Average Size (μm)	Volume Fraction	Δ_3 (μm)	Aspect Ratio
16T	17.1	1.00	139.7	1.10	23.2	5.56	67.3	--
41T	10.2	0.93	143.7	1.18	28.6	7.01	57.5	2.07
131T	17.4	1.06	165.7	1.15	29.6	5.34	78.6	2.11
134T	15.0	1.18	160.9	1.06	28.0	5.68	65.6	--
[001]	14.6 +/- 2.4	1.02 +/- 0.20	165.0 +/- 16.2	1.13 +/- 0.07	32.7 +/- 2.2	5.60 +/- 0.84	71.9 +/- 9.9	2.19 +/- 0.14
Trans.	14.9 +/- 3.3	1.04 +/- 0.10	152.5 +/- 12.7	1.12 +/- 0.05	27.4 +/- 2.8	5.90 +/- 0.75	67.3 +/- 8.7	2.09 +/- 0.03

Table A.2 (4.2). Quantitative metallography results of material received from Rocketdyne.

Bar	Pores			Eutectic γ/γ		
	Average Size (μm)	Volume Fraction (%)	Δ_3 (μm)	Average Size (μm)	Volume Fraction (%)	Δ_3 (μm)
RR 1	10.8	0.22	224.3	25.6	2.19	154.3
RR 2	8.6	0.28	204.6	24.0	1.76	158.0
RR 3	7.9	0.20	230.1	28.1	2.31	140.5
Avg.	9.1 +/- 1.5	0.23 +/- 0.04	219.7 +/- 13.4	25.9 +/- 2.1	2.09 +/- 0.29	150.9 +/- 9.2

Table A.3 (4.5) Quantitative metallography for HIP'ed samples.

Sample	Pores			Eutectic γ/γ		
	Average Size (μm)	Volume Fraction (%)	Δ_3 (μm)	Average Size (μm)	Volume Fraction (%)	Δ_3 (μm)
32 H1	7.1	0.50	200.8	23.8	2.70	103.5
134 H1	9.5	0.63	217.6	18.6	3.28	96.7
131 H1	8.3	0.57	201.2	17.2	3.13	105.2
Avg. H1	8.3 +/- 1.2	0.57 +/- 0.07	206.5 +/- 9.6	19.9 +/- 3.5	3.04 +/- 0.30	101.8 +/- 4.5
Avg. no H1	14.6	0.97	174.8	33.7	5.33	78.0
179 H2	5.1	0.05	389.5	18.1	1.70	138.9
183 H2	3.5	0.02	407.3	13.4	1.15	155.8
Avg. H2	4.3 +/- 1.1	0.035 +/- 0.021	398.4 +/- 12.6	15.8 +/- 3.3	1.43 +/- 0.39	147.4 +/- 11.9
Avg. no H2	14.1	1.00	173.5	31.2	5.16	71.9

Table A.4 (4.7) Room temperature tensile test results for samples that were unHIPed, uncharged and given the normal heat treatment.

Sample	0.2% Y.S. (MPa)	U.T.S. (MPa)	ϵ_f (%)	R.A. (%)
179 #1	1089	1142	3.1	--
179 #2	1001	1120	4.0	--
177 #1	1109	1115	2.3	2.1
177 #2	1115	1115	1.7	1.4
80 #1	1055	1118	4.4	4.0
80 #2	1112	1174	2.8	3.5
134 #1	1068	1068	6.9	7.5
134 #2	1099	1211	5.0	5.3
134 #3	1041	1041	9.2	--
134 #4	1079	1079	6.0	--
41 #1	1168	1182	2.7	--
41 #2	1150	1156	3.5	--
16 #1	1132	1146	4.2	--
16 #2	1138	1232	4.5	--
RR #1	1119	1146	4.2	4.3
RR #2	1156	1156	2.9	3.1
Avg.	1101 +/- 45.0	1137 +/- 50.2	4.21 +/- 1.89	3.90 +/- 2.22
Avg. w/o 134	1112 +/- 46.5	1153 +/- 34.2	3.36 +/- 0.91	3.07 +/- 1.21

* The average without slab 134 was reported in the main text because slab 134 was 7° off [001], and therefore it is believed that the tensile properties are not representative.

Table A.5 (4.8) Room temperature tensile test results for samples that were unHIP'ed, charged and given the normal heat treatment.

Sample	0.2 % Y.S. (MPa)	U.T.S. (MPa)	ϵ_f (%)	R.A. (%)
179 #1H	919	955	0.38	2.7
179 #2H	950	988	0.33	2.7
134 #1H	1064	1064	0.32	3.5
134 #2H	1012	1012	0.32	3.2
41 #1H	1083	1083	0.20	2.4
41 #2H	1079	1089	0.25	2.6
RR #1H	925	925	0.10	1.1
RR #1H	974	974	0.15	1.3
Avg.	1001 +/- 68.4	1011 +/- 61.5	0.26 +/- 0.09	2.40 +/- 0.84

APPENDIX B

DEFORMATION AND FRACTURE BEHAVIOR OF $\langle 130 \rangle$ SAMPLES

Tensile tests were performed to determine the effect of hydrogen on the deformation and fracture behavior of samples oriented for single slip, in contrast to the $[001]$ samples that undergo multiple slip. All experimental procedures were the same as for $[001]$ samples described in section 3.3.1. Single slip oriented samples were obtained by machining slabs perpendicular to the $[001]$ crystal growth axis, as shown in Figure B.1a. These transverse oriented samples were all taken from the same single crystal slab and were 2° off $\langle 130 \rangle$, as determined by the Laue back reflection technique and shown in Figure B.1b.

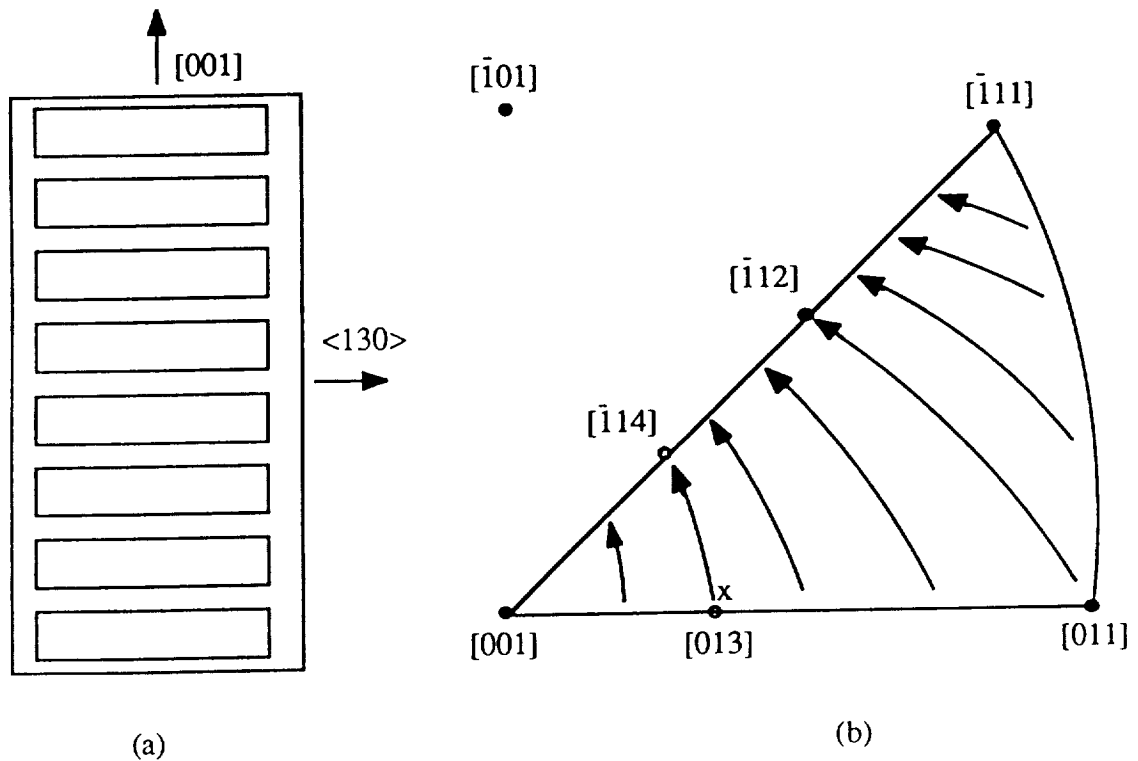


Figure B.1 (a) Orientation of $\langle 130 \rangle$ tensile samples relative to $[001]$ single crystal slab. (b) Equivalent orientation in stereographic triangle at point x.

The average tensile properties as a function of hydrogen are shown in Table B.1, and a typical stress-strain curve is shown in Figure B.2. Comparative tensile properties and stress-strain curves for [001] oriented samples are also shown in Table B.1 and Figure B.2, respectively. These tensile properties are consistent with other investigations that have studied the effect of orientation on PWA 1480 and found a lower yield strength for single slip orientations.^{1,2} It is believed that this is purely an orientation effect since the CRSS for both the [001] and <130> oriented samples is close to 450 MPa. The tensile stress-strain behavior for the two orientations is qualitatively similar, and this can be related to the single slip behavior that the [001] orientation exhibits at low strains, as discussed in section 5.3. In the [001] orientation, deformation initiates and proceeds in narrow bands of single slip until these bands harden either by multiple slip initiation or debris hardening. Similarly, the <130> orientation stress-strain behavior can be explained by initiation of single slip resulting in work softening. As the tensile axis rotates during deformation, a duplex slip orientation is reached around [114] in Figure B.1b, and the work hardening rate increases up to failure. Failed <130> samples were sectioned and examined on the TEM,

Table B.1 Tensile properties for the <130> and [001] orientations as a function of hydrogen.

	σ_{YS} (MPa)	σ_{UTS} (MPa)	ϵ_f (%)	R.A. (%)
[001] uncharged	1112	1153	3.4	3.1
[001] charged	1001	1011	0.3	2.4
<130> uncharged	929	929	24.3	25.3
<130> charged	906	906	6.9	21.2

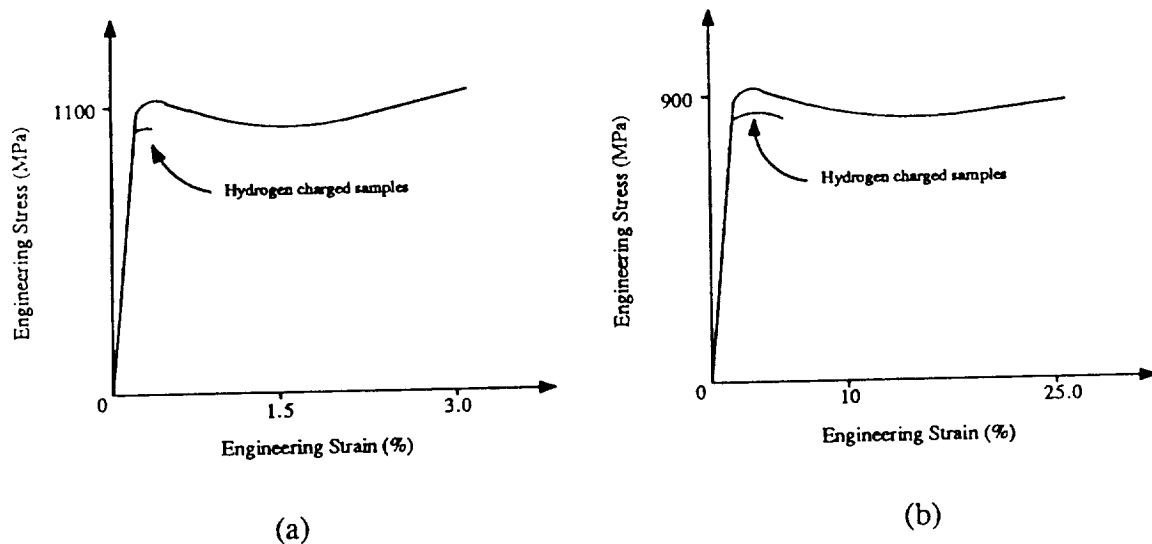


Figure B.2 Typical stress-strain curves for (a) $\langle 130 \rangle$ samples and (b) $[001]$ samples.

but the dislocation density was too high to determine the active slip systems. It was possible, however, to determine the final specimen orientation of $\langle 112 \rangle$, as predicted from typical fcc single crystal deformation.³ The rotation of the sample during deformation is supported by fractography observations, which showed that the initial circular cross-section had become oval, Figure B.3, as observed in other samples oriented for initial single slip.³

The fracture surface was macroscopically much flatter in the $\langle 130 \rangle$ samples, and fracture occurred primarily on a single $\{111\}$ plane, as opposed to multiple $\{111\}$ planes in $[001]$ samples. The microscopic ductile fracture of the γ/γ' microstructure was not affected by orientation, as seen by comparing Figures B.4 and 4.30b.

ORIGINAL PAGE
BLACK AND WHITE PHOTOGRAPH



Figure B.3 Oval cross-section of uncharged $\langle 130 \rangle$ tensile sample.

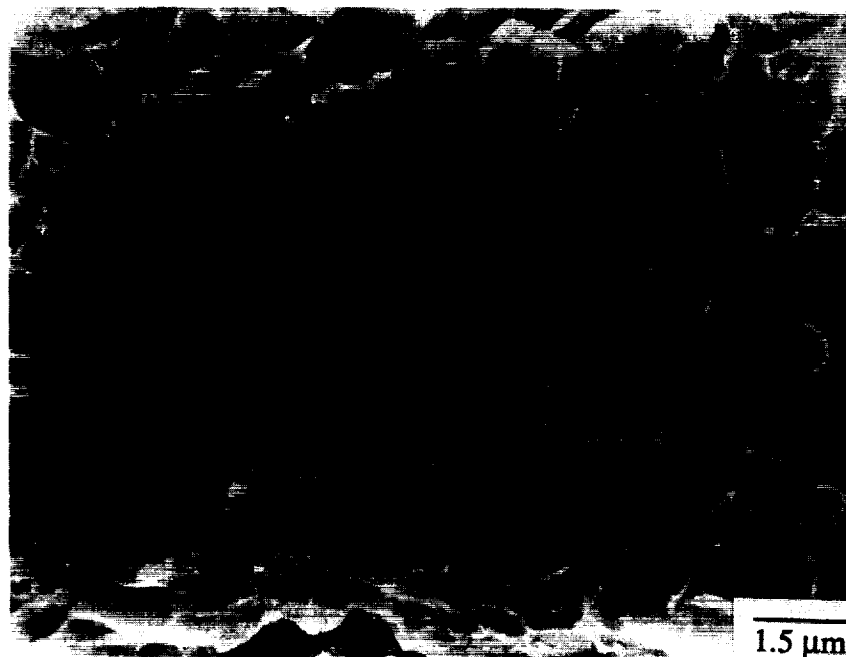


Figure B.4 Ductile fracture is not affected by orientation. Compare with Figure 4.30b.

A significant difference in the fracture behavior of the two orientations was that the eutectic γ/γ in the $\langle 130 \rangle$ oriented samples did not fail by crystallographic cleavage. Figure B.5 shows that the eutectic γ/γ failed in a more brittle manner than the surrounding γ/γ microstructure, but the characteristics of crystallographic cleavage are not present, such as river lines or a definitive fracture plane. It is possible that the $\{001\}$ cleavage plane of the eutectic γ/γ is not favorably oriented for cleavage in these samples. Assuming that the impingement of slip bands on the eutectic γ/γ initiates cleavage, it can be argued that the normal stress created by the slip bands is not as high on the $\{001\}$ cleavage plane in the $\langle 130 \rangle$ oriented samples, as in the $[001]$ samples.

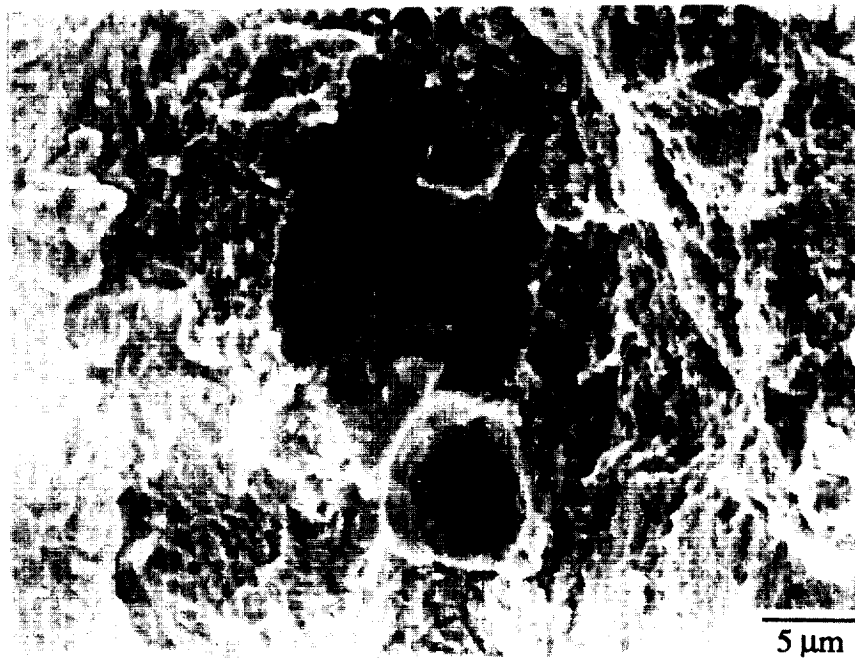


Figure B.5 Brittle fracture of eutectic γ/γ in $\langle 130 \rangle$ oriented samples.

The effect of hydrogen on the tensile behavior of the $\langle 130 \rangle$ samples was similar, but more pronounced, compared to the $[001]$ samples. For instance, the strain to failure was greatly reduced with little change in the R.A., as previously observed, but the magnitude of the values was much larger in the $\langle 130 \rangle$ samples. This provides assurance

that this effect was not merely an artifact of experimental error in the [001] samples and gives further support to the idea that hydrogen localized the plastic flow in tensile samples. Previously, it was shown that hydrogen promoted cleavage of the eutectic γ/γ' , and there was evidence in the fractography of these samples that hydrogen embrittles this constituent. The type of fracture shown in Figure B.5 was observed to a much greater extent in hydrogen-charged samples. This may be because the fracture has a more brittle appearance in charged samples and was easier to observe, rather than an actual increase in the area fraction of eutectic γ/γ' on the fracture surface, as in the [001] samples. As in the [001] samples, the presence of hydrogen did not change the microscopic ductile fracture process.

References

1. D.M. Shah and D.N. Duhl, *Superalloys 1984*, eds. M. Gell, et al., TMS-AIME, 1984, 105-114.
2. T.G. Gabb, *NASA TM 100269*, "The Cyclic Stress-Strain Behavior of a Single Crystal Nickel-Base Superalloy," 1988.
3. R.W.K. Honeycombe, *The Plastic Deformation of Metals, 2nd ed.*, Edward Arnold Publ., London, 1984, pp. 10-32.

APPENDIX C

SHORT ROD K_{IC} TESTING

C.1 Background

There are a growing number of researchers studying various smaller, alternative fracture toughness specimens in order to make the determination of K_{IC} a simpler, more economical exercise. The size of the current K_{IC} specimens has always been a drawback, as well as the tedious testing method, especially fatigue pre-cracking. J_{IC} testing offers a smaller specimen size, but the testing procedure is even more complicated. The most common alternative candidate to replace the current specimens is the short rod or short bar specimen. To add to the knowledge base in this field, these specimens will be used to measure the fracture toughness of PWA 1480 and then compared to K_Q values and valid ASTM E 813-87¹ J_{IC} values. This work primarily will be done by Jim Lucas at Sandia National Labs in Livermore, Calif. This literature review will examine the motivation and background behind these alternative specimens, and then look at experimental studies that have compared the K_{IC} values obtained in short rod specimens to valid ASTM values.

L.M. Barker is one of the leading proponents of short rod or short bar specimens and has written many articles on the theory and testing methods involved.²⁻⁴ A drawing of a short rod specimen is shown in Figure C.1. One of the primary advantages of this design is that fatigue pre-cracking is not necessary because of the chevron notch design, which allows initially stable crack growth. When considering the use of small specimens to measure plane strain fracture toughness, there are two problems that must be overcome.² First, the condition of plane strain along a vast majority of the crack must be maintained. This problem is overcome by the chevron notch design, which forces the crack tip to be well-constrained. The second dilemma is that the material response changes from an elastic nature to an elastic-plastic one.

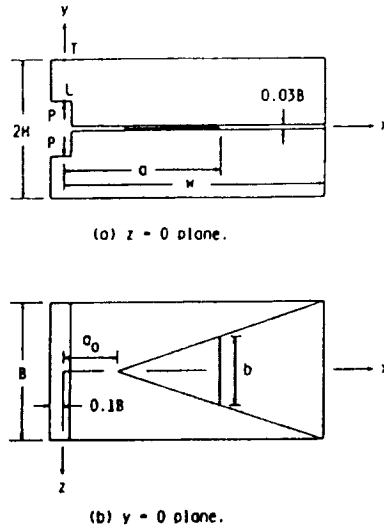


Figure C.1 Knife-edge loaded chevron notched short rod specimen.⁵

Barker's rederivation of the compliance equation to include plasticity will now be considered.² The short rod testing method provides a measure of the amount of energy per unit crack area that is required to advance a steady state crack under plane strain conditions. At first it appears that this definition violates the premise upon which K_{IC} or J_{IC} is calculated; that is measuring initial crack growth, and not steady state crack growth. However, Barker² goes through a lengthy argument stating that K_{IC} and J_{IC} testing is actually measuring steady state crack growth. Accepting this, now consider the effect of plasticity on the specimen behavior. First, the stress intensity parameter must be derived for the short rod geometry:²

$$K_{IC} = \frac{P_{max}}{B^{3/2}(1 - \nu^2)^{1/2}} f(a/b) \quad (C-1)$$

where P is the maximum load applied, B is the specimen thickness and $f(a/b)$ can be replaced by a constant for each specimen geometry. There are other expressions used in the literature that are very similar,^{6,7} but equation C-1 is generally accepted. There also is some debate over the correct value of $f(a/b)$, but after a comprehensive review, Newman⁷

gives the currently accepted values for many specimen geometries. To correct for the plasticity, Barker² uses a parameter, p , which can be calculated from the load-displacement chart upon unloading and reloading the specimen during the test. The modified K_{IC} equation becomes:²

$$K_{IC} = \left(\frac{1+p}{1-p} \right)^{1/2} K_Q \quad (C-2)$$

where K_Q is the previously calculated K_{IC} (C-1) from LEFM principles.

An important point to note is that the load used to calculate K_{IC} in (C-1) and (C-2) is the maximum load, as seen in Figure C.2.⁷ The dashed lines represent the stress intensity factors as a function of crack growth at various applied loads. The fact that they drop and form a minimum with increasing crack growth is important. Figure C.3 shows that the stress intensity for the short rod specimen (solid line) is very large when $a=a_0$.⁷ When the crack begins to grow, the stress intensity drops rapidly and reaches a minimum between a_0 and a_1 . This minimum, a_c , is constant for a given specimen geometry. As the crack reaches a_1 , the stress intensity rises and meets that for a normal through cracked specimen (dashed line). Looking again at Figure C.2, it is seen that a small load, P_1 , can initiate a crack. This crack grows until it intersects the "ideal" crack growth resistance curve (solid line) at point A. This solid line represents the curve for brittle materials. The load must now be increased to get crack growth to points B and C. When the maximum load is reached the crack driving force curve is tangent to the crack resistance curve at point D. Thus, the K value obtained is K_{IC} and the only load of concern is P_{max} .

Many researchers have performed tests on short rod samples analyzing the effect of specimen size, equation parameters and plasticity.^{4,6,8-12} It seems that specimen thickness may be as small as $1.25(K_{IC}/\sigma_{ys})^2$, although this is still being studied.⁴ The other

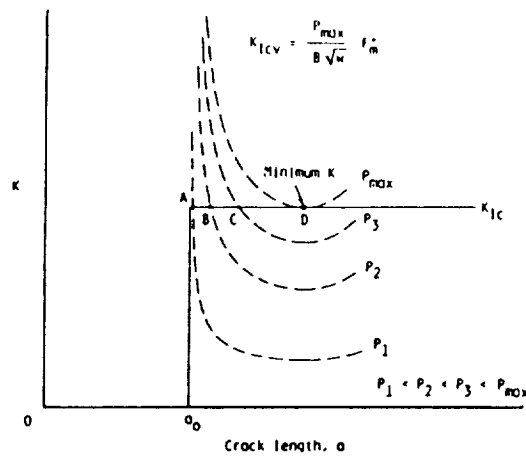


Figure C.2 Stress intensity vs. crack length.⁷

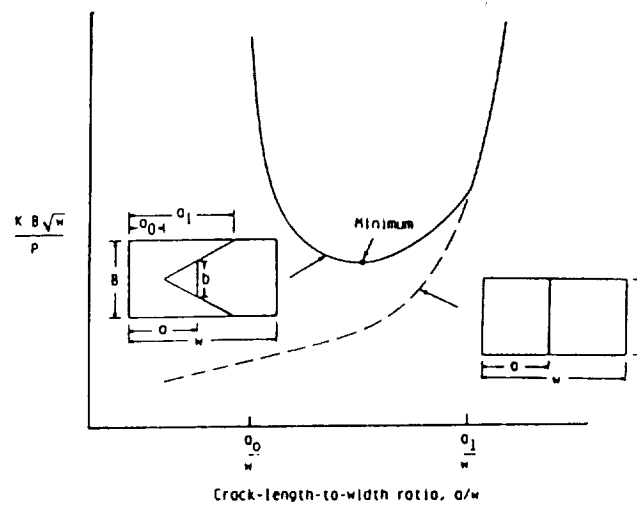


Figure C.3 Comparison of normalized stress-intensity factors for chevron-notch and straight-edge, through-cracked specimens.⁷

specimen dimensions are scaled with the thickness and initial crack length, as in normal fracture toughness testing, but standard ratios have yet to be established. As previously mentioned, Newman has compiled the data on various equation parameters and recommended the best values.⁷

In comparing short rod K_{IC} values to ASTM E 399-83¹³ K_{IC} values, there are many instances where comparative values are well within 10% of each other for a wide variety of materials, such as high Cr cast irons,⁶ various Al alloys^{2,8} and Ti-6Al-4V.⁴ However, in high toughness materials, excessive plasticity is a problem, and the comparison becomes somewhat worse.⁷⁻¹⁰ Many of these materials have rising resistance curves, which causes the estimate of K_{IC} to be too high, as seen in Figure C.4.⁷ The minimum stress intensity curve for P_{max} no longer intersects the resistance curve at a tangent, as in Figure C.2. This leads to overestimation of K_{IC} , as well as a new specimen width effect.

ORIGINAL PAGE IS
OF POOR QUALITY

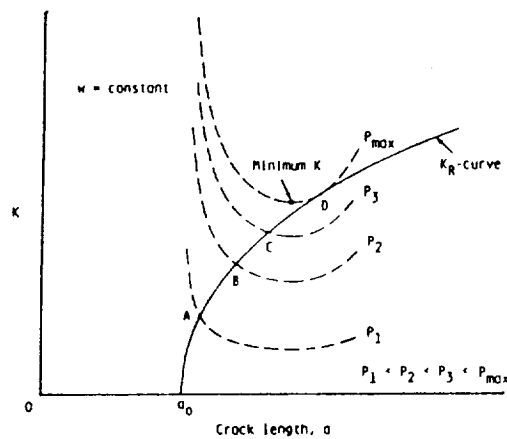


Figure C.4 Fracture of "rising resistance curve" material using a chevron-notched specimen.⁷

The problem of the rising resistance curve for some materials is one of the major drawbacks still associated with the short rod test. It seems that this method works well for relatively brittle materials, but its future for highly ductile materials is still being researched.⁷ ASTM is currently reviewing standardization, and more research can only lead to more accurate K_{IC} values along with a better understanding of the phenomena involved. It is not obvious at this point whether the short bar testing method will provide valid K_{IC} values for PWA 1480, but that is not the only goal of this research. The object is

to understand and apply the test method, and examine the results in light of the current knowledge in the area.

C.2 Experimental Procedures

Chevron-notched, short rod fracture toughness specimens were tested as a function of microstructure and hydrogen at Sandia National Laboratories by Jim Lucas. Specimens were machined from fractured halves of K_Q and J_{IC} specimens in the geometry shown in Figure C.1. Because of the configuration of the chevron notch, no pre-cracking was necessary, and loading was accomplished by special knife-edge grips at point P in Figure C.1. Short rod specimens that were to contain hydrogen were machined from charged K_{IC} specimens, and subsequently re-charged in the manner given in section 3.1.5. This led to higher hydrogen concentrations in the short rod specimens than in the K_Q specimens. As a result, the toughness values did not agree well, and subsequent samples machined from charged J_{IC} samples were outgassed prior to machining into short rod samples. The K_{IC} values and the fractography of the short rod specimens were compared to full size K_Q and J_{IC} specimens.

C.3 Results and Discussion

The results of short rod K_{IC} tests compared to ASTM E 399-83 K_Q tests are shown in Table C.1 for two orientations. For uncharged specimens the agreement is very good, but the charged short rod values are consistently lower than the ASTM E 399-83 values. This is probably due to higher hydrogen concentrations in the short rod samples, as explained above. Short rod tests are currently underway on samples machined from broken [001] J_{IC} samples and will be performed as a function of porosity, eutectic γ/γ' and hydrogen.

Table C.1 Short Rod K_{IC} values as a function of orientation and hydrogen.

Orientation	Condition	ASTM E 399-83 K_Q	Short Rod K_{IC}
[001]	no hydrogen	122 MPa \sqrt{m}	121 MPa \sqrt{m}
[001]	with hydrogen	103	82
transverse <130>	no hydrogen	133	129
transverse <130>	with hydrogen	100	83

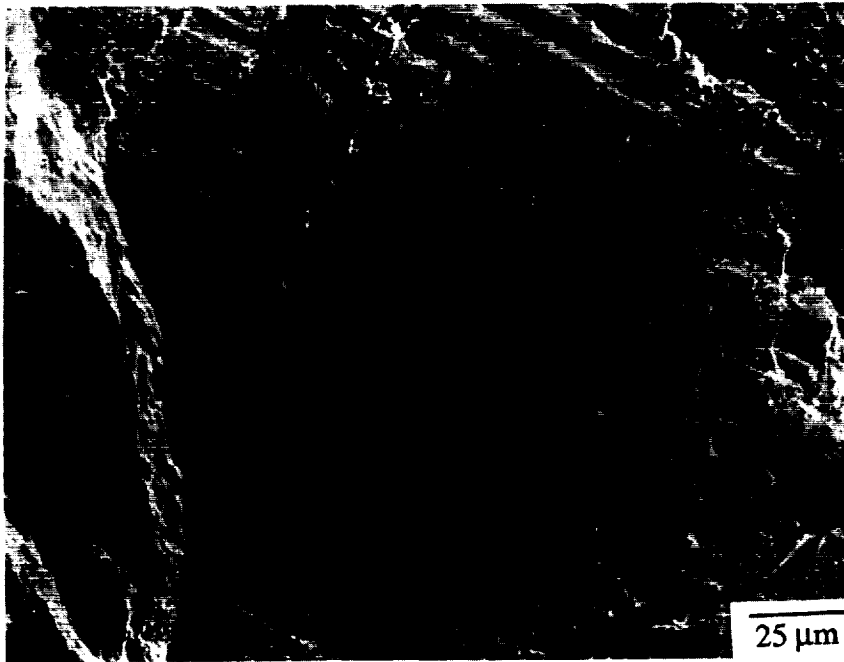
The close agreement in uncharged samples is further support for the short rod testing technique. It also shows that rising resistance curves are apparently not a problem in PWA 1480, and completed J_{IC} tests show that the resistance curve is not as steep as in Figure C.4. Based on this, the short rod toughness values obtained from the J_{IC} samples should correlate well. However, the discussion in section 5.6 concerning the discrepancy in J_{IC} versus K_{IC} values must be kept in mind. It is hoped that the results of the short rod tests will help in understanding these differences.

There were no differences in the short rod fractography compared to the full size K_Q fractography. The fracture occurred along {111} planes, and the roughness of the surface appeared similar to the full size K_Q samples. It will be interesting to see if the subsequent short rod tests show the same fractography differences that the full size K_Q and J_{IC} samples did. Like the tensile and full size K_Q samples, cleavage of the eutectic γ/γ' was seen in the [001] orientation but not in the transverse <130> orientation. It is believed that this is because the eutectic γ/γ' is no longer favorably oriented for cleavage along the {001} planes in the transverse oriented samples.

ORIGINAL PAGE
BLACK AND WHITE PHOTOGRAPH



(a)



(b)

Figure C.5 Fractography of short rod fracture toughness specimens at (a) low magnification and (b) a higher magnification.

References

1. ASTM E813-87, "1987 Annual Book of ASTM Standards", ASTM, Phila, Pa., 1987, pp. 686-700.
2. L.M. Barker, *Terra Tek Report RT 78-6R*, "Theory for Determining K_{IC} from Small, non-LEFM Specimens Supported by Experiments on Aluminum," 1978.
3. L.M. Barker, *Fracture Mechanics: 13th Conference, ASTM STP 743*, eds. R. Roberts, ASTM, 1981, 456-475.
4. L.M. Barker, *Chevron Notched Specimens, ASTM STP 855, Chevron-Notched Specimens: Testing and Stress Analysis*", eds. J.H. Underwood, S.W. Freiman and F.I. Baratta, ASTM, 1984, 117-133.
5. I.S. Raju and J.C. Newman, Jr., *ASTM STP 855, "Chevron-Notched Specimens: Testing and Stress Analysis"*, eds. J.H. Underwood, S.W. Freiman and F.I. Baratta, ASTM, Phila., Pa., 1984, pp. 32-48.
6. S.B. Biner, J.T. Barnby and D.W.J. Elwell, *Int. J. Frac.*, **26**, (1984), 3-16.
7. J.C. Newman, Jr., *Chevron Notch Specimens*, eds., J.H. Underwood, S.W. Freiman and F.I. Baratta, ASTM, Phila., 1984, 5-31.
8. K.R. Brown, *ASTM STP 855, "Chevron-Notched Specimens: Testing and Stress Analysis"*, eds. J.H. Underwood, S.W. Freiman and F.I. Baratta, ASTM, Philadelphia, 1984, 237-254.
9. J.L. Shannon, Jr. and D.G. Munz, *ASTM STP 855, "Chevron-Notched Specimens: Testing and Stress Analysis"*, eds. J.H. Underwood, S.W. Freiman and F.I. Baratta, ASTM, Philadelphia, 1984, 270-280.
10. J. Eschweiler and D. Munz, *Int. J. Frac.*, **20**, (1982), R131-R133.
11. R.T. Bubsey, D. Munz, W.S. Pierce and J. J.L. Shannon, *Int. J. Frac.*, **18**, (1982), 125-132.
12. J. Eschweiler, G. Marci and D.G. Munz, *ASTM STP 855, "Chevron-Notched Specimens: Testing and Stress Analysis"*, eds. J.H. Underwood, S.W. Freiman and F.I. Baratta, ASTM, Philadelphia, 1984, 255-269.
13. ASTM E399-83, "Annual Book of ASTM Standards", ASTM, Phila., Pa., 1983, pp. 518-553.

APPENDIX D

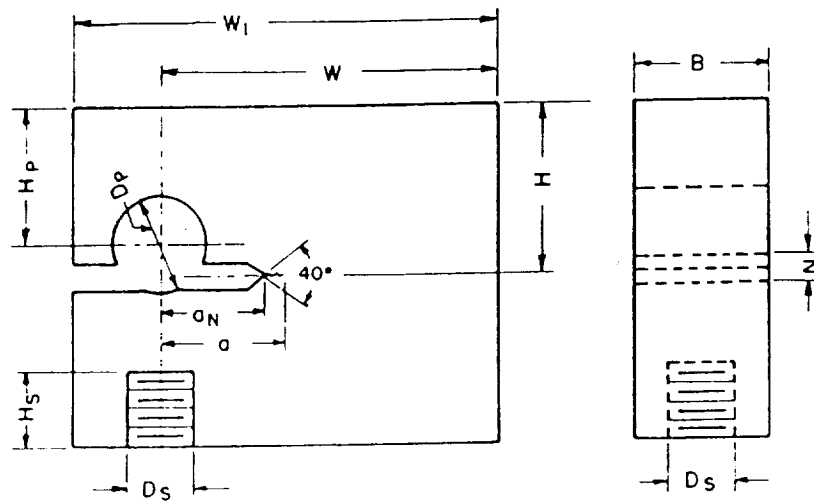
HYDROGEN-INDUCED CRACK GROWTH

D.1 Background

The determination of a material's susceptibility to sustained-load cracking in a hydrogen atmosphere is very important to design considerations. Through the use of wedge-opening-loading (WOL) specimens, it is possible to measure the stress intensity threshold (K_{TH} or K_{ISCC}) below which sub-critical cracks will not grow to a critical size in a hydrogen atmosphere.¹ Most investigations and modeling attempts have focused on crack growth in aqueous solutions and not gaseous hydrogen. However, the mechanisms of hydrogen-induced crack growth will be similar, because in both cases the presence of hydrogen at the crack tip will be the driving force for crack propagation. This section will first describe the type of specimen used in hydrogen-induced crack growth tests, along with the corresponding linear elastic fracture mechanics equations. Next, typical crack growth behavior is discussed and models that relate the stress intensity threshold to the microstructure and hydrogen concentration are covered. Finally, experiments performed on fcc alloys will be discussed in an attempt to better understand the behavior observed in PWA 1480 in this study.

The specimens typically used for hydrogen-induced crack growth are the modified WOL specimens suggested by Novak and Rolfe for environmental testing.¹ The specimen is self-stressed with a bolt, and there is constant displacement loading so that the initial K_I value decreases to a threshold value, K_{th} , as the crack propagates. Currently, there is no ASTM standard concerning WOL specimen dimensions or test procedures for determining crack growth threshold values, although standardization efforts are underway.² The

specimen dimensions proposed by Novak and Rolfe and commonly used for a one-inch thick specimen are shown in Figure D.1.



Geometry in inches:	$B = 1.00$	$W = 2.55$	$(H/W) = 0.486$
	$W_1 = 3.2$	$H_p = 1.00$	
	$D_s = 0.625$	$D_p = 0.70$	$(a/W) = 0.302$
	$a = 0.77$	$N = 0.094$	

Figure D.1 One-inch thick modified WOL specimen proposed by Novak and Rolfe.¹

Slight modifications can be made to the dimensions shown in Figure D.1; Hudak and Saxena³ have given compliance expressions for modified specimens. Stress intensity values can be calculated from:¹

$$K = \frac{PC_3(a/w)}{(BB_N)^{1/2} a^{1/2}} \quad (D-1)$$

where P is the load, $C_3(a/w)$ is a function of (a/w) , a is crack length, W is specimen depth, B is specimen thickness and B_N is specimen thickness with side grooves. $C_3(a/w)$ is analogous to $f(a/w)$ in ASTM E 399-83⁴ and is given by:¹

$$C_3(a/w) = [30.96(a/w) - 195.8(a/w)^2 + 730.6(a/w)^3 - 1186.3(a/w)^4 + 754.6(a/w)^5] \quad (D-2)$$

for samples with a height to depth ratio (H/W) of 0.486. The crack length can be independently determined from the compliance:³

$$C = \frac{BEV_{LL}}{P} = \frac{16}{[1 - (a/w)]^2} - \frac{24}{[1 - (a/w)]} - 4.5 \ln[1 - (a/w)] + 32.12 \quad (D-3)$$

where E is Young's modulus and V_{LL} is the displacement measured along the load line.

Crack growth specimens tested in a gaseous hydrogen atmosphere generally obey a three-stage crack growth rate versus stress intensity curve, as shown in Figure D.2. At low K values, the crack growth rate is dependent on the stress intensity, as well as temperature, pressure and environmental conditions. In stage II, da/dt is independent of K , and crack growth is associated with the diffusion of hydrogen through the lattice. The last stage occurs at K values approaching K_{IC} , where crack growth primarily is controlled by stress intensity effects.

Fatigue pre-cracked WOL specimens are loaded in a non-aggressive atmosphere to a stress intensity value ranging from 30% to 90% of the K_{IC} value.¹ The specimens are then immersed in the hydrogen atmosphere, and hydrogen-induced crack growth occurs causing both the stress intensity and crack growth rate to decrease. The stress intensity at which crack growth stops (K_{TH}) is considered a material property for the specimen conditions and hydrogen pressure used.⁶

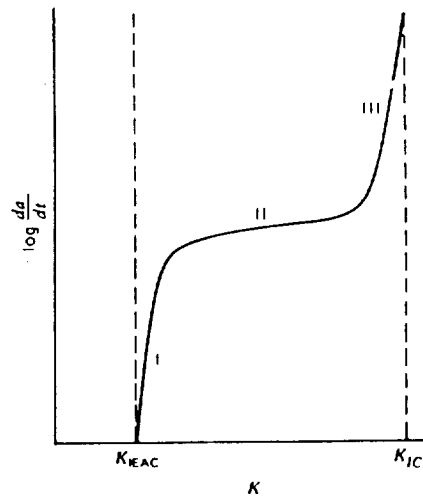


Figure D.2 Three stages of hydrogen-induced cracking under sustained load.⁵

There are several models that argue when a critical stress is exceeded ahead of the crack tip, fracture will occur.⁷⁻¹⁰ For samples tested in hydrogen, the stress ahead of the crack tip can lead to a higher local hydrogen concentration:¹¹

$$C_x = C_o \exp\left[\frac{\sigma_i V_H}{3RT}\right] \quad (D-4)$$

where C_o is the equilibrium concentration in the absence of stress, V_H is the partial molar volume of hydrogen, R is the gas constant and σ_i is the summation of the principal stresses such that $\sigma_i/3$ is the hydrostatic component of the applied stresses. The high concentration of hydrogen will lower the critical stress needed for fracture⁷⁻⁹ and can be illustrated by the simple relation:^{9,12}

$$\sigma^* = \sigma_o^* - AC_H \quad (D-5)$$

where A and σ_o^* are material dependent constants and C_H is the hydrogen concentration. Consequently, the material in hydrogen fractures at a lower critical stress and K_{TH} is much less than K_{IC} . In some cases a critical distance is introduced into the model such that the

critical stress must be exceeded over this distance.^{6,8,13,14} This relates K_{TH} to microstructural features, such as grain size or inclusion spacing.

The vast majority of hydrogen-induced crack growth studies have been performed on bcc ferrous alloys^{2,6,9} and little work has been done on fcc or nickel-base alloys.¹³⁻¹⁸ Table D.1 lists some results for two γ strengthened fcc superalloys (IN 903 and JBK 75) and a nickel-base superalloy (IN 718) tested in a gaseous hydrogen atmosphere. The results for IN 903 and IN 718 are especially applicable to this study since it was shown in section 5.1 that the diffusion constants for hydrogen in these materials closely matches that of hydrogen in PWA 1480. However, the microstructures are significantly different, and to the author's knowledge there have been no other studies on high volume fraction γ superalloys. The ratio of the fracture toughness in air (K_{IC}) to the threshold in hydrogen (K_{TH}) is typically about 3-5.5. The K_{TH} dependence on hydrogen pressure is illustrated in the IN 718 series B alloys in Table D.1. K_{TH} reaches a plateau value at a certain pressure, and this type of behavior also has been observed in IN 903.¹³

Table D.1 Available K_{TH} values of similar alloys.

Alloy	0.2% Y.S.	K_{IC}	K_{TH}	Pressure	Reference
IN 903	1080 MPa	90 MPa \sqrt{m}	30 MPa \sqrt{m}	207 MPa	19
JBK-75	924	—	65	207	18
IN 718 L	—	95	21	34.5	16
IN 718 A	1331	78	14	34.5	15, 17
IN 718 B1	1317	119	80	5	15, 17
IN 718 B2	1317	119	64	8	15, 17
IN 718 B3	1317	119	42	34.5	15, 17
IN 718 B4	1317	119	42	72	15, 17

D.2 Experimental Procedures

The dimensions for the WOL specimens used in hydrogen-induced crack growth tests are shown in Figure D.3. The important ratios for compliance calculations were preserved from Novak and Rolfe's original specimen dimension suggestions.¹ It was extremely difficult to tap this material, so electrodischarge machining (EDM) of the two holes was done. Specimen preparation was done at Carnegie Mellon and testing was done at Sandia National Labs by Neville Moody. This procedure has been developed extensively there, and Sandia possesses capabilities for testing in high-pressure hydrogen that are not available at Carnegie Mellon.

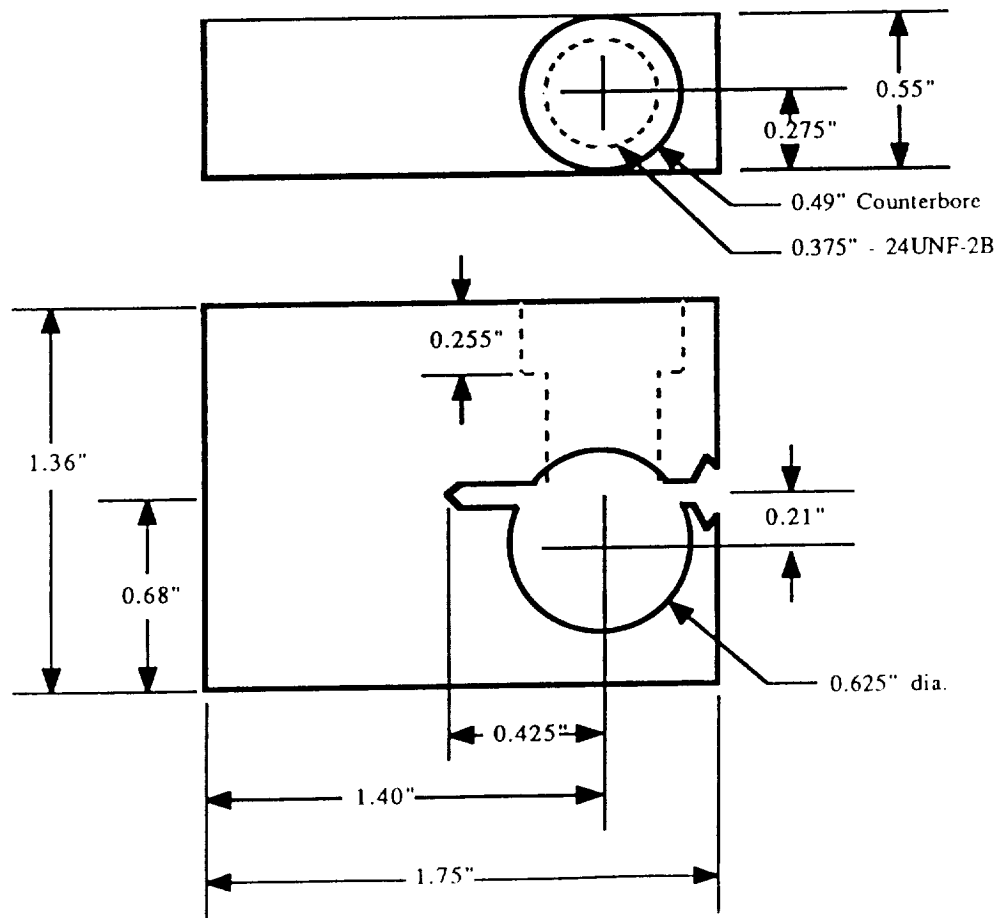


Figure D.3 Actual measurements of WOL specimens used.

The samples were fatigue pre-cracked, and subsequently a torque-wrench was used to apply a K_I value to the specimen via the bolt. Crack growth was monitored with a KRAK-GAGE™ mounted on the surface of each sample. All tests were performed at room temperature using A-286 stainless steel primary vessels that were stored within secondary safety vessels. The primary vessel could hold multiple specimens and was capable of withstanding hydrogen pressures of up to 200 MPa. Hydrogen dehumidification and purification was accomplished with a combination of sieve beds and cold traps, and a series of pressure-vacuum cycles was run to purge the gas lines of impurities. Each specimen was equipped with individually calibrated load cells similar to ones used by Loginow and Phelps.²⁰ The loaded samples were placed in the test cell, and the loads and crack lengths were continuously monitored. Average crack velocities as small as 10^{-11} m/sec could be resolved and crack arrest was defined as no detectable crack growth for four months. The threshold stress intensities were determined from the final load and crack length using the assumption of a rigid bolt and equations D-1 to D-3.

D.3 Results and Discussion

Based on the data in Table D.1 and the fracture toughness of PWA 1480, a K_{TH} value of between $25 \text{ MPa}\sqrt{\text{m}}$ and $40 \text{ MPa}\sqrt{\text{m}}$ was expected. The first set of samples immediately fractured when hydrogen gas was introduced into the system. The initial K value was about $75 \text{ MPa}\sqrt{\text{m}}$, so this was reduced on the second set of samples to $50 \text{ MPa}\sqrt{\text{m}}$ and $35 \text{ MPa}\sqrt{\text{m}}$. These samples also fractured quickly, but some data was obtained. Figure D.4 shows a typical profile of crack growth rate versus stress intensity. The crack growth rate increased in the beginning of the test and leveled off just before fracture. Normally, in a hydrogen-induced crack growth test, the crack begins growing rapidly at the onset but quickly slows down as the stress intensity decreases, as shown in Figure D.2. This is followed by a long period of steady crack growth before the crack

finally slows and stops. These stages of crack growth were never observed, and the crack grew rapidly and independently of the stress intensity level.

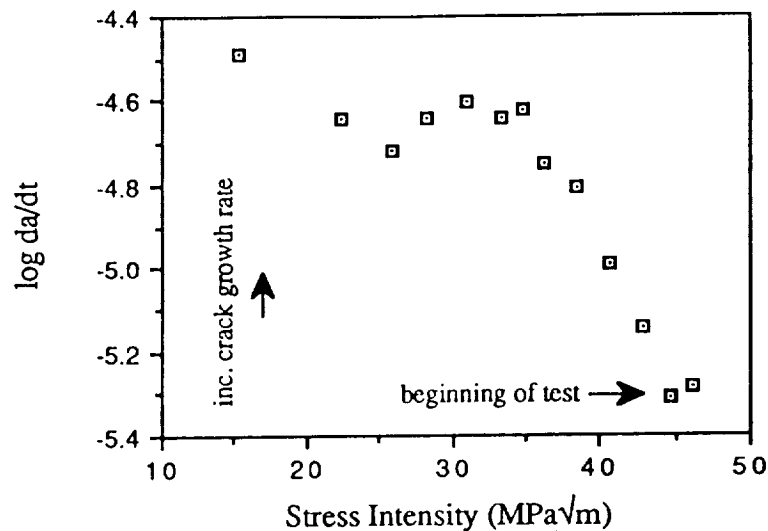
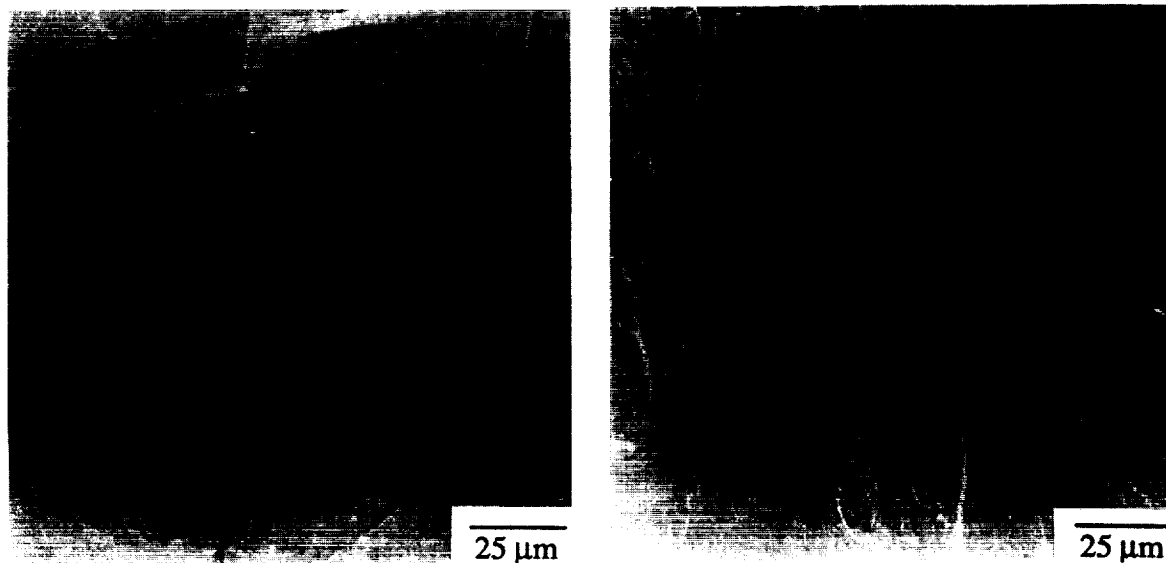


Figure D.4 Typical crack growth rate versus stress intensity in PWA 1480.

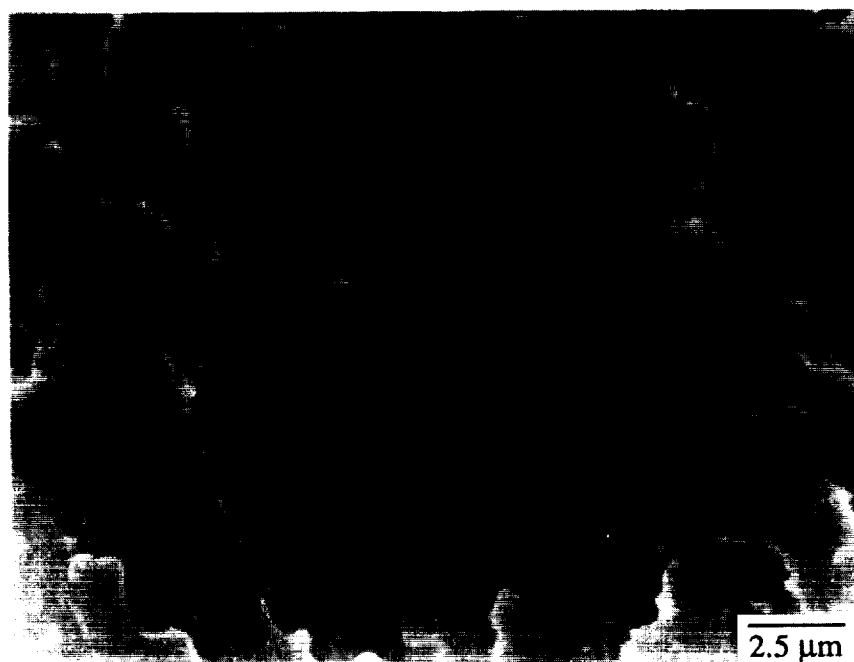
Figure D.5 shows the fractography of one of the samples. It is evident from the γ/γ' outline in Figure D.5c that the crack is growing macroscopically along $\{001\}$ planes. This type of fracture previously has been observed in these types of alloys in hydrogen charged²¹ and uncharged samples.²² Fracture along $\{111\}$ planes was observed, similar to the fracture in tensile and fracture toughness samples, however the $\{001\}$ fracture was predominant. Cube slip has not been reported at room temperature in these alloys,²³ so all of the deformation must be occurring by $\{111\}$ slip in the γ matrix. This is similar to tensile samples where the majority of deformation was in the γ matrix, but now the final fracture is probably occurring through the γ matrix on the $\{001\}$ planes instead of through both phases on $\{111\}$ planes.

ORIGINAL PAGE
BLACK AND WHITE PHOTOGRAPH



(a)

(b)



(c)

Figure D.5 Fractography of hydrogen-induced crack growth samples. (a) 100x (b) 500x (c) 5000x, showing {001} faces of γ precipitates.

The cause for this rapid failure is unknown, but some aspects become more clear by examining the role of hydrogen diffusion during the test. The final fracture is occurring within a few minutes of the introduction of hydrogen gas, and it is not believed that long range diffusion of hydrogen into the alloy is occurring. An approach similar to the one used by Johnson²⁴ can estimate the distance that hydrogen has penetrated. Using the IN 903 diffusion constant at room temperature of $1.4 \times 10^{-11} \text{ cm}^2/\text{s}$ and an average crack velocity of $2 \times 10^{-5} \text{ m/s}$, Johnson's analysis indicates that hydrogen can only penetrate about 10\AA (about four atomic spacings). This is in close agreement with the results of Perra and Stoltz²⁵ using the same approach for JBK-75. It also has been shown that the maximum local stresses are reached ahead of a crack tip,²⁶ and this has been suggested as the site of embrittlement.^{12,27} For a stress intensity of $35 \text{ MPa}\sqrt{\text{m}}$ and a flow stress of 1100 MPa , the peak stress occurs approximately $200 \mu\text{m}$ ahead of the crack tip. This is five orders of magnitude farther from the crack tip than the distance hydrogen can diffuse by bulk diffusion. This analysis suggests either that embrittlement is occurring near the surface or that bulk diffusion is not the controlling parameter.

The diffusion analysis ignored the effect of stress on diffusion, but Baskes and Melius²⁸ have shown that hydrogen diffusivity is not greatly enhanced in the presence of crack tip stress fields in fcc metals. Hydrogen transport by dislocations is another possible transport mode,²⁹ but given the almost immediate rapid crack growth that occurred, this is not likely to be an applicable mechanism. It remains that some type of surface effect is controlling crack initiation and propagation, and further studies are needed to examine this possibility. Experiments are planned using the same experimental setup but with an initial applied stress intensity of about $20 \text{ MPa}\sqrt{\text{m}}$.

References

1. S.R. Novak and S.T. Rolfe, *J. Materials*, **4**, (1969), (1969).
2. R.P. Wei and S.R. Novak, *J. Test. Eval.*, **15**, (1987), 37-75.
3. A. Saxena and J. S.J. Hudak, *Int. J. Frac.*, **14**, (1978), 453-467.
4. *ASTM E399-83, 1983 Annual Book of ASTM Standards*, Phila., Pa., 1983, pp. 518-553.
5. R.W. Hertzberg, "*Deformation and Fracture Mechanics of Engineering Materials*," Wiley and Sons, New York, 1989, 431-453.
6. K.N. Akhurst and T.J. Baker, *Met. Trans.*, **12A**, (1981), 1059-1070.
7. R.A. Oriani and P.H. Josephic, *Acta Met.*, **25**, (1977), 979-988.
8. P. Doig and G.T. Jones, *Met Trans.*, **8A**, (1977), 1993-1998.
9. W.W. Gerberich and A.G. Wright, *Environmental Degradation of Eng. Mat. in Hydrogen*, eds. M.R. Louthan, Jr., R.P. McNitt, R.D. Sisson, Jr., Virginia Tech. Publ., Blacksburg, Va., 1981, 183-206.
10. S.V. Nair and J.K. Tien, *Met. Trans.*, **16A**, (1985), 2333-2340.
11. J.C.M. Li, R. Oriani and L.S. Darken, *Z. Phys. Chem. Neue Folge*, **49**, (1966), 271-290.
12. C.L. Briant, H.C. Feng and J. S.J. McMahon, *Met. Trans.*, **9A**, (1978), 625-?
13. N.R. Moody, R.E. Stoltz and M.W. Perra, *Scripta Met.*, **20**, (1985), 119-123.
14. R.E. Stoltz, N.R. Moody and M.W. Perra, *Met. Trans.*, **14A**, (1983), 1528-1531.
15. R.J. Walter and W.T. Chandler, *Environmental Degradation of Eng. Mat. in Hydrogen*, eds. M.R. Louthan, Jr., R.P. McNitt and R.D. Sisson, Jr., Virginia Tech Publ., Blacksburg, Va., 1981, 513-522.
16. P.M. Lorenz, *Boeing Document D2-114417-1*, The Boeing Co., Seattle, Wash., 1969.
17. R.P. Jewett, R.J. Walter, W.T. Chandler and R.P. Frohberg, *NASA CR-2163*, "*Hydrogen Environment Embrittlement of Metals*," 1973.
18. R.E. Stoltz and A.J. West, *Hydrogen in Metals*, eds. I.M. Bernstein and A.W. Thompson, TMS-AIME, 1980, 541-553.
19. N.R. Moody, M.W. Perra and S.L. Robinson, *Scripta Met.*, **22**, (1988), 1261-1266.

20. A.W. Loginow and E.H. Phelps, *Corrosion*, **31**, (1975), 404-412.
21. C.L. Baker, J. Chene, I.M. Bernstein and J.C. Williams, *Met. Trans.*, **19A**, (1988), 73-82.
22. J. Telesman and L.J. Ghosn, *Superalloys 1988*, eds. D.N. Duhl, et al., AIME, 1988, 615-624.
23. R.V. Miner, R.C. Voigt, J. Gayda and T.P. Gabb, *Met. Trans.*, **17A**, (1986), 491-505.
24. H.H. Johnson, *Hydrogen in Metals*, eds. I.M. Bernstein and A.W. Thompson, TMS-AIME, 1974, 34-49.
25. M.W. Perra and R.E. Stoltz, *Hydrogen in Metals*, eds. I.M. Bernstein and A.W. Thompson, TMS-AIME, 1981, 645-653.
26. J.R. Rice and M.A. Johnson, *Inelastic Behavior of Solids*, eds. M.F. Kanninen, et al., McGraw Hill, New York, 1970, 641-672.
27. A.R. Troiano, *Trans. ASM*, **52**, (1960), 54-80.
28. M.I. Baskes and C.F. Melius, *Z. Phys. Chem. Neue Folge*, **116**, (1979), 289-299.
29. J.K. Tien, S.V. Nair and R.R. Jensen, *Hydrogen in Metals*, eds. I.M. Bernstein and A.W. Thompson, TMS-AIME, 1980, 37-56.

APPENDIX E

TRITIUM AUTORADIOGRAPHY

E.1 Background

The distribution of hydrogen in metals can be studied by autoradiography using tritium as a tracer. Tritium autoradiography for metallurgical purposes has been done on a limited scale for more than 20 years.^{1,2} The technique is not widely used in hydrogen embrittlement studies possibly because of the complicated experimental procedures involved and the considerable effort required to perfect the technique. There is also the safety aspect to consider, although tritium does not pose serious problems unless released in large quantities. The vast majority of studies have been performed on ferrous alloys,³⁻¹¹ and only two have examined nickel-base alloys.^{12,13}

Tritium autoradiography involves placing tritium-charged samples in contact with a photographic film so that upon the decay of tritium to helium-3, the emitted β particle can interact with the silver halide grains in the emulsion.¹ During subsequent photographic development, those grains that have been struck by β particles are converted into silver filaments, and the unexposed grains are dissolved. The silver grains can then be examined on the microscope and correlated to the underlying microstructure.

The introduction of tritium into the samples is similar to hydrogen charging and can be accomplished by either cathodic charging^{3-6,8,11} or gas-phase charging.^{7,9,10} In cathodic charging, tritiated water is simply added to the molten salt, and the same conditions are used as in hydrogen charging.¹⁴ Likewise, gas-phase tritium charging involves the same pressures and temperatures as in gas-phase hydrogen charging.¹⁵

After tritium charging, the photographic emulsion is applied; there are a variety of emulsions that can be used depending on the results desired. For observations where sub-

micron resolution is not required, stripping films such as AR-10 may be used.^{7,16,17} The advantages of the stripping film are that it provides a uniformly thick emulsion and gelatin layer, and is relatively easy to use. Care must be taken, however, not to introduce artifacts caused by mishandling the film. This technique has been successful when used in conjunction with optical microscopy^{7,16,17} but not with scanning electron microscopy (SEM).⁷ This stems from the thick gelatin layer (~4 μ m) that remains on the sample after photographic developing and results in charging effects and foggy pictures on the SEM.

The other type of emulsion commonly used is a liquid emulsion; Ilford L4 or Kodak NTB-2 are the two most popular brands.^{3-6,8-10,12,13} The emulsion comes in the form of a gel, and there are many procedures that must be followed to prepare the emulsion for application and ensure a uniform coating thickness. There also is a gelatin layer in these emulsions, but with careful preparation the thickness of this layer can be minimized.^{7,18} This allows easier observation on the SEM or TEM, and resolutions approaching 0.1 μ m have been reported.¹⁸

To avoid diffusion of tritium during exposure that would result in ambiguous results,¹⁹ exposure usually takes place at liquid nitrogen temperatures.^{1,18} The length of exposure and developing conditions are among the variables that must be adjusted to achieve the best results.

Tritium autoradiography has been used on ferrous alloys to determine trapping at heterogeneities, such as particle interfaces, grain boundaries and dislocations.³⁻¹¹ Attempts have been made to quantify the amount of tritium in the samples based on the appearance of the autoradiograph,^{2,7,19} but currently there are too many unknown variables to provide reliable data. Brass, et al.,¹² have found that in pure nickel, trapping of hydrogen occurs at grain boundaries. In the same laboratory, Roux, et al.,¹³ studied a single crystal alloy based on the γ' phase of CMSX-2 and found that hydrogen strongly segregated to the eutectic γ/γ' . Since the silver grains were observed uniformly through the eutectic γ/γ' , it is believed that a higher tritium solubility in this constituent compared to the surrounding

microstructure can explain the enhanced tritium concentration.²⁰ This is especially relevant to this work because of the eutectic γ/γ present in PWA 1480. There have not been any efforts to study the hydrogen solubility or trapping characteristics of the γ/γ microstructure using tritium autoradiography. Since the best resolution attainable is only about 0.1 μm , the results would be ambiguous because the γ matrix channels in the γ/γ microstructure are about 0.1 μm , and it would not be possible to separate trapping at the γ/γ interface from lattice trapping or solubility differences.

E.2 Experimental Procedures

Samples were cut to approximately 1 cm x 2 cm x 0.2 cm on a slow speed diamond cut-off wheel. The dimensions were chosen to give both a proper current density during charging and optimum resolution from the emulsion. The samples were hand-ground to 600 grit silicon carbide paper and then polished with 1 μm Al_2O_3 slurry. The tritium charging facility is housed in a self-contained glove box, and tritium levels were measured in the glove box and an interchange container by a Betatec S/N 611 ionization chamber manufactured by Overhoff Technology. Figure E.1 is a schematic of the tritium charging facility. The fume hood has a nominal flow rate of 600 cfm and exhausts to a roof vent. A small negative pressure was maintained in the glove box and monitored by a magnehelic gauge. Periodic smear samples were taken from the glove box, and continuous room air monitoring occurred during the test.

Tritium was introduced into the sample by cathodic charging in a tritiated molten salt solution. The initial amount of tritium was 10 Curies and a specific activity of 0.2 Ci/cm^3 was used. By-products of the tritiated solution were channeled through a series of condensers and traps to minimize the amount of released tritium and tritiated water vapor. The molten salt consists of 57% by weight $\text{NaHSO}_4 \cdot \text{H}_2\text{O}$ (Sodium Bisulfate) and 43% KHSO_4 (Potassium Bisulfate). Cathodic charging took place at 150°C with the sample

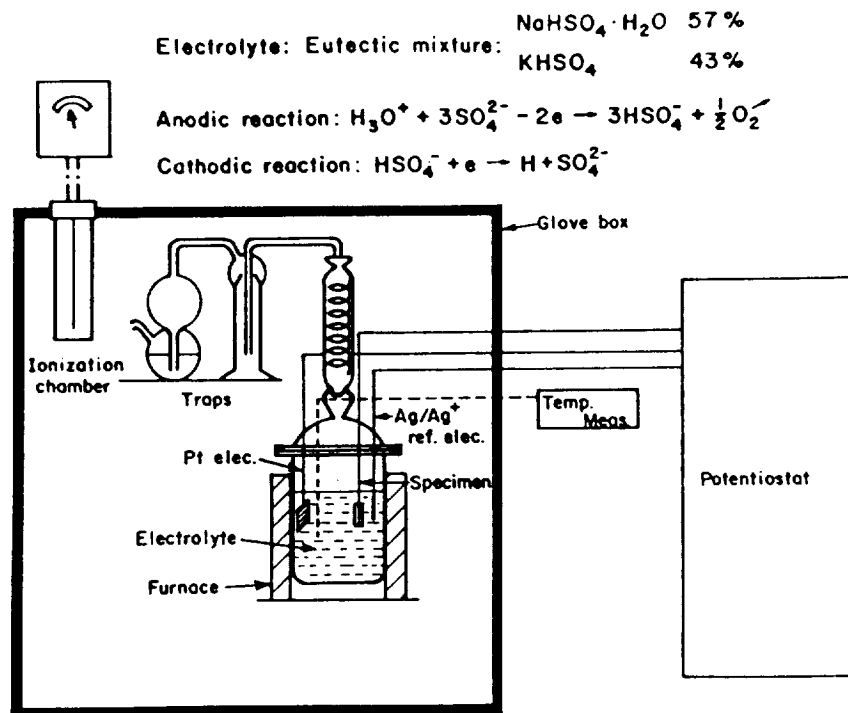


Figure E.1 Schematic of the tritium charging apparatus.

acting as the cathode. The surface of the sample was first etched by applying -25 mV and 10 mA for four minutes. Charging was done at -800 mV and 10 mA for 2-4 hours, which resulted in a low current density of 5 mA/cm². After charging, the sample was removed from the pyrex kettle and rinsed with distilled water. The tritiated absorbed layer is then removed by hand-grinding with 600 grit paper. The sample remained in the glove box at room temperature for 24 hours to allow outgassing of the "diffusible" tritium. Subsequently, it was transferred into the interchange chamber and removed after significant tritium outgassing ceased. Further sample manipulations were made using only disposable rubber gloves since the "diffusible" tritium had been removed. The sample was further polished under a fume hood using 1 μm diamond paste. After polishing, the tritium concentration was measured by a liquid scintillation counter. Typical concentrations ranged from 6,000 to 20,000 disintegrations per minute (dpm). Polishing was continued to 0.05 μm Al₂O₃ and samples were etched using one of the etches previously mentioned in section 3.3.1.

Typically, a liquid emulsion then would be applied to the sample, however in this study a stripping film containing an emulsion layer was used instead. The liquid emulsions are much harder to work with and, more importantly, only have a shelf life of two months.²¹ The liquid emulsion does have the advantage of a better resolution of slightly less than 0.1 μm ,¹⁸ however this is not sufficient to observe trapping at the γ/γ' interface. The primary concern of this study was trapping at the dendritic macrostructure and eutectic γ/γ' , so such a fine resolution was not needed. Therefore AR-10 stripping film from Kodak was used, which has a resolution of 2.0 μm and a shelf life of one year.²² The stripping layer, mounted on a glass plate, consists of a 5 μm thick emulsion coating on a gelatin layer 10 μm thick. In order to transfer the emulsion to the sample, squares slightly larger than the samples were cut and placed emulsion side down in a sugar solution of controlled bromide concentration. It is claimed that this allows better transfer and gives improved results when using long exposure times.²³ The solution consisted of 0.05 g potassium bromide, 100 g sucrose and 500 ml of distilled water. This solution is then further diluted 9:1 with distilled water.

In a darkroom using a safelamp with a Kodak Series 1 filter, the stripping film was floated emulsion side down for three minutes to allow expansion. The sample was dipped in the solution and raised at a 45° angle so that the stripping film smoothly coated the sample. It was then allowed to dry slowly in a dust-free environment. After drying, it was stored in a light-tight dry container and exposed for 3-5 days. The sample container was immersed in liquid nitrogen to minimize the background created by tritium diffusion. The developing instructions furnished with the AR-10 stripping film were followed:

- 5 minutes in full strength Dektol developer.
- Rinse in slow running water for 30 seconds.
- Fix for 8 minutes in Kodak fixer.
- Rinse in slow running water for 2-3 minutes.
- Dry slowly in a dust-free environment.

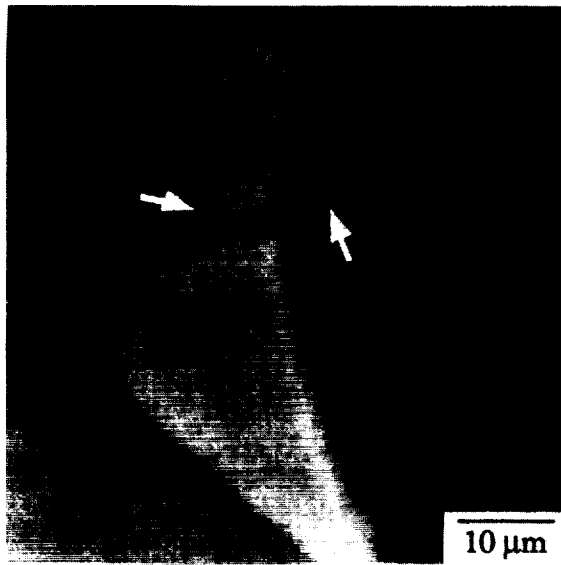
Observation of the developed sample was done on an optical microscope and SEM. The underlying microstructure can be seen easier on the optical microscope, however the distribution of the silver grains is better observed using the energy dispersive x-ray unit (EDX) on the SEM.

E.3 Results and Discussion

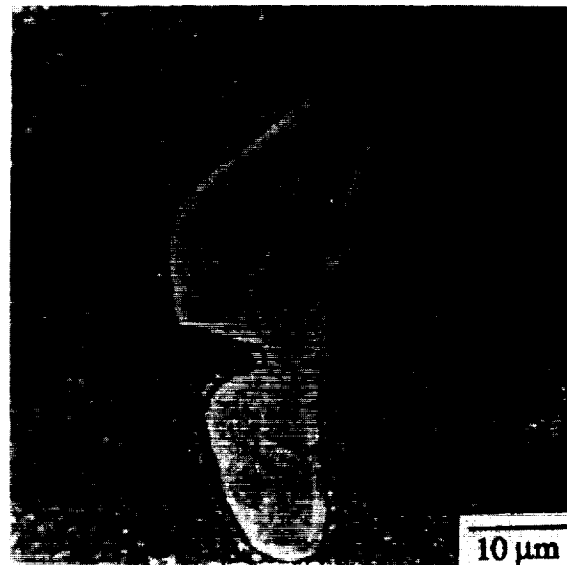
Tritium was successfully charged into many samples in sufficient concentrations to ensure that some tritium remained after polishing. After many trial and error attempts at photographic developing and subsequent observation, all experimental obstacles had been overcome. It was found that placement of the stripping film on the sample and exposure time were two of the more critical steps. Stretch marks on the emulsion layer during drying led to many artifacts, as did any dust that may have settled on the sample.

The underlying microstructure was seen quite easily on the optical microscope, and to observe silver grains, the microscope was focused on the gelatin layer above the sample. The silver grains were black, random in shape and a few micrometers in diameter. Figure E.2 shows silver grains uniformly across the sample with no segregation to the eutectic γ/γ' . In order to confirm that these were in fact silver grains, the energy dispersive x-ray unit (EDX) on the SEM was used. On the SEM the microstructure was almost indistinguishable through the gelatin layer, and there were serious charging problems. Despite these problems, it was possible to get a map of the silver distribution using the EDX unit, as shown in Figure E.3. This confirmed the optical microscopy results that showed a uniform distribution of silver. It was not possible to correlate the silver distribution with the underlying microstructure because of the effects of the gelatin layer.

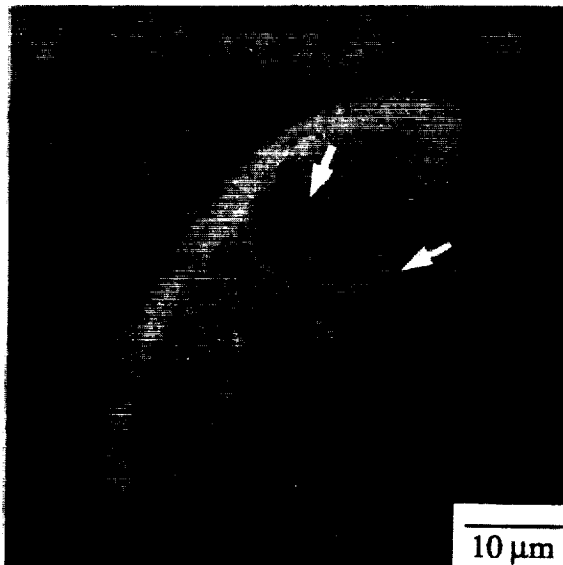
ORIGINAL PAGE
BLACK AND WHITE PHOTOGRAPH



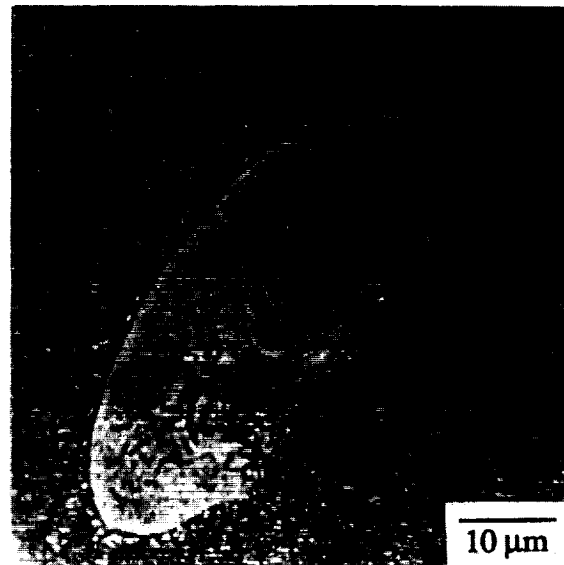
(a)



(b)



(c)



(d)

Figure E.2 (a & c) Optical micrograph of eutectic γ/γ' observed through the gelatin layer and (b & d) corresponding Ag layer.

ORIGINAL PAGE
BLACK AND WHITE PHOTOGRAPH

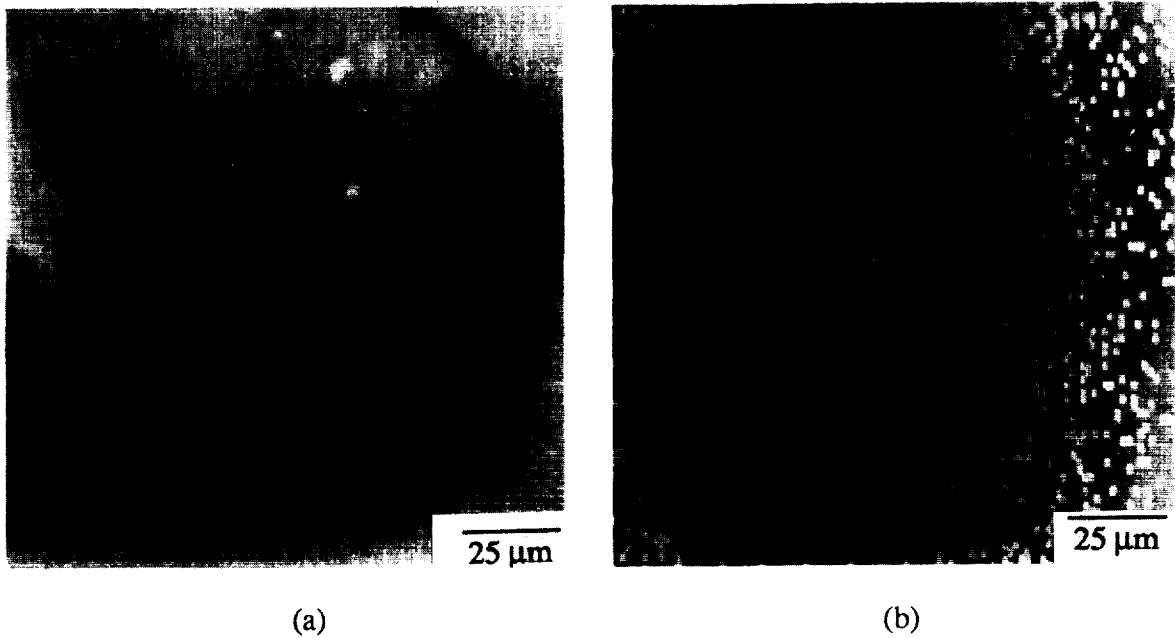


Figure E.3 (a) SEM micrograph of microstructure viewed through the gelatin layer.
(b) Corresponding uniform distribution of Ag grains.

The preliminary results differ from the results of Roux, et al.,¹³ that showed a strong segregation of the tritium to the eutectic γ/γ' . The study of Roux, et al., was performed by the group at the Université Paris-Sud, which has had extensive experience in tritium autoradiography. It remains unexplained why this study resulted in an apparent uniform distribution of tritium. A more thorough study needs to be done varying the charging conditions, outgassing and exposure times. It also would be worthwhile to use one of the liquid emulsions to facilitate observation on the SEM.

References

1. G.R. Caskey, *Adv. Tech. for Characterizing Hydrogen in Metals*, eds. N.F. Fiore and B.J. Berkowitz, Warrendale, Pa, 1981, 61-75.
2. N.A. Tiner, T.L. Mackay, S.K. Asunmaa and R.G. Ingersoll, *Trans. ASM*, **61**, (1968), 195-202.
3. M. Aucouturier, G. Lapasset and T. Asaoka, *Metallography*, **11**, (1978), 5-21.
4. J. Chéne and M. Aucouturier, *Hydrogen in Metals*, eds. I.M. Bernstein and A.W. Thompson, TMS-AIME, 1980, 583-595.
5. J.P. Laurent, G. Lapasset, M. Aucouturier and P. Lacombe, *Hydrogen in Metals*, eds. I.M. Bernstein and A.W. Thompson, ASM, 1974, 559-573.
6. M. Aucouturier, *Current Solutions to Hydrogen Problems in Steels*, eds. C.G. Interrante and G.M. Pressouyre, ASM, 1982, 407-412.
7. G.P. Marsh, *United Kingdom Atomic Energy Authority AERE-R8560*, "An Assessment of Some Techniques Available for the Local Detection of Hydrogen in Metals," 1976.
8. T.D. Le and B.E. Wilde, *Current Solutions to Hydrogen Problems in Steels*, eds. C.G. Interrante and G.M. Pressouyre, ASM, 1982, 413-422.
9. G.L. Downs, *Environmental Degradation of Engineering Materials*, eds. M.R. Louthan, Jr., R.P. McNitt and R.D. Sisson, Jr., Virginia Tech. Publ., Blacksburg, Va., 1981, 425-435.
10. G.R. Fritsche and B.M. Strauss, *Metallography*, **4**, (1971), 223-230.
11. H. Ohma, G.P. Tiwari, Y. Iijima and K. Hirano, *Proc. JIMIS-2, Hydrogen in Metals*, Japan Inst. of Metals, Minakami, Japan, 1980, 229-232.
12. A.M. Brass, A. Chanfreau and J. Chéne, *Hydrogen Effects on Materials Behavior*, eds. N.R. Moody and A.W. Thompson, TMS-AIME, 1989, to be publ.
13. R. Roux, A.M. Brass and J. Chene, *Hydrogen Effects on Material Behavior*, eds. N.R. Moody and A.W. Thompson, TMS-AIME, 1989, to be published.
14. C.L. Baker, J. Chene, I.M. Bernstein and J.C. Williams, *Met. Trans.*, **19A**, (1988), 73-82.
15. S.H. Goods, *Scripta Met.*, **20**, (1986), 565-569.
16. J.D. Braun, G.L. Downs and G.W. Powell, *Metallography*, **4**, (1971), 231-242.
17. G.W. Powell, J.D. Braun, K.F. Chaney and G.L. Downs, *Corrosion*, **26**, (1970), 223-228.

18. P. Lacombe, M. Aucouturier and J. Chéne, *Hydrogen Embrittlement and Stress Corrosion Cracking*, eds. R. Gibala and R.F. Hehemann, ASM, 1980, 79-102.
19. J. M.R. Louthan, J. D.E. Rawl and R.T. Huntoon, *Corrosion*, **28**, (1972), 172-176.
20. J. Chéne, Université Paris Sud, unpublished research.
21. *Kodak Tech Bits, Spring 1988*, "Autoradiography at the Light Microscope Level," Eastman Kodak Co., Rochester, NY, 1988.
22. *Kodak Publ. P-64*, "Kodak Products for Light Microscope Autoradiography," Eastman Kodak Co., Rochester, NY, 1987.
23. *Brit. J. of Radiology*, **42**, (1969), 862-870.

APPENDIX F

QUANTITATIVE RESULTS OF REPPICH CRSS MODEL

This appendix will quantitatively examine the applicability of the Reppich model to PWA 1480. Reppich and co-workers¹⁻³ have analyzed the increase in the flow stress due to the presence of coherent, ordered particles as a function of their size and volume fraction. To apply the model, it must be determined whether the dislocations will be weakly coupled or strongly coupled, and the critical particle size for this transition, d_{ws} , can be determined using:²

$$d_{ws} = 0.78w \left(\frac{2T}{\gamma} \right) \quad (5.6)$$

where w is a term accounting for the elastic repulsion between paired dislocations outside the particles, T is line tension and γ is the APB energy. For similar alloys $w = 2.8$,⁴ and it has been reported that $\gamma = 118 \text{ mJ/m}^2$ in PWA 1480.⁵

The constant line tension approximation is inaccurate for these anisotropic alloys, so a more exact form will be used. Ham⁶ has shown that in these types of alloys, edge dislocations are more resistant to motion than screw dislocations, and Reppich gives the line tension as:⁴

$$T = \left(K(\theta) + \frac{d^2K}{d\theta^2} \right) \left(\frac{b^2}{4\pi} \right) \ln \frac{L}{b} \quad (5.7)$$

where L is the distance between precipitates in the $\{111\}$ plane and can be calculated from $L = (\pi/6f)^{1/2}d$, where f is the volume fraction of precipitates and d is the precipitate size. The quantity $(K(\theta) + d^2K/d\theta^2)$ is equal to $G/2$ for edge dislocations, where G is the shear

modulus. Using $f = 0.7$, $d = 0.45 \mu\text{m}$ and $b = 2.5 \times 10^{-8} \text{ cm}$, the line tension for edge dislocations reduces to:

$$T = \frac{Gb^2}{3.4} \quad (5.8)$$

This is slightly different than the constant line tension approximation of $Gb^2/2$ and is close to other estimates.^{4,7} Using this line tension value and $G = 54.5 \text{ MPa}$, equation 5.6 gives a value of $0.18 \mu\text{m}$ for d_{ws} . This means that in PWA 1480 with $d = 0.45 \mu\text{m}$, $d > d_{ws}$, and strong pair coupling occurs, as expected.

According to the Huther-Reppich model,² the increase in the CRSS due to over-aged, spherical particles that are cut by strongly coupled dislocations is:²

$$\Delta\tau_o = 0.86 \frac{Twf^{1/2}}{bd} \left(1.28 \frac{d\gamma}{wT} - 1 \right)^{1/2} \quad (5.9)$$

where b is the Burgers vector and f is the volume fraction of precipitates. The stress to cause the first dislocation to penetrate the precipitate is:³

$$\Delta\tau_p = \frac{\gamma}{b} - \frac{0.72Gb}{d} \quad (5.10)$$

Since Orowan looping does not occur at room temperature because of the high volume fraction of precipitates, one of the two processes described by (5.9) and (5.10) must be controlling the CRSS. The cutting stress (5.9) was 103 MPa , and the penetration stress (5.10) was 449 MPa . The highest of these two will be the controlling strengthening mechanism, and therefore the CRSS is modeled using the penetration stress.

The Schwarz-Labusch correction⁸ must be used because the Huther-Reppich model is based on a low volume fraction of precipitates. The "reduced particle depth", η_o , is used

and for large particles can be written as:⁸

$$\eta_o = \left(\frac{f}{\pi}\right)^{1/2} \quad (5.11)$$

A value of 0.47 was obtained for PWA 1480 clearly not fulfilling the $\eta_o \ll 1$ criterion to use low volume fraction, Fleischer-Friedel type models.^{9,10} The interpolation formula to convert to high volume fraction models is:⁸

$$\Delta\tau_o = 0.95(1 + C\eta_o)\Delta\tau_{FF} \quad (5.12)$$

where $\Delta\tau_{FF}$ is the increase in CRSS due to the presence of a low volume fraction of particles, as calculated above, and C is a constant close to three for high volume fractions.⁴ The increase in the CRSS due to the presence of a high volume fraction of γ precipitates has been calculated to be 1028 MPa. To obtain the total CRSS for the alloy, the solid solution strengthening contribution of the matrix, τ_M , must be incorporated. A variety of addition rules have been used to calculate the total CRSS in this type of alloy.¹¹ Linear addition has met with some success^{7,12} and will be used in this study. Using an alloy of similar composition to the γ matrix phase of PWA 1480, $\Delta\tau_M$ was determined to be about 115 MPa at room temperature.¹³ The total τ_{CRSS} then becomes 1143 MPa, which is considerably higher than the 450 MPa obtained for PWA 1480.

While the Huther-Reppich model does not quantitatively predict the CRSS well, it does show that initial penetration of the γ precipitate is controlling the CRSS of PWA 1480. There are two reasons why the model did not predict the observed CRSS more closely. Perhaps the largest inaccuracy is that the Huther-Reppich model only considers the leading dislocation and does not account for the interaction term between the pair of dislocations. This explains why the leading term in equation 5.3 is γ/b and not $\gamma/2b$, as in other order strengthening theories.^{9,11,13,14} This would have reduced the CRSS by almost half, resulting in a reasonable value. Further, Ardell¹¹ points out that there is a large

spread in the values obtained by different investigators for the constants C and w. 4,7,12,15,16

References

1. W. Huther and B. Reppich, *Mat. Sci. and Eng.*, **39**, (1979), 247-259.
2. W. Huther and B. Reppich, *Z. Metallk.*, **69**, (1978), 628-634.
3. B. Reppich, *Acta Met.*, **30**, (1982), 87-104.
4. B. Reppich, P. Schepp and G. Wehner, *Acta Met.*, **30**, (1982), 95-104.
5. M. Dollar and I.M. Bernstein, *Superalloys 1988*, eds. D.N. Duhl, et al., TMS-AIME, 1988, 275-284.
6. R.K. Ham, *Trans. Japan Inst. Metals*, Vol. 9 supplement, (1968), 52.
7. A.W. Thompson and J.A. Brooks, *Acta Met.*, **30**, (1982), 2197-2203.
8. R.B. Schwarz and R. Labusch, *J. Appl. Phys.*, **49**, (1978), 5174-5187.
9. L.M. Brown and R.K. Ham, *Strengthening Methods in Crystals*, eds. A. Kelly and R.B. Nicholson, Wiley, New York, 1971, 96-112.
10. R.L. Fleischer, *Acta Met.*, **11**, (1963), 203-209.
11. A.J. Ardell, *Met. Trans.*, **16A**, (1985), 2131-2165.
12. P. Haasen and R. Labusch, *5th Int'l Conf. on Strength of Metals and Alloys*, eds. P. Haasen, V. Gerold and G. Kostorz, Pergamon Press, Oxford, 1979, 639-643.
13. S.M. Copley and B.H. Kear, *Trans. TMS-AIME*, **239**, (1967), 984-992.
14. A. Melander and P.A. Pearson, *Metal Sci.*, **12**, (1978), 391-398.
15. E. Nembach, *Z. Metallkd.*, **72**, (1981), 401-405.
16. M. Grohlich, P. Haasen and G. Frommeyer, *Scr. Met.*, **16**, (1982), 367-370.



National Aeronautics and
Space Administration

Report Documentation Page

1. Report No. NASA CR-185219		2. Government Accession No.		3. Recipient's Catalog No.	
4. Title and Subtitle The Effect of Hydrogen and Microstructure on the Deformation and Fracture Behavior of a Single Crystal Nickel-Base Superalloy				5. Report Date April 1990	
				6. Performing Organization Code	
7. Author(s) William S. Walston				8. Performing Organization Report No. None	
				10. Work Unit No. 553-13-00	
9. Performing Organization Name and Address Carnegie-Mellon University Pittsburgh, Pennsylvania 15213				11. Contract or Grant No. NAG3-463	
				13. Type of Report and Period Covered Contractor Report Final	
12. Sponsoring Agency Name and Address National Aeronautics and Space Administration Lewis Research Center Cleveland, Ohio 44135-3191				14. Sponsoring Agency Code	
15. Supplementary Notes Project Manager, Robert L. Dreshfield, Materials Division, NASA Lewis Research Center. This report was a thesis submitted to Carnegie-Mellon University in January 1990 in partial fulfillment of the requirements for the degree of Doctor of Philosophy in Metallurgical Engineering and Materials Science.					
16. Abstract A study has been conducted on the effects of internal hydrogen and microstructure on the deformation and fracture of a single crystal nickel-base superalloy. In particular, room temperature plane strain fracture toughness and tensile tests were performed on hydrogen-free and hydrogen charged samples of PWA 1480. The role of microstructure was incorporated by varying the levels of porosity and eutectic γ/γ' through hot isostatic pressing and heat treatment. The room temperature behavior of PWA 1480 was unusual because precipitate shearing was not the primary deformation mechanism at all strains. At strains over 1%, dislocations were trapped in the γ matrix, and an attempt was made to relate this behavior to compositional differences between PWA 1480 and other superalloys. Another unique feature of the tensile behavior was cleavage of the eutectic γ/γ' , which is believed to initiate the failure process. Fracture occurred on $\{111\}$ planes and is likely a result of shear localization along these planes. Elimination of the eutectic γ/γ' greatly improved the tensile ductility, but porosity had no effect on tensile properties. Large quantities of hydrogen (1.74 at.%) were gas-phase charged into the material, but surprisingly this was not a function of the amount of porosity or eutectic γ/γ' present. Desorption experiments suggest that the vast majority of hydrogen is at reversible lattice trapping sites. This large, uniform concentration of hydrogen dramatically reduced the tensile strain to failure, but only slightly affected the reduction in area. Further evidence of strain localization due to hydrogen was observed in the deformation structure. Available hydrogen embrittlement models were examined in light of these results and it was found that the hydrogen enhanced localized plasticity model can explain much of the tensile behavior. K_{IC} fracture toughness tests were conducted, but it was necessary to also perform J_{IC} tests to provide valid data. Unexpectedly, the values from these tests did not agree; further, the crack growth behavior and fractography differed greatly. The eutectic γ/γ' behaved differently in these two types of tests, and the possible effect of the unloading present in J_{IC} tests on this constituent was examined.					
17. Key Words (Suggested by Author(s)) Superalloys Single crystals Hydrogen effects Nickel-base alloy			18. Distribution Statement Unclassified - Unlimited Subject Category 26		
19. Security Classif. (of this report) Unclassified		20. Security Classif. (of this page) Unclassified		21. No. of pages 255	22. Price* A12



National Aeronautics and
Space Administration

Lewis Research Center
Cleveland, Ohio 44135

Official Business
Penalty for Private Use \$300

FOURTH CLASS MAIL

ADDRESS CORRECTION REQUESTED



Postage and Fees Paid
National Aeronautics and
Space Administration
NASA-451

NASA
